BEARING WORLD

www.bearingworld.org

Journal

Volume 3_2018

Editors: G. Poll _ A. Grunau _ C. Kunze

Imprint

Volume 3_2018

···

Dear reader,

Globalization increasingly requires more and more international networking between research and development engineers. In response to this, the German Research Association for Drive Technology (FVA) launched the first Bearing World conference in 2016. With that inaugural meeting, the FVA initiated a very fruitful international dialogue in which researchers and developers from universities and bearing manufacturers came together with users and experts from the industry. The Bearing World conference is held every two years; more than 280 experts from 18 countries met at the last Bearing World conference in 2018 in Kaiserslautern, Germany, to share the latest research findings in the world of bearings. The next meeting will take place in Hannover, Germany, on March 31 and April 1, 2020.

The Bearing World Journal, which is published annually, serves to foster exchange between international experts during non-conference years by featuring peer-reviewed, high-quality scientific papers on rolling element bearings as well as plain bearings. As an international expert platform for publishing cutting-edge research findings, the journal intends to contribute to technological progress in the field of bearings.

We are now starting to prepare the 2019 edition of Bearing World Journal and are looking forward to new contributions from the scientific and industrial communities. We would like to thank all authors for their fascinating contributions to Bearing World Journal No. 3.

_ **Prof. Dr.-Ing. Gerhard Poll,** Initiator, Head of international Scientific Board
_ **Dr.-Ing. Arbogast Grunau,** President of the FVA Management Board
_ **Christian Kunze,** Editor-in-chief

Bearing World Scientific Board

Content

Evaluation of the effects of geometrical deviations on the fatigue life and vibrations of cylindrical roller bearings

R. Dahiwal[1], A. Aschenbrenner[2], B. Schleich[2], S.Wiesker[1], T. Kiekbusch[1], S. Tremmel[2], S. Wartzack[2], B. Sauer[1]

[1] *Institute of Machine Elements, Gears and Transmissions (MEGT,) University of Kaiserslautern, dahiwal@mv.uni-kl.de*
[2] *Engineering Design, Friedrich-Alexander-University Erlangen-Nürnberg, aschenbrenner@mfk.fau.de*

Abstract – Due to uncertainties in manufacturing processes all components suffer from geometric deviations and imperfections, even high-precision components like roller bearings. In general, tolerances define the allowable deviations of components and ensure their manufacturability, mountability and operational behavior. Nevertheless, geometric deviations can still unpredictably influence the operational behavior of components. Indeed, studies have shown that deviations together with the operating clearance can significantly affect the dynamic behavior and thus the fatigue life of roller bearings.

In this contribution, two simulation methods are employed in order to consider and study the effect of geometric deviations like roundness or dimensional deviations of bearings and their adjacent components (shaft and housing) on a cylindrical roller bearing's vibrational behavior and fatigue life. First, a statistical simulation model is introduced allowing an easy way to screen the operational clearance and fatigue life of a large number of cylindrical roller bearings. Afterward, a multibody dynamic model is used to gather detailed information about the load distribution on each rolling element and the inner ring displacement during operation. These methods allow a user of roller bearings a better understanding of the correlation between geometric deviations and a roller bearing's vibrational behavior as well as fatigue life. The methods should also aid a user to optimize the geometric definition and tolerancing of their components. After a detailed description of the methods, their application is demonstrated for a use case.

Keywords – Cylindrical Roller Bearing, Geometric Definition and Tolerancing, Statistical Variation Simulation, Dynamic simulation method

1. Introduction and Problem definition

Rolling Bearings are high-precision components which are applied in a great variety of machines. In general, not a single rolling bearing but a bearing system is used. Such a bearing system contains two or more rolling bearings. Key characteristics of a bearing system are service life, frictional loss, acoustics and vibrations. Among other things, these properties are influenced by geometric deviations, which are unavoidable due to manufacturing imprecision [1]. In order to limit these deviations to ensure the functional behavior and the mountability of a roller bearing, geometric definition and tolerancing is employed. However, the task of tolerancing is quite challenging: Too big tolerance values can lead to a loss of function, whereas too small tolerance values enormously affect the manufacturing costs [2]. Thus, guidelines are needed to assist a design engineer with the geometric definition and tolerancing of their components (namely shaft and housing).

From the literature, generic information regarding the tolerancing of a bearing's adjacent components can already be obtained (cf. [3] or [4]). What is more, some bearing components and dimensions are standardized, for instance, the bearing clearance classes (cf. ISO 5753-1 [5]), the bore diameter and outer diameter of a bearing according to a tolerance classes (cf. ISO 492 [6] or the cylindrical rolling elements (cf. DIN 5402-1 [7]). Moreover, there are a couple of publications dealing with the influence of different kinds of deviations on the functional behavior of rolling element bearings.

In [8] Oswald et al. derive life factors for interference fits of cylindrical roller bearings. However, only hoop stress is considered. The reduction of the bearing clearance due to the deformation of the interference fitted bearing rings was compensated. Yet, operating clearance influences the load distribution and thus the fatigue life of a rolling bearing (cf. ISO 16281 [9]). Therefore, Oswald et. al. also performed parametric studies to analyze the influence of varying radial clearance on the load distribution and fatigue life of ball bearings and cylindrical roller bearings [10].The operational clearance itself is influenced by the tightness of a fit [8] and the thermal deformations of shaft and housing (cf. [3] or [4]).

In respect to roundness deviations, Harris shows a significant influence of the out-of-roundness of bearing seats on waviness of bearing raceways [11]. Wardle [12] deals with the influence of raceway waviness on vibration forces. However, the presented model is restricted to lower rotational speeds, due to the negligence of ball-centrifugal forces. In addition to this, the tribological behavior of the bearing is not considered in this study. Harsha [13] introduces an extended calculation approach based on the potential and kinetic energy of the components. He takes into account the dynamic contribution of a rotor. A dynamic analysis of a ball bearing was carried out by Changqing et. al. [14]. They have taken the waviness of the bearing raceways and rollers as well as different operational clearance and the effects of preloading into account. To summarize, although there is some information on the tolerancing of bearing components and their adjacent components, the linkage between the actual effect of a deviation on a bearing's functional properties and the resulting consequences for the tolerancing of the involved components is missing.

In general, the effects of components with dimensional and geometric deviations on an actual assembly can be investigated with variation simulations. For this purpose, different methods like worst-case searching or statistical variation simulations are available [15]. Moreover, there are a couple of methods to

determine which input parameter contributes the most to the response of a system consisting of deviating components (so-called sensitivity analysis) [16].

However, for a design engineer, it might be uneconomic to apply advanced (dynamic) simulations methods or variation simulations on each use-case. Therefore, this contribution aims to study the deviations of the bearing seat, choose component tolerance classes and analyze their effects on fatigue and vibrational behavior of the bearing system with the help of introduced simulation approaches. The studies were carried out at the Friedrich-Alexander-University Erlangen-Nürnberg - Engineering Design (KTmfk) and at the Technical University of Kaiserslautern by the Institute of Machine Elements, Gears, and Transmissions (MEGT).

2. Approaches for Tolerance Analysis

For the evaluation of the effects of the geometric deviations on the fatigue life and vibrational behavior of cylindrical roller bearings, two different approaches are employed. On the one hand, the results of a variation simulation of cylindrical roller bearing's operating clearances are linked to fatigue life calculation. The variation simulation allows the consideration of a vast amount of combinations. It is therefore utilized for screening the design space of a cylindrical roller bearing system (consisting of the cylindrical roller bearing and its adjacent components). On the other hand, a method based on multibody simulations is used to gain a more detailed insight on specific design points within the design space. Both methods are discussed in the following subsections.

2.1. Variation simulation of cylindrical roller bearings

A tolerance analysis covers the representation of the geometrical deviations, the description of the behavior of a system consisting of deviating components and the application of proper analysis methods [15]. In terms of geometrical deviations, dimensional as well as geometrical accuracy (such as deviations from circular or cylindrical form) can be considered. In general, it is not feasible to analyze all deviating features of a product but only so-called functional key characteristics (FKCs). According to Thornton [17], FKCs are those features of a product, a subassembly or a part, which have a significant influence on the cost, performance or safety of a product. Thus, FKCs can represent the behavior of a deviating system or product. Although there are FKCs that can be described by only one deviating parameter, they normally have several influential contributors. In case of machine systems, the service life, reliability and maintenance intensity is often determined by the service life of individual machine elements, such as the fatigue life of its rolling element bearings. Thus, the fatigue life can be considered as one of the main FKCs. As the operating clearance directly influences the fatigue life of a rolling element bearing it could be considered as a FKCs as well. In contrast to fatigue life, the operating clearance is a purely geometric quantity and can be directly determined by a tolerance analysis. Hence, within the variation simulation, the results of the operating clearance are used to assess the influence of geometric deviation on the fatigue life of cylindrical roller bearings.

In general, different analysis methods can be utilized for the analysis of FKCs and their contributors, such as worst-case searching or statistical variation analysis. As the purpose of the herein described variation simulation is the screening of the design

space of a cylindrical roller bearing system, a statistical approach is applied. The workflow of the method follows the previously described threefold division [15] and is shown in Figure 1.
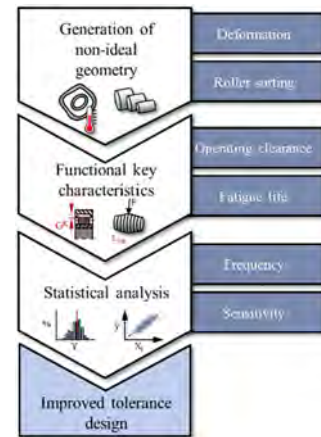
Figure 1: Workflow of the variation simulation of cylindrical roller bearings

At first, a huge amount of virtual bearing rings and adjacent components (namely shaft and housing) is sampled – each with its own unique dimensional and geometric deviations. These components are then randomly combined. Afterwards, the dimensions of the raceways of the bearing rings are used to select a roller sort to sample the rollers of this cylindrical roller bearing system. Within a roller sort, dimensional deviation may occur as well.

After the generation of the non-ideal components, the operating clearances of all virtual roller bearings are calculated using contact detection algorithms. These results are then linked to the determination of the fatigue life of each cylindrical roller bearing system using the calculation specifications of ISO/TS 16281 [9]. Afterwards, a statistical analysis is performed for both, operating clearance and fatigue life. For the statistical analysis, some statistical characteristics are evaluated such as the sample mean, the sample standard deviation and sensitivity of the FKCs with respect to the deviating geometrical parameters. This information can not only be used to identify critical or outstanding combinations for further examination but also for the improvement of the tolerance design of a cylindrical bearing system. In the following subsections, all steps are described in greater detail.

2.1.1. Generation of non-ideal geometry

Besides uncertainties related to the geometric deviations, which occur during the manufacturing of the bearing components, the operating clearance may also vary due to the deformation of the bearing rings. Deformation can result from the mounting of the bearing rings as well as of the thermal expansion of the bearing components. For the generation of the non-ideal geometry, all three aspects should be regarded.

In order to keep the complexity and the calculation efforts for the screening relatively low, only one 2D-radial cut of each bearing is considered. Within such a 2D section only the surfaces of the deviating components have to be considered for the evaluation of the operating clearance. Thus, the volumes of the components are neglected. Following the idea of [18], the non-ideal geometries are represented by a discrete geometry approach, i.e. surface meshes. A surface mesh is composed of vertices and edges. The position of

each vertex can be expressed in polar coordinates. In terms of angular distance, the vertices are equally distributed on the surface. The radial coordinate of each vertex could be obtained using mathematical descriptions such as the Discrete Fourier Transformation [19]. For the edges, linear as well as trial functions with the higher polynomial degree can be chosen (p-method). However, computation time will increase tremendously with the polynomial degree. Thus, linear edges are used. To make up for the resulting discretization error, the number of vertices is increased (h-method).

In case of the shaft and housing dimensional as well as geometrical deviations are considered. However, the tolerance design of the inner geometry of a cylindrical roller bearing is confidential company know-how of each bearing manufacture. Hence, only dimensional deviations of the bearing components are regarded. Tolerance values for the outer dimensions can be found in ISO 492 [6]. For a first approximation, the values of the inner dimensions can be derived from the values of the adjacent components of needle cages with a comparable size. While the sampling of the dimensional deviations is quite straight-forward, the aforementioned Fourier Transformations are employed for sampling the out-of-roundness of the adjacent components.

Bearing manufactures normally try to manufacture bearing components in such a manner, that the actual initial bearing clearance is near to the mean initial bearing clearance of a specific clearance class. For this purpose, the rolling elements are classified by their diameter, whereby each class has very tight specification limits. For instance, the allowable radial deviation of roller diameters smaller than 26 mm is 1 µm or less [7]. Once the bearing rings with their dimensional deviations are sampled, the values of the actual raceway diameters can be used to individually select a roller diameter class for each cylindrical roller bearing.

When all components have been sampled, the mounting of the bearing rings can be simulated. If the bearing rings are mounted with interference between the bearing rings and their adjacent components, they will deform during the mounting process. Besides dimensional deformations (i.e. the expansion of the inner ring and the contraction of the outer ring), bearing rings also tend to adapt the out-of-roundness of their adjacent components. This is due to the relatively small wall thickness of bearing rings [20]. Normally, the deformations of the bearing rings can be evaluated using a Finite Element Analysis (FEA). Yet, FEAs imply high computational cost and are therefore not practicable for statistical approaches, as several hundred or thousand samples are evaluated. At least the dimensional deformation of the bearing rings can be easily approximated analytically using the calculation rules for interference fits in DIN 7190-1 [21]. The calculation of interference fits is based on the determination of the cylinder stress in thin- or thick-walled cylinders (depending on the diameter ratio) [22]. Unfortunately, geometric deviation like out-of-roundness cannot be considered.

Nevertheless, this approach could be used to derive a modified calculation formula for the evaluation of the local deformations of the bearing rings. For this purpose, the components are subdivided into very thin slices using the discrete geometry representation. For each slice, the actual interference is calculated. Afterward, each slice is treated like a closed cylinder for which the radial deformation can be calculated following the calculation rules for interference fits. The resulting radial deformations can then be used to radially translate the corresponding vertices.

This modified calculation formula was compared to the results of several FEAs. Since the deformation of the bearing rings was overestimated, the results of the FEAs were divided into training and test data and a linear regression model based on the training data was implemented. Afterward, the regression model was tested with the remaining test data. Since the coefficient of prognosis was about 99.70 % and the mean absolute deviation was around 0.01 µm, the results seem quite promising. However, the modified calculation formula has just been tested for harmonic waviness. Hence, further testing is mandatory.

Although in most applications the temperatures of the bearing components nearly remain constant after run-up [23], the thermal expansion of the bearing rings can affect the operating clearance too. In many applications of cylindrical roller bearings, the inner ring will be warmer than the outer ring. As a result, the expansion of the inner ring is greater than the expansion of the outer ring and the operating clearance decreases. Therefore, thermal linear expansion of the bearing components is considered. Although deviations of the thermal gradient could be easily considered, the cylindrical roller bearings shall operate in a steady state, for reasons of simplicity.

2.1.2. Determination of the functional key characteristics

As aforementioned, both, the operating clearance and the fatigue life of the cylindrical roller bearings, are regarded as FKCs. First, the operating clearance is evaluated. The results are thereafter used to calculate the fatigue life. A concept for the determination of the operating clearance of cylindrical roller bearings has already been published by Aschenbrenner and Wartzack in [24]. The concept is based on a ray trace algorithm and consists of four major steps depicted in Figure 2. Nevertheless, the necessary steps are shortly summarized in the following.
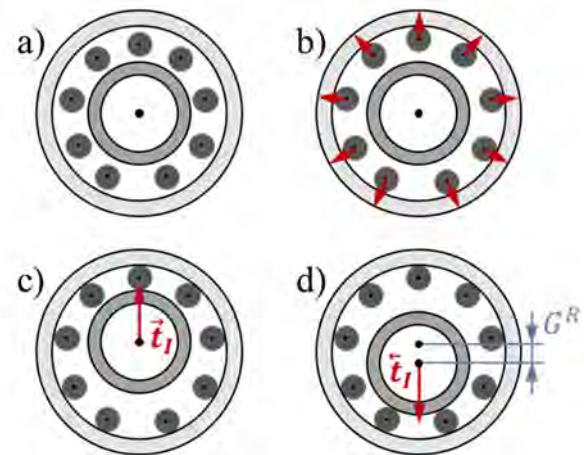
Figure 2: Process for the evaluation of the operating clearance
a) Initial positioning of the non-ideal bearing components
b) Registration of the rollers on the outer raceway
c) Registration of the inner ring onto the roller(s)
d) Registration of the inner ring onto the roller(s) in opposing direction

Firstly, all non-ideal bearing components are positioned with respect to a global coordinate system. In the beginning, the center points of the rollers are located on the pitch circle diameter of the

roller set with an angular distance equal to the separation angle corresponding to the number of rollers. The bearing rings are concentrically arranged around the global center point. Thereafter, the bearing components are registered onto each other. For this purpose, contact detection algorithms are employed. Following [12], contact detection algorithms can be classified as broad-phase and narrow-phase contact detection algorithms. Broad-phase contact detection algorithms preselect those bodies, which might be or get into contact. Therefore, fast but imprecise approaches are employed. For instance, the real bodies are substituted by a simple generic geometry element (so-called hitboxes, such as a circle in 2D or spheres in 3D). For this generic geometry elements, the evaluation of intersection is of very low computational costs (e.g. circles intersect if the distance between the center points is less than or equal to the sum of their radii). The employed broad-phase algorithm makes use of the fact that the polar coordinates of each surface vertex as well as of the center points of the rollers are known or could be easily determined ex-ante. The concept of the broad-phase algorithm is shown in Figure 3.
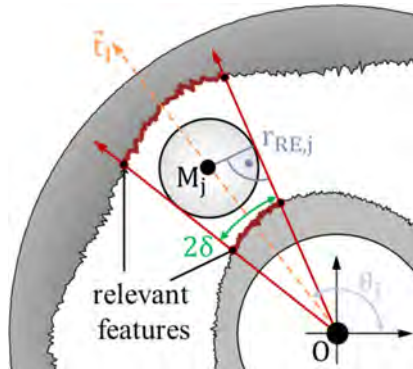
Figure 3: Broad-phase algorithm for the registration of the bearing clearance

The (deviating) radius of a roller $r_{RE,j}$ can be used to calculate the angle δ_j within the right-angled triangle described by the point of contact of a tangential vector, the fixed center point and the center point of the roller. The relevant features (i. e. a vertex or an edge) are all those features located within the arc between $\theta_j - \delta_j$ and $\theta_j + \delta_j$. This algorithm works fine for the registration of the rollers onto the outer ring, because each roller has to have contact with the outer ring. However, the inner ring may not have contact to all rollers at once, as depicted in Figure 2 c) and d). To overcome this flaw, a preselection of the rollers based on the separation angle could be done for a given direction of translation $\vec{t}_I$.

Once all relevant bodies and body features are selected, they can be used in a narrow-phase algorithm to determine the exact contact points. Following the idea of Schleich and Wartzack [18], a ray-trace algorithm is used for the narrow-phase contact detection of both, the registration of the rollers onto the outer ring as well as the registration of the inner ring onto the rollers. According to [25], a ray is emitted from each surface vertex. All rays point in the same predefined direction of translation $\vec{t}_I$. If a ray hits a feature of another body (i.e. a vertex or an edge), a point of intersection can be calculated. The intersection point, for which the distance to the emitting point is the smallest, is the actual contact point and the distance is the possible translation in this direction. To obtain the operating clearance, this procedure has to be repeated for the opposing direction of translation $\overleftarrow{t}_I$. Thus, the operating clearance

is the sum of the translation distance in both directions as depicted in Figure 4. Since the value of the operating clearance strongly depends on the selected direction, the operating clearance should be evaluated multiple times for different pairs of directions.

Finally, the results of the operating clearance can be used to determine the fatigue life using the calculation rules for the reference rating life in ISO/TS 16281 [9]. The calculation is based on a lamina model for which all rollers are cut into several laminae. For each lamina, the dynamic load rating as well as the dynamic load, is determined. For the determination of the dynamic load rating, further calculation specifications are provided by ISO/TR 1281-1 [26]. The dynamic loading of a lamina can be obtained by iteratively solving a force and momentum equilibrium, whereby the stress in the edge areas of a roller can vary due to tilting and surface profiles of the bearing components (e.g. crowning of rollers). In ISO/TS 16281 a formula for standard barrel-like crowns is provided. More complex surface profiles
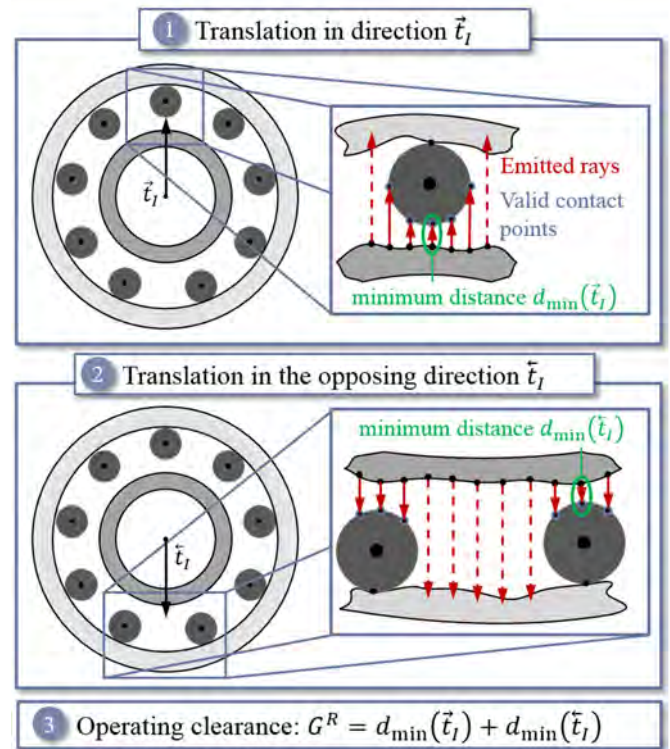
Figure 4: Determination of the operating clearance for a cylindrical roller bearing with geometric deviations using ray tracing

make it necessary to use advanced numerical solution for contact problems such as [27] or [28].

2.1.3. Statistical analysis of the functional key characteristics

After the operating clearance and the fatigue life of hundreds of virtual cylindrical roller bearings are calculated, the results must be appropriately processed. For this purpose, statistical key figures like sample mean, sample standard deviation, different quantiles, sample minimum and sample maximum can be determined. Furthermore, visual auxiliary tools like histograms or scatter plots can be utilized. These evaluation options may already assist a user in adjusting the geometric definition and tolerancing of their cylindrical roller bearing system. Nevertheless, knowledge about the kind and strength of the relationship between input and output

parameters can provide additional help for a user to perform a target-oriented adjustment and in understanding the behavior of a system with its varying input parameters. Sensitivity analysis has established as a method for this purpose. There are several sensitivity analyses, all with specific pros and cons as well as specific ranges of application (cf. in the case of cylindrical roller bearings, the sorting of the rollers leads to statistical dependencies, disabling a couple of sensitivity analysis like those, requesting statistical independence (e.g. Pearson correlation) or rely on a specific sampling (e.g. (extended) Fourier Amplitude Sensitivity Test). Among the possible sensitivity analyses, the moment independent uncertainty indicator by Borgonovo [29] is chosen due to its simple interpretability. The values range from 0 to 1, with 0 indicating independence (i.e. no influence) and 1 indicating absolute dependence (i.e. very high influence) between an output parameter and an input parameter. The moment independent uncertainty indicator is a density-based global sensitivity analysis which uses conditional probability densities (i.e. the probability density that results, if one input parameter is fixed to a specific value). According to [30], for a given set of data, these conditional densities could be obtained by classifying the values and perform a kernel density estimation using kernel smoothing for each value class.

Once the statistical key figures and sensitivities are calculated, a user can purposefully use this information. For instance, a cylindrical roller bearing system should have an extended fatigue life. Thus, the user will shift the dimensional definition and tolerancing of his components (shaft and housing) towards those combinations achieving high values for the fatigue life (i.e. the maximum value) and tries to avoid those combinations showing weaker performance (i.e. the minimum value). Nevertheless, uncertainties are inevitable due to imprecisions that are inherent to all manufacturing processes [1]. Hence, a cylindrical roller bearing system should possess a robust behavior so that its fatigue life will not tend to vary much due to dimensional and geometric deviations of the components. The sensitivities could be used to identify the geometric characteristics mainly affecting the uncertainties of the fatigue life (i.e. those input parameters with high sensitivities), and pay particular attention to these geometric characteristics during the manufacturing of the shaft and housing. In contrast, geometric characteristics hardly influencing the fatigue life might receive much less attention and their tolerances might even be widened. As a result, a user may obtain a more robust cylindrical roller system for less manufacturing cost.

Albeit, the purpose of the herein presented variation simulation of cylindrical roller bearings is the screening of a huge design space. Therefore, it is based on fast but simple quasi-dynamic models of the behavior of cylindrical roller bearings. A closer look at the dynamic behavior of a bearing can grant further insights and thus guidance for improving a cylindrical roller bearing's geometric definition and tolerancing. In the next section, a method for dynamic analysis of deviating cylindrical roller bearing systems is presented which is based on multibody dynamic simulations.

2.2. Dynamic simulation of cylindrical roller bearings

Dynamic simulations are intended to observe the dynamic responses of a system in motion. It helps to describe the overall behavior of a system in the simulation environment. Thus, dynamic simulations can be considered as a virtual testing environment. With the help of these simulations, mass inertias of the bodies, their velocities and accelerations along with the forces acting on the rigid bodies like reaction forces, centrifugal and frictional forces can be analyzed in detail like in the real physical environment. Such simulation models are developed and extended at the MEGT [31] [32]. In order to make a detailed analysis of the effects of the geometric deviations (dimensional and roundness deviations) of the cylindrical roller bearing and their adjacent components on the dynamic behavior, these models are employed and adapted for further investigation in this contribution.

The investigation of these deviations can be performed with the suitable CAE simulation methods and the subsequent evaluation is carried out analytically. Thereby, threshold values (High, Low and Median) of dimensional deviations (bearing operating clearances), obtained by screening the design space using variation simulation and roundness deviations of the raceways, obtained by the FE model are considered in this approach. The tolerance values for the adjacent components are chosen based on the manufacturer's specifications (cf. ISO 16281 [9]). Tolerances are well defined for the outer dimensions of a bearing's inner- and outer rings as well as for its adjacent components. However, no guidance is available for the tolerances of the bearing raceways. Therefore, finite element analysis (FEA) is used to evaluate the effects of production-related form deviations of adjacent components on the deformation of the bearing raceways. Roundness deviation of the bearing rings is neglected.

Figure 5 gives insight into the detailed approach to the dynamic simulation of cylindrical roller bearing [31], where geometrical deviations of adjacent components are considered in FE- and MBS model. The raceway deformations, arise due to the deviations are further described as a waviness (surface irregularities). It is implemented as a harmonic wave function by superimposing the multiple waves to define the form error of the raceway in the MBS Model. Subsequently, the multibody simulations are performed and the dynamic behavior is closely investigated. This strategy helps to study the fundamental influence of deviations on the additional functional key characteristics (FKCs) like bearing fatigue life and the vibrational behavior of the bearing. After the evaluation and the analysis, recommendations and guidelines to optimize the tolerancing of bearing systems are available for the users.
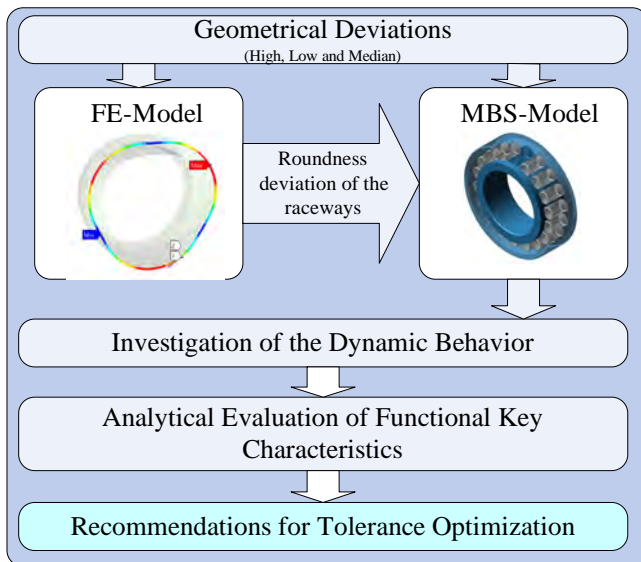
Figure 5: The approach to the dynamic simulation of cylindrical roller bearing

The model additionally possesses the ability to simulate a multiple number of combinations and analyze them subsequently. The high, low and median value of deviation can lead to a large number of combinations. It is highly impractical to enter all these values manually for each of the combinations. Besides, simulation and evaluation of the respective model is also time-consuming. Therefore, a strategy for quickly sampling the input variables has been developed. Solving of the models, evaluation, generation of the plots and its comparison can take place automatically with the Matlab script. So, this helps to minimize the investigation time.

2.2.1. Development of the FE model

Geometric imperfections affect the nominal dimensions of the bearing. As aforementioned, bearing raceways tend to deform during mounting. The deformation of the raceways has a significant influence on the bearing load distribution, bearing stiffness and the contact pressure. Eventually, it influences the bearing life and overall dynamic behavior of the bearing. The resultant overall deformation of bearing raceways can be obtained with the help of FE model.

To determine the deformation of the raceways, a parametric FE model for a cylindrical roller bearing (NU206) was established. The geometrical data of the bearing is provided in Table 2. This model can be modulated and regenerated easily for other bearing types by manipulating different geometrical parameters.
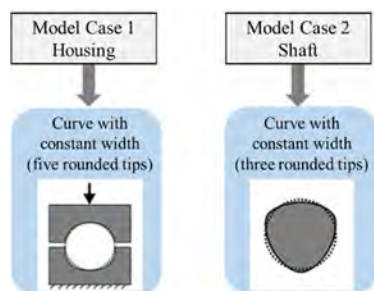

Figure 6: Exemplary consideration of form deviations for the housing and the shaft

As shown in Figure 5, two model cases for adjacent components of the bearings, one for the shaft and another for the housing are established. Roundness deviation of the housing is defined by a curve of constant width with five rounded tips. For the shaft, a curve with three rounded tips is considered in the model. For each of these model cases, two models will be established separately that take into account the High and Low case of the deviation values.

Raceway deformations are the output of the FE simulation. Further, the necessary analysis was carried out on the deformation with the Fast Fourier transformation to extract the number of waves (frequency of waviness) and the respective amplitudes. The exemplary decomposition of the deformation of the raceways can later on, be used in the MBS models.

2.2.2. Fundamentals of the Multibody Dynamic Model

Many physical processes within a bearing are difficult to detect and investigate by experiments, as for example the local friction phenomena. Further, the stress distribution and kinematics of rolling bodies are also difficult to determine by experiments. Numerical dynamic simulations allow for a better understanding of the processes within a roller bearing. Their theoretical investigation can be done with the self-developed dynamic models based on the commercially available softwares like MSC.Adams [32] and Simpack [33]. Furthermore, own routines were implemented to describe the interaction in the bearing contacts [32]. They are numerical models and are solved by simulation solvers. The models available so far are the deep groove ball bearings and angular contact bearings, cylindrical-, tapered- and spherical roller bearings.

These models are parametrically realized so that the modifications within the geometry, lubrication properties and operating parameters can be adjusted easily as per the purpose and the requirement. That allows generating the models for different bearing types that fit the research purpose [34]. The biggest advantage of these models is that they can be simulated as an individual bearing or they can be integrated into some complex system e.g. intermediate shaft of a spur gearbox, pinion shaft of a differential gearbox, an electric motor shaft or a connecting rod of an engine.

As mentioned earlier, MBS model describes the dynamic behavior of a bearing through the numerical simulation and the contact routines calculate the necessary reaction forces for each of the contact. These routines also describe the output values of the simulation results and analyze the tribological processes in contact.

Figure 7 shows the solution approach that solves the dynamic simulation of the roller bearings, which includes contact point detection, normal and frictional force calculation as a function of the rolling bearing geometry and the specified boundary conditions (load, rotational speed, lubricant etc.). For each contact e.g. roller-raceway, roller-cage pocket or roller-rib, separate routines are implemented. In this contribution, the focus is on the contact calculations in the roller-raceway contact.
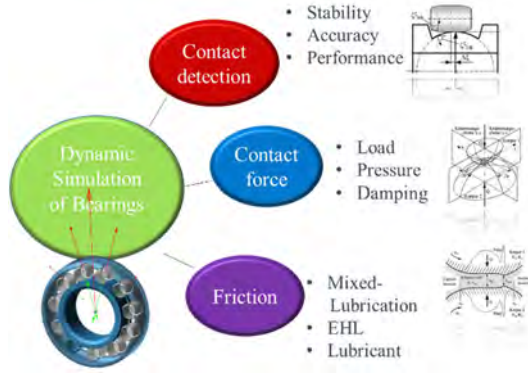
Figure 7: Partial tasks in dynamic simulation of roller bearings and solution approaches at the MEGT

The first step in the contact calculation is the detection of the contact point and is carried out with the help of geometrical variables of the rolling elements and the bearing rings as well as their respective distances from each another [31]. This model provides the possibility to find the contact point precisely and numerically efficient.

In the case of cylindrical rolling elements, a line contact occurs between the rolling elements and the raceway. For a precise determination of the contact conditions, a lamina model is used in which the contact area is discretized into a predefined number of laminae (cf. ISO/TS 16281 [9]). The contact will be determined for each lamina. This procedure is the basis for the calculation of the normal, damping and friction forces in the rolling element-raceway contact.
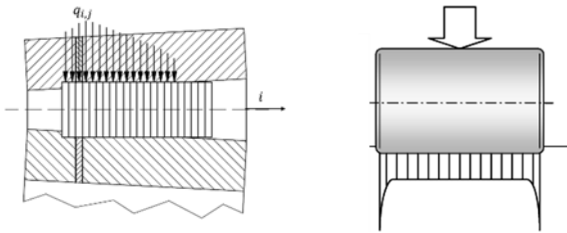

Figure 8: Lamina model [9] and qualitative pressure distribution between plane-cylinder contacts without tilting of the rolling body [32]

The normal force calculation has been carried out with force-deformation relationships based on Hertz for line contact (cf. [35] or [36]). However, for these contacts the pressure distribution differs significantly from the uniform pressure distribution, especially the end of the rolling elements usually suffers from high stresses. These high stresses in concentrated contacts (see Figure 8) have a decisive influence on the load carrying capacity and the fatigue life. In order to avoid these stress peaks at the end of the rolling elements, raceways and/or rolling elements are profiled. These stress concentrations can still occur in the case of profiled rolling elements when bearings are highly loaded or under the tilting load. The established roller bearing model can also take into account this phenomenon of stress peaks at the ends through the Alternative Slicing Technique (AST), which allows a more accurate calculation of the pressure distribution in line-contacts [37]. This detailed pressure distribution leads to a more accurate fatigue life computation. This is also necessary for the calculation of frictional forces since the pressure distribution is an important

influencing factor. Thus, the (local) changes in the lubricating properties, temperature distribution and friction conditions associated with the non-uniform normal pressure distribution can be taken into account. In addition to the determination of the normal forces, damping effect is considered by a simple parametric approach (damping as a function of penetration) [38]. Different frictional phenomenon (dry-, boundary- and mixed friction [39] are also considered in the model for a realistic calculation of the frictional moment.

The developed MBS model was adapted in such a way that all the relevant input variables can be examined. Thus, the model for cylindrical roller bearings has been extended by the possibility of considering a geometrical deviation of the raceways.

In the contact calculation, roundness deviation of the raceways can be considered as the waviness by implementing harmonic wave function with an arbitrary number of waves and amplitudes over the circumference. This form error will be reproduced with the following formula and implemeted directly into the contact calculation:

$$D_{race} = D_{race_{nominal}} + amp_1 \cdot sin\,(wave_1 \cdot \varphi) + \cdots\cdots amp_n \cdot sin\,(wave_n \cdot \varphi)$$

where, D_{race} is the diameter of the raceway, $D_{race_{nominal}}$ is nominal raceway diameter, amp_n is amplitude of the waviness, $wave_n$ is the frequency of the waviness and φ is the angle over the raceway.

Thus, a variety of common geometrical form deviations can already be generated. As shown in Figure 9, two waves per the circumference produce the ellipsoid form (i.e. frequency of waviness 2) and a curve with three rounded tips (i.e. frequency of waviness 3) can be reproduced with three waves and so on. Furthermore, any roundness deviations per circumference can be reproduced by superimposing the number of waves and their respective amplitudes (see Figure 9) in a similar way as Fourier series [40].
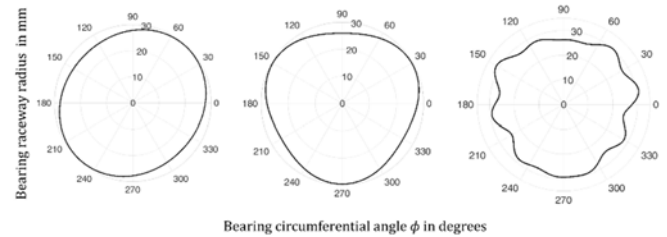
Figure 9: Different possible geometrical deviations of the raceways in the MBS model (here exemplary) by selecting the number of waves over the circumference (from left: 2 waves (oval), 3 waves (curve with constant width), superimposed multiple waves)

In order to define the dimensional deviation of the raceways, bearing operating clearances can be used. On the basis of these operating clearances, corrected raceway diameters can directly be put into the MBS model parameters.

In this contribution, cylindrical roller bearing of type NU206 has been selected for the investigation purpose. The bearing model is solved systematically to examine the contact forces and vibrations. Bearing data along with operating parameters for the FE- as well as for the MBS model are summarized in Table 2.

2.2.3. Investigation of the dynamic behavior and evaluating FKCs

Simulation results enable the understanding of the inner dynamics of the roller bearings. Rotational speeds of the rolling element or the cage, translational displacements of the rings and load acting on each rolling contact can be investigated thoroughly, on the basis of which vibrational behavior and bearing fatigue life can be evaluated. For the investigation of the dynamic behavior of the cylindrical roller bearing, it is regarded to operate in a steady state condition, i.e. external load is constant in value and direction and the inner ring is accelerated to a stationary speed.

Exemplary rotational speeds of inner ring, cage, rolling element and the load on the rolling element over the simulation time are shown in Figure 10. Simulation parameters are listed in Table 1 and the inner bearing geometrical parameters including considered tolerances are listed Table 2

Table 1: Simulation Parameters

Simulation Time	1s
Simulation Steps	6000
Radial Load	5000 N
Rotational Speed	1000 rpm
Solid Friction Model	Cubic Friction Model
Static friction co-efficient	0.1
Dynamic friction co-efficient	0.08
Elastohydrodynamic Friction Model	Model according to Dowson and Higginson [41]
Damping Model	Cubic Damping Model
Damping co-efficient	100
Rolling Element Profile	Logarithmic Norm Profile DIN ISO 281
Lubricant type	FVA3
Lubricant Temperature	40° C

These simulation models have been verified experimentally several times in different research projects [31] [32] [33] [34]. It can be seen that the inner ring is accelerated to its stationary speed within the first 0.1 s of simulation (green curve) time. The rotational speed of the rolling element increases at the beginning of the simulation. During this time period, rolling element (black dotted curve) is located in the load zone. In the no-load zone, the rolling element speed reduces and it accelerates again during the entry into the load-zone. Within the load zone, the speed remains constant and the rolling element rotates approximately at its kinematic speed.
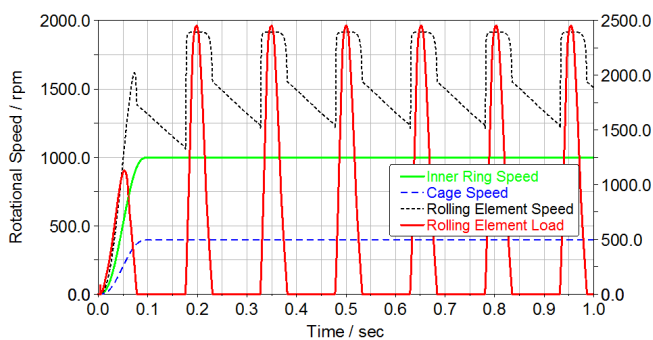

Figure 10: Exemplary results of the load distribution on the single roller element along with rotational speeds of the inner ring, cage and the rolling element

These results like rolling element load distribution and the translational displacement of the inner ring (introduced in 3.2) are then used to evaluate the FKCs. The analytical evaluation of the relevant functional key characteristics is carried out as follows:

Excitations of vibrations: The dynamic simulation provides the radial displacement of the inner ring relative to the outer ring and is investigated in the stationary condition in order to extract the vibration excitations. Therefore, for this particular region, a spectrogram is produced with a Fourier analysis, in the direction of the load and transverse to the direction of the load. Order of vibration and the respective amplitudes are registered. The maximum amplitude of the respective variable is assigned as the comparison parameter with the other combinations of threshold values.

Fatigue life: The evaluation of the fatigue life is carried out by calculating the equivalent load on the bearing based on (cf. ISO/TS 16281 [9]). The data of rolling element load distribution (load spectrum) is used from the dynamic simulation. In this context, the load spectrum explains the load not only for a single fixed time step, but over the entire simulation time and for each lamina. After this, the reference rating life L_{10r} for different combinations of the threshold values are then calculated and compared with each other for the analysis purpose.

3. Application of the methods

The application of both methods is shown for a cylindrical roller bearing of the type NU206 with a normal tolerance class (P0) and bearing clearance (CN). A radial load of 5000 N is applied to the cylindrical roller bearing, where the inner ring is circumferentially and the outer ring is point loaded. Thus, there is an interference fit between the shaft and the inner ring of the cylindrical roller bearing, whereas the outer ring is mounted with a loose fit. The cylindrical roller bearing should operate under stationary operating conditions with a rotational speed of 1000 rpm and a steady-state temperature of 40° C for the lubricant and the rolling element set. The inner ring is slightly warmer (42.5° C) while the outer ring is slightly colder (37.5° C). For the definition of the diameters ISO code system according to ISO 286-1 [42] is used, except for the bore diameter and the outer diameter of the cylindrical roller bearing, which correspond to ISO 492 [6]. In addition, the value range of the diameter of the rolling elements composes of three diameter classes. The range of each class corresponds to DIN 5402-1 [7]. It is supposed, that shafts and housings are all manufactured with their own specific manufacturing process leading to a characteristic out-of-roundness (so-called signature, cf. [19]). For the shape of the shafts tri-lobed profiles are assumed (i.e. the frequency of waviness is 3) and the shape of the housings should follow ellipsoids (i.e. the frequency of the waviness is 2). All value ranges and assumptions are summarized in Table 2.

Table 2: Values for the application use case

Category	Input parameters	Values
Bearing properties (NU 206)	Dynamic load rating C_r	45000 N
	Fatigue load rating C_s	5700 N
	Initial clearance $G^{R,0}$ according to clearance class CN (ISO 5753-1 [5])	[20 μm; 45 μm]
	Tolerance class	P0
	Number of rolling elements	11

Mechanical load	Radial load P	5000 N
	Rotational speed ω	1000 rpm
	Type of loading on the inner ring	Circumferential loaded
	Type of the loading on the outer ring	Point loaded
Thermal load	Lubricant temperature T_{lub}	40° C
	Temperature of outer ring T_{OR}	37.5° C
	Temperature of rolling element set T_{D_w}	40° C
	Temperature of inner ring T_{IR}	42.5° C
Shaft	Diameter S: Ø30k6	[30.002 mm; 30.015 mm]
	Roundness tolerance a_S (corresponds to IT4/2 for Ø30)	[0 µm;3 µm]
	Frequency of waviness f_S	3
Housing	Bore diameter H_i: Ø62H6	[62 mm; 62.019 mm]
	Roundness tolerance a_H (corresponds to IT6/2 for Ø62)	[0 µm; 9.5 µm]
	Frequency of waviness f_H – statistical analysis	2
	Number of rounded tips in the FE Model	5
	Outer diameter H_o	[94 mm; 96 mm]
Inner Ring	Bore diameter d	[29.99 mm; 30 mm]
	Raceway diameter F (corresponds to Ø37.5h5)	[37.489 mm; 37.500 mm]
Outer Ring	Raceway diameter E (corresponds to Ø55.5G6)	[55.501 mm; 55.529 mm]
	Outer diameter D	[61.987 mm; 62 mm]
Rolling Element	Length l_W	10 mm
	Chamfer radius r_2	1 mm
	Diameter classes D_W	[8.988 mm; 8.990 mm[
		[8.990 mm; 8.992 mm[
		[8.992 mm; 8.994 mm]

Firstly, the design space is screened using the variation simulation of the cylindrical roller bearings. A total amount of 10000 cylindrical roller bearing systems are evaluated. As aforementioned, the operating clearance and the fatigue life are analyzed. Thereafter, the combinations with the highest and lowest fatigue life as well as the middle value (median) are analyzed in greater detail utilizing multibody simulations. In addition to the fatigue life, the vibrational behavior of the cylindrical roller bearing systems (in terms of the displacement of the inner ring) is evaluated. Both methods use the results to determine the influence of the deviations on the functional key characteristics. A discussion of the results for each method can be found in the following two subsections.

3.1. Statistical tolerance analysis of bearing clearances and the fatigue life

For the application of the statistical variation simulations, all dimensional values are assumed to be normally distributed with a minimum process capability index of $c_{pk} = 1$. The mean diameters of the shafts and housings should be centered between their lower and upper limits, while the mean values of the bearing dimensions are not centered but shifted 1/3 towards the cutting side, i.e. bores tend to be smaller and outer diameters tend to be greater than their arithmetic mean value. For the roundness deviations of the adjacent components a folded normal distributed is supposed, i.e. values are sampled using a standard normal distribution but the absolute values of this samplings are used. For the rollers, one normal distribution is assumed across all diameter classes.

Firstly, the operating clearance is evaluated. The frequency distribution is shown in Figure 11.
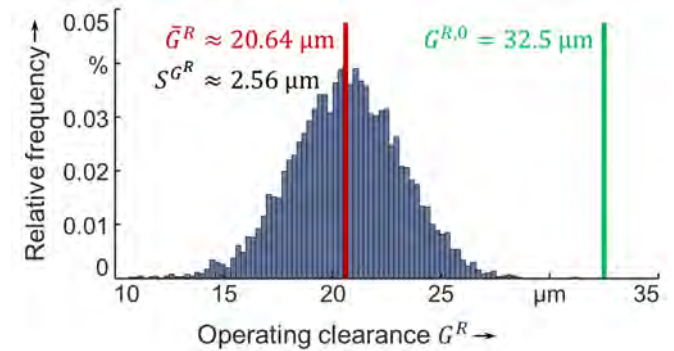
Figure 11: Frequency distribution of the resulting operating clearances

Due to the thermal expansion of the bearing components and the assembly-related deformations, the values of the operating clearances are smaller than the mean value of the initial bearing clearance (32.5 µm). This results in a mean shift of about 11.86 µm for the operating clearance. However, no negative clearance (interference) occurred. In fact, the values of the operating clearance range from circa 8.00 µm to 31.28 µm Thus, mountability is guaranteed for all combinations. The standard deviation of the operating clearance, resulting from the deviations, is 2.56 µm. To analyze, which deviation contributes the most to the uncertainty of the operating clearance, the aforementioned moment independent uncertainty indicator is employed. The results can be seen in Figure 12.
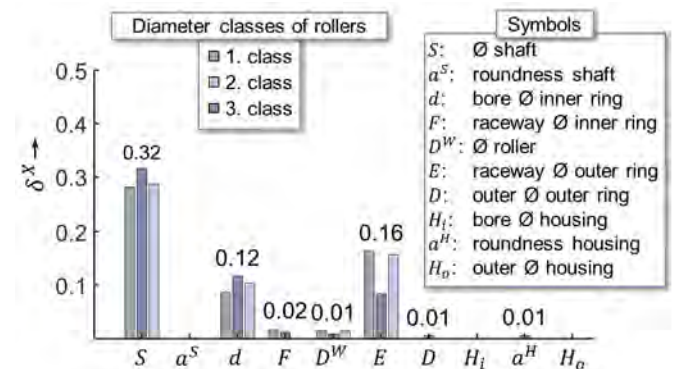
Figure 12: Moment independent uncertainty indicators of the considered deviation.

In order to avoid falsification of the results due to statistical dependence and other effects related to the sorting of the rollers, the moment independent uncertainty indicators are evaluated for each diameter class separately. As expected, the deviation of the shaft diameter influences the operating clearance the most, due to the interference fit. In contrast, because of the loose fit, the deviating parameters of the housing have almost no effect on the uncertainty of the operating clearance. The next most important contributors are the deviations of the raceway diameter of the outer ring and the bore diameter of the inner ring. The initial bearing clearance only depends on the inner geometry of a cylindrical roller bearing (i.e. the raceway diameters and the roller diameters) and the operating clearance derives from the initial bearing clearance. Within the group of inner geometry parameters, the raceway diameter of the outer ring possesses the biggest variation (cf. Table 2) and therefore contributes the most to the uncertainty of the operating clearance. As the tightness of the fit between the shaft and the inner ring depends on both, the shaft diameter and the bore diameter of the inner ring, it is no surprise, that the bore diameter of the inner ring noticeably influences the operating clearance. However, the effect of the roundness deviation of the shaft on the operating clearance seems to be negligibly small.

Considering these results so far, if a user wants to reduce the variation of the operating clearance of their cylindrical roller bearing systems, special attention to the interference fitted adjacent components (in this use case: the shaft) should be paid. Both, a restriction of the diameter tolerance as well as sorting the adjacent components and their corresponding bearing rings might be applicable. On the other hand, roundness deviations might not be further restricted.

Besides the operating clearance, the effects of the deviations on the fatigue life should be considered. The frequency distribution for this use case is depicted in Figure 13.
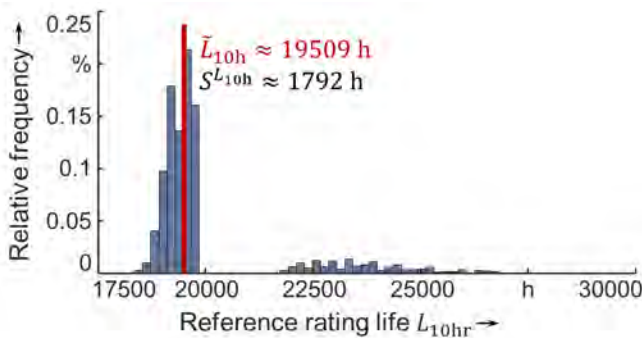

Figure 13: Frequency distribution of the resulting reference rating life

In comparison to the operating clearance, the reference rating life shows a different statistical behavior. While the operating clearance is almost normally distributed around the mean value, the majority of the values of the reference rating life are located around their median (19509 h) with a few outliers possessing a significantly higher reference rating life. This leads to an increased standard deviation for the fatigue life. Thereby, the uncertainty of the cylindrical roller bearing systems rises, leading to a decreased predictability of the maintenance and, thus, loss of quality of such systems. For better understanding, the statistical behavior of the reference rating life, the relationship between the operating clearance and the reference rating life is depicted in a scatter plot in Figure 14.
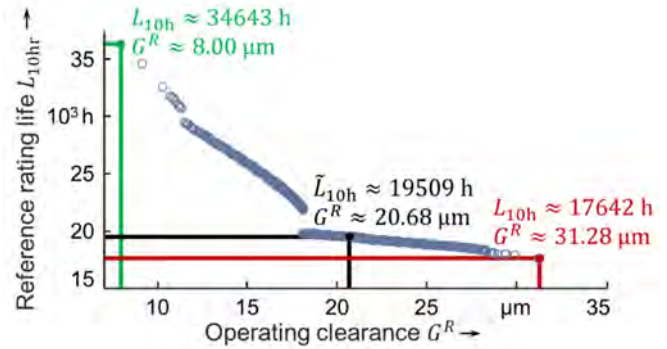
Figure 14: Relationship between operating clearance and reference rating life

Once the operating clearance sinks beneath a certain value (approximately 18.12 µm and 11.50 µm), not only an abrupt rise but also a change of the gradient of the relationship between the operating clearance and the fatigue life can be observed. These discontinuities occur due to the fact that a decreasing operating clearance leads to additional rollers within the load zone [10]. In order to achieve a robust behavior of their cylindrical roller bearing systems, a user should try to choose his geometric definition and tolerancing in such way, that these discontinuities are avoided. Of course, a higher fatigue life is preferable proposing smaller operating clearances and therefore tighter fits of the adjacent components. The variation simulation of the cylindrical roller bearings could assist a user in the tolerance specification of the shaft and housing by screening the possible design space.

Nevertheless, a closer look at the best as well as the worst performing design points could give a greater insight into what design is preferable and what value combinations should be avoided. For this purpose, a dynamic analysis with multibody simulations could be used, which also allows a better understanding of the vibration behavior of a cylindrical roller bearing systems. Therefore, the combinations with the highest and lowest fatigue life as well as the middle value (median) are analyzed in greater detail in the next subsection.

3.2. Dynamic analysis of the fatigue life and the vibrational behavior

As aforementioned, those values of operating clearances are utilized in the dynamic analysis, at which the highest and the lowest as well as the median fatigue lives are obtained. Consequently, the roundness deviation effects are considered by taking into account the waviness values obtained from the FE model. These values of the roundness deviations are shown in Figure 15. The effects of these wavy raceway profiles on the fatigue life as well as on the vibrations of the bearings are subsequently analyzed.
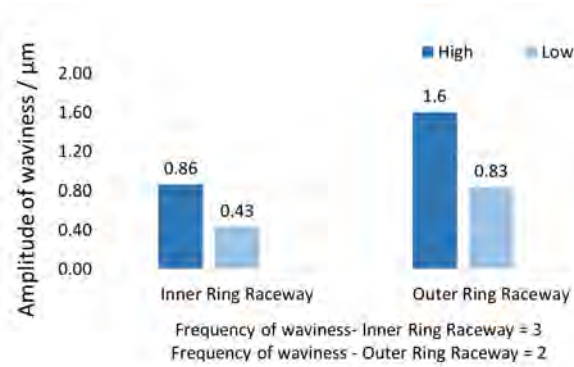
Figure 15: Output values of the roundness deviations of the FE model considered in the MBS Model

As mentioned earlier that the simulation models are verified many times through several research projects. But, the effects of the waviness of the raceway profiles on bearing dynamics are not experimentally or by other means verified so far. The results obtained here are planned to verify in the follow-up project, in order to check their validity.

Figure 16 shows the exemplary results of the load distribution on a single roller element in the steady-state condition (equilibrium), for the cases of ideal raceway (red) and the wavy raceway (blue) profile over the simulation time. It can be seen that the waviness leads to a significant maximum load increase. This load increase can be recognized by the load peaks in the diagram (blue).

Figure 16: Load distribution on a single roller element for an ideal (red) as well as for a wavy (blue) raceway form in the stationary condition of the inner ring

Furthermore, it has been noticed that the waviness of the raceways affects not only the load distribution but consequently the translational displacement of the inner ring. Figure 17 shows the displacement of the inner ring (IR) relative to the outer ring (OR) under the influence of an ideal (solid) and wavy raceway (dotted) profile in the direction of the applied load as well as transverse to the direction of the load. It is noticeable that the waviness causes inner ring to vibrate and initiates excitations within the bearing. The transverse displacement is more pronounced for the given load case (green dotted). The displacement in the load direction shows almost no influence.

Figure 17: Inner ring translational displacement relative to the outer ring for an ideal raceway and for a wavy raceway in the direction and transverse to the direction of the load

(a)

(b)

Figure 18: Spectrogram of the inner ring vibrations (transverse to the direction of the load) for an ideal (a) and a wavy raceway profile (b)Influence of the geometrical deviations on the fatigue life

In the next step of the analysis, the frequencies and amplitudes of vibration of the inner ring are extracted by the application of Fast-Fourier transformation to the inner ring displacement signal. Spectrogram of th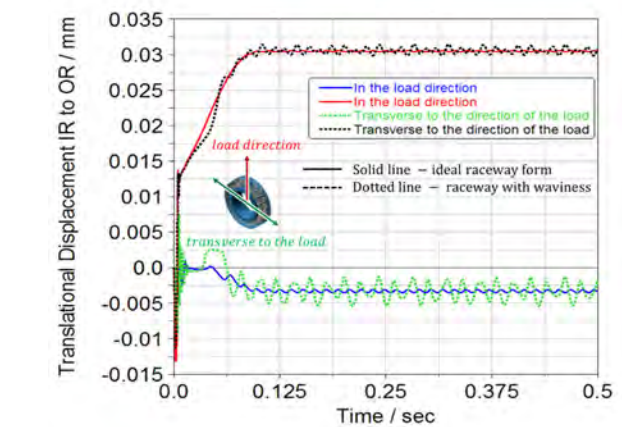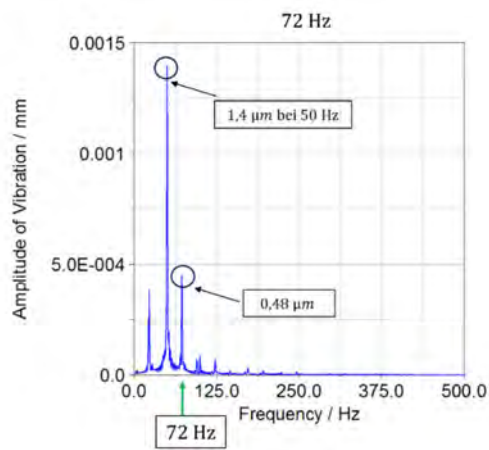e inner ring vibrations is shown in Figure 18. On the one hand, an ideal raceway profile (Figure 18 (a)) shows an amplitude of the vibration less than 0.2 µm at a frequency of 72 Hz, which represents the roller passing frequency and is negligible. On the other hand, in case of a wavy raceway profile (see Figure 18 (b)) inner ring vibrates at an amplitude of 0.48 µm with the same frequency and at 50 Hz attains the maximum amplitude. In this case, the amplitude of vibrations increases by a factor of around 3 for the same vibration frequencies. Thus, the waviness demonstrates a negative influence on the rolling bearing dynamics. The FFT analysis will be carried out separately for other waviness values and are compared subsequently in section 3.2.1.

In this section, effects of the geometrical deviations on the fatigue life of the bearing is evaluated and compared for threshold values. For the the purpose of analysis, histograms are used. Evaluation is carried out for the reference rating life L_{10r} under the specified operating conditions.
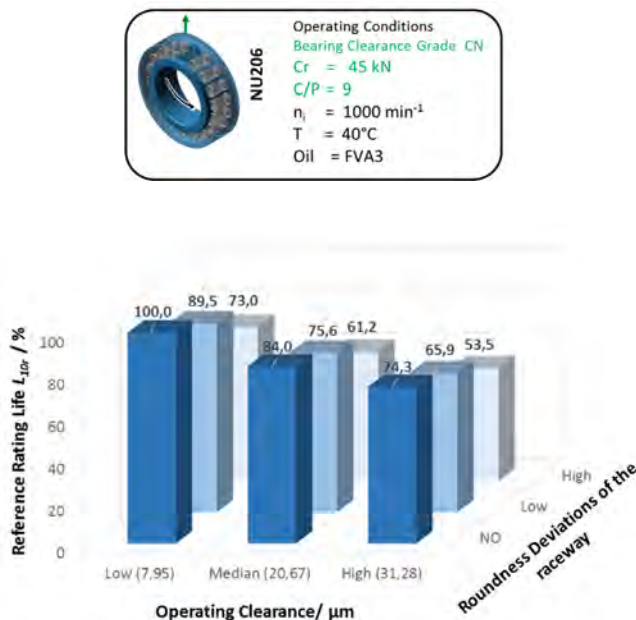

Figure 19: Effect of the Operating Clearance and the Roundness Deviation of the raceway on the bearing fatigue life

Figure 19 shows the influence of different combinations of operating clearances and the roundness deviations of the investigated cylindrical roller bearing of type NU206 on the reference rating life. The rating life is expressed as a percentage of the value of the rating life of the source model (bearing without geometrical deviations - ideal raceway profile – "Low" operating clearance). On the one hand, figure shows the effects of bearing clearance on the fatigue life. It is clear from the figure that the bearing clearance "High" reduces the fatigue life of the bearing by approximately 25 % and "Median" by 16 %. With the operating clearance "Low" bearing achieves the maximum fatigue life. The difference between the fatigue lives of "Low" and "Median" itself is quite high. Thus, an influence of the change in the operating clearance on the life of the bearing is quite recognizable. This can be explained by the major discrepancies in the resulting load distribution in the contact, arise

due to the different values of operating clearances. "High" clearance value causes the small load zone in the bearing and the number of rollers in the load zone also recedes. This means that overall load on the bearing being shared by a few number of rollers and those will be loaded to a great extent.

On the other hand, influence of the roundness deviation for different operating clearance combinations can also be clearly seen. Rating lives with "Low" and "High" values of the roundness deviations (for values of roundness deviations please ref. Figure 15) are compared with the rating lives without roundness deviation. It can be seen clearly that with the "Low" waviness value and the "Low" operating clearance, the rating life of the bearing is reduced by approximately 10 %. On the contrary "High" waviness with the same operating clearance tends to reduce the fatigue life even further by 27 %. This can be explained by the deviations that result in higher roller peak loads and eventually affect the load distribution in the contact (see Figure 16).

Furthermore, it can be seen that the lowest rating life has reached by superimposing the "High" waviness and "High" operating clearance. This superimposition reduces the life of bearing to approximately 50 %. This would be the worst-case scenario.

The waviness affects significantly the bearing overall behavior. As per the above discussion, it can be concluded that the roundness deviation has recognizable deviance on the fatigue life together with the operating clearances. It can further be noted that the "High" waviness arise due to the "High" values of roundness tolerances and "Low" waviness arise due to the "Low" tolerance values that are taken from the manufacturer catalog. So, it can also be concluded that by using "Low" tolerance values we can achieve almost 17 % increase in the fatigue life over "High" values of roundness tolerances.

3.2.1. Influence of the geometrical deviations on the vibrations

As aforementioned, waviness affects the inner ring displacement as well. From Figure 20, the amplitude of vibrations at respective dominant order of vibrations of the inner ring for the "NO"- as well as "High" and "Low" waviness values of the raceway can be found.
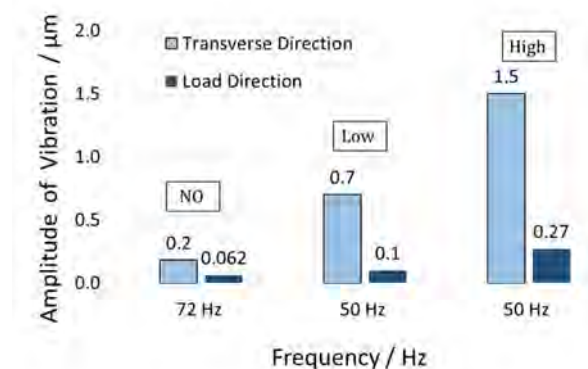
Figure 20: Comparison of the influence of the waviness on the amplitude of vibrations in the direction of the load as well as in the transverse direction

In the case of "NO" waviness, negligible amplitudes in the transverse ($\approx 0.2\ \mu m$) as well as in the direction of the load ($\approx 0.062\ \mu m$) are observed. The frequencies at such small amplitudes are the roller passing frequencies and have no effect on the excitations of the inner ring. However, "Low" and "High"

waviness produces comparatively higher vibration amplitudes in the transverse direction than in the direction of the load. This can be explained by the fact that the inertia forces act against the applied external load in the direction of the load, while in the direction transverse to the load this action has no significant effect. It can be seen that for the "High" corrugation value the vibration amplitudes are around double the value for the "Low" corrugation for the same frequencies (50 Hz). From these results, it follows that the corrugation causes the excitations of the inner ring, which eventually leads to a worse acoustic behavior.

3.2.2. Insights into the results

The observations show that both the operating clearances and the waviness of the raceways, strongly influence the fatigue life of the investigated cylindrical roller bearing. Increase in the value of the operating clearance reduces the life of the bearing drastically. Furthermore, could be observed, that the waviness of the raceway profiles also has a critical influence on the vibrations of the bearing, which eventually affect the overall bearing dynamic. For "High" waviness, low fatigue life of the bearing has been observed.

Nevertheless more closely, it could be concluded that optimum dynamic behavior (optimum fatigue life) can be achieved by a minimum bearing clearance ($\approx$ 7,95 µm) and waviness value of "Low". Hereby, it would be recommended to use the normal tolerance grade of the bearing as PN and roundness tolerances IT6 / 2 for the housing, IT5/ 2 for the shaft. It is further recommended not to expand further the roundness tolerances of the adjacent components. The user should not only pay attention to the dimensional and roundness tolerances but additionally to the operating parameters, where the dynamic simulation of the bearings could assist the user.

4. Summary and recommendations for actions

This contribution aims to evaluate and study the effects of geometric deviations on a cylindrical roller bearing's functional key characteristic. In order to investigate their effects, two different simulation approaches were introduced. On the one hand, a variation simulation of cylindrical roller bearings was carried out to investigate the effects of geometrical deviations on the operating clearance and the fatigue life. For this purpose, a statistical tolerance simulation model for the evaluation of the operating clearances was employed. In this simulation model thermal as well as fit-induced deformations of the bearing rings were taken into account. Furthermore, sorting of the rolling elements was considered. Once the operating clearance was determined by utilizing contact detection algorithms, these results were used for the calculation of the reference life according to (cf. ISO 16281 [9]). In order to statistically secure the results for the operating clearance and the fatigue life, several thousand virtual rolling bearings were evaluated. On the other hand, dynamic simulations were used for a detailed evaluation of specific design points. In this approach, the effect of threshold values of the geometrical deviations of the bearing components on the bearing dynamic was investigated. Threshold values of the operating clearances, obtained by the variation simulation approach, are used here. The values of roundness deviations and the resultant deformation of the raceways were evaluated using FE simulations. The effects of these deformations on the functional key characteristics, like bearing fatigue life and the vibrational behavior, are then analyzed in detail with a multi-body-simulation tool. For both the approaches, a cylindrical roller bearing of type NU206 was used for the investigation.

Both approaches show that the fatigue life is influenced by the bearing operating clearance. This once again reverts to the research that has been carried out since decades. Thus, a user should aim at the smallest possible operating clearance, in order to achieve the maximum possible fatigue life. This can be achieved by means of tight fit on both the bearing rings, whereby restrictions with respect to the mountability must be observed. On the one hand, the statistical analysis has shown that the roundness deviations have little to no influence on the operating clearances and thus on the reference rating life of the investigated cylindrical roller bearings. On the other hand, dynamic simulation analysis has shown that the roundness deviations and operating clearances have significant effect on the vibrational behavior and thus on the fatigue life of the cylindrical roller bearing. This reverts back to the fact that the roundness deviation has a direct influence on the load distribution at the contact. Statistical analysis provides the additional information which can be attributed to the fact that the variation simulation model is based on the quasi-static model and a wide range of parameterfield can be simulated with the advantage of computation time. Whereas, even though the multi-body simulation does not permit these possibilities, but a much more detailed consideration of behavior is possible. However, it should also be noted that in the case of a multi-body simulation, limiting values are considered, which are statistically very rare. On the basis of the investigation, a further expansion of the roundness tolerances of the adjacent components cannot be supported at the present time.

In this way, the described approaches also help a user to optimize the geometric definition and tolerancing of his products. An optimized tolerancing of the bearing seats could decrease scrape rate and manufacturing requirements as well as increase fatigue life of a cylindrical roller bearing by obtaining a small operating clearance and minimum roundness deviation. Thus, the application of both methods could decrease manufacturing as well as maintenance costs. For this purpose, firstly a user should perform a screening using statistical tolerance analysis. Afterward, particularly favorable combinations can be viewed in detail by means of multi-body simulations.

Further investigations and validations are necessary to elucidate the outcomes and to provide a better understanding of the relationship between fluctuations in the roundness deviation, vibrations and fatigue life.

Nevertheless, additional input factors like transient operating conditions or arbitrary roundness deviations should be considered. Moreover, both methods are restricted to radial tolerances and pure radial loads. These should be extended to axial tolerances and combined load. At the same time, the results are to be verified experimentally and this will be planned accordingly in the follow-up project.

Acknowledgment

References

[1] M. Zhang, N. Anwer, L. Mathieu and H. B. Zhao, "A discrete geometry framework for geometrical product specifications," *21th CIRP Design Conference,* pp. 142-148, 2011.

[2] M. S. J. Walter, T. C. Sprügel and S. Wartzack, "Least Cost Tolerance Allocation for Systems with time-variant Deviations," *Procedia CIRP,* vol. 27, pp. 1-9, 2015.

[3] SKF Group, "Rolling Bearings," 2016.

[4] Schaeffler Technologies AG & Co., K. G., "Rolling Bearings," 2012.

[5] ISO 5753-1, *Rolling bearings -- Internal clearance -- Part 1: Radial internal clearance for radial bearings,* Geneva/Switzerland: International Organisation for Standardization, 2009.

[6] ISO 492, *Rolling bearings - Radial bearings - Dimensional and geometrical tolerances,* Geneva/Switzerland: International Organization for Standardization, 2014.

[7] DIN 5402-1, *Rolling bearings - Parts of rolling bearings - Part 1: Cylindrical rollers,* Berlin/Germany: Deutsches Institut für Normung, 2017.

[8] F. B. Oswald, E. V. Zaretsky and J. V. Poplawski, "Interference-Fit Life Factors for Roller Bearings," *Tribology Transaction,* vol. 52, no. 4, pp. 415-426, 2009.

[9] ISO/TS 16281, *Rolling bearings – Methods for calculating the modified reference rating life for universally loaded bearings,* Geneva/Switzerland: International Organization for Standardization, 2008.

[10] F. B. Oswald, E. V. Zaretsky and J. V. Poplawski, "Effect of Internal Clearance on Load Distribution and Life of Radially Loaded Ball and Roller Bearings," *Tribology Transactions,* vol. 2, no. 55, pp. 245-265, 2012.

[11] T. A. Harris and M. N. Kotzalas, Rolling Bearing Analysis. Essential Concepts of Bearing Technology, 5 ed., Boca Raton, Florida and U.S.A. [u.a.]: CRC /Taylor & Francis, 2007.

[12] F. Wardle, "Vibration forces produced by waviness of the rolling surfaces of thrust loaded ball bearings Part 1: Theory & Part 2: Experimental Validation.," *Proceedings of the Institution of Mechanical Engineers, Part C: Journal of Mechanical Engineering Science,* pp. 305-319, 202 5 1988.

[13] S. P. Harsha, "Nonlinear dynamic analysis of a high-speed rotor supported by rolling element bearings," *Journal of Sound and Vibration,* pp. 65-100, 2006.

[14] B. Changqing and X. Qingyu, "Dynamic model of ball bearings with internal clearance and waviness," *Journal of Sound and Vibration,* vol. 294, pp. 23-48, 2006.

[15] J.-Y. Dantan, N. Gayton, A. Etienne and A. J. Quereshi, "Mathematical issues in mechanical tolerance analysis," *13. Colloque National AIP PRIMECA,* pp. 1-12, 2012.

[16] A. Saltelli, K. Chan and E. M. Scott, *Sensitivity Analysis,* West Sussex/England: John Wiley & Sons Ltd., 2000.

[17] A. C. Thornton, "A Mathematical Framework for the Key Characteristic Process," *Research in Engineering Design,* no. 11, pp. 145-157, 1999.

[18] B. Schleich and S. Wartzack, "A discrete geometry approach for tolerance analysis of mechanism," *Mechanism and Machine Theory,* vol. 77, pp. 148-163, 2017.

[19] B. M. Colosimo, G. Moroni, S. Petro and Q. Semeraro, "Manufacturing Signature of Turned Circular Profiles," *Manufacturing, Modelling, Management and Control,* vol. 15, no. 2, pp. 1-6, 2004.

[20] P. Eschmann, L. Hasbargen and K. Weigand, Ball and Roller Bearings – Theory, Design and Application, Chichester/England, New York/USA, Brisbane/Australia, Toronto/Canada and Singapore: John Wiley and Sons, 1985.

[21] DIN 7190-1, Interference fits – Part 1: Calculation and design rules, Berlin/Germany: Deutsches Institut für Normung, 2013.

[22] S. R. Schmid, B. J. Hamrock and B. O. Jacobson, Fundamentals of Machine Elements, Hoboken/USA: CRC press, 2014.

[23] R. M. Mitrović, I. D. Atanasovska, N. D. Soldat and D. B. Momčilović, "Effects of Operation Temperature on Thermal Expansion and Main Parameters of Radial Ball Bearings," *Thermal Science,* vol. 19, no. 5, pp. 1835-1844, 2015.

[24] A. Aschenbrenner and S. Wartzack, "A Concept for the Consideration of Dimensional and Geometrical Deviations in the Evaluation of the Internal Clearance of Roller Bearings," *Procedia CIRP,* vol. 43, pp. 256-261, 2016.

[25] J. Havel and A. Herout, "Yet faster ray-triangle intersection (using SSE4)," *IEEE transactions on visualization and computer graphics,* vol. 16, no. 3, pp. 434-438, 2010.

[26] ISO 1281-1, *Rolling bearings – Explanatory nodes on ISO 281 – Part 1: Basic dynamic load rating and basic rating life,* Geneva/Switzerland: International Organization for Standardization, 2008.

[27] J. De Mul, J. J. Kalker and B. Frederiksson, "The Contact Between Arbitrarily Curved Bodies of Finite Dimensions," *Journal of Tribology,* vol. 108, no. 1, pp. 140-148, 1986.

[28] M. Harnett, "A General Numerical Solution for Elastic Body Contact Problems," *ASME Applied Mechanics Division,* vol. 39, pp. 51-66, 1980.

[29] E. Borgonovo, "A new uncertainty importance measure," *Reliability Engineering and Systems,* vol. 92, pp. 771-784, 2007.

[30] E. Plischke, E. Borgonovo and C. L. Smith, "Global sensitivity measures from given data," *European Journal of Operational Research,* vol. 107, pp. 432-436, 2012.

[31] T. Kiekbusch, Strategien zur dynamischen Simulation von Wälzlagern, Dissertation, Tech. Univ. Kaiserslautern, 2017.

[32] R. Teutsch, Kontaktmodelle und Strategien zur Simulation von Wälzlagern und Wälzführungen, Dissertation, Techn. Univ. Kaiserslautern, 2005.

[33] R. Dahiwal, T. Kiekbusch and B. Sauer, "Abschlussbericht zum FVA-Forschungsvorhaben Nr. 625 II: Entwicklung eines Berechnungsmoduls zur Dynamiksimulation und Betriebsanalyse von Zylinderrollenlagern unter Berücksichtigung der Umgebungskonstruktion in Simpack," Forschungsvereinigung Antriebstechnik e. V, Frankfurt/Main, 2016.

[34] T. Kiekbusch, V. Aul, M. Marquart and B. Sauer, "Experimental and Simulative Studies of Friction Torque in Roller Bearings with Minimum Amount of Lubrication," in *International Colloquium Tribology 2012 – Tribology*, Ostfildern, 2012.

[35] K. Kunert, "Spannungsverteilung im Halbraum bei elliptischer Flächenpressungsverteilung über einer rechteckigen Druckfläche," *Forschung auf dem Gebiete des Ingenieurwesens,* pp. 165-174, 1961.

[36] J. H. Tripp and B. J. Hamrock, "Surface Roughness Effects in Elastohydrodynamic Contacts," National Aeronautics and Space Administration, Scientific and Technical Information Branch, Washington, D.C., 1985.

[37] R. Teutsch and B. Sauer, "An Alternative Slicing Technique to Consider Pressure Concentrations in Non-Hertzian Line Contacts," *Journal of Tribology,* pp. 436-442, 2004.

[38] P. Dietl, Damping and Stiffness Characteristics of Rolling Element Bearings, Dissertation, Wien: Technische Universität Wien, 1997.

[39] R. S. Zhou and M. R. Hoeprich, "Torque of Tapered Roller Bearings," *Journal of Tribology,* pp. 590-597, 1991.

[40] A. Weidinger, "Prüfung von Geräusch und Welligkeit bei Wälzlagern," VDI Berichte Nr. 2147, 2011.

[41] D. D and G. H. R, "A Numerical Solution to the Elastohydrodynamic Problem," *Journal Mechanical Engineering Science,* pp. 6-15, 1959.

[42] ISO 286-1, *Geometrical product specification (GPS) - ISO code system for tolerances on linear sizes - Part 1: Basis of tolerances, deviations and fits,* Geneva/Switzerland: International Organization for Standardization, 2011.

Bearing Fatigue Life of a Multi-Material Shaft with an Integrated Raceway

Timm Coors, Florian Pape, Gerhard Poll

Institute of Machine Design and Tribology, Leibniz Universitaet Hannover, coors@imkt.uni-hannover.de

Abstract– The development progress in engineering regarding weight reduction, increase in performance and functional integration implies an optimisation of rolling bearings. Conventional components, which are manufactured from monolithic materials, often lead to a conflict of objectives when it comes to high-stressed parts, which also have to be light, cost-effective and resource-efficient. To achieve this, a multi-material shaft with an integrated raceway is presented in this paper. Through a deposition welding process, a mild steel is hard-cladded with a higher strength steel, which covers the fatigue life-determining material volume under cyclic rolling contact fatigue. A subsequent forming process offers material and process-related advantages.

To design the properties of the wear protection layer, a calculation model was developed. A three dimensional finite element model represents the tribological contact between the rolling element and the shaft. The numerical solution of this model delivers the stress state resulting from the boundary conditions and an external load. The contact pressure, which is superimposed by the residual stress state, induces a subsurface maximum of orthogonal shear stress. Peak value and location of this stress field can be used to calculate the bearing fatigue life of the multi-material shaft based on an approach of IOANNIDES and HARRIS. This approach puts a material dependent stress fatigue limit τ_u into relation with a fatigue stress criterion τ_i. In this paper, the Dang-Van damage criterion is used. The simulations are verified by bearing endurance tests, which were carried out on a three-bearing test bench. These first results will be presented and compared with shafts manufactured from monolithic material.

Keywords – bearing fatigue life, multi-material roller bearing, tailored forming, residual stress

1. Introduction

Energy efficiency and lightweight design continues to be driving forces in mechanical engineering. A further enhancement of components functionality and lifespan relies on the material and its purity, which however offers a trade-off between the mechanical properties and its ecological and economical characteristics. Conventional components, which are manufactured from monolithic materials, often lead to a conflict of goals when it comes to high-stressed parts under multiaxial load, which also have to be light, cost-effective and resource-efficient. The development of new process chains makes it possible to manufacture components with tailor-made properties. Thus, a significant increase in production quality and efficiency can be obtained by combining different materials in one component. With the use of semi-finished work pieces, it is possible to design mechanical components with a multi-material approach (see Figure 1-1).
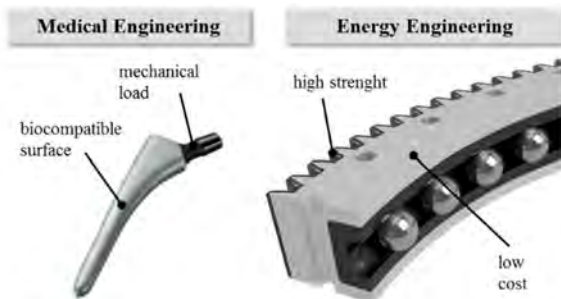

Figure 1-1: Examples of multi-material components: femoral implant (left) and slewing bearing (right).

Within this paper, roller bearings were used as components with partly conflicting requirements: On the one hand, roller bearings have to offer a high durability under complex stresses with low frictional losses under difficult lubrication conditions. For these part zones, a high strength material with a high fatigue limit and enhanced boundary layer properties has to be utilized. On the other hand, roller bearings must enable a precise and accurate mounting of rotating parts. For this connecting structure, an easily available, cheap or low specific weight base material is sufficient.

2. Collaborative Research Centre (CRC) 1153 "Tailored Forming"

In order to help resolve the described trade-off, a multi-material shaft with an integrated raceway for a cylindrical roller bearing type RNU204 is presented in this paper (see Figure 1-2, right). This component is used as an example of load-adjusted machine elements with tailored properties as an analogous model on a laboratory scale. The multi-material shaft was designed and manufactured within the Collaborative Research Centre (CRC) 1153 "Tailored Forming" at Leibniz University Hannover by a new process chain to produce load-adjusted hybrid solid components by using joined semi-finished workpieces (see Figure 1-2). Through a powder metallurgical deposition welding process (PTA: plasma transferred arc welding), tempered steel (material number 1.0402) was hard-faced with a higher strength steel (1.7035). The cladding steel is considered to be poorly weldable [1].
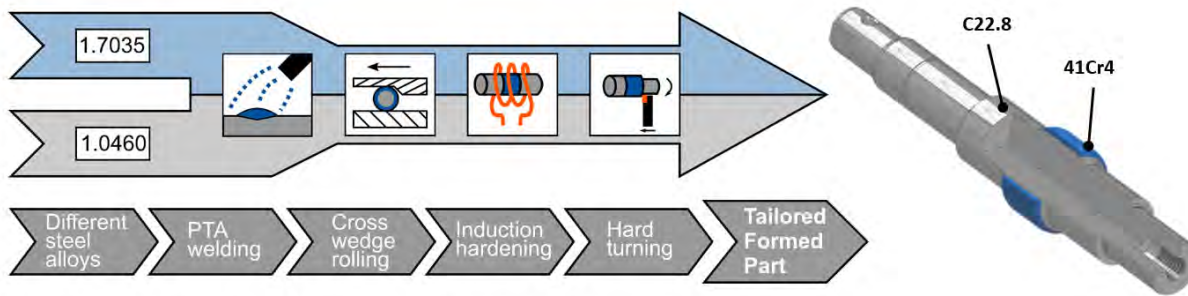
Figure 1-2: Process chain of tailored forming technology.

The hard facing has to include the fatigue life-determining part zone, which is defined by the load-induced stress under cyclic rolling contact fatigue through the rolling elements. The shaft combines certain demands like resistance against elongation and mechanical wear with a cheap and well processable base material.

A subsequent forming process through cross wedge rolling takes place, which is a warm forming process for reshaping rotationally symmetrical workpieces with variable diameter in axial direction using two oppositely moving wedge-shaped tools. By forming the semi-finished workpiece, the following material and process-related advantages can be obtained:

1. The joining zone of the different metals can have a simple joining zone geometry, which leads to a reliable process control for the joining process.
2. The subsequent forming leads to an improvement of the joining quality, because the welding microstructure can be transferred to a forming microstructure with a grain refinement through the process based thermomechanical treatment.
3. A near net shape forming facilitates hard machining.

Finally, a finishing process through local inductive hardening with spray cooling and hard machining of the relevant functional surfaces was carried out.

3. Methodology

The aim of these investigations was to prove the feasibility of this new production method for load-adapted components under rolling contact fatigue, where a high strength steel is joined coaxially on a base material. By combining modelling, numerical and experimental investigations, it will be possible to optimize machine elements like rolling element bearings of different types for their respective application.

To calculate the bearing fatigue life of a multi-material machine element, numerical investigations were carried out. Through a finite element analysis (FEA) it is possible to calculate the stress state of the component, resulting from external loads and residual stresses. This finds input in a damage accumulation model by IOANNIDES and HARRIS [4], which allows a prediction for bearing fatigue life through rolling contact fatigue. The calculation is validated by bearing fatigue tests.

3.1. *Numerical modelling of hybrid components*

Figure 1-3 shows a microsection of a tailored forming specimen with circular welding of the cladding material (cf. Figure 1-2). The cladding on the specimen using deposition welding showed an unequal distribution along the main axis. Within the weld pool, both materials were mixed and the joining zone is showing a waviness. In the middle section of the specimen, forming through cross wedge rolling has been carried out. The subsequent forming operation improves the quality of the coating by transforming the microstructure based on welding to a forming microstructure with grain refinement due to the thermomechanical treatment. The forming process also improves the flatness of the cladding and straightens the waviness of mixed materials. Investigations on the microstructure can be found in [2] and [3].
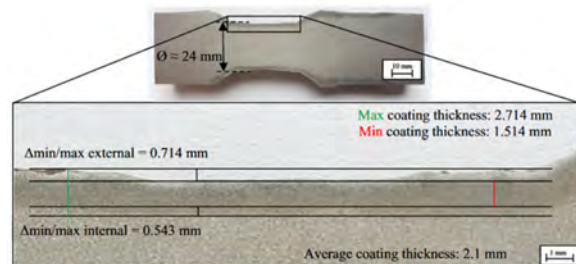
Figure 1-3: Multi-material workpiece after cross wedge rolling [2].

With this knowledge of the joining zone geometry, an FE-model of the contact zone has been set up in *Ansys Mechanical APDL* (cf. Figure 1-4, middle). By using the symmetry of geometry, a 18°-segment of the multi material shaft is modeled. It represents the cladding with a variable height *h*, an interlayer with a constant height of 0.2 mm and the base material. The highest loaded rolling element of the RNU204 cylindrical roller bearing is also modelled as the contact partner for the FEA. In the contacting area, the model is fine meshed to ensure the convergence of the contact problem. The FE model is fully parameterised for parameter studies and sensitivity analysis. The results of the FEA include shear stresses and hydrostatic stresses of the components.

Figure 1-4: Flow chart of fatigue life calculation; h: cladding layer height.

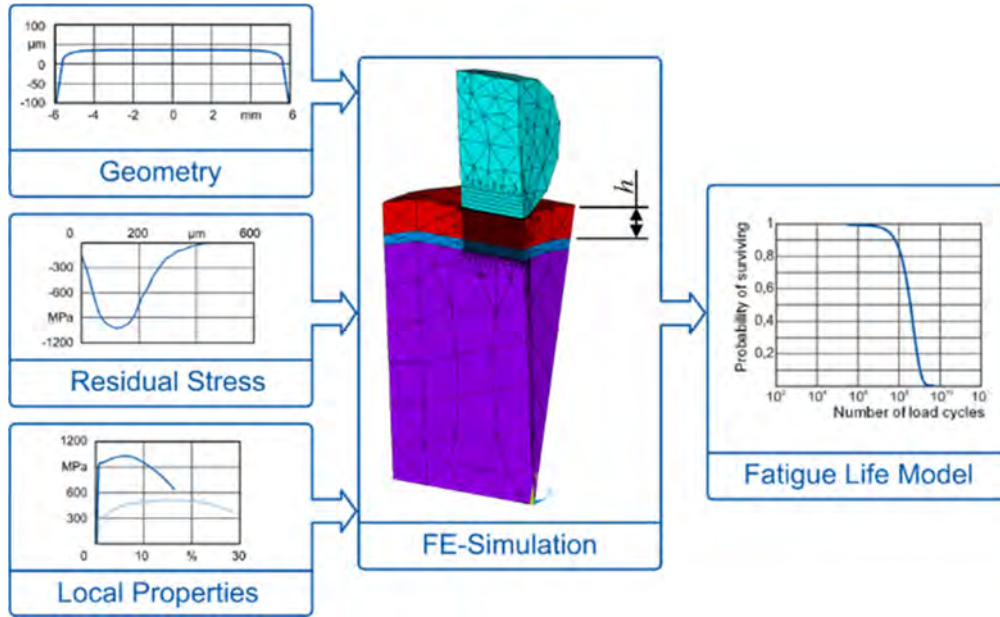### 3.2. *Fatigue life model*

In order to determine the bearing fatigue life of the multi-material shaft shown in Figure 1-2 (right), the aforementioned component stresses resulting from the FEA are integrated into a fatigue life calculation. Figure 1-4 shows the flow chart of the numerical approach with focus on the inner raceway in order to compute the fatigue life under cyclic contact load of a multi-material component.

The three dimensional finite element model represents the tribological contact between the rolling element and the multi-material shaft. The numerical solution of this model has the three-dimensional stress state resulting from the boundary conditions and an external load as output. The external load is applied as pressure distribution on the outer raceway – rolling element contact. Additional input variables are the geometry of the contact zone and a residual stress depth profile, which results from the manufacturing process. The residual stress depth profile is imposed as initial stress to the simulation. Local material properties are regarded for the cladding and base material. The interlayer properties are interpolated linearly. Rough surfaces are disregarded for this simulation. The roughness of the shaft is defined to comply with the requirement that no surface induced damages occurs.

The Hertzian contact pressure, which is superimposed by the residual stress state, induces a subsurface maximum of orthogonal shear stress. Peak value and location of this stress field can be used to calculate the bearing fatigue life of the multi-material shaft based on the approach of IOANNIDES, BERGLING and GABELLI [5]:

$$\ln\left(\frac{1}{S}\right) \approx N^e \int_V \frac{(\tau_i - \tau_u)^c}{z'^f} \, dV \qquad (Eq. \ 1\text{-}1)$$

S:	Probability of survival
N:	Number of load cycles
V:	Damage risk volume [mm³]
e:	Exponent in the bearing life equation

c:	Exponent for stress criterion
τ_i:	Fatigue stress criterion (Pa)
τ_u:	Shear stress fatigue limit (Pa)
z':	Stress weighted depth (depth from the surface) (m)
f:	Factor in the bearing life equation

This approach, which is based on a WEIBULL-statistics [6] evolved on the model of LUNDBERG and PALMGREN [7], provides the probability of surviving S for a volume in damage risk V in dependence of the number of load cycles N. This is based on the assumption that fatigue occurs due to subsurface crack formation from cyclic shear stress of the rolling element. Ongoing cyclic load then leads to crack growth, which extends to the surface and causes pittings. The parameter z' represents a stress-weighted depth from the surface.

For the volume in damage risk, the damage relevant stresses ($\tau_u - \tau_i$) are calculated (Figure 1-5). In our case a maximum value of 620 MPa is calculated. This puts a local stress related fatigue criterion τ_i and a material dependent stress fatigue limit τ_u, below which the volume element will not fail by fatigue, into relation.
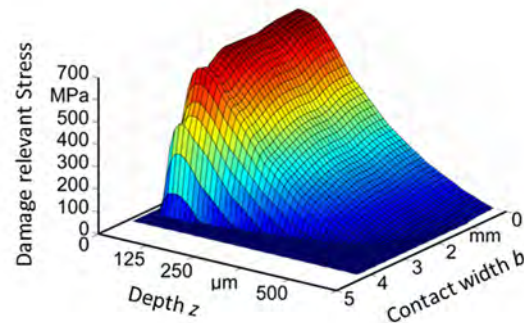

Figure 1-5: Damage relevant stresses $\tau_u - \tau_i$.

For the high-strength material, a stress fatigue limit of τ_u (41Cr4) = 300 MPa was assumed. For the base material τ_u (C22.8) = 210 MPa.

As fatigue stress criterion, the DANG VAN fatigue criterion [8] was used:

$$\tau_i = \left(\tau_{0,max} - k_{hyd} \cdot p'_{hyd}\right)_i \qquad (Eq. \ 1\text{-}2)$$

$\tau_{O,max}$:   Maximum shear stress (Pa)

k_{hyd}:   Weighting factor for hydrostatic stresses

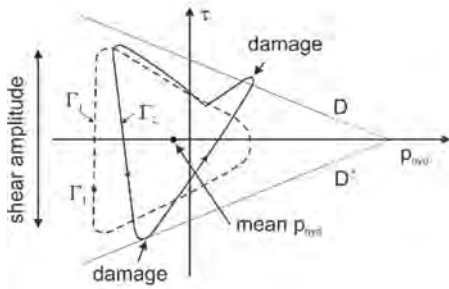p'_{hyd}:   Hydrostatic stress including compressive stresses (Pa)

Figure 1-6: Model for the DANG VAN stress criterion, based on [8].

It sets the orthogonal shear stress τ_O in relation to the hydrostatic stress p'_{hyd}. DANG VAN stated a linear relationship between these quantities which can be seen in Figure 1-6. Two straight lines delimit the safety domain (no fatigue crack initiation). In this figure, the ordinate is the shear stress τ acting on an oriented direction and the abscissa is the hydrostatic stress p_{hyd}. Two more loading paths are shown: Path r_1 is non-damaging because it entirely lies within the straight lines that delimit the safe domain, whereas a small portion of path r_2 induces damage. The hydrostatic stresses required to calculate the DANG VAN stresses are calculated locally using the FE method.

3.3. *Experimental studies*

The simulations were validated by bearing endurance tests, which were carried out on a three-bearing radial fatigue test bench (see Figure 1-7). Here, the specimen is mounted with two conventional supporting bearings. The integrated raceway on the shaft acts as an inner ring for a cylindrical roller bearing (CRB) RNU204. On the tested CRB, a radial preload of 2 kN is applied through a spring assembly, which leads to rolling contact fatigue and rotating bending on the shaft. This equals a specific load ratio of $C/P = 7$ for the tested bearing. However, one has to keep in mind that this specific load rated by the manufacturer only applies to the outer ring – roller contact, because the shaft is made out of a different material. The Hertzian contact stress at the inner ring is 1.8 GPa. Additional test parameters are shown in Table 1-1. Within the path of load, vibrational measurements are carried out, by which bearing failure through the formation of pittings can be measured and which were used shut down the test bench.
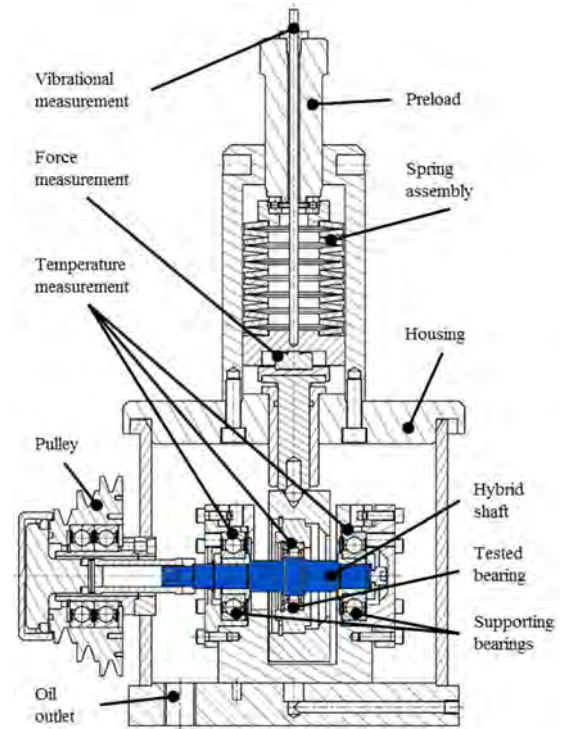
Figure 1-7: Three-bearing radial fatigue test bench.

Table 1-1: Fatigue test parameters.

Rotational speed	n_{IR}	3,000 min^{-1}
Radial load	F_{rad}	2,000 N
Specific load equivalent	C/P	7
Hertzian contact stress	$p_{max,IR}$	1.8 GPa
Viscosity at 40 °C	ν_{40}	68 mm²/s
Oil temperature	T_{set}	70 °C
Viscosity ratio	κ	1.77

4. Results and discussion

4.1. *Bearing fatigue tests with monolithic specimen*

In the absence of a large number of multi-material samples, first tests were carried out on specimen made from monolithic 41Cr4. These tests were used to validate the concept of tailored forming by comparison with conventional parts. Figure 1-8 shows the Weibull probability plot of conventional shafts, made from monolithic 41Cr4. For the aforementioned load parameters, a nominal bearing life of 150 hours with a 50% probability of failure could be determined ($L_{50} = 150$ h). The shape parameter of the WEIBULL distribution is $\beta_{max} = 2.1$.
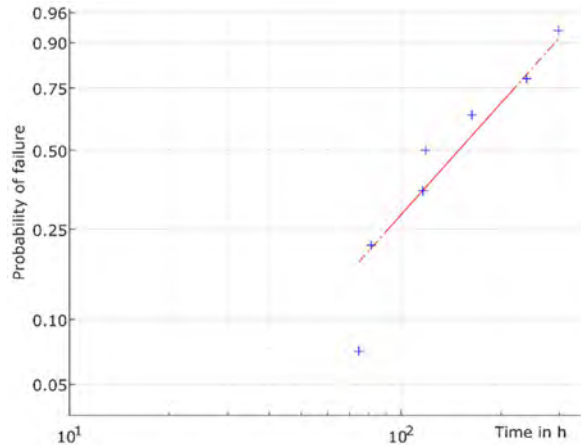

Figure 1-8: Weibull probability plot of monolithic material shafts.

These specimens failed, as expected, due to rolling contact fatigue which leads to pittings on the surface (see Figure 1-9). The damage occurred on the lower strength and higher loaded inner raceway on the shaft. The maximal depth of the pitting was 170 μm which is the depth of maximal orthogonal shear stress under load. Failures on the rollers or the outher ring of the CRB (both made from 100Cr6) did not occur.
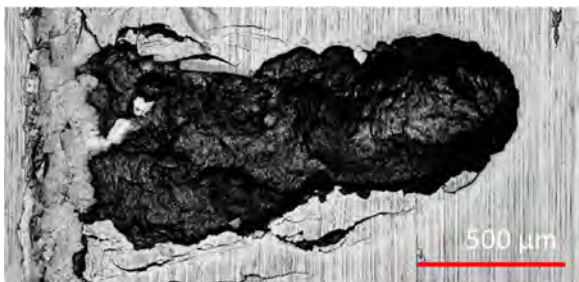

Figure 1-9: Micrograph of pitting due to rolling contact fatigue on monolithic shaft made from 41Cr4.

4.2. *Preliminary studies with multi-material shafts*

Three multi-material shafts were investigated in preliminary studies on tailored formed components. One of these samples did not undergo the forming process, resulting in an early failure after 16 hours (see Figure 1-10). The origin of this failure due to pitting was a material imperfection in the cladding layer, which lead to crack growth under the shear stress from the cyclic rolling load. A second multi-material specimen failed after 21 hours due to a similar pitting.
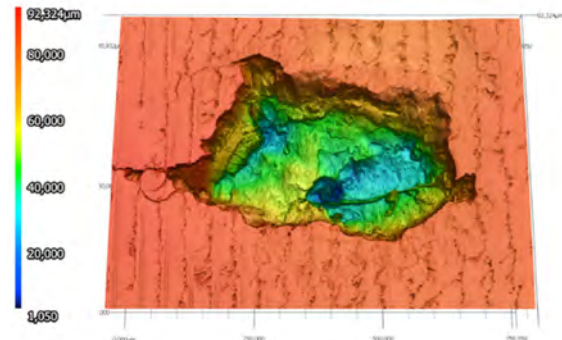

Figure 1-10: Laserscanning image of early failure due to material imperfection in the cladding layer

A third specimen passed more than 450 hours of fatigue testing without failure. This is 3 times the L_{50} rating life of the monolithic shafts, which is why no failure is expected for the third specimen. With improved cladding quality (no early failures due to material imperfection), the fatigue of the multi-material specimens is expected to be equal or higher than conventional parts due to the forming process.

4.3. *Calculational results*

To clarify the following results, the radial load on the investigated CRB was increased to 5.9 kN. The Hertzian contact stress on the inner raceway is 2.5 GPa. The fatigue life calculation will later also be carried out with the previous values according Table 1-1.

4.3.1. *Influence of cladding thickness*

As explained in section 3.2, the subsurface stress state of the component (particularly the orthogonal shear stresses) is necessary for the fatigue life calculation. Figure 1-11 depicts the calculated three-dimensional orthogonal shear stress state for two different cladding thicknesses in the plane of symmetry in longitudinal direction. In this case, the cladding height h of the higher strength 41Cr4 material is 1.5 mm (top) and 0.5 mm (bottom). The subsurface maximum of orthogonal shear stress for both thicknesses is $\tau_{yz,max} = 610$ MPa. Furthermore, the cheaper base material is affected by higher stresses. The cladding height h has an influence on local equivalent stress and the loading of base material depends on cladding height, because the thinner layer concentrates the stress maximum in a smaller volume. Therefore, a minimal cladding height is necessary to protect the lower strength interface and base material from excessive loads and rolling contact fatigue. A thin and therefore cheap cladding layer would be insufficient dimensioned. Evident from equation (1-1) is the demand for a high-strength material with a high stress fatigue limit τ_u.
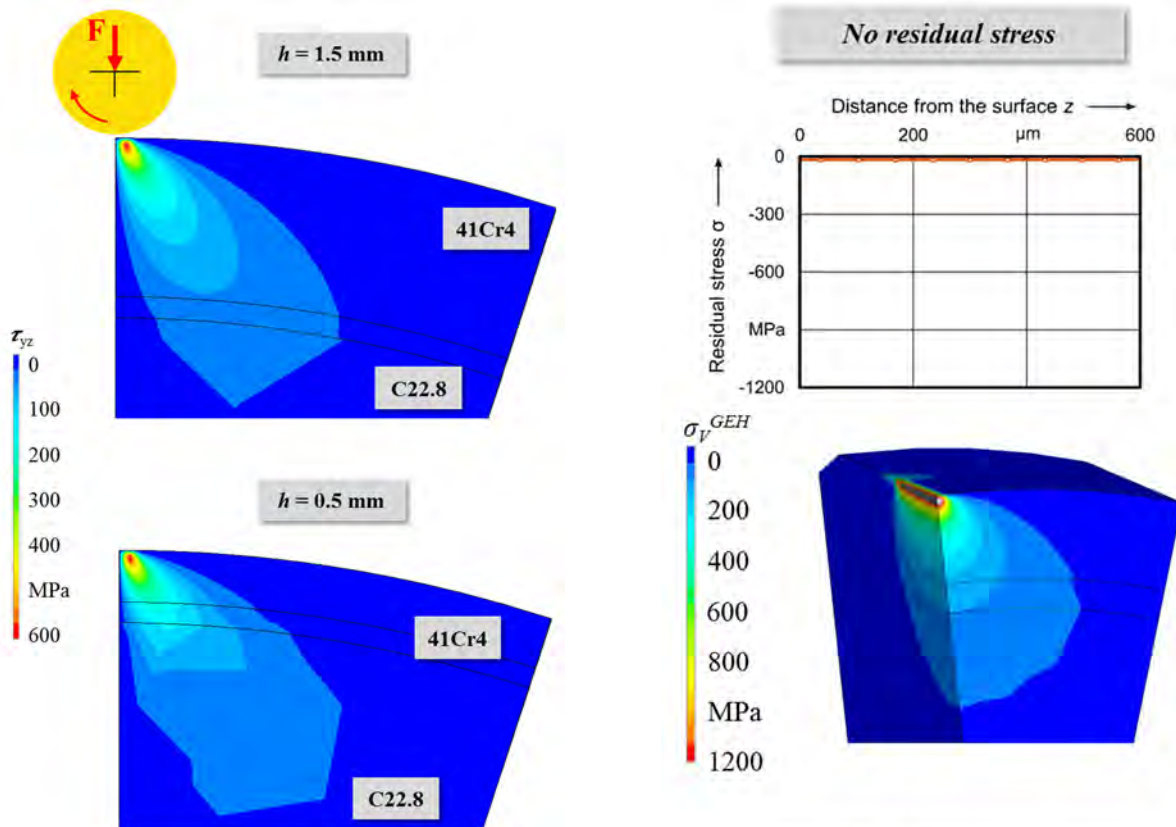
Figure 1-11: FE-simulation of a shaft segment under contact load: Orthogonal shear stress for different cladding heights.

4.3.2. *Influence of residual stress*

Previous studies showed a positive influence of load-induced stresses on bearing fatigue life, which has to be regarded [9], [10], [11]. Therefore, the influence of residual stress was investigated by imposing a residual stress state as initial stress to the simulation.

In Figure 1-12 and Figure 1-13, the VON-MISES stress of the multi-material shaft regarding the residual stress state is depicted for a cladding height $h = 1$ mm. Without pre-induced residual stresses, only the load stresses from the rolling element are visible. The von Mises equivalent stress shows a maximum of 1420 MPa at a depth of 100 μm below the surface. After hard turning (Figure 1-12 bottom), however, residual stresses with a maximum value of - 700 MPa at a depth from the components surface of 20 μm were induced. An additional planned deep-rolling process (Figure 1-13) allows inducing residual stresses with a higher maximum value of -840 MPa at a higher depth from the surface of 200 μm. This reduces the von Mises equivalent stress to 1328 MPa and moves the maximum of the stress closer to the surface. It is now at a depth of about 68 μm below the surface.
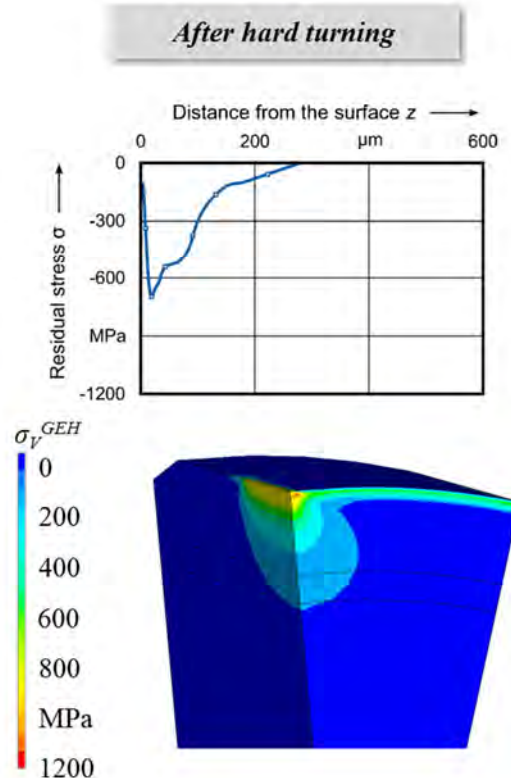

Figure 1-12: Von-Mises stress of the multi-material shaft including the residual stress state; cladding height h = 1 mm.
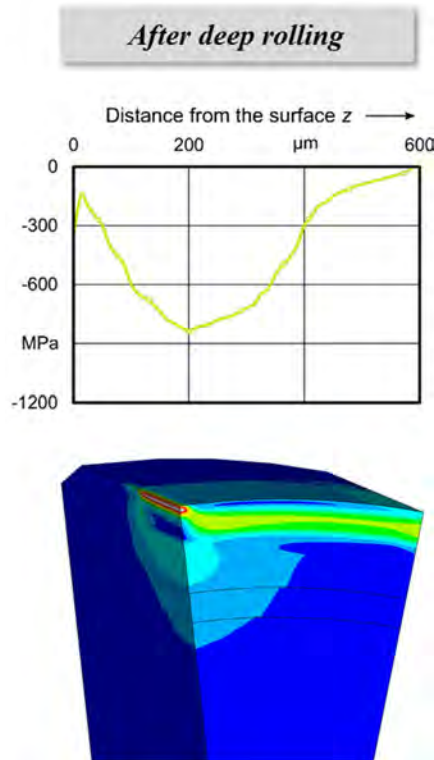
Figure 1-13: Von-Mises stress after additional deep rolling; cladding height h = 1 mm.

4.3.3. *Bearing fatigue life*

The bearing fatigue life of the multi-material shaft can be calculated according to Figure 1-4. By using the same material properties for all three zones of the modelled shaft segment, the bearing fatigue life of the monolithic component can also be calculated. Figure 1-14 displays the calculated bearing fatigue life regarding different radial loadings and cladding heights. The fatigue life simulation was carried out for a radial loading force on the tested CRB of 2 kN with a resulting Hertzian contact pressure of 1.8 GPa and for a force 5.8 kN (2.5 GPa). Furthermore, Figure 1-14 shows the calculated fatigue life and experimental data from monolithic specimen. The calculated bearing life L_{50}, where 50% of the specimen are expected to have failed, is $23.5 \cdot 10^6$ revolutions. This is within an error margin of 16% of the bearing fatigue life from the experimental studies. The basic trends of the calculated probability of survival are represented by the experimental values L_{10} and L_{63}.

A too thin cladding layer reduces fatigue life of multi-material machine elements by a factor of 3. With a cladding height of $h > 0.3$ mm the difference in fatigue life compared to monolithic parts is within a 15% margin. For the investigated load parameters a layer thickness of $h > 0.5$ mm shows a similar calculated probability of survival as monolithic shafts.

Due to manufacturing, the bearings are equipped with residual stresses in the depth of the highest load induced stresses, which is also included. In the zone of the highest load induced stresses beneath the surface, the critical fatigue stress is highest. By inducing residual stresses in this depth, the critical stress is reduced and the bearing fatigue life can be influenced positively by a factor of 1.4.
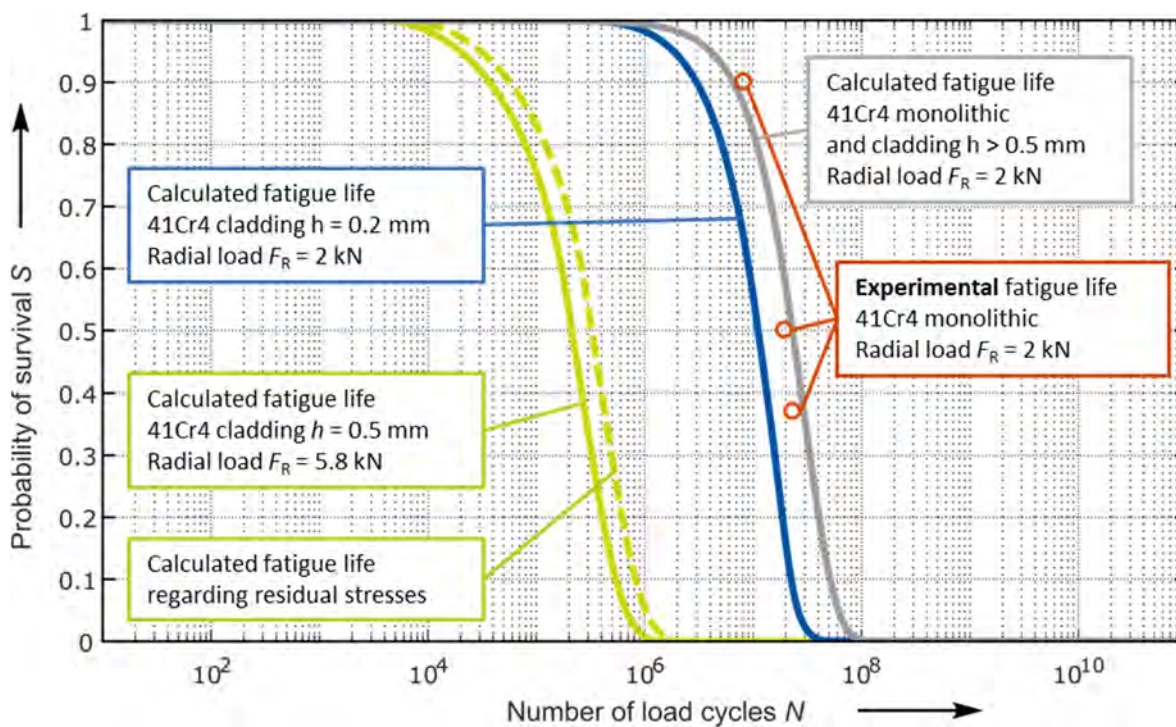

Figure 1-14: Bearing fatigue life of a multi-material shaft with an integrated raceway

4.4. *Discussion*

Based on the presented approach, the influence of boundary layer properties on bearing fatigue life of multi-material components could be worked out. A correlation between simulation and experiment for monolithic components could be shown.

The design of the material zone with higher fatigue strength enables an increase in fatigue life for multi-material machine elements. This can be transferred to components with larger geometric dimensions like slewing bearings, which allows manufacturing cost-efficient and resource saving parts with locally adapted material characteristics. Especially such big components, which are usually not made of classical bearing steel (like 100Cr6) due to costs, are suitable for the tailored forming approach.

During the bench tests however, it became clear that the experimental fatigue life of components made from multiple types of metallic material strongly dependents on the quality of production. Several early failures occurred due to pores and cavities, which required an optimization of the welding process in the future.

5. Conclusion and Outlook

In this paper, a new process chain for manufacturing multi-material machine elements by tailored forming has been presented. Using the example of a shaft, a calculation approach for estimating the fatigue life of a tailored forming component under the influence of cyclic rolling loads was presented. This was done by combining a statistical model with numeric simulations and experiments.

The presented findings help optimizing load-adjusted parts with tailored properties. An adaptable approach makes it possible to transfer the results to other tribologically stressed parts in any system with interacting surfaces in relative motion. In the future it should be possible to optimize components properties with regards to their respective application. Doing so, different multi-material machine elements like cylindrical roller thrust bearings [10] will be investigated using the presented simulation model. In order to transfer the findings to real world applications it is necessary to set up design guidelines for the development and manufacturing of these machine elements. The approach allows to save resources by combining cheap steel with a pure high reference hard facing made from bearing steel. By combining a lightweight base material with a protective hard facing it will be also possible to achieve a reduced power consumption during the components period of application [13].

Acknowledgment

References

[1] Mildebrath, M.; Blohm, T.; Hassel, T.; Stonis, M.; Langner, J.; Maier, H. J.; Behrens, B.-A.: Influence of Cross Wedge Rolling on the Coating Quality of Plasma-Transferred Arc Deposition Welded Hybrid Steel Parts, International Journal of Emerging Technology and Advanced Engineering, 2017

[2] Blohm, T.; Mildebrath, M.; Stonis, M.; Langner, J.; Hassel, T.; Behrens, B.-A.: Investigation of the coating thickness of plasma-transferred arc deposition welded and cross wedge rolled hybrid parts, Production Engineering Research and Development, DOI: 10.1007/s11740-017-0734-7, 2017

[3] Pape, F.; Coors, T.; Barroi A.; Hermsdorf, J.; Kaierle, S.; Matthias, T.; Bonk, C.; Chugreeva, A.; Bouguecha, A.; Mildebrath, M.; Hassel, T.; Maier, H. J.; Behrens, B.-A.; Overmeyer, L.; Poll, G. (2018): Tribological Investigations on Tailored Formed Axial Bearing Washers. Tribology online (in print).

[4] Ioannides, E.; Harris, T.A.: A new fatigue life model for rolling bearings, Transactions of the ASME, Journal of Tribology, Vol. 107 (1985) pp. 367-378

[5] Ioannides, E., Bergling, G., Gabelli, A., "An analytical formulation for the life of rolling bearings", Acta Polytechnica Scandinavica, Mechanical engineering series No. 137, 1999

[6] Weibull, W.: A Statistical Theory of the Strength of Materials. Generalstabens litografiska anstalts förlag, Ingeniörsvetenskapsakademiens handlingar 1939

[7] Lundberg, G.; Palmgren, A.: "Dynamic Capacity of Rolling Bearings", Acta polytechnica. Mechanical engineering series, Generalstabens Litografiska Anstalts Förl., 1947

[8] Dang-Van, K.: "Sur la resistance la fatigue des metaux", Sci Tech Armement, 1973

[9] A.P. Voskamp, Rolling Contact Fatigue and the Significance of Residual Stresses, Deutsche Gesellschaft für Metallkunde, Proceedings: Residual Stresses in Science and Technology (1987), 713-720.

[10] T.A. Harris, M.A. Ragen, R.F. Spitzer, The Effect of Hoop and Material Residual Stresses on the Fatigue Life of High Speed, Rolling Bearings, Tribology Transactions, 35:1 (1992), 194-198, DOI: 10.1080/10402009208982109

[11] Neubauer, T.: "Betriebs- und Lebensdauerverhalten hartgedrehter und festgewalzter Zylinderrollenlager", Leibniz Universität Hannover, 2016

[12] Pape, F.; Coors, T.; Barroi, A.; Hermsdorf, J.; Mildebrath, M.; Hassel, T.; Kaierle, S.; Matthias, T.; Bonk, C.; Chugreeva, A.; Bonhage, M.; Bouguecha, A.; Behrens, B.-A.; Overmeyer L.; Poll, G. (2017): Tribological Investigations on Tailored Formed Axial Bearing Washers, 6th World Tribology Congress, 17th – 22th September 2017, Beijing, China

[13] Coors, T, Pape, F., Poll, G. (2017): Concept for enhancing machine elements by residual stresses and tailored forming, Proceedings, IAMOT 2017, Vienna, ISBN: 978-3-200-04986-4

A Study on the Frictional Torque and Temperature Behavior in Tapered Roller Bearings

Marco Schwarz [1], Jürgen Liebrecht [2], Attila Gonda [2], Bernd Sauer [2]

[1] *Component Development / ZF Friedrichshafen AG, marco.schwarz@zf.com*

[2] *MEGT / TU Kaiserslautern / j.liebrecht@mv.uni-kl.de, attila.gonda@mv.uni-kl.de, sauer@mv.uni-kl.de*

Abstract– This paper presents an experimental study on tapered roller bearings with the main focus on the frictional torque and temperature behavior. It also looks at the oil quantity necessary to ensure safe operating conditions. By using a modified test bench from MEGT, tapered rolling bearings from three different suppliers are compared with one another. The critical operating conditions are identified by varying the amount of lubricating oil. In addition to the oil quantity, the direction of the oil supply is also investigated in these tests as an influential factor on the frictional torque and the temperature behavior. The results presented in this paper provide an overview of the required oil supply for tapered roller bearings, factoring in speed and load. Furthermore, the results show that not only the load capacity should be taken into account when selecting suitable rolling bearings, but also the number of rolling elements, which improves efficiency.

Keywords – efficiency, lubrication, frictional torque, tapered roller bearings, oil flow rate, starvation

1. Introduction

Due to rising fuel costs and environmental requirements, it is becoming increasingly important to introduce measures to reduce fuel consumption in all vehicles. In the foreground are often individual components of the powertrain, including rolling bearings in engines or transmissions. Tapered roller bearings represent a critical rolling bearing type especially with regard to efficiency or power losses. Also, at particularly higher speeds and loads, tapered roller bearings (TRB) contribute significantly to higher power losses and poorer efficiency.

Tapered roller bearings consist of a cup – roller – cone design. Besides having a cage to separate the rollers, one important part in every tapered roller bearing is the guiding rib of the inner ring that contacts the rollers on the big roller end and guides the rollers in circumferential direction.
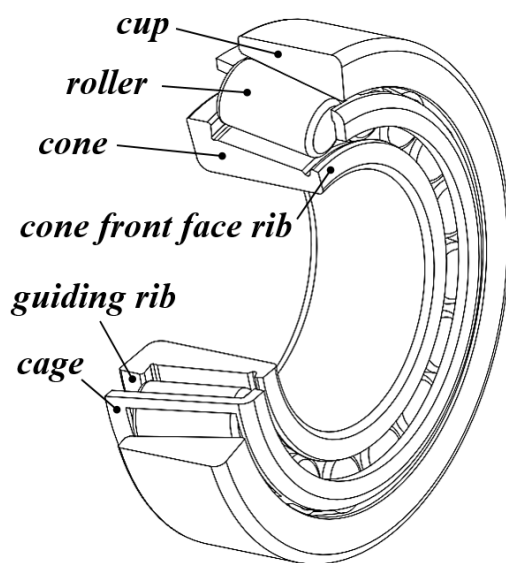

Figure 1: Tapered roller bearing

Losses in tapered roller bearings can be divided into load-dependent and load-independent losses. Load-dependent losses are caused by rolling friction between the rollers and inner and outer ring raceways; sliding friction between the rollers and the cage as well as between roller ends and the guiding rib. The latter is the result of different taper angles on the inner and outer ring raceways. Because of these differences, a radial load generates an axial force which is supported by the rib. In order to predict the load-dependent power losses and frictional torque of this roller bearing type, many calculation methods have been developed. An analytical method for axially loaded TRB is presented by *Aihara* in [1]. The analytical equations presented by the author take into account the elastohydrodynamic lubrication (EHL) rolling resistance as well as the sliding friction in roller end and rib contact. The amount of losses due to sliding friction between the rolling elements and the cage is assumed to be negligibly low and is therefore not factored in. *Zhou* and *Hoepprich* present in [2] a more detailed calculation model for TRB that also neglects the cage friction. The special feature of this model is that the thermal effects and surface roughness were taken into account in the calculation of the oil film thickness and the description of mixed friction in on-board contact. Other authors also used this approach of accounting for mixed friction conditions in their friction calculation models for tapered roller bearings [3]. Different methods are available to calculate the significant friction part of the rib-roller end contact. *Houpert* [4] uses a calculated local friction coefficient that depends on the oil film parameter Lambda. A similar approach with an experimentally determined friction coefficient is used by the authors in [5]. The influence of the resulting deformation in the roller end-rib contact on the oil film and the friction is evident from the EHL analysis in [6]. Besides the aforementioned possibilities of calculating frictional torque in tapered roller bearings, further models and approaches are available. Some of these models and approaches, especially calculating load-dependent losses, are presented in [7].

Another significant factor in total frictional losses of rolling bearings are the load-independent drag and churning losses [8]. These losses are the result of the oil being displaced by the rolling elements as well as the shear stress on the surfaces of the rolling bearing elements. This shear stress may significantly influence the

rolling element kinematics and thus the frictional torque behavior of the rolling bearings [9].

Different approaches and models are also available for calculating load-independent losses. Since an analytical calculation of these losses is not yet possible, most of the available calculation models are empirical or based on the boundary layer theory according to *Schlichting* [10]. One of these models for roller bearings, which factors in the drag torque acting on the roller surfaces and the cage, is presented by *Rumbarger et. al* in [11]. Another calculation approach that distinguishes between the drag and churning torque is presented by *Gupta* in [12]. An empirical model that calculates the load-independent losses of roller bearings as a function of the oil quantity is provided by *Koryciak* [13]. Models for estimating drag and churning torque in tapered roller bearings and deep groove ball bearings for symmetrical operating conditions with regard to oil distribution are presented in [14] and [15]. These models were derived from experimental studies and CFD simulations by applying theories of fluid mechanics. Furthermore, rolling bearing manufacturers provide their own methods for calculating load-dependent, but also load-independent losses [16].

The calculation models and approaches presented above highlight the influencing factors that are responsible for the total frictional torque of tapered roller bearings. These factors include the applied load, rotational speed, quantity and viscosity of the oil, number and length of rolling elements, cage design as well as the profiling of the rib and raceways. To reduce the power losses in rolling bearings, one option is to geometrically optimize the bearing components (profiling of the raceways, reducing the number of rolling elements, cage design [17] etc.); a second is to optimize the amount of oil supply [18].

As part of a joint project between the Institute for Machine Elements, Gears and Transmissions (MEGT) and ZF Friedrichshafen AG, the operating behavior of tapered roller bearings has been examined in order to learn more about the frictional torque and the temperature behavior. In this context, two main questions regarding the frictional torque behavior had to be answered. The first test series was carried out in order to see which of the bearings was the most efficient, i.e., which bearing shows the lowest frictional loss under the given boundary conditions of higher loads, higher speeds and a specific oil quantity. The goal of the second test series was to determine what the minimum oil quantity is for stable operating behavior of tapered roller bearings working under higher loads and higher speeds.

This paper presents the results of these experimental studies. It also explains the causes of friction in tapered roller bearings, describes the test setup as well as the procedure for measuring the friction in tapered roller bearings. Lastly, it presents and discusses the measurement results regarding the operating behavior under increased load, increased speed as well as reduced oil quantity.
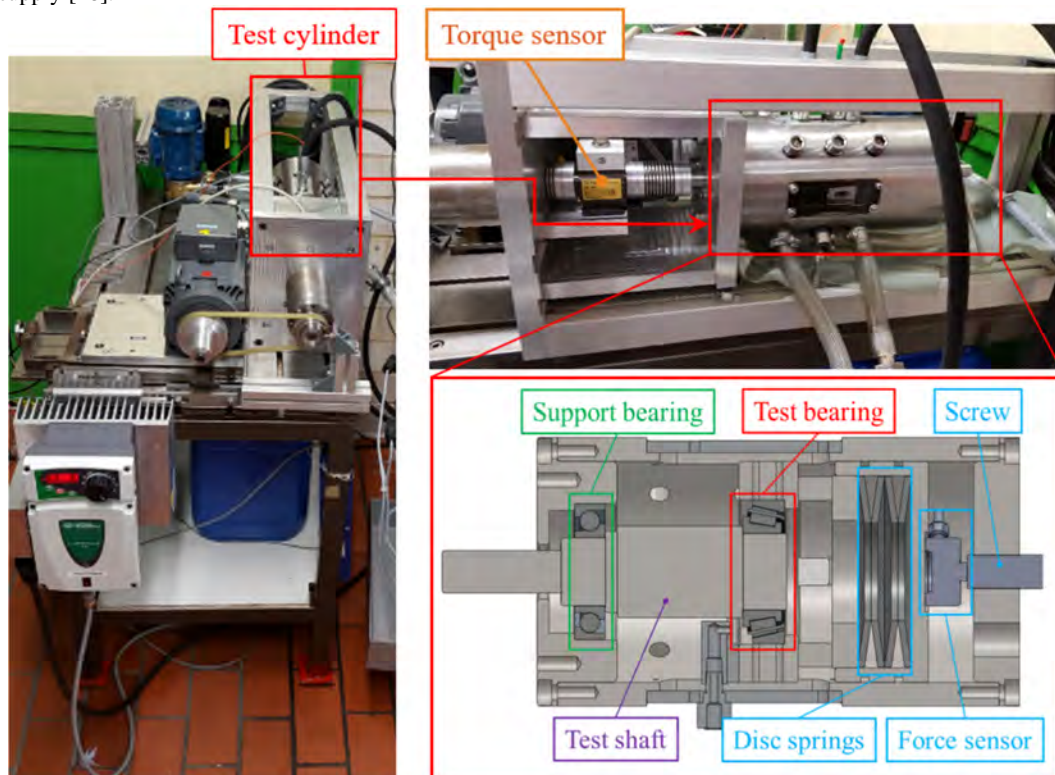

Figure 2: Test rig for measuring frictional losses on rolling bearings

2. Experimental approach

2.1. *Test rig*

Figure 3 shows the test rig used for the experimental studies on tapered roller bearings under axial load. As seen in the figure, the experiments were carried out with a back-to-back rolling bearing arrangement consisting of the test bearing and a support bearing (angular contact ball bearing 7208). An electric motor is used to drive the bearings arrangement. The test shaft is connected to the drive via a torque sensor. This means only the total frictional torque of the bearing arrangement can be measured. An axial load device is used to apply the test load. It is composed of a screw, a force sensor and disc springs. The disc springs compensate for the thermal expansion in the test shaft. To monitor the flow around and through the test bearing, two vision panels are attached to the test cylinder. To continuously monitor operating conditions, sensors to measure rotational speed and temperatures are used. Table 3 shows the main properties of the test rig.
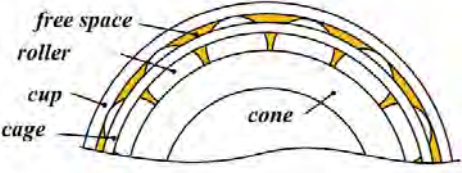
Table 3: Properties of the test rig

Characteristics	Unit	Value
Speed	rpm	≤10.000
Axial load	kN	≤20
Bearing size (outer ring)	mm	≤110
Measuring range	Nm	≤5

2.2. *Test bearings*

Three tapered roller bearings of the same size, but from different bearing suppliers were selected as the test bearings. The main differences between the test bearings are the material, cage design, number of rollers and supplier-specific differences like crowning and surface topography. However, all bearings have roughly the same dynamic and static load capacities. The main data for the test bearings are presented in Table 4.

Table 4: Dynamic and static load rating of the test bearings

Characteristics	Tapered Roller Bearings		
Supplier	TRB1	TRB2	TRB3
C_r	82 kN	81 kN	82
C_0	101 kN	98 kN	100 kN
No. of rollers	n	n	n-1
Free space	$0.95 \cdot A_0$	$0.93 \cdot A_0$	A_0

2.3. *Lubrication*

The test bearing and the support bearing each have an individual oil supply. For changing oil quantities in the test bearing, the oil quantity in the support bearing can be the same for each test. As explained in 2.1, the frictional moment is the sum of the test bearing and the support bearing. Only by keeping the oil quantity constant for the support bearing in each test will the effects of varying oil quantities in the test bearing be able to be assessed.
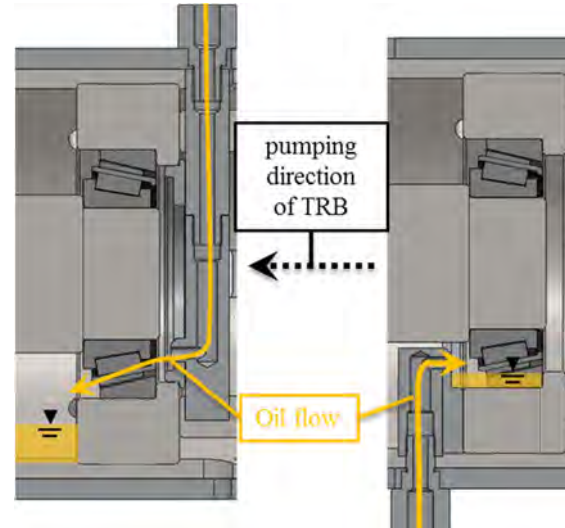

Figure 3: Lubrication in (left) and against (right) pumping direction

The oil supply for a tapered roller bearing has a major impact on the resulting frictional torque. In tapered roller bearings, a "pumping action" phenomenon exists in which oil is being pumped from the cone front face rib in the direction of the guiding rib. To examine the impact of the oil supply direction and the pumping direction on frictional losses, two oil supply circulation set-ups were tested. Both of them are shown in Figure , one with the test bearing being lubricated in the pumping direction and the other against. A synthetic transmission oil with a kinematic viscosity of 54 mm^2/s at 40 °C was used.

3. Comparison of frictional losses

In the first test series, three tapered roller bearings from different suppliers were investigated with regard to the frictional losses and temperature behavior. The main goal of the test series was to determine which of the bearings showed the lowest frictional losses under the given boundary conditions of higher loads, higher speeds and specific oil quantity.

3.1. *Test Procedure*

For this test series, a specific axial load was applied to the test bearings. The run-in period was set to 3000 rpm for 8 h at a specified oil quantity of 0.5 l/min. After the run-in period was finished, the actual frictional torque measurements were performed under various operating conditions, including different speeds ranging from 500 rpm up to 6000 rpm and 2 oil quantities of 0.3 l/min and 0.6 l/min. To compare the frictional losses of the three

tapered roller bearings, the measurements were carried out by supplying the oil in the pumping direction. In this test series, the bearing temperature is the result of the applied operating condition, namely speed, load, oil temperature and oil quantity.

3.2. Results

3.2.1. Run-in period

The difference in frictional torque and temperature behavior can be seen directly during the run-in period. Figure 4 shows the frictional torque of the three bearings during the run-in period. From the figure, it can be concluded that TRB3 shows lower frictional losses compared to TRB1 and TRB2. TRB1 and TRB2 also show a wider band during the run-in period at 0.5 l/min compared to TRB3.

The wider band of TRB1 and TRB2 can be reduced to a similar band as for TRB3 by increasing the amount of oil. The difference in frictional torque behavior is caused by a blocking effect of the tapered roller bearings and can be explained by the difference in the number of rolling elements.
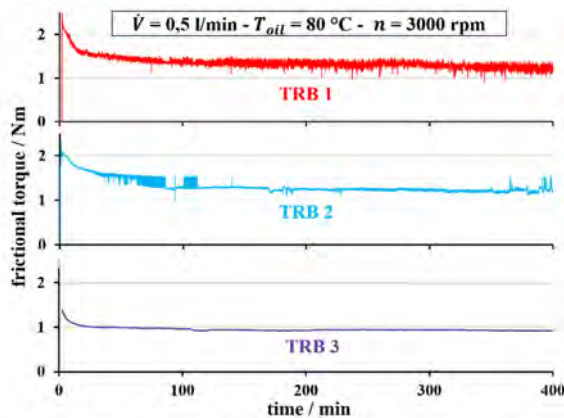

Figure 4: Comparison of the frictional behavior between the test bearings during the run-in period - oil supplied in the pumping direction

3.2.2. Blocking effect

TRB1 and TRB2 have a higher number of rolling elements. For this reason, the oil that passes the bearing in the pumping direction is blocked (blocking effect), thus disturbing the oil film built up at the guiding rib. In Figure 5, the influence of the oil quantity on the frictional torque behavior of TRB1 can be seen. The wider band and higher frictional losses while operating at 0.5 l/min, can be reduced by increasing the amount of oil to 0.6 l/min. At 0.5 l/min, the oil passing through the bearing is blocked which means the bearing is operating in mixed friction conditions. Because of this, the frictional torque shows a wider band and higher frictional losses. By increasing the amount to 0.6 l/min, more oil is passing through the bearing more constantly, thus allowing the oil film to build up. The oil film that builds up at the guiding rib is improved and, due to the higher amount of oil at 0.6 l/min, TRB1 shows an improved frictional torque behavior. Besides an improved frictional torque behavior, the temperature of the outer ring also decreases.
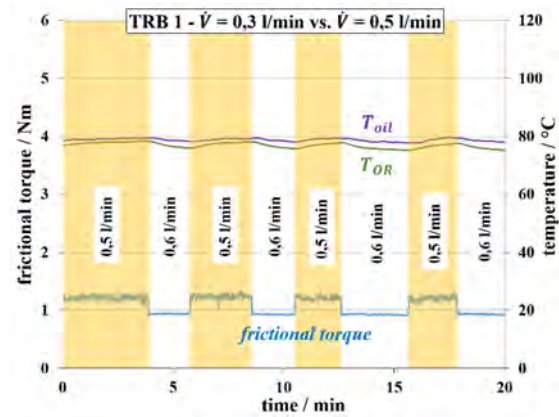

Figure 5: Blocking effect – Influence of oil quantity on the frictional torque behavior of TRB1 – lubrication in pumping direction

In comparison, TRB3 does not show this kind of behavior at the specified operating conditions. The reason for this is that TRB3 has a lower number of rolling elements compared to TRB1 and TRB2. This creates more space in between the rolling elements for the oil to pass through, which improves the oil film build-up at the guiding rib contact zone, provided that the oil is supplied in the pumping direction.

3.2.3. Comparison

After finishing the run-in period, the actual frictional torque measurements were carried out for different speeds and using 2 different oil quantities. The results of the measurements can be seen in Figure 6.
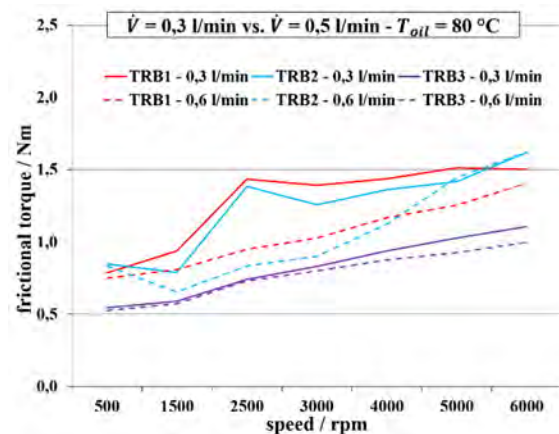
Figure 6: Comparison of frictional losses – oil supplied in the pumping direction

As already seen during the run-in period, TRB3 shows lower frictional losses compared to TRB1 and TRB2. TRB3 shows lower frictional losses at all speed levels and for both oil quantities. In general, higher speed levels result in higher frictional losses because of higher rolling friction. In addition, for higher oil quantities, the frictional losses are lower because, with more oil, the bearing can build up the oil film at the guiding rib better. Finally, for TRB1 and TRB2, the higher oil quantity of 0.6 l/min

eliminates the blocking effect that is present for an oil quantity of 0.3 l/min and at certain speeds.

3.2.4. *Variation of frictional torque results*

In order to assess the variation between samples from each supplier, the tests were repeated using additional samples from each bearing supplier. Figure 7 displays the frictional torque and temperature curves during the run-in period for sample TRB1-1 and sample TRB1-2.

Figure 7: Frictional torque and temperature of TRB 1 during the run-in period - oil supplied in the pumping direction

Figure 8: Frictional torque and temperature of TRB 3 during the run-in period - oil supplied in the pumping direction

The curves for sample TRB3-1 and sample TRB3-2 are displayed in Figure 8. Both cases show that the findings observed in 3.2.1 and 3.2.2 regarding the frictional torque behavi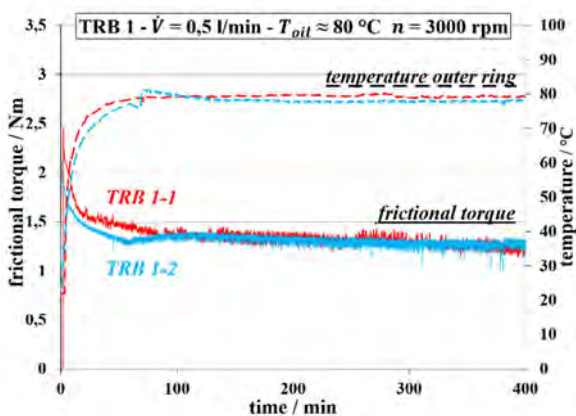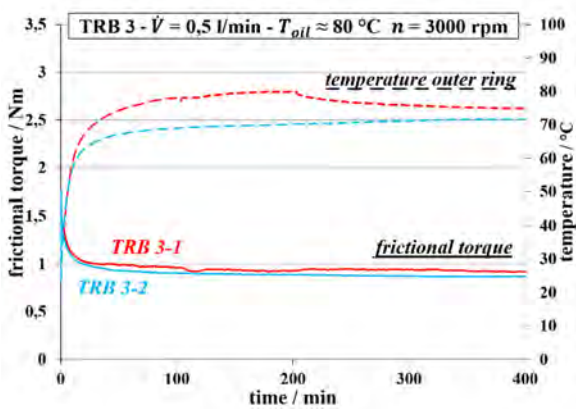or is the same for each of the bearing suppliers. In TRB1-1 and TRB1-2, there is a wider band in the frictional torque curves. In addition, the frictional torque value is nearly identical. For TRB3-1 and TRB3-2, identical frictional torque behavior can also be observed. Only a slightly higher frictional torque value in TRB3-1 can be seen compared to TRB3-2.

3.2.5. *Influence of pumping direction*

What is significant for frictional losses in tapered roller bearings is the resulting friction between the rolling elements and the guiding

rib, especially when operating at high oil temperatures and low oil viscosities. The reason for increased heat development in axially loaded tapered roller bearings is usually mixed friction conditions at the rib contact. Further tests were carried out to determine whether the frictional losses can be reduced by changing the direction of the oil supply. For this purpose, in a first test run, the injector was placed against the pumping direction (see Figure) and in a second test run directly above the inner ring rib of the bearing, as shown in Figure 9.
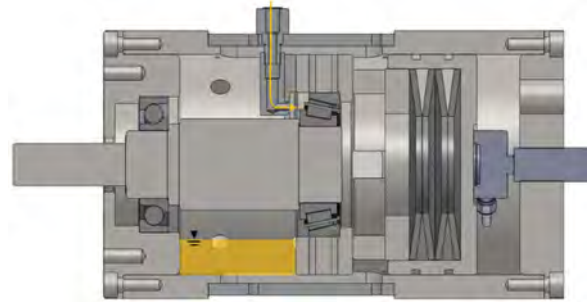
Figure 9: Targeted lubrication of the guiding rib

The results of these tests are shown in Figure 10 and Figure 11. By comparing the results of the oil supply in the pumping direction (see Figure 7 and Figure 8) and against the pumping direction, no significant change in frictional losses can be noted. In contrast, the results for the targeted lubrication of the inner ring guiding rib show a significant decrease in frictional losses for both test bearings.

Decreases in frictional losses are due to a higher oil quantity in the rib contact as well as lower hydraulic losses. When the oil is supplied against the pumping direction, this means there is enough cooler oil at the guiding rib, which improves the oil film build-up. Particularly with TRB1, operation in mixed friction conditions is avoided, unlike with the oil supply in the pumping direction. The hydraulic losses are reduced because the oil does not flow through the bearing. That is why the oil is not displaced and sheared by or on the rolling bearing elements; this results in lower drag and churning losses.
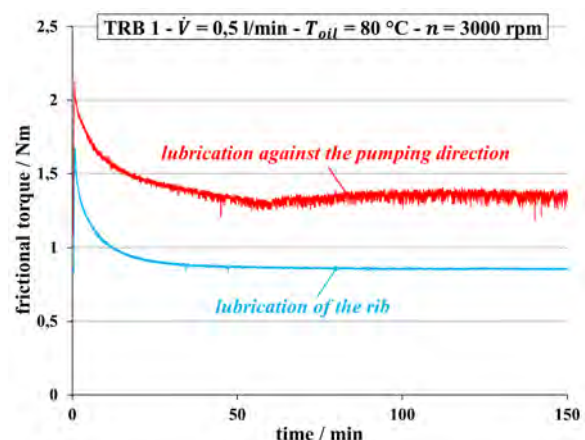
Figure 10: Frictional torque of TRB 1 depending on the position of the oil supply
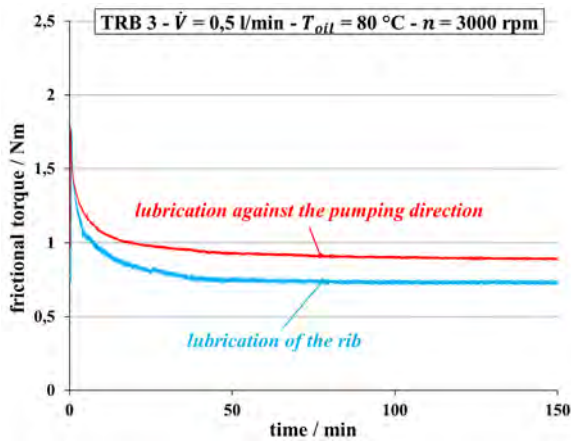
Figure 11: Frictional torque of TRB 3 depending on the position of the oil supply

When comparing the two tapered roller bearings regarding the frictional torque and the direction of the oil supply, it should be noted that in both cases the frictional behavior improves significantly by a targeted lubrication of the inner ring guiding rib (see *Table 5*). The TRB1 shows a drop in frictional torque of approx. 30%. The tapered roller bearing with fewer rolling elements (TRB 3) shows an improvement of approx. 15%.

*Table 5: Influence of the oil supply direction*

	TRB1		TRB3	
	Lub. of the rib	In PD	Lub. of the rib	In PD
Oil supply l/min	Torque / Nm	Torque / Nm	Torque / Nm	Torque / Nm
0.5	0.86	1.26	0.74	0.87
	~ 30%		~ 15%	

4. Determining the minimum oil quantity

For the second test series the main focus was on finding the minimum oil quantity the tapered roller bearings were still able to operate in. Therefore, the oil quantity was successively reduced over time during each test run.

During the previous test series, TRB1 and TRB2 showed similar behavior for frictional torque and temperature behavior. Because of this, only TRB3 and TRB1 were investigated with regards to the minimum oil quantity.

4.1. *Test Procedure*

The test procedure for this test series can be seen in Figure 12. A specific axial force (identical to the previous test series), rotational speed and oil quantity were defined before the start of each test run. Each test run was started without a run-in period. Over time, the oil quantity was reduced successively, as can be seen in Figure 12. The test run was stopped when the test bearing showed instationary behavior of the frictional torque. In contrast to test series 1, for this test series, the oil supplied to the test bearing was heated up to 100 °C. By lubricating the test bearing with heated oil, a higher oil temperature was selected to reduce the viscosity of the oil and influence the lubrication conditions. At 100°C, the kinematic viscosity of the oil was 9.3 mm²/s.
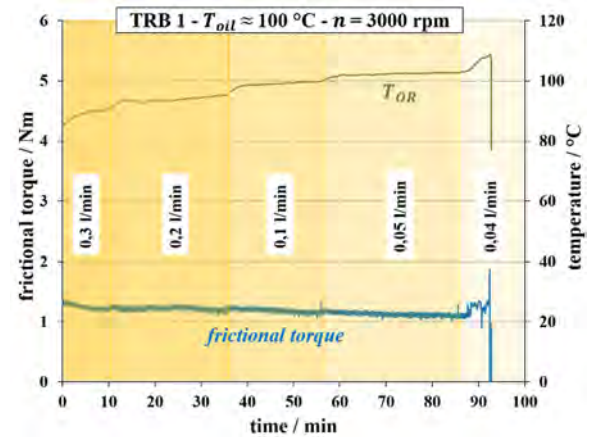
Figure 12: Test procedure for test series 2 – reduction of oil quantity over time

4.2. *Results*

4.2.1. *Minimum oil quantity*

Exemplary test results of TRB1 and TRB3 for speeds of 3000 rpm and 6000 rpm with the oil supply in pumping direction are shown in Figure 13 to Figure 16. Each figure shows the frictional torque curves. At the beginning of each test run, all bearings were supplied with an adequate amount of oil. Therefore, the bearings show regular operating behavior. Figure 13 shows the frictional torque behavior of TRB1 at a constant speed of 3000 rpm. Up until 0.15 l/min, the operating behavior of the bearing is stable.
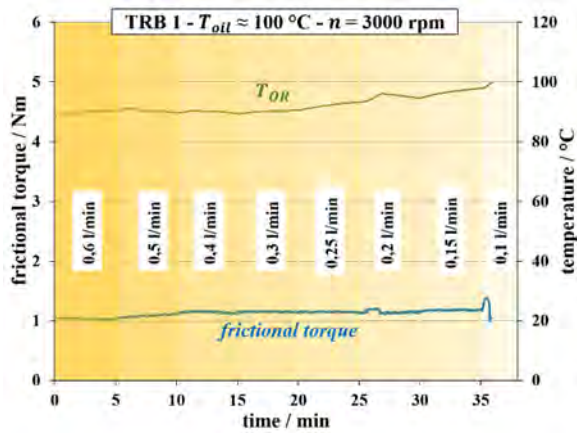
Figure 13: Mimimum oil quantity of TRB1 at 3000 rpm – Oil supply in the pumping direction
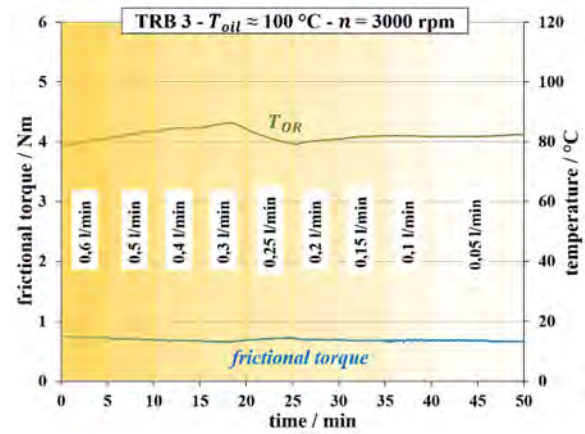
Figure 14: Mimimum oil quantity of TRB3 at 3000 rpm – Oil supply in the pumping direction
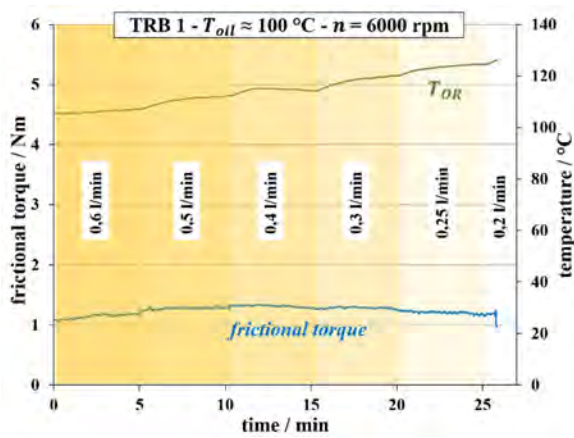
Figure 15: Mimimum oil quantity of TRB1 at 6000 rpm – Oil supply in the pumping direction
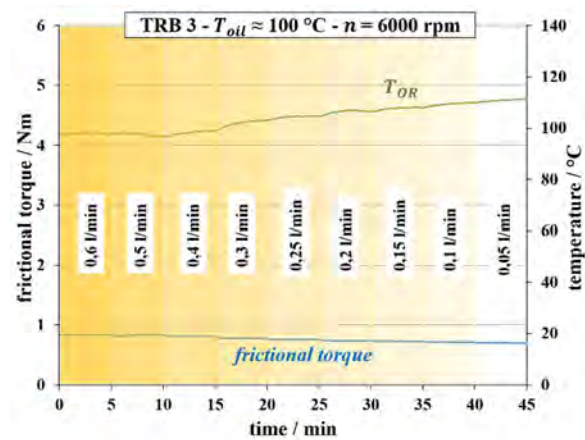
Figure 16: Mimimum oil quantity of TRB3 at 6000 rpm – Oil supply in the pumping direction
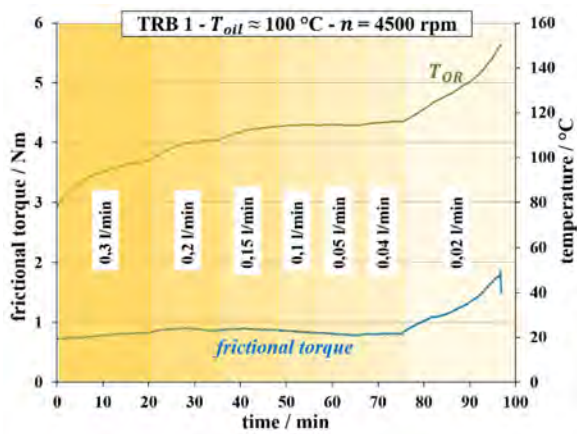
Figure 17: Mimimum oil quantity of TRB1 at 4500 rpm – Oil supply against the pumping direction
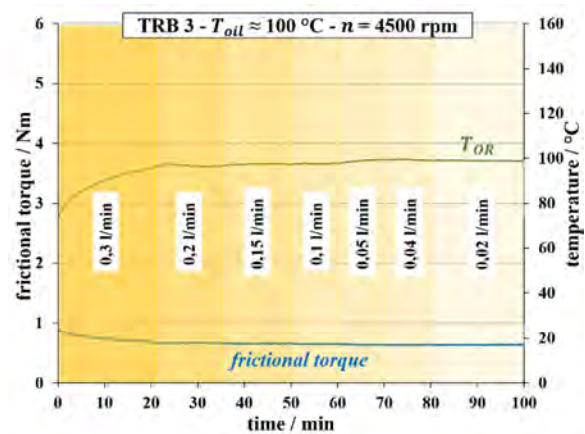
Figure 18: Mimimum oil quantity of TRB3 at 4500 rpm – Oil supply against the pumping direction

Reducing the amount of oil to 0.1 l/min will result in an instationary reaction of the frictional torque. At this point, the test run was stopped. In comparison, for TRB3, such behavior was only present after completely turning off the oil supply to the bearing. Increasing the speed to 6000 rpm will also increase the amount of oil required for TRB1 to still be able to operate at

0.2 l/min. In comparison, the minimum oil quantity for TRB3 is also increased to 0.05 l/min.

4.2.2. *Influence of oil supply direction*

Supplying oil against the pumping direction reduces the minimum amount of oil necessary for both TRBs to operate in. For TRB1, the minimum oil quantity is reduced from 0.05 l/min

in the pumping direction to 0.02 l/min at a speed of 4500 rpm as shown in Figure 17.

In comparison, TRB3 can operate in stable conditions at all speeds, even when the oil supply has been turned off (See Figure 18)
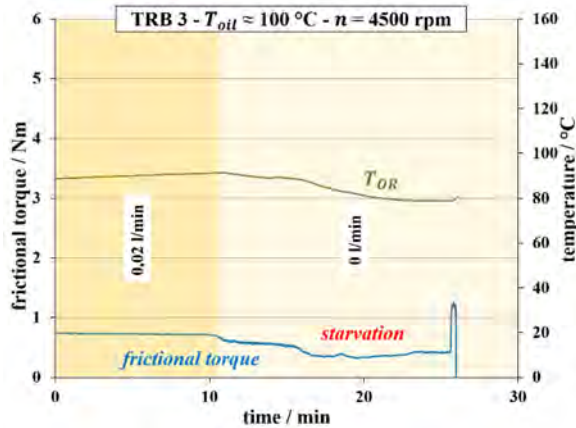
Figure 19: Minimum oil quantity of TRB3 at 4500 rpm – without lubrication

By changing the oil supply to against the pumping direction, as shown in Figure , a small oil reservoir can build up in front of the outer ring. If the oil supply is turned off, there is still a small oil reservoir at the bearing. As long as there is oil in the reservoir and the bearing can supply itself with oil, the bearing was still able to continue operating, as shown in Figure 19. After a certain period of time, there will be no oil left in the oil reservoir. At that point, the bearing is running dry and shows the usual instationary behavior at which the test run is stopped.

4.2.3. *Comparison of overall results*

The overall results for minimum oil quantity at different operating conditions for supplying oil in and against the pumping direction are presented in Table 6.

Table 6 Minimum oil quantity of test series 2

Test Bearing	rpm 1/min	In PD l/min	Against PD l/min
TRB1	3000	0.04	< 0.02
	4500	0.05	0.02
	6000	0.2	0.05
TRB3	3000	0*	0*
	4500	0*	0*
	6000	0.05	0*

0* does not represent actual zero, i.e. the bearing cannot operate without oil. Instead, it means that as long as there is some oil inside the bearing and the oil reservoir, the bearing can still operate in a stable condition under the given load conditions.

4.2.4. *Increase of axial load*

At the end of this test series, TRB3 was further examined to find the axial load limit at which the bearing has the same behavior as for the specified axial load for test series 1 and test series 2.

For the first test run, the axial load was increased by 28%. As can be seen in *Figure 20*, the bearing was still able to operate at 6000 rpm and the frictional torque did not show any instationary behavior. After reaching 6000 rpm, the oil quantity was successively reduced. However, the bearing only showed instatonary frictional torque behavior when the oil supply was turned off.

For the second test, the axial load was further increased to 56% based on the initial axial load from the previous test series. Still, with an increased axial load of 56%, the tested tapered roller bearing showed the same behavior as during the first test run with an increase of 28%. Finally, with an increase in the axial load to 85%, the speed level of 6000 rpm could not be achieved with an oil amount of 0.3 l/min. To achieve 6000 rpm, a higher amount of oil would have been necessary.

At 0.3 l/min, the bearing was able to operate stably at 3000 rpm, as shown in *Figure 22*, but at 3500 rpm, the limit for stable operating conditions was reached. It was concluded that the increase in axial load of 85% presents the increase limit for the axial load for TRB3 under the given operating conditions, at which the test series was completed.

5. Conclusions

The aim of the experimental studies was to examine tapered roller bearings and the impact of the oil supply, load and rotational speed on the frictional torque and temperature behavior. This study should provide information on critical operating conditions. For this purpose, standard tapered roller bearings from different manufacturers were compared to one another. The characteristic variable for evaluating the frictional losses was the frictional torque in the test bearings. By using test bearings from different manufacturers, the significance of the inner geometry of the rolling bearings as well as the number of rolling elements should be determined.

Based on the results, it can be concluded that the tapered roller bearing with one less roller has significantly lower frictional losses when using circulating oil lubrication, compared to the other tested tapered roller bearings. The reason for this is that there is more space between the rolling elements, thus ensuring better lubrication. Furthermore, the direction of the oil supply is also a significant factor. The results show that due to lower hydraulic losses, the oil supply against the pumping direction reduces frictional losses. Another important finding is that a small amount of oil can be sufficient for tapered roller bearings to operate safely and stably. Critical operating conditions only occur when the oil is completely used up because of starvation. The most critical factor is, as expected, the axial load. As the results with a high increase in the axial load illustrate, even an increase in the oil quantity does not prevent the bearing failure.
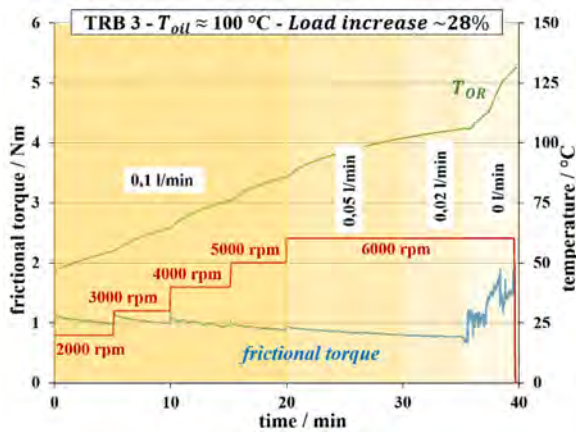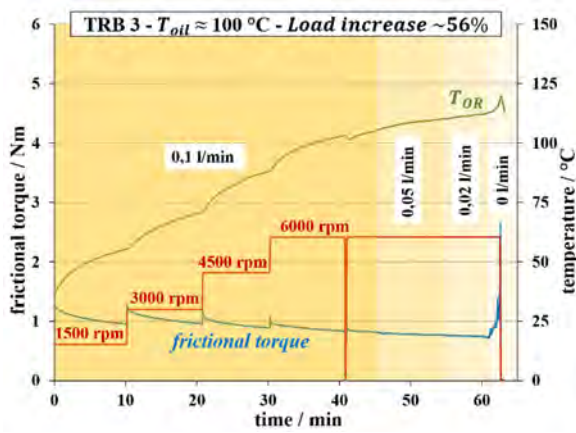
Figure 20: Increase in axial load by ~ 28%
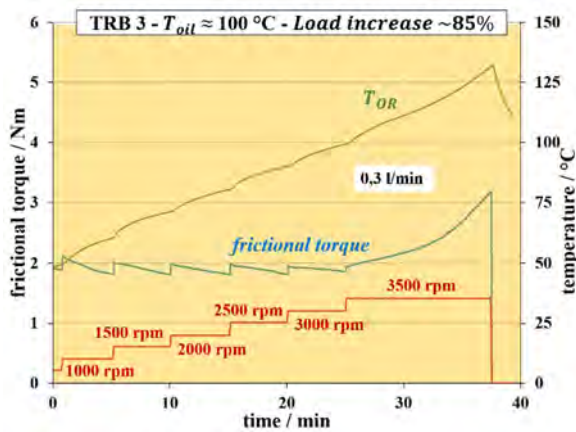

Figure 21: Increase in axial load by ~ 56%

Figure 22: Increase in axial load by ~ 85%

References

[1] Aihara, S.: A New Running Torque Formula for Tapered Roller Bearings Under Axial Load. Journal of Tribology 109/3 (1987), p. 471-477

[2] Zhou, R. S.; Hoeprich, M. R.: Torque of Tapered Roller Bearings. Journal of Tribology 113/3 (1991), S. 590–597.

[3] Cretu,S., Bercea, I., Mitu, N.: A dynamic analysis of tapered roller bearing under fully flooded conditions: Part 1: Theoretical formulation. WEAR 188 (1995) , p. 1-10

[4] Houpert, L.: Ball Bearing and Tapered Roller Bearing Torque. Analytical, Numerical and Experimental Results. Tribology Transactions 45/3 (2002), p. 345-353

[5] Matsuyama, H.; Kamamoto, S.: Analysis of Frictional Torque in Raceway Contacts of Tapered Roller Bearings. KOYO Engineering Journal English Edition (159E) (2001), p. 53–60

[6] Zhang, Z.; Qiu, X.; Hong, Y.: EHL Analysis of Rib-Roller End Contact in Tapered Roller Bearings. Tribology Transactions 31/4 (1988), p. 461–467

[7] Kiekbusch, T.: Strategien zur dynamischen Simulation von Wälzlagern. Dissertation, Technische Universität Kaiserslautern, 2017, Maschinenelemente und Getriebetechnik Berichte Bd. 23/2017

[8] Liebrecht, J., Si, X., Sauer, B., Schwarze, H.: Investigation of Drag and Churning Losses on Tapered Roller Bearings. Strojniški vestnik - Journal of Mechanical Engineering (2015), Nr. 6

[9] Kiekbusch, T.; Liebrecht, J.; Sauer, B.: Dynamiksimulation von Wälzlagern unter Berücksichtigung der Plansch- und Schleppverluste. 12. VDI-Fachtagung Gleit- und Wälzlagerungen. 27.-28. Juni, 2017. Schweinfurt. p. 207-217

[10] Schlichting, H.; Gersten, K.: Grenzschicht-Theorie. 9. neubearbeitete und erweiterte Auflage. Berlin: Springer, 1997

[11] Rumbarger, J. H.; Filetti, E. G.; Gubernick, D.: Gas Turbine Engine Mainshaft Roller Bearing-System Analysis. In: Journal of Lubrication Technology 95(4) (1973), S. 401-416.

[12] Gupta, P. K.: Advanced Dynamics of Rolling Elements. New York: Springer, 1984

[13] Koryciak, J.: Einfluss der Ölmenge auf das Reibmoment von Wälzlagern mit Linienberührung. Dissertation, Ruhr-Universität Bochum, 2007

[14] Liebrecht, J., Si, X., Sauer, B., Schwarze, H.: Technisch-mathematischer Ansatz zur Berechnung der Plansch- und Strömungsverluste am Kegelrollenlager. In: Tribologie und Schmierungstechnik 4/2016, p. 5-13.

[15] Liebrecht, J., Si, X., Sauer, B., Schwarze, H.: Calculation Approach of Drag and Churning Losses of Rolling Bearings. International Bearing Conference, April 2016, Hannover, p. 78-81

[16] SKF Gruppe: Wälzlager. PUB BU/P1 10000/2 DE. 2014.

[17] Matsuyama, H.: High efficiency and tribology in rolling bearings. In: JTEKT Engineering Journal: English Edition (1009E) (2012), p. 108–113

[18] Wen, Y., Miyata, S.: CFD Analysis of Tapered Roller Bearings and Ball Bearings for reducing Agitation Torque. VDI-Berichte, Nr. 2187, 2013, p. 481-496

An Empirical Investigation of the Impact of an Axially Oscillating Shaft on Friction and Lubrication in Cylindrical Roller Bearings

Andreas Meinel[1], Stephan Tremmel[2]

[1] *Engineering Design, Friedrich-Alexander-Universität Erlangen-Nürnberg (FAU), meinel@mfk.fau.de*
[2] *Engineering Design, Friedrich-Alexander-Universität Erlangen-Nürnberg (FAU), tremmel@mfk.fau.de*

Abstract – Rolling element bearings experience dynamic axial thrust and oscillating shaft movements of various frequencies and amplitudes in a multitude of applications, especially in heavy-duty machinery. These operating conditions can cause significant friction losses which entails higher operating temperatures and lower lubricant operating viscosities. Dynamic axial shaft movements increase shearing between rollers and raceways excessively which impairs the mechanical stability of the lubricant. In consequence, this results in accelerated lubricant degradation and may cause insufficient lubrication or even premature bearing failure. In order to choose a suitable lubricant for such a bearing application that experiences axial shaft movements or to be able to adequately schedule lubricant maintenance intervals, the occurring shear- or friction forces between rollers and raceways due to the axial oscillations are of particular interest. Therefore, in an experimental study, an oil-lubricated cylindrical roller bearing NU210 has been subjected to dynamic axial shaft movements of various frequencies and amplitudes. Two specifically designed bearing test rigs are introduced within the scope of this paper and the experimental procedure is presented. The results obtained which include measurements of axial friction forces between rollers and raceways, steady-state operating temperatures, bearing friction losses as well as cage slippage are discussed in detail and an axial friction coefficient is derived from the results. Concluding, a short assessment is given, to what extend axial shaft movements might exhibit a critical impact on lubricant performance, friction and wear.

Keywords – *cylindrical roller bearings, oscillations, bearing friction, lubrication.*

1. Introduction

Rolling element bearings experience dynamic oscillations in a multitude of applications, such as industrial gearboxes, heavy-duty cranes, paper- and weaving machines, crushers and milling plants. Oscillations also occur in agricultural machinery like tractors or harvesters and in high-speed trains [1]. Wind turbine gearboxes, for example, experience axial shaft oscillations during operation [2].

The term 'dynamic oscillations' comprises various types of oscillations like dynamically changing bearing loads or rotational speeds as well as axially oscillating shafts or housings, for instance. Such oscillations range from high frequency, low amplitude vibrations to low frequency but high amplitude oscillations.

This evokes two problems that need to be solved to arrive at an optimal bearing design for such machinery. Firstly, it is often not known beforehand whether a bearing experiences dynamic oscillations and if so, in what form and with which frequencies and amplitudes these oscillations appear. Secondly, it is not yet known in what way these oscillations affect bearing performance, cause higher friction losses, lead to accelerated bearing fatigue or even lead to premature bearing failures due to increased wear and lubricant degradation.

In consequence, engineers are dimensioning bearings too cautiously which often leads to massive, energy inefficient bearing designs.

For some applications that are known to experience vibrations or oscillations, literature suggests, to multiply the equivalent bearing load by a caution factor to account for oscillations [3]. This impedes with important goals in engineering design like downsizing and energy efficiency.

To overcome this problem, it is essential to know the impact that different forms and magnitudes of oscillations have on a rolling element bearing. In [4], several forms of high frequency vibrations were evaluated regarding possible damage on lightly loaded cylindrical roller bearings. Axial shaft oscillations with various frequencies and amplitudes have not yet been investigated although they are expected to exhibit a severe impact on friction and lubrication in cylindrical roller bearings.

Therefore, this paper presents an empirical study of the effects of an axially oscillating shaft on an oil-lubricated cylindrical roller bearing. It is investigated, how these oscillations influence bearing friction and cage slippage and how this is contingent on oscillation amplitude and frequency as well as radial load or rotational speed.

Furthermore, the impact of axial shaft oscillations on wear, power losses, operating temperatures and lubricant behaviour is being examined. Subsequently, the test rigs that are used for the experimental part are presented, the experimental procedure is explained and the obtained results are presented and discussed in detail. Finally, a brief conclusion is given.

2. Bearing Test Rigs

Two specially designed test rigs are being utilized for the experimental part of this paper. All tests with axial shaft oscillations are performed on the Oscillation Test Rig. The Bearing Friction Test Rig is used to conduct reference measurements of friction losses without any oscillations. Both test rigs are described subsequently.

2.1. *Oscillation Test Rig*

The oscillation test rig is specially designed to subject cylindrical roller bearings NU210 with various forms of oscillations. The test rig is capable of superimposing radial (load), tangential (torque) and axial (shaft) oscillations up to 25 Hz, of which only the latter will be investigated in the context of this paper. As can be seen in Figure 0-1, the test rig is encased in a wooden housing and an air/water heat exchanger ensures constant ambient temperatures.

Figure 0-2 shows the test bearing unit. It is driven by an electric motor via a belt drive with rotational speeds up to 6 000 rpm. All bearings are lubricated with FVA reference oil with a viscosity grade of 68 (31 % FVA 2, 69 % FVA 3). For that, a minimum-quantity oil-air-lubrication system is being utilized. The amount of lubricant fed into the bearings is constant throughout every experiment at 0.1 ml/h each which is ten times the minimally required volume but still considered minimum quantity lubrication. This ensures proper lubrication even with superimposed axial sliding motions between the contact partners.

In the upper right corner of Figure 0-2, one can see a mechanical eccentric which superimposes axial oscillations onto the test bearing shaft. A similar eccentric is applied to generate load oscillations, additionally to a static radial load of up to 20 kN. The radial load is monitored with a force sensor. It is created with a step motor that drives a lifting spindle which is connected to the underside of the test bearing housing in a way that does allow for small axial displacements of the test bearing housing to not impede with the measurements which are later on described.

Figure 0-3 shows a schematic diagram of the oscillation mechanism of the oscillation test rig. A cross-section of the eccentric for the axial oscillations is shown in Figure 0-4.
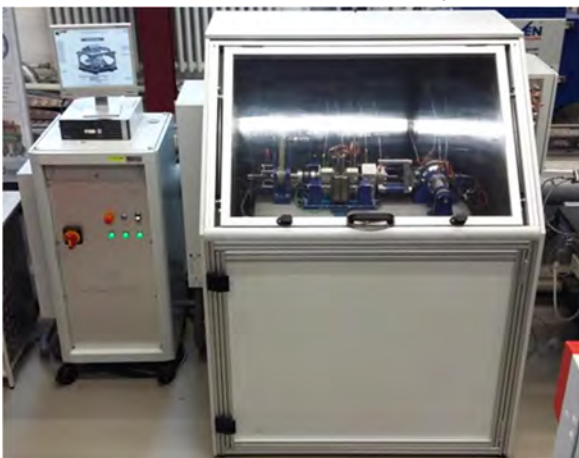
Figure 0-1: Overall View of the Oscillation Test Rig with housing and control system.
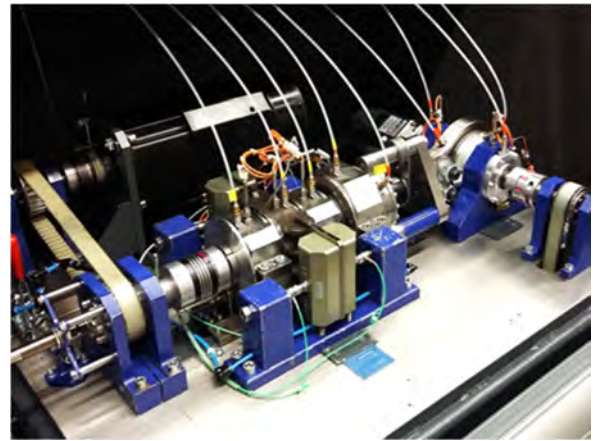
Figure 0-2: Test bearing unit and eccentric of the Oscillation Test Rig.

An electric motor rotates a shaft with an eccentric sleeve and generates oscillations with frequencies up to 25 Hz. A step motor shifts this eccentric sleeve to adjust the peak-to-peak oscillation amplitude between 0 and 1 mm. As can be seen in Figure 0-3 the eccentric is designed in a way so that the oscillations are purely linear.

Figure 0-5 shows a cross-section of the test bearing unit. The test bearing is mounted symmetrically between two identical support bearings. The eccentric for the axial oscillations is connected to the test bearing shaft via two preloaded spindle ball bearings that sit inside a journal bearing.

The axial movements of the shaft are recorded with an eddy current sensor that sits in the bottom left corner. It measures its distance towards an aluminium disk which is mounted on the shaft and oscillates with it. To minimize measurement error this disk face is precisely grinded.

The oscillating shaft causes axial forces on the test bearing housing which allow quantifying the additional sliding friction in axial direction between the rollers and the inner ring raceway. Therefore, four piezoelectric sensors are installed to hold the test bearing housing in place.
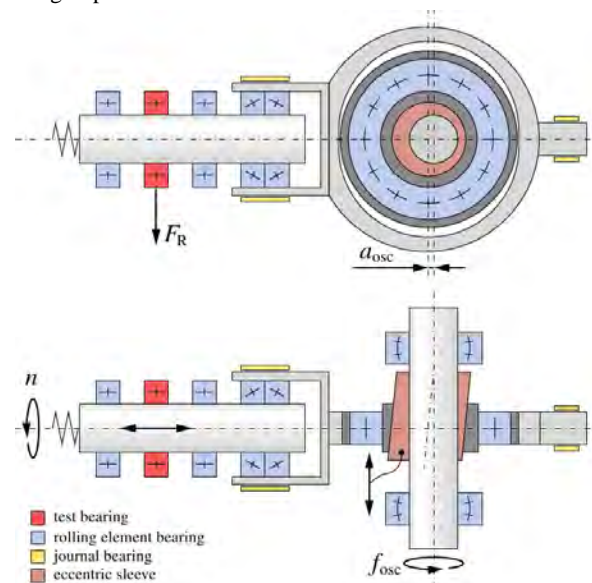
Figure 0-3: Schematic diagram of the oscillation mechanism of the Oscillation Test Rig.
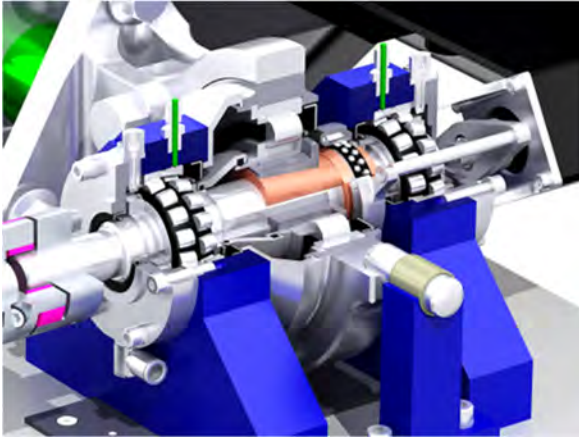
Figure 0-4: Cross section of the eccentric of the Oscillation Test Rig.

Four air bearings with ball joints at their backs are employed to connect each piezoelectric sensor to the test bearing housing. Each sensor may be adjusted individually to ensure proper aligning of the test bearing housing as well as sufficient preloading of the sensors.

In order to not create any tilting or skewing of the housing and to only measure axial forces resulting from axial oscillations of the shaft, it is essential that the preloading of the sensors and aligning of the test bearing housing is carried out meticulously beforehand. The preloading of the four piezoelectric sensors needs to be adjusted until each sensor measures the same amount of axial force during bearing operation. In this case, the occurring amount of tilting and skewing is considered to be negligible. However, due to the load distribution inside the test bearing itself, the axial oscillations cause some skewing of the rollers in the cage pockets.

Since bearing friction directly corresponds with bearing operating temperatures, PT 100 resistance thermometers are mounted on top of the test bearing- and the support bearing housings, alongside the oil-air-lubrication nozzles, to record the outer ring temperatures in the load zone and the load-free zone, respectively.

An additional PT 100 sensor is integrated in the shaft, measuring the inner ring temperature of the test bearing and wirelessly transmitting the signal.
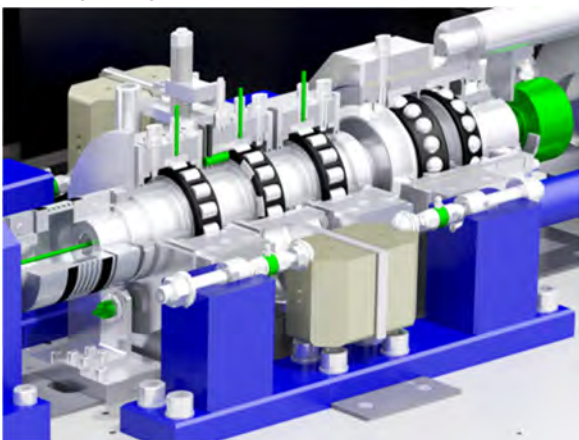
Figure 0-5: Cross section of the test bearing unit of the Oscillation Test Rig.

Eight little pieces of sheet metal that are glued into shallow grooves in the side of the test bearing cage are counted as they pass an inductive sensor. At the free end of the test bearing shaft sits another sensor to record the rotational speed. From this information, the cage slippage can be determined.

2.2. Bearing Friction Test Rig

The purpose of the Bearing Friction Test Rig, which is displayed in Figure 0-6, is to examine the influence of speed and load spectra on friction torque and operating temperature in radial ball and roller bearings [5]. For this paper, it is being used for reference measurements of bearing friction losses without any oscillations.

Figure 0-6: Overall View of the Bearing Friction Test Rig and control system.

This test rig is capable of imposing either 30 kN radial load or 10 kN axial load onto the test bearing shaft. These loads are generated via two pneumatic bellows cylinders and monitored by force sensors. An electric motor accelerates the test bearing shaft up to rotational speeds of 12 000 rpm.

If radially loaded bearings are being tested, the test bearing shaft carries four bearings of identical size and type. For the experiments presented in this paper, three test bearings NU210 and one locating bearing NUP210 are mounted on the test bearing shaft.

As Figure 0-6 and 0-7 show, the radial load is applied to the underside of the bearing housing that envelops the inner two bearings.

Figure 0-7: Test bearing unit of the Bearing Friction Test Rig.

The outer two bearings function as support bearings and each has its own housing. The bearings are positioned symmetrically on the shaft and therefore carry the same radial load.

Each bearing is lubricated with FVA reference oil of a viscosity grade of 68 via a minimum-quantity oil-air-lubrication system, identical to the one of the oscillation test rig. Figure 0-8 depicts a cross-section of the test bearing unit.

The frictional moment of the test bearing shaft is being measured with a torque sensor which is located at the right-hand side of the test bearing shaft. To get the frictional moment of one bearing, this value has to be divided by four. A PT 100 temperature sensor measures the outer ring temperature in the load free zone of the left bearing, another PT 100 sensor records the outer ring temperature in the load zone of the second left bearing.

As can be seen in Figure 0-6, the test bearing unit is encased by acrylic glass which is connected to a fume extractor. This keeps the ambient temperature between 20 °C and 25 °C during the experiments.
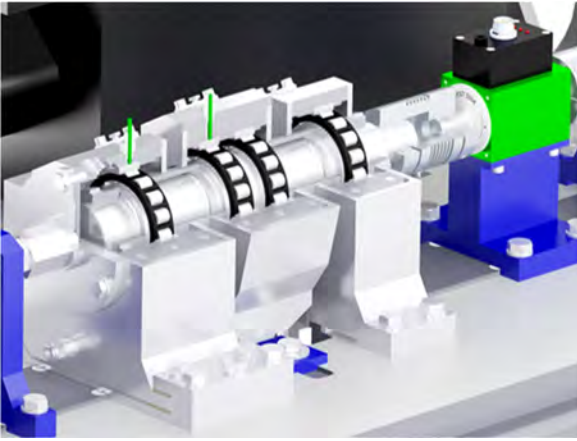

Figure 0-8: Cross section of the test bearing unit of the Bearing Friction Test Rig.

3. Experimental Procedure

The objective for the experiments is to find out how axial shaft oscillations impact friction and lubrication in cylindrical roller bearings and how this is influenced by oscillation amplitude and frequency as well as radial load or rotational speed. Therefore, four series of nine experiments each are being conducted and each factor is being varied one at a time.

Test series A varies the radial load from zero to 12 kN in 1.5 kN steps. In test series B the rotational speed is increased incrementally from 50 rpm to 3 200 rpm. Variations of the oscillation frequency from zero (no oscillations) to 24 Hz with a step size of 3 Hz are performed in test series C. The oscillation amplitude is increased in test series D from zero (no oscillations) to 0.8 mm in 0.1 mm increments.

The factors that are not varied at the time are set constant at 7.5 kN radial load, which equals 10 % of the basic dynamic load rating and 2 000 rpm rotational speed, which is 21% of the limiting speed. The oscillations are applied with 24 Hz frequency and 0.8 mm peak-to-peak amplitude. Table 0-1 summarizes the parameter specifications for each experiment of the four test series.

Table 0-1: Test parameters of the experiments.

Test	Parameter (Unit)	Experiment Number								
		1	2	3	4	5	6	7	8	9
A	F_R (kN)	0	1.5	3.0	4.5	6.0	7.5	9.0	10.5	12.0
	n (rpm)	2 000								
	f_{osc} (Hz)	24								
	a_{osc} (mm)	0.8								
B	F_R (kN)	7.5								
	n (rpm)	50	400	800	1200	1600	2000	2400	2800	3200
	f_{osc} (Hz)	24								
	a_{osc} (mm)	0.8								
C	F_R (kN)	7.5								
	n (rpm)	2 000								
	f_{osc} (Hz)	0	3.0	6.0	9.0	12.0	15.0	18.0	21.0	24.0
	a_{osc} (mm)	0.8								
D	F_R (kN)	7.5								
	n (rpm)	2 000								
	f_{osc} (Hz)	24								
	a_{osc} (mm)	0	0.1	0.2	0.3	0.4	0.5	0.6	0.7	0.8

Hence, the central point of the experiment design is being run four times (A-6, B-6, C-9, D-9) and is being used to ascertain the statistical spreading of the measurements. The two experiments without oscillations (C-1 and D-1) serve as a reference to assess whether the impact of the oscillations is significant.

The variable of interest for these experiments is the total axial friction force F_A that is generated by the axial shaft movements. The axial shaft oscillations create sliding friction between the inner ring raceway and the 16 rolling elements. The resulting axial friction forces are then transferred to the outer ring, either via friction or via roller-flange-contact. The outer ring then transmits the axial forces to the four piezoelectric sensors.

Figure 0-9 illustrates the forces of the sensors which, will, henceforth, be referred to as L1 and L2 for the ones on the left side of the test bearing housing and R1 and R2 for those on the right side.

The target variable, the cumulative axial friction force F_A of all 16 contacts between rolling elements and inner ring raceway at an arbitrary time t, may be calculated from the four sensor signals by applying the principle of balanced forces to Figure 0-9 which yields:

$$F_A(t) = F_{L1}(t) + F_{L2}(t) - F_{R1}(t) - F_{R2}(t). \quad (Eq.\ 0\text{-}1)$$

Since the measured force signals behave highly dynamic, a constant scalar value for F_A that adequately represents the occurring amount of axial sliding friction is required.
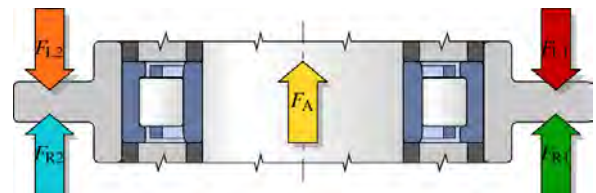

Figure 0-9: Equilibrium of forces between the axial force due to shaft oscillations and the forces opposed by the four sensors.

Therefore, the axial forces are recorded for a sample time t_s and the mean axial friction force is being calculated using:

$$F_A = \frac{1}{t_s} \int_0^{t_s} |F_A(t)| \, dt. \qquad \text{(Eq. 0-2)}$$

In addition, the maximum of the axial friction force $F_{A,max}$ is determined for each sample:

$$F_{A,max} = max(F_A(t)) \text{ with } t \in [0, t_s]. \qquad \text{(Eq. 0-3)}$$

A sample time t_s of ten seconds has been chosen since it has proven to be a suitable choice. With the test rig's sampling rate of 1 000 Hz this results in 10 000 measurement values per sample.

The axial friction force F_A is a well-suited criterion to quantify the impact of axial shaft oscillations on friction and lubrication in cylindrical roller bearings. However, since the axial force is strongly dependent on the applied radial load, it is not readily transferable to applications with different radial loads.

For that reason, subsequently, to provide a more general applicability for the results of this paper, an axial friction coefficient μ_A for the roller raceway contacts which is independent of the radial load is being determined.

As depicted in Figure 0-10, an external radial load F_R that is subjected to a rolling element bearing is transferred simultaneously through the several rolling elements within the load zone, each one carrying a different fraction Q_i of the radial load and each one transmitting a fraction F_{Ai} of the axial friction force F_A due to the axial shaft oscillations.

The mentioned axial friction coefficient μ_A is derived from the axial friction force F_{Ai} for each rolling element i that is subjected to a radial load Q_i:

$$F_{Ai} = \mu_A \cdot Q_i. \qquad \text{(Eq. 0-4)}$$

Equation 0-4 is based on the postulate that the friction coefficient μ_A is identical for each roller-raceway contact which is subsequently verified in Section 4.2.
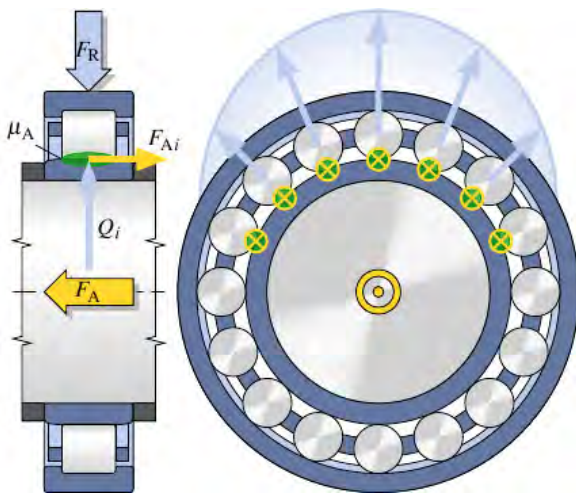

Figure 0-10: Radial load distribution in a cylindrical roller bearing and axial friction forces at each rolling element inside the load zone.

Summation over each of the Z rolling elements yields the total axial force F_A transferred to the outer ring due to axial sliding friction between rollers and inner ring raceway:

$$F_A = \sum_{i=1}^{Z} F_{Ai} = \mu_A \cdot \sum_{i=1}^{Z} Q_i. \qquad \text{(Eq. 0-5)}$$

The individual rolling element loads Q_i can be derived from the distribution $Q(\varphi)$ of the bearing's radial load which is iteratively calculated from the displacements and deformations of the bearing components.

Alternatively, since Equation 0-5 only requires the sum of all rolling element loads, it can be solved by using the mean rolling element load Q_m instead. Q_m is determined as follows [6]:

$$Q_m = \frac{k_1 \cdot F_R}{Z} \qquad \text{(Eq. 0-6)}$$

where Z is the number of rolling elements and k_1 is an empirical parameter which is dependent from the radial load zone angle φ and takes bearing stiffness, clearance as well as preloading into account. In standard radial bearing applications, k_1 is to be assumed as 2.8 [6].

Therefore, Equation 0-5 simplifies to:

$$F_A = \mu_A \cdot Q_m \cdot Z = \mu_A \cdot k_1 \cdot F_R. \qquad \text{(Eq. 0-7)}$$

Hence, one receives for the mean axial friction coefficient μ_A:

$$\mu_A = \frac{F_A}{k_1 \cdot F_R}. \qquad \text{(Eq. 0-8)}$$

Using the maximum instead of the mean for the axial friction force yields the maximal axial friction coefficient $\mu_{A,max}$:

$$\mu_{A,max} = \frac{F_{A,max}}{k_1 \cdot F_R}. \qquad \text{(Eq. 0-9)}$$

The axial friction coefficient describes a combined rolling-sliding motion since the inner ring rotates and oscillates at the same time. The ratio β of oscillation to rotation is depicted in Figure 0-11 and mathematically expressed as:

$$\beta = \frac{2 \cdot f_{osc} \cdot a_{osc}}{\pi \cdot n \cdot D_{IR}}. \qquad \text{(Eq. 0-10)}$$

For lubricated contacts, the friction coefficients are usually within the range of 0.001 to 0.005 in case of rolling friction and lie between 0.001 and 0.1 in case of sliding friction, depending on lubricant properties, surface quality and whether purely liquid friction or mixed friction occurs.
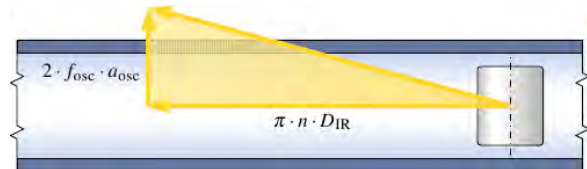

Figure 0-11: Ratio of axial oscillation velocity over rotational velocity.

Since μ_A is a combination of rolling and sliding friction it falls between these intervals. It has been established that the friction coefficient increases with higher slide-to-roll-ratios [7].

Although neither the rotational speed nor the oscillation frequency or amplitude appear in Equation 0-8, these variables are expected to influence the axial friction coefficient μ_A since they change the oscillate-to-roll-ratio.

In addition to the axial friction force and the axial friction coefficient, the cage slippage is being determined from the measurements of the rotational speeds n of the test bearing shaft and n_C of the test bearing cage as follows:

$$S = 1 - \frac{n_C}{n_{C0}} \qquad \text{(Eq. 0-11)}$$

with the theoretical rotational speed n_{C0} of the test bearing cage being calculated as [6]:

$$n_{C0} = \left(1 - \frac{D_w \cdot cos(\alpha)}{D_{pw}}\right) \cdot \frac{n}{2}. \qquad \text{(Eq. 0-12)}$$

The pitch diameter D_{pw} of all rolling elements and the rolling element diameter D_w are both listed, along with other specifications of the test bearing NU210, in Table 0-2.

The determination of the cage slippage with Equation 0-11 gives a good indication whether axial shaft oscillations also impede with cage and roller kinematics.

The axial oscillation velocity $v_{osc}(t)$ can be determined from the measurements of the axial movements $s_{osc}(t)$ of the shaft as:

$$v_{osc}(t) = \dot{s}_{osc}(t). \qquad \text{(Eq. 0-13)}$$

Multiplication of the oscillation velocity $v_{osc}(t)$ with the axial friction force $F_A(t)$ yields the friction losses $P_{osc}(t)$ at a certain point t in time due to the sliding friction between rollers and inner ring raceway which is caused by the axial shaft oscillations:

$$P_{osc}(t) = \left|v_{osc}(t) \cdot F_A(t)\right|. \qquad \text{(Eq. 0-14)}$$

Since $P_{osc}(t)$ behaves highly dynamic, the mean friction losses P_{osc} during the sample time t_s of the measurements will be calculated using:

$$P_{osc} = \frac{1}{t_s} \int_0^{t_s} P_{osc}(t)\,\mathrm{d}t. \qquad \text{(Eq. 0-15)}$$

To be able to put the friction losses due to axial oscillations into perspective, an additional reference measurement (E-1) on the aforementioned bearing friction test rig is being conducted and the rotational bearing friction moment M_{rot} is being determined.

The bearing friction losses are then calculated as follows:

$$P_{rot}(t) = 2 \cdot \pi \cdot M_{rot}(t) \cdot n(t). \qquad \text{(Eq. 0-16)}$$

Table 0-2: Specifications of the test bearing NU210.

Symbol	Parameter	Value
C_r	Basic dynamic load rating (radial)	75 kN
$C_{r,min}$	Minimum load	1.2 kN
n_G	Limiting speed	9 700
Z	Number of rollers	16
D_{IR}	Inner ring raceway diameter	59.5 mm
D_w	Roller diameter	11 mm
D_{pw}	Pitch diameter	70.5 mm
α	Contact angle	0°
k_1	Empirical value	2.8

In accordance to the central point of the experiments listed in Table 0-1, the rotational speed for this experiment is also set to 2 000 rpm, the radial load that is applied to each of the test bearings is set at 7.5 kN and no oscillations are applied. The experiment is being run until steady-state-temperatures of the outer rings are reached. This requires approximately two hours of running time.

The friction losses due to oscillations also lead to an increase in bearing operating temperatures which changes the lubricant viscosity and can accelerate lubricant ageing and deterioration.

To quantify this increase in operating temperatures two additional experiments (F-1 and F-2) are conducted on the oscillation test rig, the first one without any additional oscillations, the second one with superimposed oscillations of 0.8 mm amplitude and 24 Hz frequency. A rotational speed of 2 000 rpm and a radial load of 7.5 kN were chosen for both experiments.

Like experiment E-1, experiments F-1 and F-2 are run until steady-state temperatures of inner and outer rings are reached which also takes approximately two hours. During the experiments both inner and outer ring temperature of the test bearing, as well as the ambient temperature inside the test rig housing are recorded.

Finally, to find out, whether the axial shaft oscillations cause mixed friction and induce additional wear on raceways and rollers, a long run (G-1) is being conducted at 2 000 rpm rotational speed, 7.5 kN radial load, 24 Hz oscillation frequency and 0.8 mm oscillation amplitude. The test duration is set to 231.5 hours which amounts to approximately $2 \cdot 10^7$ oscillations.

The test bearing is then thoroughly examined and the running surfaces are analysed under a laser scanning microscope (Keyence VKX-200).

The results and findings from these experiments are described and discussed in detail in the remainder of this paper.

4. Results

As described in Chapter 3, numerous experiments were conducted and the results are subsequently presented and discussed, starting with a brief assessment of the validity of the experiments and continuing sequentially with the results from test series A to G.

4.1. *Plausibility and Reliability*

The central vantage point of the experiment design is at 2 000 rpm rotational speed, 7.5 kN radial load, 0.8 mm oscillation amplitude and 24 Hz oscillation frequency.

For experiment D-9, Figure 0-12 shows the axial forces measured from the four piezoelectric sensors over a time period of 200 ms. In compliance with Figure 0-9, the red and orange force measurements pertain to the sensors on the left-hand side. The blue and green curves represent the sensors on the right-hand side.
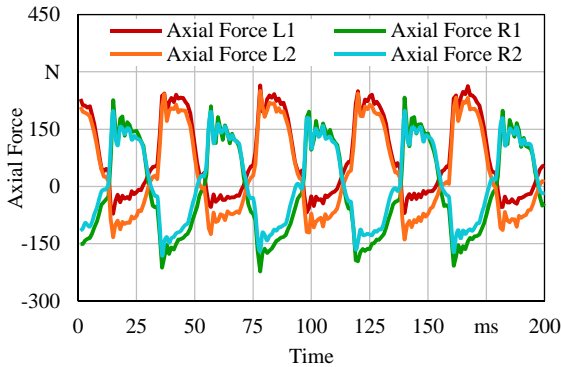

Figure 0-12: Axial forces on the test bearing housing at 0.8 mm oscillation amplitude, 24 Hz oscillation frequency, 2 000 rpm rotational speed and 7.5 kN radial load (experiment D-9).

It is obvious that the left- and right-hand side sensors have opposite signs due to the equilibrium of forces (see Figure 0-9 and Equation 0-1). The sine wave due to the shaft oscillations is clearly pronounced and fairly regular at the superimposed oscillation frequency. This suggests that the friction between rollers and raceway due to the shaft oscillations is the predominant cause for the measured forces.

There is a slight offset from zero visible for each of the four signals which is due to the preloading process of the sensors. However, this does not affect the results since it cancels out in the summation in Equation 0-1. The maxima and minima of the curves occur at the point of highest oscillation velocity as is observable by comparing Figure 0-12 to Figure 0-13 which shows the according oscillating shaft movements over the same period. At the turning points of the axial shaft oscillations, where the axial shaft oscillation has its extrema, the curves of the axial forces meet near zero.
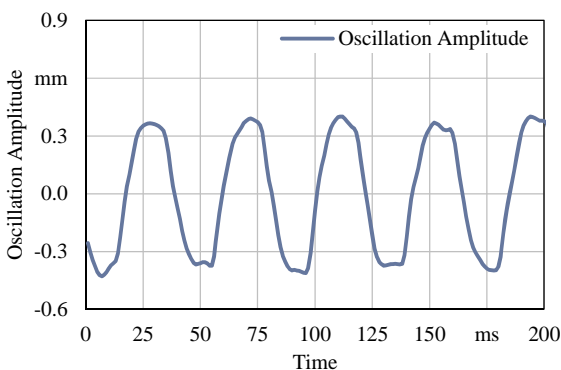

Figure 0-13: Axial Shaft Oscillations according to Figure 0-12 (experiment D-9).

This shows that the forces measured are indeed caused by sliding friction between rollers and inner ring raceway rather than by mass inertia which would exhibit an extrema at the turning points of the shaft oscillation.

Both, the axial friction forces and the axial shaft movements, depicted in Figure 0-12 and Figure 0-13, respectively, appear uniformly and with good repeatability.

This parameter combination has been tested four times, once in each test series (see Table 0-1). The mean axial friction forces resulting from Equation 0-2 as well as the maximal axial friction forces derived from Equation 0-3 are listed in Table 0-3. Table 0-3 also gives the arithmetic mean and the (relative) standard deviation, both of the mean and maximal axial friction force.

Table 0-3: Results for the central point of the experiments.

Test Number	F_A	$F_{A,max}$
A-6	419.8 N	916.0 N
B-6	410.6 N	919.2 N
C-9	418.1 N	997.3 N
D-9	417.8 N	944.2 N
Arithmetic Mean	416.6 N	944.2 N
Standard Deviation	3,2 N	29.1 N
Relative Deviation	0.76 %	3.08 %

The low relative standard deviation of 3.1 % for the maximum of axial friction force shows good repeatability and reliability of the measurement results. The very low relative standard deviation of 0.8 % for the mean axial friction force is not only due to a flawless test rig design and high precision sensors but also a consequence of the way of determining the mean axial friction force.

Since each result for F_A is itself a mean value of, in this case, 10 000 measurement points (see Equation 0-2) the standard deviation of the four values of F_A has to approach zero, a fact that can be derived from GAUSS's Central Limits Theorem.

In comparison to the measurements depicted in Figure 0-12, Figure 0-14 displays the axial forces measured at the same operating conditions of 2 000 rpm rotational speed and 7.5 kN radial load but without any superimposed oscillations. The axial forces of the sensors L1 and L2 still show opposite signs to those of R1 and R2 but, in this instance, they appear random and unpredictable.

Nevertheless, there are axial forces detectable although there are no oscillations and the test bearing is not a locating bearing. This is ascribed to a bearing phenomenon called axial thrust. It is known that cylindrical roller bearings exhibit axial forces that are generated within the bearing itself due to skewing of the rollers inside their cage pockets and which have nothing to do with the superimposed shaft oscillations.

These forces due to axial thrust still need to be quantified and are used as a base line to decide, whether a set of measured axial friction forces due to oscillations is significant or not.
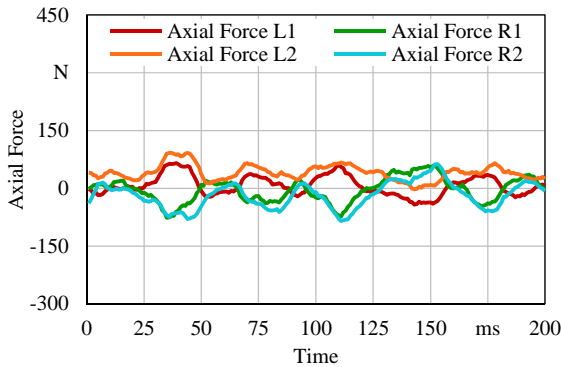
Figure 0-14: Axial forces on the test bearing housing at 2 000 rpm rotational speed and 7.5 kN radial load, without any superimposed axial oscillations (experiment D-1).

In the two experiments where either the oscillation frequency or the amplitude are set to zero (experiments C-1 and D-1), which is tantamount to no oscillations, the mean axial forces (see Equation 0-2) due to axial thrust amount to 95 N or 98 N, respectively. The maximum of axial force (according to Equation 0-3) that occurred lay at 384 N or 385 N, respectively.

To consider measured axial forces significant, they need to exceed the forces due to axial thrust. Having established reliability and repeatability as well as a base line, the effects of the parameter variations are subsequently analysed.

4.2. *Test Series A: Radial Load*

In test series A, the radial load is being varied from zero in 1.5 kN increments to 12.0 kN (see Table 0-1). Figure 0-15 presents the mean axial friction forces (blue curve) and the maxima of axial friction forces (red curve) resulting from these experiments. Furthermore, the results of experiments B-6, C-9 and D-9 are added to visualize the scattering of the measurements.

Both curves in Figure 0-15 show an almost linear increase with higher radial loads. This is to be expected and shows that the simplification of using COULOMB's friction law in Equation 0-4 is a valid assumption. However, at zero radial load, both, the blue and red curves exhibit axial forces of 99.0 N and 161.8 N, respectively. The curve of the mean axial friction force also presents itself with a slight curvature at low radial loads.
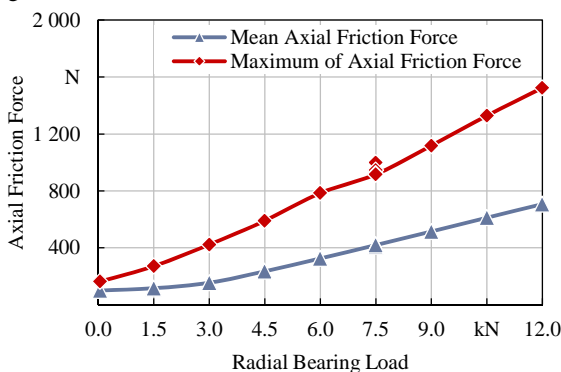

Figure 0-15: Influence of radial load on maximal and mean axial friction forces at 0.8 mm oscillation amplitude, 24 Hz oscillation frequency and 2 000 rpm rotational speed.

This is ascribed to the aforementioned axial thrust that occurs in cylindrical roller bearings and does not necessarily require radial loading. At lower radial loads the forces due to axial thrust amount to a higher percentage of the radial load and therefore cause the curvature. Since the red curve takes only the maxima of axial friction force into account, its inclination is steeper than that of the blue curve.

The mean and maximal axial friction coefficients that are calculated by applying Equation 0-8 from the results shown in Figure 0-15 are depicted in Figure 0-16.

The mean axial friction coefficient amounts to 0.02, the maximal axial friction coefficient amounts to 0.05 which is the order of magnitude of purely hydrodynamic friction.

The curvature left of 1.5 kN of radial load is, again, ascribed to axial thrust. The steep increase of both mean and maximal axial friction coefficients towards zero radial load is simply a mathematical issue as dividing by a radial load approaching zero in Equation 0-8 leads to an infinitely high friction coefficient.

Most importantly, Figure 0-16 shows that the assumption that the friction coefficient is the same in each of the 16 roller raceway contacts (see Equation 0-4), or in other words, that it is independent of the rolling element load, seems to be correct. Were it not, the friction coefficient would change with increasing radial loads and, in consequence, higher rolling element loads.

In general, the amount of radial loading increases the width of the load zone and possibly the number of rollers within. Figure 0-16 suggests, that this has no, or at least no significant effect on the axial friction coefficient.

Figure 0-17 depicts the effect of the axial shaft oscillations on cage slippage in dependence of the radial bearing load (blue curve). As a reference, the cage slippage measurements of experiments C-1 and D-1 are included (red diamonds).

An increase in cage slippage is observable at zero radial loading. This is not a result of the oscillations. It is due to the fact that the minimal load require-ments of the bearing are not met which is known to cause excessive cage slippage.
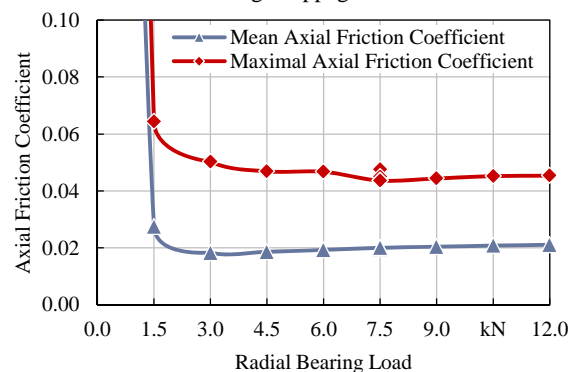

Figure 0-16: Influence of radial load on maximal and mean axial friction coefficients at 0.8 mm oscillation amplitude, 24 Hz oscillation frequency and 2 000 rpm rotational speed.
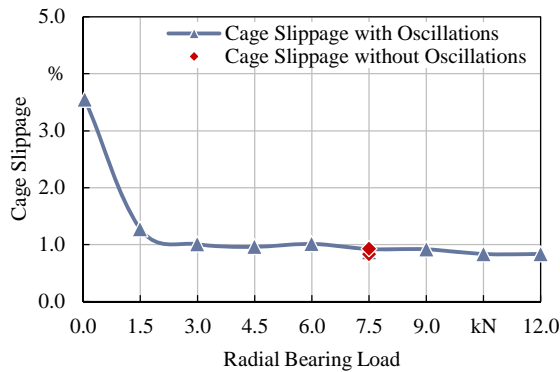
Figure 0-17: Influence of radial load on cage slippage at 0.8 mm oscillation amplitude, 24 Hz oscillation frequency and 2 000 rpm rotational speed.

With radial loads higher than the minimally required loading of 1.2 kN (see Table 0-2), axial shaft oscillations do not exhibit any significant effect on cage slippage. Albeit barely perceptible, the cage slippage measurements of experiments B-6, C-9 and D-9 are additionally included in Figure 0-17 which shows an extremely low variance of the measurement data.

Therefore, in summary, axially oscillating shafts do exhibit a greater impact on friction losses with higher radial loads but neither the axial friction coefficients nor the cage slippage are influenced by changes in radial loading.

4.3. *Test Series B: Rotational Speed*

Variations of the rotational speed, ranging from 50 rpm up to 3 200 rpm, are carried out in 400 rpm increments during test series B. The measurements of the mean and maximum axial friction forces obtained from these experiments are documented in Figure 0-18.

Again, further measurement data, resulting from experiments A-6, C-9 and D-9, is added to display the deviation between the measurements.

Towards low rotational speeds both the mean (blue curve) and the maximum (red curve) of axial friction force increase significantly. This is because the viscosity ratio κ declines with slowing rotational speeds until mixed friction occurs which causes higher friction forces than purely hydrodynamic friction. (see Figure 0-19).
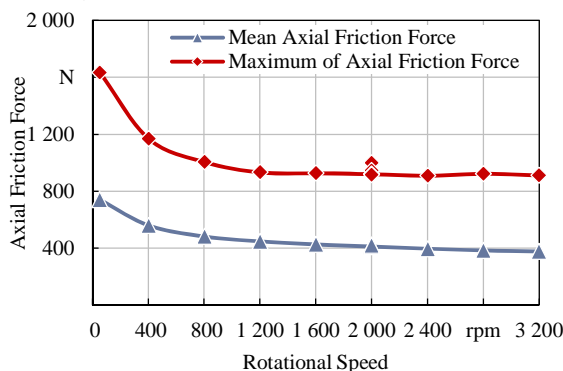

Figure 0-18: Influence of rotational speed on maximal and mean axial friction forces at 0.8 mm oscillation amplitude, 24 Hz oscillation frequency and 7.5 kN radial load.

With sufficiently high rotational speeds to ensure fully hydrodynamic contact conditions, there occurs only a very slight decrease of the mean axial friction force with increasing rotational speed, which barely registers as significant in the experiments. This is the case because the ratio of oscillating velocity over circumferential speed changes (see Figure 0-11) and the rolling friction coefficients are usually lower than sliding friction coefficients in lubricated contacts.

As Equation 0-8 does not account for the rotational speed, Figure 0-19, which shows the mean and maximal axial friction coefficients, looks similar to Figure 0-18.

But, Figure 0-19 shows that, if purely hydrodynamic friction is achieved, the rotational speed does barely interact with the axial sliding friction between rollers and raceway. Only a very slight decrease of the mean axial friction coefficient is observable as the ratio of oscillating to rolling in the roller-raceway contacts decreases with higher rotational speeds.

In accordance with test series A, the mean and maximal axial friction coefficients resulting from test series B amount to 0.02 and 0.05, respectively, provided that the rotational speed is sufficiently high to ensure proper hydrodynamic conditions.

The measurements of cage slippage of test series B which are depicted in Figure 0-20, exhibit no significant effect of the shaft oscillations with varying rotational speeds. The cage slippages with oscillations (blue curve) and without oscillations (red diamonds, experiments C-1 and D-1) both amounted to slightly less than 1 %. Merely a slight elevation at low rotational speeds is observable. Whether this is due to interactions of the shaft oscillations with the fairly slow rotational speeds or simply statistical spreading of cage slippage while the bearing is running cannot be deduced from the experiments.

The results obtained from varying the rotational speed prove that not the oscillation amplitude or frequency, but the rotational speed is the key factor that assures hydrodynamic friction or causes mixed friction. Even the highest possible setting at the test rig of 0.8 mm peak-to-peak amplitude and 24 Hz oscillation frequency could not provoke mixed friction during the experiments if the rotational speed is sufficiently high.
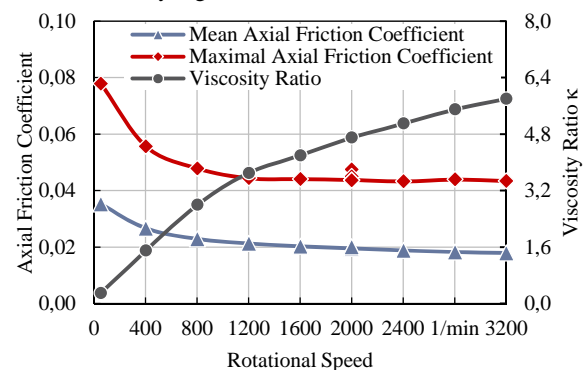

Figure 0-19: Influence of rotational speed on maximal and mean axial friction coefficients at 0.8 mm oscillation amplitude, 24 Hz oscillation frequency and 7.5 kN radial load.
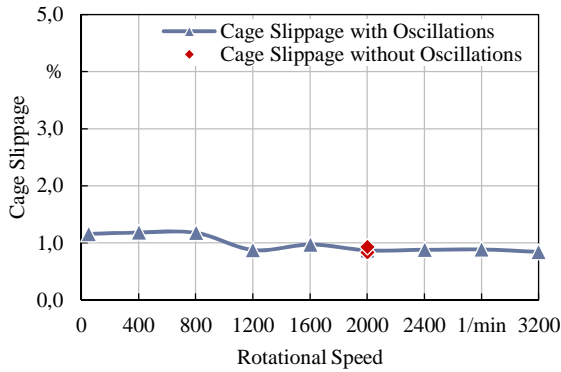
Figure 0-20: Influence of rotational speed on cage slippage at 0.8 mm oscillation amplitude, 24 Hz oscillation frequency and 7.5 kN radial load.

4.4. *Test Series C: Oscillation Frequency*

So far, the oscillation frequency has been set constantly at 24 Hz. In test series C, the oscillation frequency is being increased in 3 Hz increments from zero (no oscillations) to 24 Hz.

The obtained results from test series C and experiments A-6, B-6 and D-9 for the mean (blue curve) and maximal (red curve) axial friction force are plotted in Figure 0-21.

The previously mentioned axial thrust of 95 N for the mean axial friction force and 384 N for the maximum of axial friction force is observable in Figure 0-21 at the oscillation frequency of zero. From this offset from zero the axial friction forces of both curves increase with higher oscillation frequencies. The mean axial friction force (blue curve) approaches a limit at approximately 400 N.

In consequence, the maxima of axial friction forces must also reach a limit value, although this is not clearly distinguishable in Figure 0-21. Since the statistical variation of the maxima is higher than that of the mean values it appears, for this set of measurements, as if the red curve does not yet reach its limit value.

As the oscillation frequency is not factored in for the calculation of the axial friction coefficient (Equation 0-8), Figure 0-22 which displays the mean (blue curve) and maximal (red curve) axial friction coefficient for various oscillation frequencies, is similar to Figure 0-21. Nevertheless, the blue curve allows for two observations:
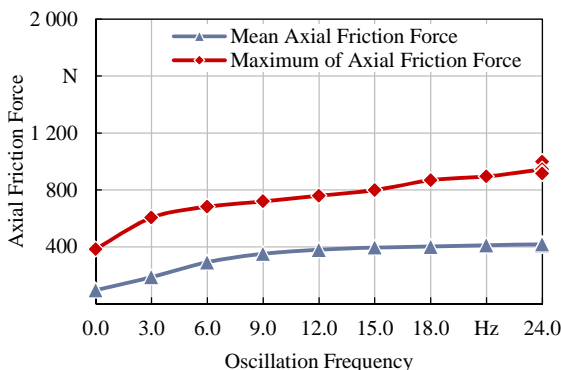

Figure 0-21: Influence of oscillation frequency on maximal and mean axial friction forces at 0.8 mm oscillation amplitude, 2 000 rpm rotational speed and 7.5 kN radial load.

Figure 0-22: Influence of oscillation frequency on maximal and mean axial friction coefficients at 0.8 mm oscillation amplitude, 2 000 rpm rotational speed and 7.5 kN radial load.

Firstly, at relatively moderate oscillation frequencies (0 to 12 Hz) a linear increase of the mean axial friction coefficient is discernible. Increasing the oscillation frequency leads to a higher oscillate-to-roll ratio which leads to an elevation of the axial friction coefficient.

Secondly, at higher oscillation frequencies (12 to 24 Hz) the mean axial friction coefficient converges with a threshold of 0.02. This happens because mineral oils are non-Newtonian liquids that exhibit shear thinning, which means that the lubricant viscosity decreases with increasing strain rates and the relation between strain rate and transmittable shear stresses is non-linear.

In this case, the strain rate corresponds to the oscillation velocity which is proportional to the oscillation frequency and the shear stresses correlate with the axial friction forces.

Figure 0-23 shows measurements of cage slippage with varying oscillation frequencies. It is evident that changing the oscillation frequency has no effect on cage slippage.

The cage slippage with oscillations (blue curves) does not deviate at all from the cage slippage without any oscillations that was determined in experiments C-1 and D-1 (red diamonds).

From test series C can be concluded that the amount of friction that occurs due to axial shaft oscillations is primarily determined by the properties of the lubricant and its behaviour in response to dynamic shearing.

Figure 0-23: Influence of oscillation frequency on cage slippage at 0.8 mm oscillation amplitude, 2 000 rpm rotational speed and 7.5 kN radial load.

4.5. *Test Series D: Oscillation Amplitude*

The nine experiments of test series D are run with incrementally increasing oscillation amplitudes, starting from zero (no oscillations) and ending at 0.8 mm peak-to-peak amplitude. The resulting mean (blue curve) and maximal (red curve) axial friction forces, appended with the results from experiments A-6, B-6 and C-9, are shown in Figure 0-24.

Again, the measurements show axial thrust of 98 N for the mean axial friction force and 385 N for the maximum of axial friction force without any oscillations (oscillation amplitude equals zero). With small axial shaft oscillations of 0.1 mm peak-to-peak amplitude neither the mean nor the maximal axial friction force exhibit any change. This particular experiment (D-2) was repeated, to ensure that there was no error in measurement, which yielded identical results.

To find out whether these small oscillations really do not impact the axial friction forces, Figure 0-25 displays some of the measurement data of each of the four force sensors.

Contrary to Figure 0-12, where the oscillations are clearly pronounced, Figure 0-25 displays no periodic oscillations of the measurements and the signals appear random. Comparison of Figure 0-25 with Figure 0-14, where no oscillations were imposed, shows that both measurements appear very similar. This suggests, that the aforementioned axial thrust is the dominant effect and that small oscillations do not seem to have an impact.

Further increase of the oscillation amplitude leads to a significant increase in both the mean and maximal axial friction force (see Figure 0-24). Therefore, the oscillation amplitude is an influential parameter but it needs to exceed a certain threshold to exert its impact on the axial friction forces.

In Figure 0-24, this threshold seems to be located around 0.1 mm of oscillation amplitude. This is approximately the amount of axial clearance between rollers and outer ring flanges. During the oscillations, the roller rolls and drifts axially with the inner ring until it touches the outer ring flange.

Only after that does a sliding motion occur between rollers and inner ring raceway which creates significantly higher friction forces that are recorded by the sensors and which leads to the steep increase of both curves in Figure 0-24.

Figure 0-25: Axial forces on the test bearing housing at 0.1 mm oscillation amplitude, 24 Hz oscillation frequency, 2 000 rpm rotational speed and 7.5 kN radial load (experiment D-2).

With higher oscillation amplitudes, which entail also higher oscillation velocities since the oscillation frequency has not changed, both curves reach a limit of transmitted axial friction force. This is due to the aforementioned shear thinning effect as the lubricant behaves in a non-Newtonian manner.

The curves of the mean and axial friction coefficients which are depicted in Figure 0-26 look similar to Figure 0-24 since the oscillation amplitude is not required for Equation 0-8.

But, for oscillation amplitudes greater than 0.2 mm, the curves in Figure 0-26 also shows excellent accordance with those in Figure 0-22. The steps of the parameters oscillation frequency and oscillation amplitude are chosen though that the respective experiments of test series C and D result in identical oscillation velocities.

Therefore, one can deduct from the results shown in Figure 0-26 and Figure 0-22 that the oscillation velocity is the relevant factor that determines the axial friction coefficient of, in this case, 0.02 and 0.05 for the mean and maximal axial friction coefficient. The oscillation velocity is also the main driver of lubricant shearing.

With regard to cage slippage, changing the oscillation amplitude bears no effect on cage slippage, as it is shown by Figure 0-27. The cage slippage with oscillations (blue curve) does not deviate from the cage slippage without oscillations of experiments C-1 and D-1 (red diamonds).

Figure 0-24: Influence of oscillation amplitude on maximal and mean axial friction forces at 24 Hz oscillation frequency, 2 000 rpm rotational speed and 7.5 kN radial load.
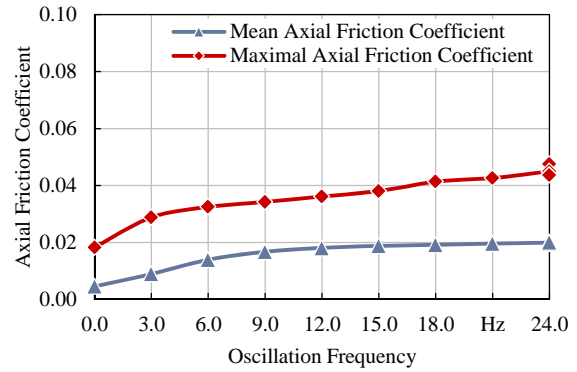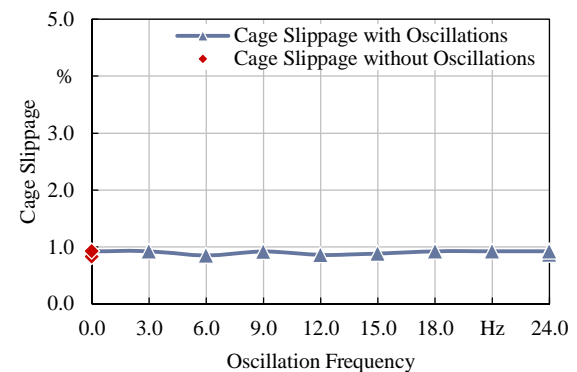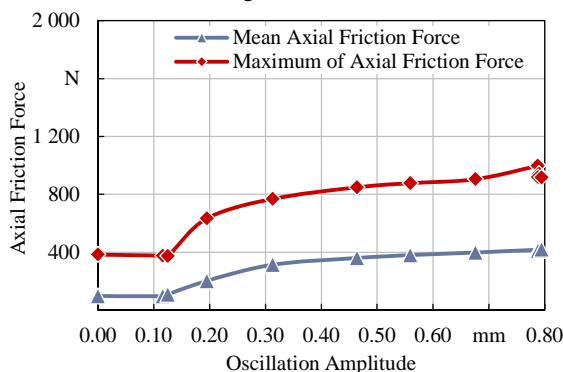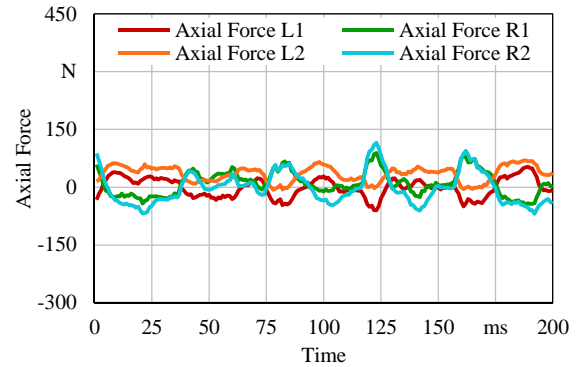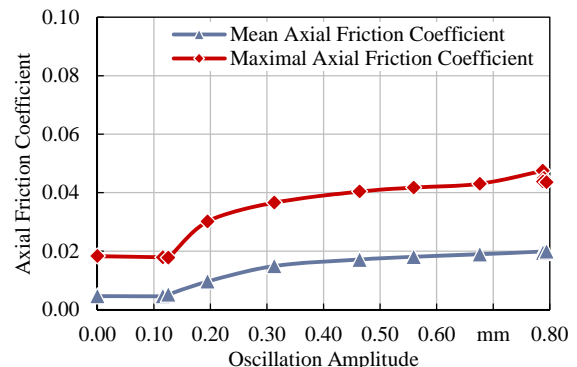

Figure 0-26: Influence of oscillation amplitude on maximal and mean axial friction coefficients at 24 Hz oscillation frequency, 2 000 rpm rotational speed and 7.5 kN radial load.
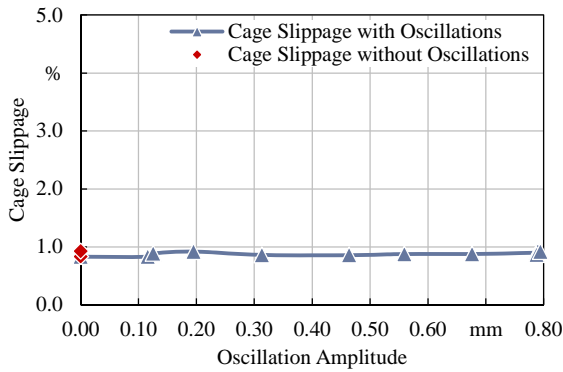
Figure 0-27: Influence of oscillation amplitude on cage slippage at 24 Hz oscillation frequency, 2 000 rpm rotational speed and 7.5 kN radial load.

Inferring from test series D, as long as the oscillation amplitude does not exceed the axial clearance of the roller bearing in question, axial shaft oscillations do not exhibit a significant impact on axial sliding friction. For oscillation amplitudes greater than the axial clearance, the oscillation velocity, as the product of amplitude and frequency (see Equation 0-14) is the crucial influencer regarding friction due to axial shaft oscillations.

4.6. Test E: Friction Losses

So far, test series A to D have established that axial shaft oscillations cause substantial axial forces. This inevitably causes additional friction losses which can be calculated using Equation 0-14.

The resulting axial friction losses $P_{osc}(t)$ due to oscillations of 0.8 mm amplitude and 24 Hz frequency at 2 000 rpm rotational speed and 7.5 kN radial load from experiment D-9 are plotted in Figure 0-28 (blue curve).

Since the friction losses fluctuate with the oscillation velocity, the mean friction losses P_{osc} are being determined using Equation 0-15 (red line) and amount to 20 W.

In comparison, Figure 0-29 depicts the friction losses due to axial thrust without any oscillations, determined in the same way from experiment D-1, using Equation 0-15. Although the axial forces due to axial thrust reached about 23 % of the axial forces due to oscillations, the mean friction losses due to axial thrust only amount to 0.6 W which corresponds to 3 % of the friction losses due to oscillations.
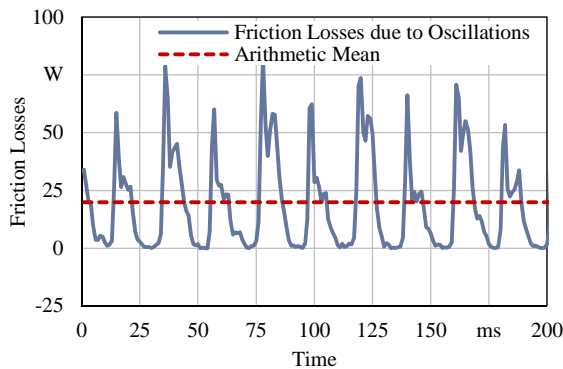
Figure 0-28: Friction Losses due to axial oscillations of 24 Hz frequency and 0.8 mm amplitude at 2 000 rpm rotational speed and 7.5 kN radial load (experiment D-9).
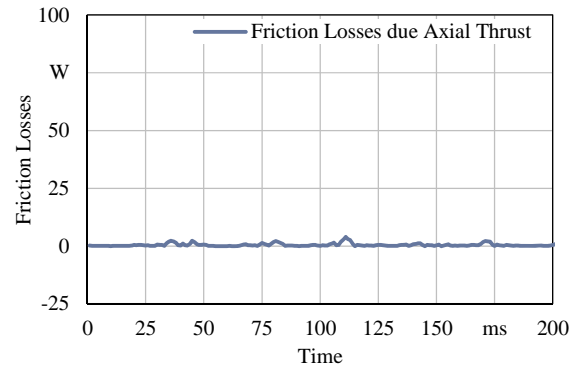
Figure 0-29: Friction Losses due to axial thrust at 2 000 rpm rotational speed and 7.5 kN radial load (experiment D-1).

This vast discrepancy between the two percentages is due to the fact that axial thrust does not generate any axial movements of the test bearing shaft which is required to generate friction losses (see Equation 0-14).

To establish whether these friction losses of 20 W are significant compared to the friction losses that are generated with normal bearing operation, Figure 0-30 shows a measurement from the bearing friction test rig. This test (experiment E-1) was conducted with the same rotational speed of 2 000 rpm and radial load of 7.5 kN but without oscillations. The friction losses levelled out at 33.5 W.

This concludes that axial shaft oscillations can be a substantial cause of friction losses and increase the total friction losses of cylindrical roller bearings significantly.
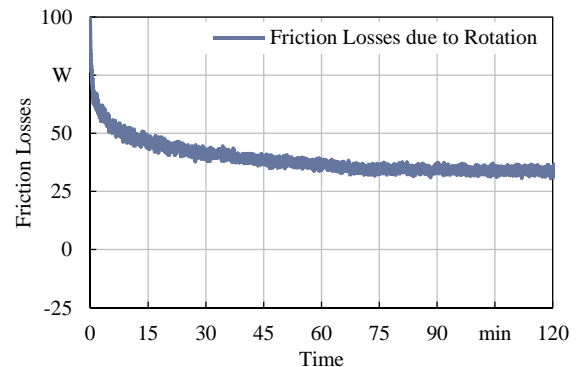
Figure 0-30: Bearing friction losses due to standard operation at 2 000 rpm rotational speed and 7.5 kN radial load.

4.7. Test Series F: Operating Temperatures

The substantial impact of an axially oscillating shaft on friction and lubrication also entails significant increases in operating temperatures. Therefore, two additional experiments (F-1 and F-2) with a duration of two hours each are being conducted at rotational speeds of 2 000 rpm and radial loads of 7.5 kN, one without oscillations and one with oscillations of 0.8 mm amplitude and 24 Hz frequency. In both experiments the inner and outer ring temperatures are recorded.

Figure 0-31 compares the inner ring temperatures with (red curve) and without (blue curve) oscillations, Figure 0-32 displays the respective outer ring temperatures in the middle of the load zone.

Figure 0-31: Operating temperatures of the test bearing inner ring at 2 000 rpm rotational speed and 7.5 kN radial load, with and without additional oscillations of 0.8 mm amplitude and 24 Hz frequency.

The results show that the superimposed axial shaft oscillations cause significant increases in operating temperatures, not only at the inner ring where the sliding friction between rollers and raceway occurs but also at the outer ring due to increased roller flange contacts and due to heat conduction from the inner ring through the rollers into the outer ring.

The lubricant viscosity reacts very sensibly to temperature changes and decreases with rising temperatures. In consequence, this leads to a lower lubricant film thickness and possibly inadequate lubrication and mixed friction. Furthermore, higher operating temperatures accelerate lubricant ageing and degradation.

In this case, the inner ring temperature rise up to 54 °C due to the oscillations is still in the designated operating temperature range since rotational speed and radial load are relatively moderate compared to the basic dynamic load rating C_r of 75 kN and to the limiting speed n_G of 9 700 rpm for the test bearing.

But, under more challenging operating conditions with higher radial loads and rotational speeds axial shaft oscillations can well be responsible for overheating and premature bearing failure.

In consequence, lubrication for bearing applications which are subject to axial shaft oscillations needs to be deliberately chosen and maintained, especially, when the operating temperatures are expected to be high.

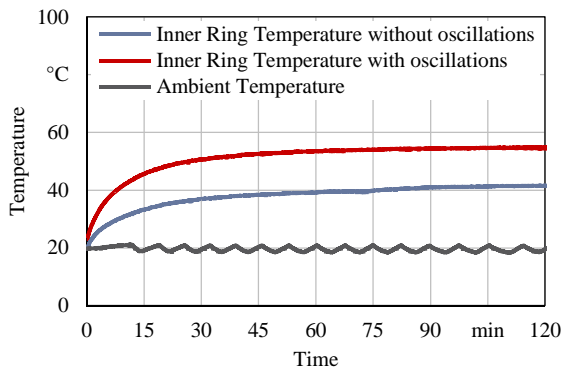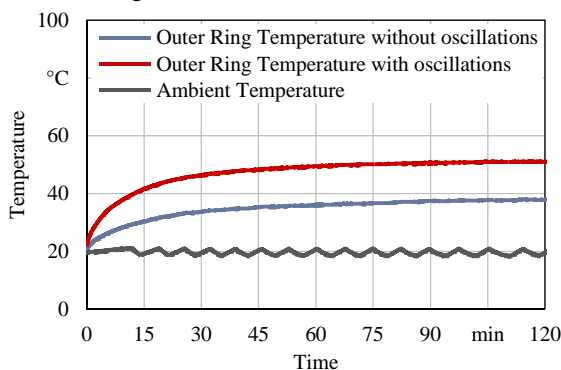*Figure 0-32: Operating temperatures of the test bearing outer ring at 2 000 rpm rotational speed and 7.5 kN radial load, with and without additional oscillations of 0.8 mm amplitude and 24 Hz frequency.*

4.8. *Test G: Wear*

So far, the results obtained from the experiments listed in Table 0-1 suggest that axial shaft oscillations do not cause improper lubrication and should, therefore, not generate any additional wear. To test, whether this hypothesis holds, another cylindrical roller bearing is subjected to axial shaft oscillations in a long run test. Table 0-4 lists the chosen test parameters and resulting operating conditions.

Table 0-4: Test parameters and operating conditions for the long run test.

Test Parameters and Conditions	
Rotational speed	2 000 rpm
Radial load	7.5 kN
Oscillation frequency	24 Hz
Oscillation peak-to-peak amplitude	0.8 mm
Test duration	231.5 h
Inner ring steady-state-temperature	55° C
Viscosity ratio at steady-state-temperature	3.5

The test duration of 231.5 h amounts, at the applied oscillation frequency of 24 Hz to approximately $2 \cdot 10^7$ oscillations. With the chosen oscillation peak-to-peak amplitude of 0.8 mm, this results in a total axial sliding distance between inner ring and each of the 16 rollers of approximately 32 km.

If axial shaft oscillations cause mixed friction, definitive traces of wear should be observable on rollers and raceways. Subsequent to the long run, the test bearing is dismounted, disassembled, cleaned and thoroughly examined. Neither on the raceways nor on the rollers were obvious traces of wear observable. The axial oscillations lead, however, to discoloration of the running surfaces as can be seen in Figure 0-33 which shows the inner ring and some of the rollers after the examination.

The well-defined borders of the discoloured areas and the fact that the operating temperatures during the long run were not unusually high suggest that the discolouration is due to chemical reactions of the lubricant.

These chemical transformations are provoked by the additional shearing of the lubricant due to the axial oscillations. It tears the molecule chains and leads to oxidation and accelerated degradation of the lubricant. The lubricant residue that was removed from the bearing during the cleaning process also appeared blackened due to oxidation.

Figure 0-33: Cleaned inner ring and selected rollers of the test bearing after a long run under oscillations.

The discoloured area of the inner ring raceway corresponds to the effective length of the rollers. Interestingly, a small not discoloured stripe of approximately 1 mm in width appears in the middle of the discoloured area of the inner ring raceway. Correspondingly, a small discoloured stripe of about the same width is visible in the middle of the otherwise not discoloured running surfaces of the rollers.

Why this is the case is not yet fully understood. It suggests, however, that these darkened traces are a degradation product of the lubricant and are not due to wear and should therefore be adhesive rather than abrasive.

For a more detailed investigation of the discolorations on the inner ring raceway, a laser scanning microscope (Keyence VKX-200) was being used to examine the surface of inner ring raceway. Figure 0-34 shows a magnification of one of the borders of the not discoloured stripe in the middle of the discoloured area.

The discoloured area is shown on the left-hand side and exhibits a well-defined border towards the not discoloured stripe on the right-hand side. The vertical lines along the rolling direction are ascribed to the bearing manufacturing process.

Figure 0-35 shows a measurement of the surface roughness of the exact same surface area on the inner ring raceway. Higher points of the surface profile (roughness peaks) are depicted reddish, lower ones blueish.

It becomes obvious that the surface profile on the left-hand side, where the discolouration is, appears a fraction of a micrometre higher than that on the right-hand side. This shows, that the surface discolouration is indeed adhesive and due to lubricant deterioration and not wear related.

Therefore, the long run under oscillations supports the earlier findings that axial oscillations generate an excessive amount of shearing within the lubricant in the roller raceway contacts which induces chemical alterations of the lubricant which propagates lubricant degradation.

The long run test supports the earlier observations that, in case of proper lubrication conditions, axial shaft oscillations do not impede with lubricant film build-up and do not lead to mixed friction and therefore do not increase wear.
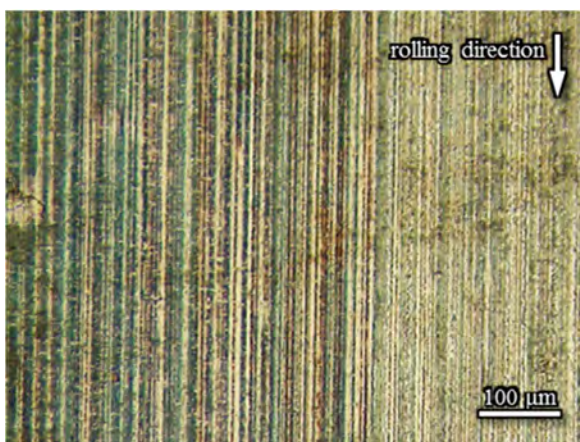

Figure 0-34: Discolouration of the inner ring raceway.
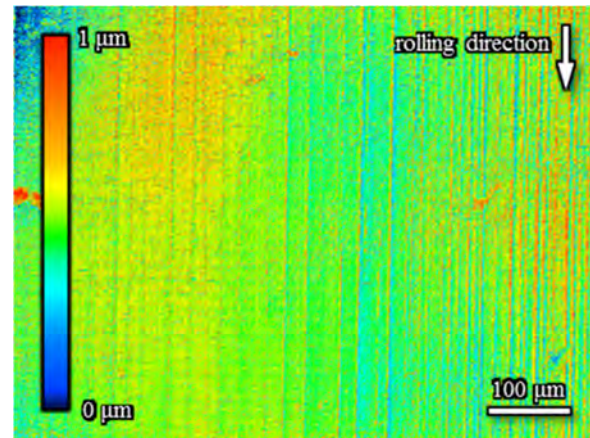
Figure 0-35: Roughness of the inner ring raceway.

However, under mixed-friction conditions with an insufficient lubricant film build-up (small viscosity ratio), axial shaft oscillations can increase wear significantly. It is therefore advisable to aim for a high enough viscosity ratio in any application that might experience axial shaft oscillations.

5. Conclusions

The objective of this paper is to examine, how axial shaft oscillations affect friction and lubrication in cylindrical roller bearings. Therefore, this paper presents a unique test rig and an experimental study and points out the following results:

Firstly, it is shown that axial shaft oscillations cause a substantial amount of sliding friction between rollers and inner ring raceway which leads to axial forces on the outer ring that are significantly higher than forces due to axial thrust. These forces behave dynamically and in unison with the oscillation velocity.

Variations in radial load show that the impact of axial shaft oscillations increases with radial loads but the axial sliding friction coefficient of the roller raceway contacts does not change.

Alterations of the rotational speed indicate that axial shaft oscillations do not cause mixed friction as long as the rotational speed is sufficiently high to ensure hydrodynamic lubrication without oscillations.

Testing various oscillation frequencies revealed that the occurring axial friction forces strongly depend on the properties of the lubricant and its non-Newtonian behaviour when sheared.

Changing the oscillation amplitude demonstrates that the axial shaft oscillations need to exceed the axial clearance between rollers and flanges to exhibit a significant effect on the axial friction forces.

The mean axial friction coefficients for the roller-raceway contacts, calculated from the measurement data, results in 0.02, which indicates purely hydrodynamic friction. The axial shaft oscillations do not exhibit any effect on cage slippage.

The conducted measurements of friction losses with and without oscillations prove that axial shaft oscillations contribute substantially to the total friction losses of the cylindrical roller bearing. As observed in the experiments, this leads to significant increases in operating temperatures of the test bearing inner and outer ring.

Finally, a long run test with axial shaft oscillations does not cause any wear at the running surfaces. However, it leads to discolouration and increased lubricant degradation due to shearing of the lubricant and temperature rises.

Therefore, lubrication proves to be the critical issue when a roller bearing is subjected to axial shaft oscillations. The lubricant choice needs to be carefully considered and maintenance has to be adjusted accordingly.

References

[1] J. Gegner: Tribological Aspects of Rolling Bearing Failures. In: Tribology. Chang-Hung Kuo (Ed.). InTechOpen. pp. 33–94. 2011.

[2] K. Stadler, A. Stubenrauch: Premature bearing failures in industrial gearboxes. In: Antriebstechnisches Kolloquium. 2013.

[3] Schaeffler Technologies (Ed.): The Design of Rolling Bearing Mountings. Design Examples covering Machines, Vehicles and Equipment. Publ. No. 00200/6 EA. 2012.

[4] S. John, T. Kiekbusch: Einfluss von Vibrationsanregung auf Wälzlager. Bewertung von Schwingungsanregung hinsichtlich möglicher Schädigung an Wälzlagern unter Einbeziehung der Umgebungskonstruktion. FVA. Project 589 I. Final Report. Frankfurt am Main. 2014.

[5] T, Stahl, S. Tremmel, H. Meerkamm, S. Wartzack: The influence of speed and load spectra on the friction of rolling bearings. In: 65th STLE Annual Meeting & Exhibition. Las Vegas. 2010.

[6] T. Harris, M. Kotzalas: Essential Concepts of Bearing Technology. Rolling Bearing Analysis. Fifth Edtion. CRC Press. 2006.

[7] H. Spikes: Basics of EHL for practical application. In: Lubrication Science. Vol. 27, no. 1. 2015.

List of Symbols

Symbol	Explanation
a_{osc}	Oscillation peak-to-peak amplitude
C_r	Basic dynamic load rating (radial)
$C_{r,min}$	Minimal loading
D_{IR}	Inner ring raceway diameter
D_{pw}	Pitch diameter
D_w	Roller diameter
F_A	Axial friction force
F_{Ai}	Axial friction force at roller i
$F_{A,max}$	Maximum of axial friction force
F_{L1}	Axial force measured by sensor L1
F_{L2}	Axial force measured by sensor L2
f_{osc}	Oscillation frequency
F_R	Radial bearing load
F_{R1}	Axial force measured by sensor R1
F_{R2}	Axial force measured by sensor R2
k_1	Empirical value
M_{rot}	Rotational bearing friction moment
n	Rotational speed
n_C	Measured rotational speed of the bearing cage
n_{C0}	Theoretical rotational speed of the bearing cage
n_G	Limiting rotational speed
P_{osc}	Friction losses due to axial oscillations
P_{rot}	Friction losses without oscillations
Q_i	Load of rolling element i
Q_m	Mean rolling element load
$Q(\varphi)$	Distribution of radial load
S	Cage slippage
s_{osc}	Axial shaft movement
t	Time
t_s	Sample time
v_{osc}	Oscillation velocity
Z	Number of rolling elements
α	Contact angle
β	Oscillate-to-roll-ratio
μ_A	Mean axial friction coefficient
$\mu_{A,max}$	Maximal axial friction coefficient
φ	Angular coordinate

The Influence of the Centripetal Acceleration on the Temperature Behavior of Rolling Bearings

David Hochrein[1], Stephan Tremmel[2], Sandro Wartzack[3]

[1] *Friedrich-Alexander-Universität Erlangen-Nürnberg (FAU), Engineering Design, hochrein@mfk.fau.de*
[2] *Friedrich-Alexander-University Erlangen-Nürnberg (FAU), Engineering Design, tremmel@mfk.fau.de*
[3] *Friedrich-Alexander-University Erlangen-Nürnberg (FAU), Engineering Design, wartzack@mfk.fau.de*

Abstract – The bearing temperature is one of the essential variables in order to describe a bearing system. Especially under extreme conditions such as external accelerations, an unsuitable temperature development at the bearing position can cause significant damage. This work examines the temperature behavior under the influence of high centripetal accelerations up to 1 000-times gravity. Therefore, the factors centripetal acceleration, relative speed of the specimen and the oil flow rate were varied systematically. Contrary to our expectations, the temperature does not rise with an increase of the centripetal acceleration. This behavior can essentially be explained by the impact of the acceleration to the supplied oil flow rate. Therefore the increased injection speed of the lubricating and cooling oil leads to a better cooling of the roller bearings and the bearing temperature nearly remains constant. If the relative speed of the specimen increases, the bearing temperature behaves as with bearings, which are not exposed to the influence of high accelerations. E.g. the temperature rises, even if only moderate. The temperature behavior was analyzed and evaluated in the context of the present frictional moment. In order to achieve a sufficient cooling effect by the lubricating oil flow an appropriate amount of lubricant is necessary. The present investigation showed that with roller bearings exposed to centripetal accelerations the necessary amount of oil is about ten times higher than under normal circumstances. Appropriate flow rates depending on the requirements were identified by the variation of the oil flow rate. A look at the overall context shows that the bearing temperature is not an exclusion criterion for the use of roller bearings exposed to high accelerations. With an appropriate design of the oil supply also a self-regulation effect of the oil flow rate can be achieved by the present accelerations.

A small excerpt of this research work has already been published in the proceedings of the bearing world conference [1].

Keywords – roller bearings, centripetal acceleration, temperature behaviour, appropriate oil supply quantity

1. Introduction

Then as now, roller bearings contribute significantly to the success of many technical systems and are still an essential part of bearing systems today. As long as the machine element roller bearing exists, different research activities try to improve or at least understand this element or the whole bearing system. Even though the roller bearing has a very simple structure, consisting of outer and inner rings, roller elements and cages, a lot of questions concerning the system knowledge of this machine element have not been answered yet. One reason for this could be the simple structure itself. Since the complexity of the assembly is basically low also the possibilities for improvement are limited. In addition, the large number of internal, but especially the large number of external influencing variables and importantly the complex interaction of all variables could be a further reason for this.

Frequently analyzed parameters are the frictional moment of roller bearings or even the influences on the bearing nominal lifetime like external loads, pressure distribution, lubrication, vibrations as analyzed in [2, 3, 4, 5]. In many cases the investigation of the temperature is the aim of the research activities [2, 6, 7], although this parameter often seems to be less important for users and during the design process. However, the bearing temperature is a quite decisive factor for a trouble-free operation of roller bearings.

The temperature influences many properties of the roller bearing elements. This includes the surface hardness, the strength, the elasticity, the dimensional accuracy, the shape accuracy as well as the wear resistance and the frictional moment [8]. Additionally the temperature also affects the viscosity of the lubricant and the aging-process of the lubricant. Consequently the aging-process reduces the lubricant service life and so can limit the bearing operating time. Seals and cages can be further temperature-sensitive components, which contribute to the operating time, if they consist of non-metallic materials.

A further problem is that the change of the properties can sometimes cause contradictory effects that may cancel each other out or not. To give an example, if temperatures higher than 100 °C lead to carbide precipitations that reduce the component volume, temperatures over 150 °C lead to retained austenite transformation that affects an increase of the component volume [8, 9].

Beside contradictory effects, there are also effects that show an unsteady behavior. Due to the rise of the bearing temperature during operation, the bearing clearance often decreases. Figure 1-1 shows that a reduction of the bearing clearance does not have to be considered negatively.

As the reduction of the bearing clearance – up to a given limit – causes a significant increase of the nominal bearing life time in the area of pretension. However, the nominal life time shows a sharp decrease, if the limit is exceeded. Such an abruptly change of the component properties can have serious consequences for the operation of the bearing and is difficult to manage, in practice.
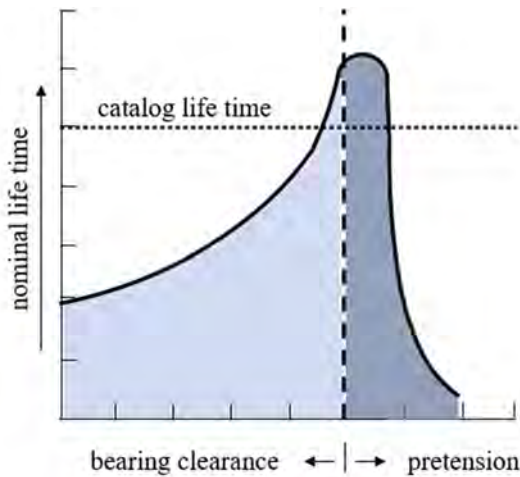
Figure 1-1: Nominal lifetime as a qualitative function of the bearing clearance according to [10].

The consequence of too high bearing temperatures could for example be a hot running. In figure 1-2 a hot running of a supporting bearing of a test rig is shown.

Figure 1-2: Hot-running of a test rig bearing.

The damage of this bearing took place without any prior notice as quite typical for such processes. After a long period of operation, the temperature rapidly increased followed by the bearing failure. It could not be determined by the failure analysis, whether the hot running was the primary reason of damage, but it was definitely the resulting cause of damage.

This example shows the difficulty to identify temperature caused damages and their origins. Thermal effects can produce an enormous extent of damage up to a total destruction of the bearing and a shutdown of the machine.

Therefore, the analysis of the bearing temperature is an important step to a better understanding of the whole bearing system. This is particularly true if it concerns operating states with special, so far little researched conditions. This is relevant for roller bearings exposed to centripetal accelerations. Typical applications for such bearings are connecting rod bearings of combustion engines and planet bearings of planetary gears.

In contrast to bearings running under conditions with no centripetal accelerations, all components such as the rings, roller elements, cage, seals and lubricant are exposed to high accelerations in addition to their usual operating loads. This can lead to a changed bearing kinematic [11]. Several aspects contribute to this effect. First of all the cages of outer ring guided bearings can rest on the outer rings. So the cage behaves like a small plain bearing [11] and creates an additional heat source and frictional moment. Besides this, also larger elastic deformations of the cage [11] and rings are expected, which can influence the contact situation of rings and rolling elements. This can result in larger or even additional load zones, which also influence the dynamic behavior. The bearing lifetime can also be affected.

Moreover, the rolling elements themselves are higher loaded because of the centripetal acceleration. They are additionally pressed against the raceway and so the local roller element load rises for each single roller. This leads, although the load in general has rather a lower affect to the film thickness, to smaller lubricant films, to higher shear stresses and to higher temperatures.

In this context, the lubricant is an important component. Under high external accelerations, it is much more difficult to build an appropriate lubricant film. Beside the challenges already mentioned above, the influence of the acceleration on the lubricant itself can be a very serious problem. On the one hand, the lateral outflow of the lubricant is increased by the acceleration, so the film thickness decreases, and on the other hand, it remains unclear whether the oil can reach the lubrication points of the bearing, or whether it is simply ejected by the acceleration field. And finally the viscosity of the lubricant, which is a function of the temperature, is a key parameter for the lubricating conditions.

Further questions arise here, whether the lubricant is able to cool and lubricate the bearing sufficiently under the influence of high accelerations or if the extreme temperature rises? Moreover, it remains unclear, whether the changed movement sequences of roller elements and cage, as they occur with bearings exposed to centripetal accelerations [11], influence the bearing temperature.

In this work, the aspects concerning the temperature behavior were investigated and analyzed in detail. Of course, further aspects like the axial thrust behavior and the development of the frictional moment will also be investigated in more detail in the future.

2. Experimental test setup

The focus of the investigations of roller bearings exposed to high accelerations is the general – application-independent – analysis of the roller bearing system. In order to analyze the behavior of roller bearings a new test rig was built. With this test rig roller bearings can be exposed to centripetal accelerations up to 3 000-times gravity. The basic functional principle of the test rig has already been presented in [12]. In order to get a better understanding of the analyses that have been done, the test rig will be described in more detail.

The whole unit has a total mass of 16 tons and occupies a total area of 22 square meters. Due to the high occurring accelerations, the test rig has a massive protective hood in order to protect the environment against flying parts. For this reason, the unit is placed in a bunker as well.

According to typical applications mentioned under chapter 1, the unit is designed like an open planetary gear, shown in figure 1-3.
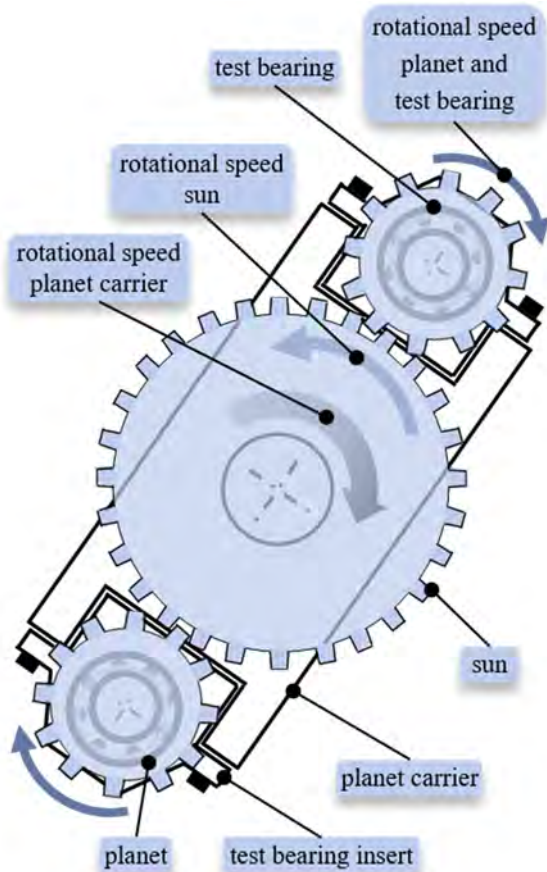

Figure 1-3: Functional principle of the test rig according to [12].

By the rotation of the planet carrier, the test bearings move on a circular path. The center of the circular path is eccentric to the center of the test bearing. So the test bearings are exposed to a radially outwards directed acceleration. Due to a separate drive unit for the sun wheel, the rotational (relative) speed of the planets and therefore the rotational speed of the specimens around its own axis can be regulated without influence by the rotational speed of the planet carrier.

The test bearings are in an insert, which is fixed to the planet carrier with several screws. The insert contains the complete measuring system, the support bearings of the test shaft and the planet gears. The planet gears provide the drive of the test shaft. The design of the insert is as axially symmetrical as possible. Especially the shaft of the test bearings and the connecting components surrounding the test bearing are designed strictly symmetrical.

On the one hand, this is the only way to achieve a balance quantity for the whole unit, which allows trouble-free measuring conditions with a less amount of vibrations. On the other hand, the symmetrical design prevents the development of axial thrust, which is caused by an unequal deformation of the test bearing shaft. Axial

thrust is caused by tilting and tooth setting of cylindrical roller elements. Therefore, deformations of the raceways such as those that occur with an unequal deformation of a shaft can produce this effect or strengthen it.

In order to describe the behavior of roller bearings under the influence of extreme conditions accurately, various measurement variables are directly measured on the test bearing itself. The frictional moment of the specimens is measured at the bearing outer ring, as shown in figure 1-4. The outer ring of the test bearing is not mounted in a bearing housing as under usual conditions. Here, the ring can move freely in radial as well as in axial direction.
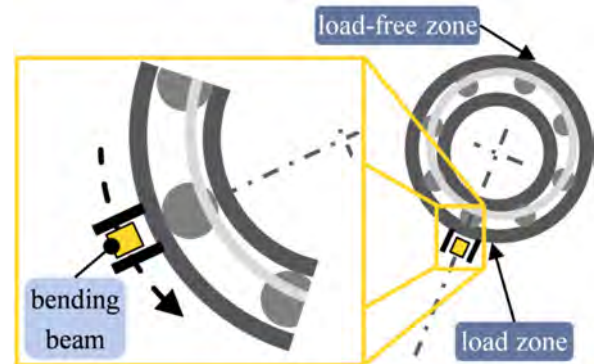
Figure 1-4: Functional principle of measuring the frictional moment according to [12].

The freely movable ring is turned radially by the existing frictional moment. This radial turn is measured by a bending beam, which is equipped with strain gauges. The bending beam is connected to the outer ring by a slider element. Therefore, the connection between bending beam and outer ring is designed in such a way that an axial movement of the outer ring is not prevented.

The axial movement of the outer ring is measured by sensors at each front side of the outer ring, as shown in figure 1-5. These are also bending beams, which are equipped with strain gauges. There are three sensors at each front side. So even a tilting of the outer ring can be measured. The axial shifting force of the outer ring is measured, which corresponds to the axial thrust force of the test bearing. Due to this design of the measurement system, the outer ring is shifted to the bearing center, if axial thrust occurs. An eccentric position of the outer ring can lead to the situation that the rolling elements are mainly rolling on its edges. This effect is intensified by the application of eccentric load, which is caused by the accelerated mass of the outer ring. To avoid this effect the free space between axial thrust sensors and outer ring is minimized.

Figure 1-5: Functional principle of measuring the axial thrust according to [12].

In addition to the already mentioned parameters, also the bearing temperature is measured, as shown in figure 1-6.
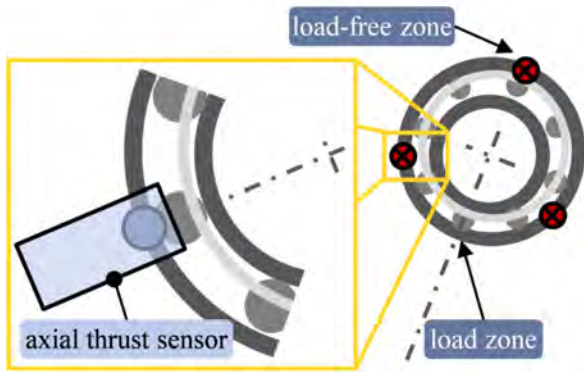
The measurement is done by sensors, which are embedded in the outer ring. For each test bearing two sensors are used. One sensor is located in the load zone and one is shifted to the load zone by 180°.

On the basis of this structure of the sensors it is possible to detect temperature gradients inside the bearing and so determine the temperature distribution of the bearing. Furthermore, the bearing temperature can be used as a reference to the lubricant temperature. Besides all, the bearing temperature of the test bearing is the most important parameter to determine the thermal steady state.

Beside the mentioned test bearing-specific measurement parameters, which describe the behavior of the specimens, there are also some measurement parameters, which describe the state of the auxiliary media and of the connecting geometry.

With the help of these parameters, the state of the environment, within the specimens are tested, can be described. These include the supplied oil flow rate and the oil temperature of the supplied oil. The measured parameters also include the relative speed of the specimens, the present acceleration and the bearing load.

The bearing load is generated by the accelerated mass of the outer ring. Since the outer ring cannot support itself in a bearing housing, the whole in the acceleration field accelerated mass of the outer ring acts as radial load of the test bearing.

An oil supply unit, as shown in figure 1-7, provides the oil flow rate and the oil temperature. In this unit, the oil is pumped from a tank via a flow heater to a rotary feedthrough. The rotary feedthrough feeds the oil into the shaft of the rotating planet carrier.

From the shaft lubrication holes lead the oil to the test bearing. In the lubrication holes also a nozzle is located. This nozzle has a defined distance to the specimen and the supplied oil has a constant temperature of 35 °C. The escaping oil of the test bearing is radially ejected from the insert with the test bearing. An encapsulation collects the oil splashed away and returns it to the lubricant circuit. Oil stagnation can be prevented by the direct and simple ejection of the used oil.
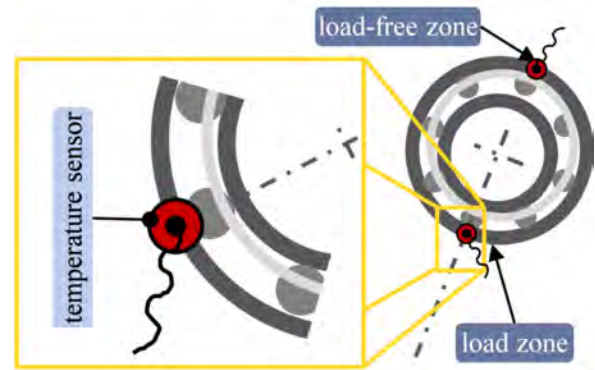
Figure 1-6: Functional principle of measuring the axial thrust according to [12].

The acceleration is a function of the rotational speed of the planet carrier and of the distance between the insert and the center of rotation. The distance between the center of rotation and insert is not variable. The rotational speed of the test bearings is a function of the rotational speed of the planet carrier and the rotational speed of the sun wheel. The test rig is designed in such a way that the rotational speed of the specimen can be varied from the minimum to the maximum value over the entire acceleration setting range, in contrast to the applications.

Needle rollers and cage assemblies are used as test bearings. These roller bearings are often used in planetary gears as planet bearings or as connecting rod bearings in combustion engines. The cages of the specimens are guided by the outer ring. Therefore, the raceway of the outer ring is the guiding surface and so the cages can attach to them. The cages are made of steel and have a carbon based coating system. The coating system is used to reduce the frictional moment and protect against wear, if poor lubrication occurs.

The cage profile is designed in such a way that the entire cage bars have the same outer diameter over the whole cage wide and can be supported by the raceway of the outer ring. This cage profile is called A-profile.

Figure 1-7: Illustration of the oil supply unit and the oil cycle.

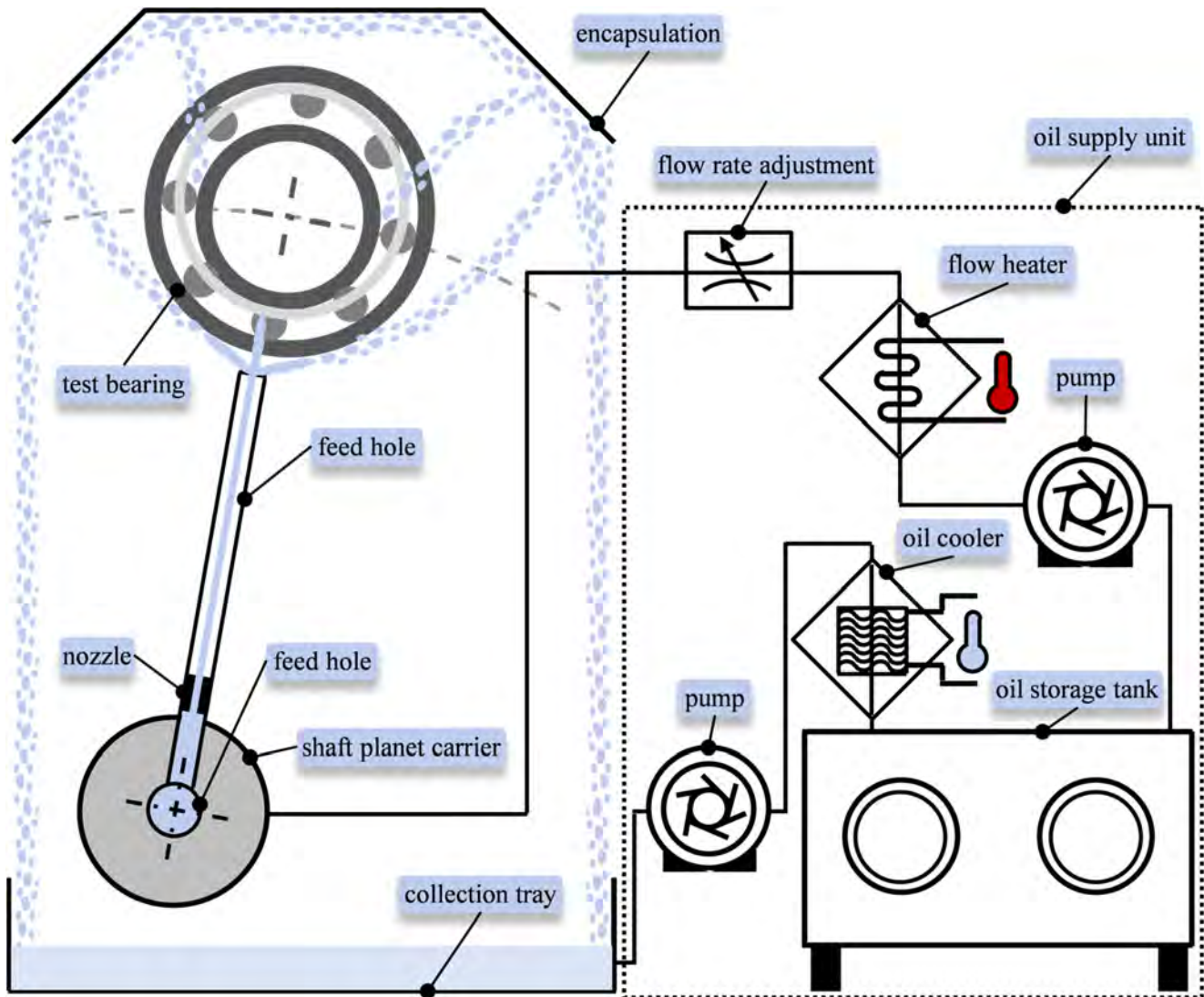The test bearings have an inner diameter of 35 mm, a total wide of 20 mm and an outer diameter of 42 mm, see figure 1-8.

The used test oil is Shell Spirax S2 ATF AX. It is a gear oil for automatic transmissions for application in passenger cars and commercial vehicles. At a temperature of 40 °C or 100 °C the oil has a kinematic viscosity of 34.6 mm²/s or 7.1 mm²/s.

With this test setup, an experimental plan is created in which the parameters centripetal acceleration, the rotational speed of the specimens and the oil flow rate are changing. The variation of the acceleration takes place in fixed steps within a range from 0-1 000 *g*.

The rotational speed of the specimen was also varied in fixed steps of 1 000 rpm, 2 000 rpm, 3 000 rpm and 4 000 rpm.

The oil flow rate was not changed at each acceleration step. It was only varied at the three acceleration steps 156 *g*; 400 *g* and 750 *g*. Since, it has to be carried out with acceptable effort. For these steps the oil flow rate is varied in such a range that the state of poor lubrication as well as overlubrication can be simulated. Therefore the oil flow rate is changed in a range of 0-1.0 l/min. The exact experimental plan can be seen in figure 1-9. The experimental plan shows that in a range of 700 *g* up to 1 000 *g* no tests were done with

a rotational speed of 1 000 rpm. The reason for this is a resonance frequency in this speed range. In order to protect the test rig this speed area is omitted.

Since it was unclear at the beginning of the investigation, which oil quantity is necessary for roller bearings exposed to high centripetal accelerations, for the majority of the tests an oil flow rate of 0.5 l/min was chosen. For usual conditions without external accelerations the applied amount of oil is very high. However, this procedure can ensure that the bearings are always lubricated sufficiently. To avoid negative effects of too high oil quantities, a gap was designed, so that the remaining oil can flow off without any problems.

The design of the testing program specifies that if the single test points are set, all the other parameters are kept constant until a steady state is reached [13]. The steady state is reached if the change in temperature is smaller than 1 °C. When this state is reached, the measurement is continued for further 60 s. For the evaluation only the steady state area is used [13].
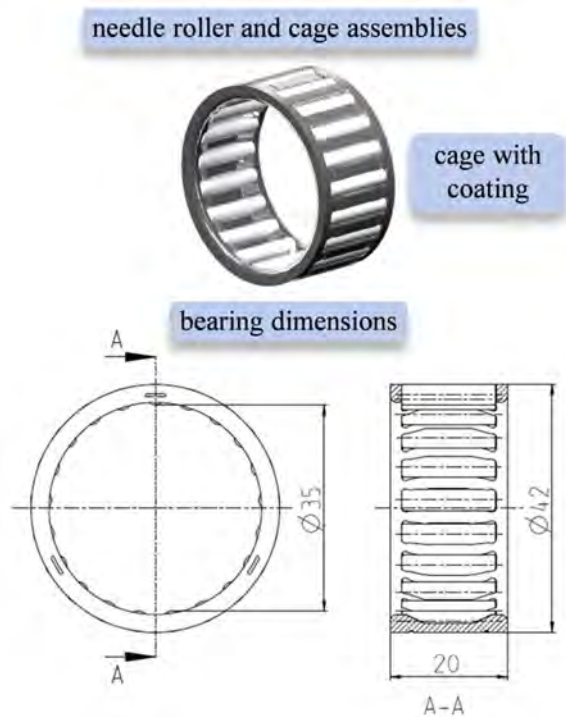
Figure 1-8: Test bearing.

Figure 1-9: Experimental plan.

3. Results and discussion

In a first step the change of the bearing temperature as a function of the rotational speed of the test bearings is examined. For this investigation the results at a centripetal acceleration of 200 *g* and 400 *g* are exemplary shown in figure 1-10.

With a constant oil supply temperature of 35 °C and a constant oil flow rate of 0.5 l/min a moderate increase of the bearing temperature was observed. With an increase in the rotational speed of 1000 rpm, the bearing temperature rises by 5 °C. This behavior can be analyzed in the load zone and shifted by 180° to the load zone, in the so called load-free zone.

This behavior of roller bearings is already known from [14] and therefore corresponds to the usual behavior of bearings, if the rotational speed increases. Essentially two aspects are responsible for this behavior. On the one hand, the rise of the frictional moment is the reason and on the other hand, the reduced oil throughput of the bearing is the origin [14].

From [14] it is known that the frictional moment rises with an increase of the rotational speed. The same results can be seen in the measured frictional moment of the realized tests. It is shown in figure 1-11. In general, the rise of the frictional moment with the rotational speed is moderate. This is shown by the results of figure 1-11. The rise of the bearing temperature as a result of a lower oil throughput with higher rotational speeds is certainly secondary to the influence of a higher frictional moment, but also contributes to the rise of the bearing temperature.
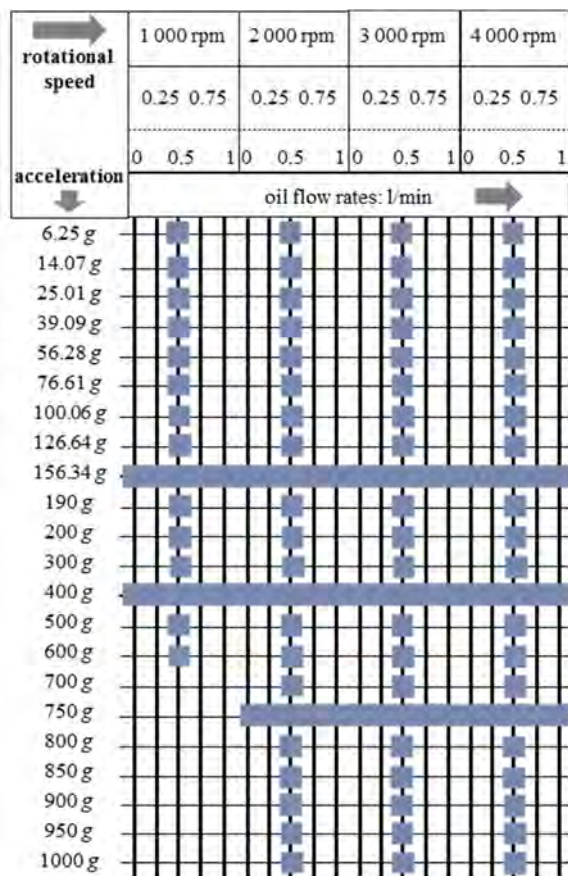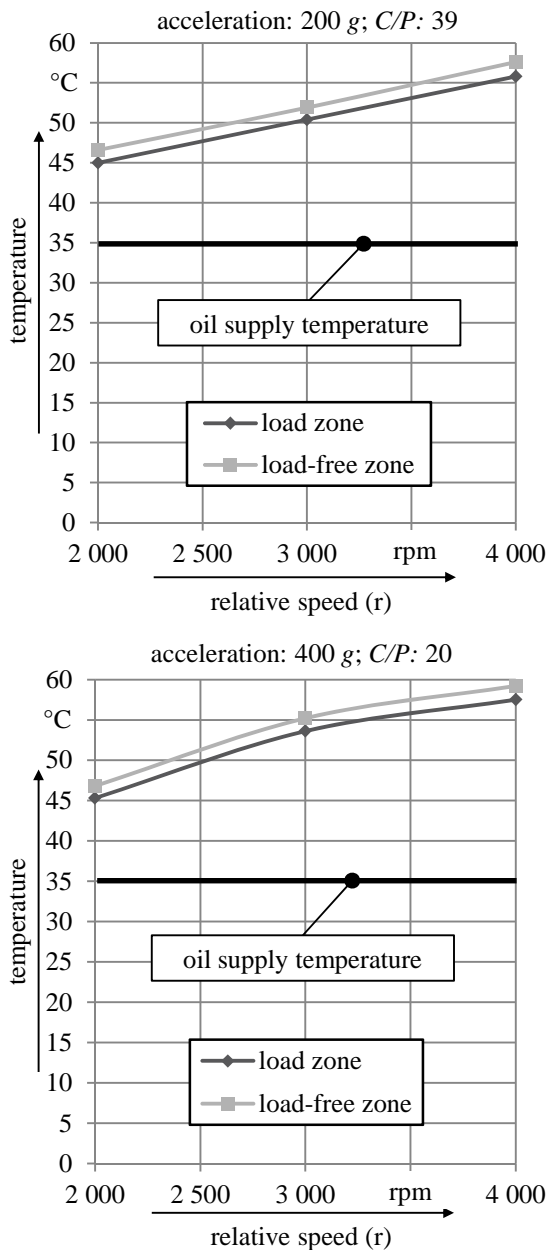
Figure 1-10: Bearing temperature as a function of the relative speed with an acceleration of 200 and 400 times gravity.

If a closer look is taken at the results of figure 1-10, it can already be seen that there is almost no increase of the temperature of the single test points, if you compare the results of constant rotational speeds at the acceleration steps of 200 g and 400 g.

In figure 1-12 you can find the results of the bearing temperature as a function of the acceleration with a rotational speed of 4000 rpm. Here the results of the whole acceleration range are shown. Again the oil supply temperature had a constant temperature of 35 °C and the oil flow rate had a constant value of 0.5 l/min. Even here no or at least only a moderate increase of the bearing temperature can be seen over the whole range.

Beside the acceleration stress, the rise of the centripetal acceleration also leads to an increase of the radial bearing load. The reason for this correlation is the bearing load, which is caused by the acceleration of the mass of the outer ring as already mentioned

above. The load factor reaches a value up to 8. A load factor of this value shows that the bearing load is in a normal to a high range.
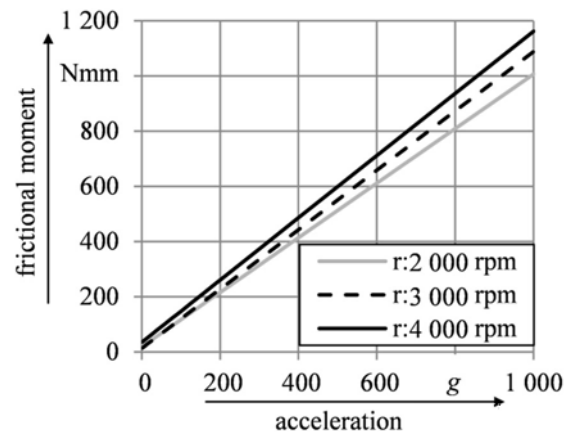

Figure 1-11: Bearing frictional moment as a function of the acceleration and the relative speed according to [1].

As all elements of the bearing, but especially the roller elements and the cage are considerably more stressed by the significant rise of the acceleration and the bearing load, also an enormous rise of the bearing temperature would be expected. The reason for this is in particular that the frictional moment substantially increases with an increasing acceleration and load, as shown in figure 1-11. The additional frictional energy generated has to be dissipated to the adjacent parts as heat and so should cause a significant rise of the bearing temperature. In particular, the missing rise of the bearing temperature is unusual, even if a moderate rise of the frictional moment depending on higher rotational speeds of the specimen leads to a clear rise of the bearing temperature.

In general, there is one question left. What effects can be the reason that the temperature remains constant? As figure 1-11 shows a clear rise of the frictional moment, a constant frictional moment and so the lack of an additional heat source cannot be a possibility. The only left cause can be a better cooling of the bearing.

A better cooling of the bearings can be achieved by higher heat dissipation to the adjacent parts or to the surrounding area. To improve the heat dissipation to the adjacent parts, these elements have to be changed. Possible variations are an improved heat transfer between the parts, because of magnified contact surfaces, materials with improved thermal conductivity or a bigger volume of the elements and so a greater thermal capacity. As the design of the test rig was always the same, this cannot be the reason.

Since the centripetal acceleration is generated by the rotation of the planet carrier, as shown in chapter 2, a higher acceleration generates a greater air flow speed of the surrounding air. The convection, forced by the surrounding air, consequently increases the possible transferable heat-flow. Due to this effect, a better cooling can be reached in principle.

However, with the design of the test rig, the air flow cannot reach the specimen, like it is shown in figure 1-13. As the outer ring of the test bearing is not mounted in the encapsulation (=housing), but can move freely, like already described in chapter 2, the bearing is isolated from the air flow. Therefore, this effect is also not the reason for a better cooling of the bearing.
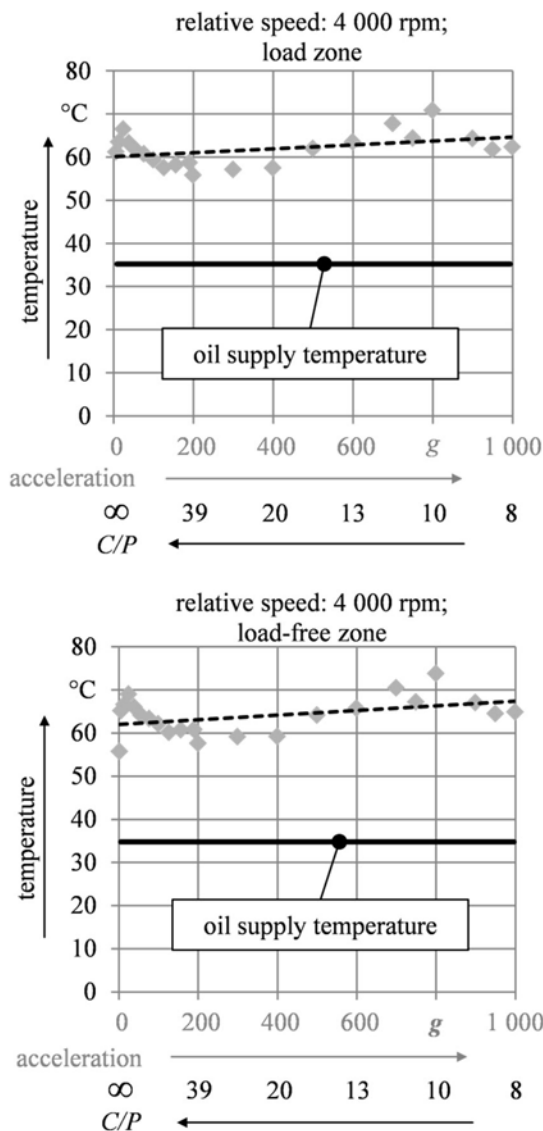
**relative speed: 4 000 rpm;
load zone**

**relative speed: 4 000 rpm;
load-free zone**

Figure 1-12: Bearing temperature as a function of the acceleration with a rotational speed of 4000 rpm according to [1].

A further possibility to improve the heat dissipation of the bearing is a better heat dissipation by the lubricant. Here, either a bigger oil flow rate can be provided or the temperature gradient can be increased by using a cooler oil supply temperature. But as already described above, both parameters remain constant over the entire acceleration range, so even these options cannot be the reasons for a missing rise of the temperature.

The situation described above proves to be disadvantageous. The behavior of the test bearing changes, although all setting parameters remain constant.

In figure 1-14 all relevant parameters are summarized in an overview picture of the test rig again. This figure shows that the rotational speed of the planet carrier is the only changing parameter in order to generate the different acceleration values. Furthermore, it can be seen that the oil flow rate is influenced by the acceleration field, too.
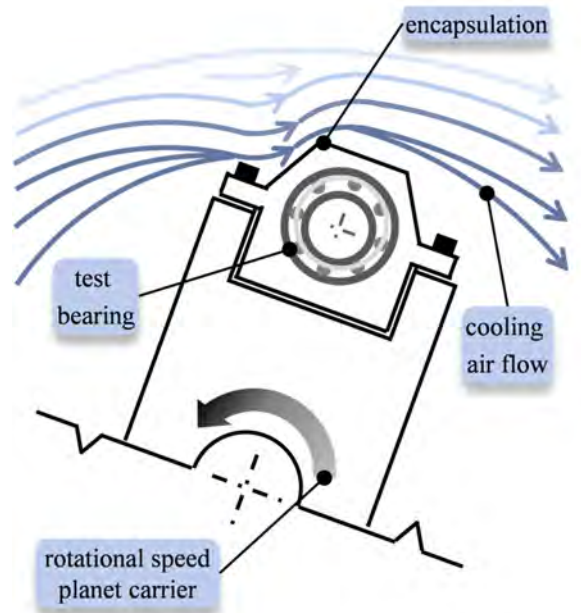

Figure 1-13: Encapsulation of the test bearing against the cooling air flow.

Directly after the nozzle an outlet velocity as a function of the nozzle diameter, the feed pressure and the oil flow rate is set. As the escaping oil jet flows into an acceleration field, the oil velocity does not remain constant, but is influenced by the acceleration field. In figure 1-15 the course of the oil jet is considered in detail. The acceleration influences each element of the oil jet and thus accelerates each lubricant element. It should be noted that the value of the acceleration field is changing, since the acceleration is a function of the distance between the center of rotation and the present position of the oil element.

The resulting jet velocity is a function of the acceleration and the acceleration distance and so even a function of the distance between the center of rotation and the present element position. This corresponds to the usual conditions of each accelerated motion, but since the acceleration is itself a function of the described distance, the rise of the velocity is enormous.

Due to this correlation the velocity of the lubricant directly before entering the test bearing – the so called injection speed – increases massively. With an acceleration of 1 000-times gravity in the center of the specimen the injection speed rises by 30 m/s. Under normal conditions without external accelerations, the recommended upper limit for the injection speed of injection lubrication is 30 m/s [14]. This comparison illustrates the enormous influence of the centripetal acceleration on the injection speed.

Furthermore, it is known that the oil throughput of a bearing increases with a rise of the injection speed [14]. Consequently it can be expected that the oil throughput of the test bearing increases with a rise of the acceleration. If the oil throughput of the bearing improves, even the cooling effect of the lubricant rises significantly. Finally, this has the consequence that the bearing temperature remains constant, although the frictional moment increases with a rise of the acceleration.
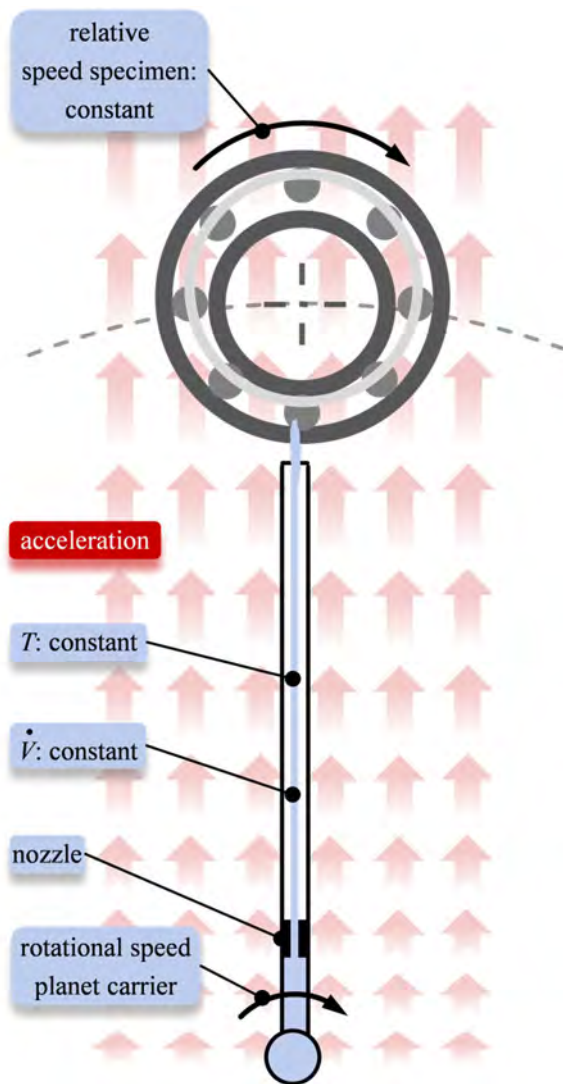
Figure 1-14: Design of the oil supply system and possible setting parameters.

But the oil throughput of the specimen can only be improved as the constant provided oil supply quantity by the oil supply unit represents an overflow. With low accelerations the unnecessary part of the oil quantity can exit without pressure directly in front of the specimen through a gap, like it is shown in figure 1-16. In front of the test bearing the constant total oil flow rate Q_1 is divided into the oil flow rates Q_2 and Q_3. Q_2 is the amount that enters the test bearing as lubricant and coolant. Q_3 is the amount that represents the oil overflow.

With usual oil injection lubrication the oil is injected between cage and inner ring. So also the front side of the roller elements or the roller elements itself are cooled from the side by the oil overflow. In the presented lubrication system this effect cannot occur, because the oil is directly injected into the raceway and not into the front side. This is the normal procedure with connecting rod bearings of combustion engines and planet bearings of planetary gears that represent a possible application for bearings exposed to centripetal accelerations [15, 16].
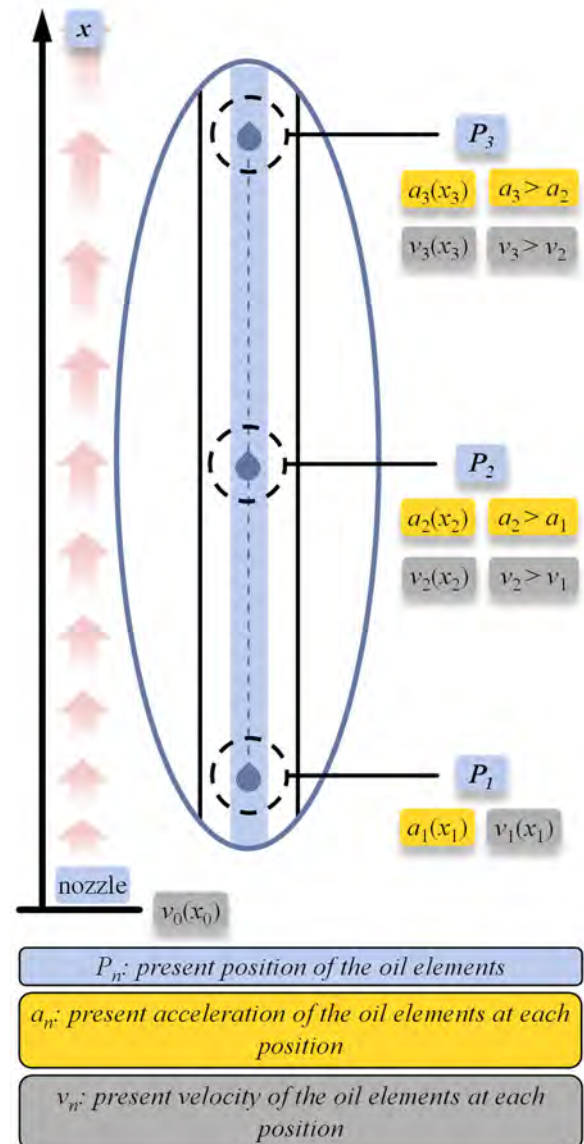
Figure 1-15: Velocity and acceleration profile of the oil flow.

Due to this special design of the lubrication system an increased oil throughput of the bearing has greater influence on the cooling effect and so on the bearing temperature. Therefore, a missing rise of the bearing temperature is a consequence of the design of the oil feeding system and so far plausible.

At this point it is still to be solved, why an oil quantity of 0.5 l/min was used. From the literature [14] we know reference points for appropriate oil flow rates depending on the bearing dimension, the relative speed and the lubricant method. But these reference points are all suitable for bearing lubrication under normal conditions without the influence of external accelerations. The reference values for oil injection lubrication are in general higher than for oil circulation lubrication with pressure-free inlet. The reference points for oil injection lubrication are valid for oil injection between cage and inner ring. As this is not true for the present system, the use of these limits is questionable. For this reason and since there are no literature values for oil injection lubrication for the present speed parameters, the upper limits for oil circulation lubrication were used. According to [14] the used test bearing has

a permitted upper limit of the oil quantity of 0.05 l/min. In order to be sure that enough lubricant is available, ten times the recommended quantity was used. This oil quantity is also greater than the limits for oil injection lubrication determined on the basis of extrapolated data.

Figure 1-16: Distribution of the oil flow rate before entering the test bearing.

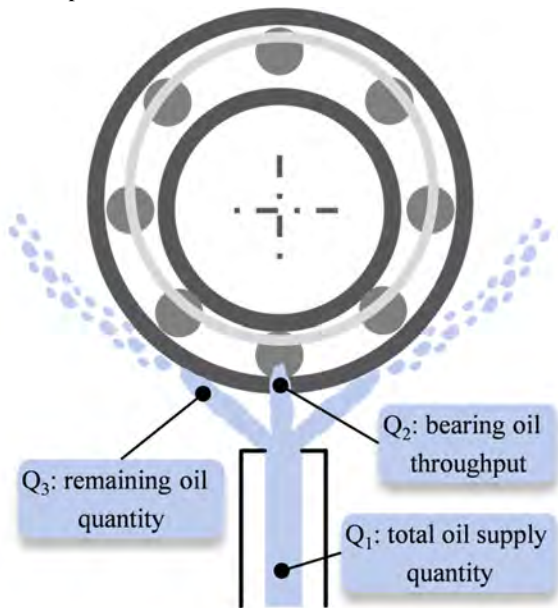This situation is not satisfactory, because for a trouble-free operation of the bearing system, the exact oil quantity to get a sufficient lubrication and cooling is necessary. Therefore, as in chapter 2 described, the supplied oil quantities were also varied. Since 0.5 l/min is a rather large oil quantity, the oil flow rates were mainly reduced for the further tests. To get a reference point for the maximal generated energy by the bearing, also tests without lubricant were carried out.

In order to analyze a thermal appropriate oil quantity, it is important to define selection criterions for a thermal appropriate state. A thermal appropriate state is reached, if a further rise of the oil flow rate does not lead to a further decrease of the bearing temperature. If the oil flow rate is great enough for the cooling of the bearing, also the lubrication of the bearing can be guaranteed, because the necessary oil quantity for lubricating the bearing is much smaller than for cooling. Therefore, a sufficient oil quantity is automatically reached, if the temperature remains constant.

In figure 1-17 and 1-18 the results of the changed oil flow rates are exemplarily shown. These are the results for an acceleration of 400 g with a relative speed of 3 000 rpm and 4 000 rpm. The qualitative course of the curves for a relative speed of 3 000 rpm and 4 000 rpm is the same.
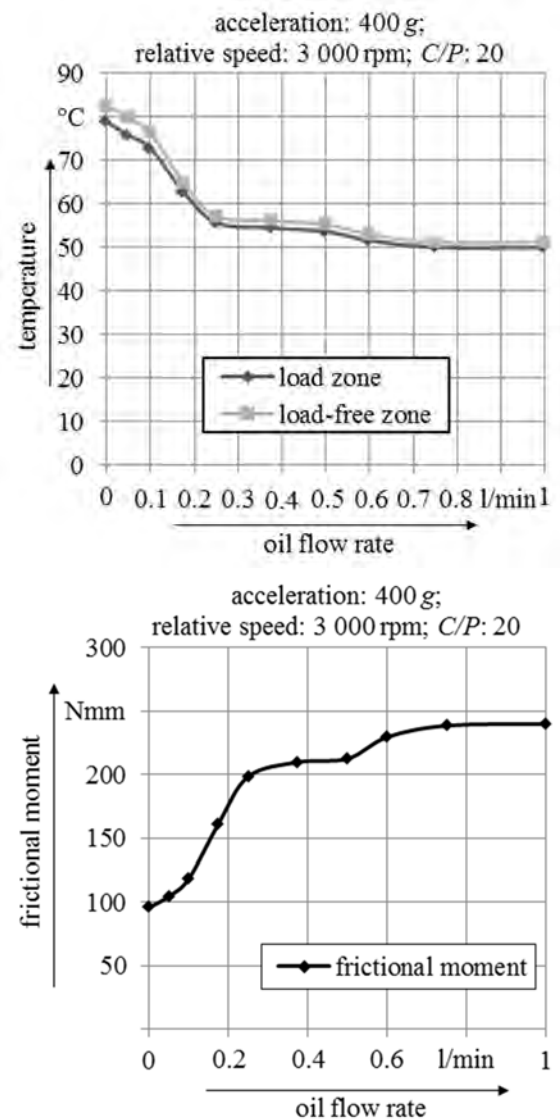
Figure 1-17: Bearing temperature and the frictional moment as a function of the oil flow rate.

In detail, it is still to be determined with which oil flow rate a constant temperature behavior is reached. Of course, not every application needs an absolute temperature consistency. An appropriate upper limit for the oil flow rate depends on the operating conditions and on the design of the adjacent parts.

If the bearing temperatures are within a range of about 70 °C a further increase of the oil flow rate and so a reduction of the bearing temperature by 10 °C can maybe not be useful. In this case, the limit for an appropriate oil flow rate is not so strict. If the bearing temperatures are within a range of 100 °C a further rise of the oil flow rate that leads to a reduction of the bearing temperature by 5 °C can be useful in order to guarantee a sufficient distance to the standard bearing application limit of 120 °C. Finally the determination of an appropriate oil flow rate will always be a compromise and therefore also dependent on the overall energy balance.

In figure 1-17 and 1-18 it can be seen that there are no major temperature differences for an oil flow rate of more than 0.5 l/min. Certainly this reference limit depends on the present parameter setting and will be still variable, but it can be used as a rough guide

for a practical, maximum oil flow rate with respect to the cooling effect. This value does not represent an absolute optimum concerning all parameters of the bearing system. For example, it is also known, that the frictional moment increases with a rise in the oil flow rate. Therefore, this value is only to be regarded as a useful guide value in relation to the minimum achievable temperature development. This rough guide particularly also shows that the appropriate upper limit for the oil flow rate of roller bearings exposed to centripetal accelerations is much higher than for roller bearings exposed to standard operating conditions.
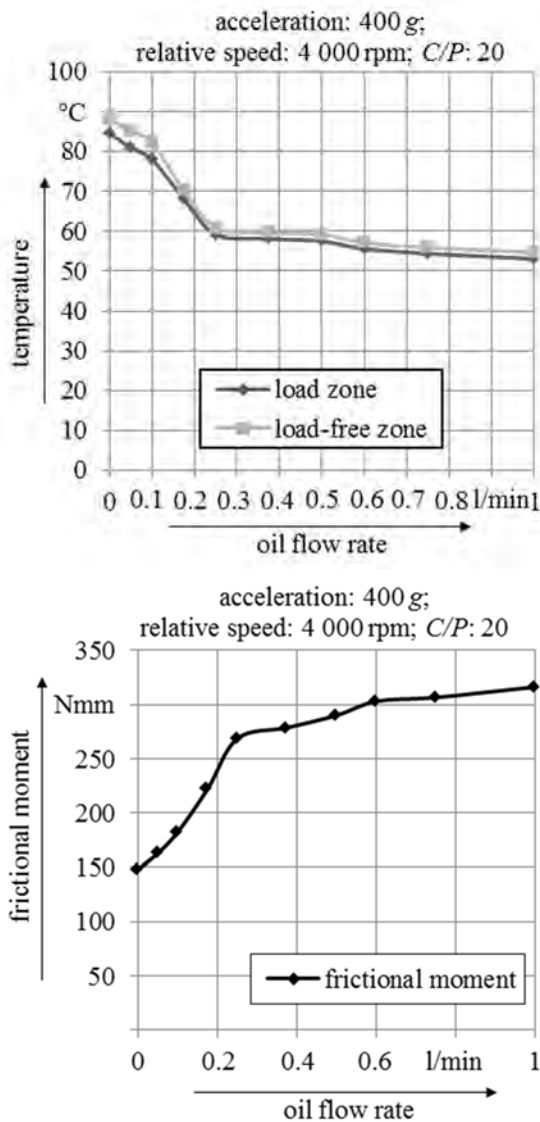

Figure 1-18: Bearing temperature and the frictional moment as a function of the oil flow rate.

4. Conclusions

Important conclusions for the application of roller bearings exposed to centripetal accelerations can be drawn from the studies on the bearing temperature under the influence of high external accelerations. The most important conclusion is the fact that the temperature behavior is controllable also under the influence of high accelerations. The temperature levels shown in figure 1-12, 1-17 and 1-18 are within a normal temperature range for roller bearings. Temperatures up to 120 °C are quite normal for standard bearings. But in this context, it is also important to consider that the present bearing temperatures could only be achieved for sufficient oil flow rates and for rather low oil supply temperatures. Furthermore, in this study the test bearings are not influenced by external heat sources. If the oil supply temperature has a greater value and external heat sources are present the temperature level can rise.

However, also this changed situation is no exclusion criterion, because the oil supply temperature can easily be reduced by technical devices and so the bearing temperature can cool down to the here shown temperature levels. However, for the application of bearings exposed to centripetal accelerations it is important to keep in mind such negative influences.

It has also been shown that, despite the high accelerations, a sufficient lubrication and cooling of the roller bearings is possible and that the lubrication oil can consequently fulfil its function.

However, with rising accelerations a greater oil flow rate is necessary. The flow rate is 10 times higher than in normal applications. Consequently applications under the influence of high external accelerations need a higher oil turnover. Therefore, the oil pumps need more energy and the entire oil quantity of the lubrication system rises. If the oil feeding system can be designed appropriately, the acceleration can cause a self-regulation effect of the oil throughput. The positive result of this effect is that the cooling effect rises with an increase of the acceleration and so the bearing temperature remains constant or nearly constant.

Therefore, the centripetal acceleration has no influence on the bearing temperature and is no setting parameter for the bearing temperature. A readjustment of the oil flow rate with a rise of the acceleration is not necessary and so the power of the pumps can remain constant. This behavior requires a sufficient distance between nozzle and injection point of the test bearing and the flow indication arrow of the oil flow rate has to point into the direction of the acceleration vector. A similar design of the lubrication system, which uses the centripetal acceleration to lead the oil to the lubrication points, can be found in the patents [17, 18]. The lubrication systems of these designs are not exactly the same as those of the test rig, but could be optimized in this direction.

The influence of the relative speed of the specimens is the same with bearings under normal conditions without centripetal accelerations. The temperature rises with an increase of the relative speed.

The variation of the oil flow rate showed a significant influence on the bearing temperature. The determination of an appropriate oil flow rate is a function of several parameters and can vary considerably depending on the present application. For the tested specimen an oil flow rate of at least 0.5 l/min is considered to be appropriate in order to reach a maximum cooling of the roller bearing. But of course on the other hand it has to be considered that there is almost a maximum of the frictional moment for this value, like shown in figure 1-17 and 1-18. That is one reason, that there is no further reduction in temperature like shown by the increase of the frictional moment. The additional friction energy is emitted in the form of heat, so there is no longer a further decrease in temperature if the value is exceeded.

Acknowledgments

References

[1] Hochrein, D.; Tremmel, S.; Wartzack, S: Temperature Behavior of Rolling Bearings Exposed to Centripetal Acceleration. In: FVA – Forschungsvereinigung Antriebstechnik e.V. (Hrsg.): Bearing World 2018. International Bearing Conference. 06.03. – 07.03.2018, Kaiserslautern. Frankfurt: FVA, 2018, pp. 15–18.

[2] Stahl, T.: Einfluss von Drehzahl- und Lastkollektiven auf die Entwicklung von Reibmoment und Temperatur in Wälzlagern. Ph.D. thesis, Universität Erlangen-Nürnberg, 2011.

[3] Cousseau, T. et al.: Experimental measuring procedure for the friction torque in rolling bearings. lubrication science Vol. 22 (2010), Issue 4, pp. 133-147.

[4] von Hollen, J.: Reibung von Kurbelwellen-Wälzlagern. PhD thesis, Universität Hannover, 2013.

[5] Kahraman, A.; Hilty, D. R.; Singh, A.: An experimental investigation of spin power losses of a planetary gear set. mechanism and machine theory Vol. 86 (2015), pp. 48-61.

[6] Dengler, K.: Temperaturverteilung in Rillenkugellagern und ihr Einfluss auf die Lagerluft. Ph.D. thesis, Technische Universität Carolo-Wilhelmina zu Braunschweig, 1970.

[7] Baalmann, K.: Ein Verfahren zur Bestimmung der stationären Betriebstemperatur von Wälzlagerungen. Ph.D. thesis, Universität Hannover, 1994.

[8] Rüblinger, W.: Optimierung feststoffgeschmierter, hochbelasteter Kugellager bei Temperaturen bis 300 °C. Ph.D. thesis, Technische Hochschule Darmstadt, 1984.

[9] Kleinlein; E. et al.: Einsatz von Wälzlagern bei extremen Betriebs- und Umgebungsbedingungen. Renningen-Malmsheim: Expert, 1998.

[10] Ruß, A., G. et al.: Wälzlagertechnik Teil 2. Berechnung von Lagerungen und Gehäusen in der Antriebstechnik. Ehningen bei Böblingen: expert-verlag, 1988.

[11] Seiler, K. et al. Dynamics simulation of rolling element bearings considering elastohydrodynamic cage contacts. In: FVA – Forschungsvereinigung Antriebstechnik e.V. (Hrsg.): Bearing World Journal. Volume 1_2016. Proceedings of the Bearing World Conference. 12.04. – 13.04.2016, Hanover. Frankfurt am Main: VDMA Verlag GmbH, 2016, pp. 75–85.

[12] Hochrein, D.; Graf-Goller, O.; Tremmel, S.; Wartzack, S.: Vorstellung einer neuen Prüfstandsgruppe zur Untersuchung des Fliehkrafteinflusses auf das Reibungsmoment von Wälzlagern. Tribol. Schmierungstech. Vol. 64 (2017) No. 5, pp. 47–54.

[13] Hochrein, D.; Tremmel, S.; Graf-Goller, O.; Wartzack, S.: Untersuchung des Reibungsverhaltens von Wälzlagern unter dem Einfluss von Zentripetalbeschleunigungen zur energieeffizienten Gestaltung von Lagerungen. In: VDI Wissensforum GmbH (Hrsg.): 12. VDI-Fachtagung Gleit- und Wälzlagerungen. Gestaltung, Berechnung, Einsatz. 27.06.– 28.06.2017, Schweinfurt. Düsseldorf: VDI Verlag GmbH, 2017, pp. 347-351.

[14] BRÄNDLEIN, J. et al.: Ball and Roller Bearings. Theory, Design an Application. 3. Edition. Chichester: Wiley, 1999.

[15] AFFENZELLER, J., GLÄSER, H.: Lagerung und Schmierung von Verbrennungsmotoren. In: LIST, H.; PISCHINGER, A. (Hrsg.): Die Verbrennungskraftmaschine. Band 8. Wien: Springer-Verlag, 1996.

[16] BUCHMILLER, V.: Wälzgelagerter Kurbeltrieb - Potenzial von Wälzlagern im Verbrennungsmotor. Ph.D. thesis, Technische Universität Kaiserslautern, 2013.

[17] BARNBECK, A.; SAHL, H.; THIEL, A.: Schmiermittelzuführung für ein Planetengetriebe. Patent, Europa, EP 1319871B1, 27.05.2009.

[18] BAUR, E.; KONRAD, H.; POHLENZ, J.: Planetengetriebe. Patent, Deutschland, DE 19945089A1, 22.03.2001.

Damage mechanisms in pivoting rolling bearings and their differentiation and simulation

Markus Grebe[1], Jürgen Molter[1], Fabian Schwack[2], Gerhard Poll[2,]

[1] Competence Centre for Tribology (CCT), Mannheim University of Applied Sciences,
m.grebe@hs-mannheim.de
[2] Institute of Machine Design and Tribology (IMKT), Leibniz Universitaet Hannover

Abstract – This paper presents the current state of research in the field of false brinelling and standstill marks on roller bearings. The main topic will be the differences between brinell marks (due to plastic deformation), false brinelling marks (due to small swivel movements) and standstill marks (due to vibrations, micro movements). Furthermore, a simulation model will be used to show the occurring slip and frictional work in the reciprocating contact spot.

From the authors' point of view, it is scientifically necessary to clearly differentiate these different load conditions from one another, since different sources of causes are responsible and different mechanisms act in the contact zone between raceway and roller.

This research work is becoming increasing relevant in connection with wind turbines due to the fact that the newest control technologies such as individual pitch control (IPC) lead to more critical parameters for the pitch bearings. However, the topic is also still relevant for the "classic" areas such as hydraulic applications, automotive components, construction machinery and numerous applications in special machinery.

In addition, the problem of machine transport with vibration excitation is still not solved. Especially the transport of cars or machines in new market areas (especially cold regions with poorer infrastructure) gives cause for concern.

1. Introduction

The first time false brinelling is mentioned was in the 1930s. It is reported that new automobiles that were transported by ship or train for delivery showed severe wheel bearing damage when they were unloaded. On further inspection, it turned out that many wheel bearings showed periodical marks in the raceways. The damage was probably traced to rocking of the cars by the vibrations of the large diesel engines on the ships or the regular impact every time a railroad car wheel passed a track joint. These conditions led to the first false brinelling research work of ALMEN at General Motors [1].

Although the auto-delivery problem seemed to be solved, there are many other examples. Generators or pumps may fail or need service, so it is common to have a nearby spare unit which is left off most of the time but brought in to service when needed. Surprisingly, vibration from the operating unit can cause bearing failure in the unit which is switched off. When that unit is turned on, the bearings may be noisy due to damage, and may fail completely within a few days or weeks even though the unit and its bearings are otherwise new.

As already mentioned in the abstract, the problem of car transportation also recurs, as new production sites and markets' infrastructure have last century conditions, and in some cases unfavourable climatic conditions prevail.

In addition to the field of wind power plants already mentioned [2, 3], we expect future problems in the area of hybrid and electric vehicles. In hybrid vehicles, as a result of the internal combustion engine or range extender, there is a high vibration load on the roller bearings of the electric motor. Additional problems are the dynamic driving vibrations due to the high speeds of these electro drives and therefore the high number of revolutions per minute, where standstill marks lead to a significantly reduced lifetime of those bearings.

One big problem is that the term "false brinelling" is not clearly defined and in science and literature covers a wide variety of damage symptoms, which are partly caused by different mechanisms [4]. Beside special damage due to electrical continuity, electrolytic corrosion and mechanical reasons such as scoring or plastic deformation, the wear symptoms in tests with micro oscillation differ significantly from the tests with relatively wide oscillation movements in the range of above two times the half contact width (in our test scenario > 1°), as in the normal laboratory testing methods such as the Fafnir or SNR-FEB2-test. Such macroscopic oscillation movement leads to typical "real" bearing processes and not to the micromovements which occur and are particularly problematic with seemingly motionless bearings (see Figure 3). This results in incorrect input in the development of improved materials and lubricants [4].

As long as lubrication in the contact zone can be ensured, oscillating motions can be calculated by ISO approaches by modifying the equivalent load rating or the equivalent load [5]. Depending on the amount of the pivoting angle, different approaches are available. HARRIS et al consider two different angles. The critical angle Θ_{crit} (Figure 1) is the angle of the inner raceway relative to the outer raceway when one rolling element touches but does not overlap the raceway portion of an adjacent rolling element. Furthermore, the dither angle Θ_{dith}.

Figure 2) represents the relative movement of inner and outer raceway that results in such a small motion of the rolling element that parts of its contact ellipse will always stay in contact [6].

While the definition of Θ_{crit} is only dependent on geometric parameters, Θ_{dith} is a function of the size of the Hertzian contact ellipse and therefore is dependent on the applied load. In Schwack et. al. the proposed equation Θ_{crit} was [7] applied to a wind turbine pitch bearing with a pitch diameter of 4650 mm, which is designed for a generic 7.5 MW wind turbine. For this bearing Θ_{crit} was 2.5°. The analysis of the pitch cycles showed that when pitch is active, 35.9% of the pitch amplitudes were smaller then Θ_{crit}.
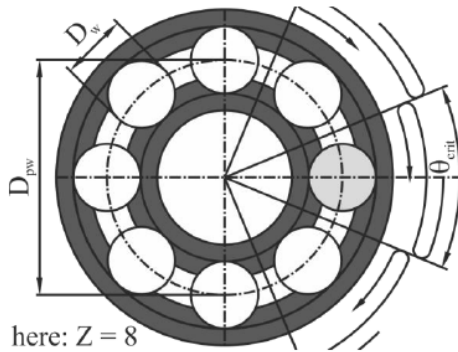

Figure 2: Definition of the critical dither angle [5]

Figure 3 shows the influence of different tilting angles on the rolling path for the typical test bearing type 51206 for SNR- and standstill tests.

Figure 1: Definition of the critical angle [5]
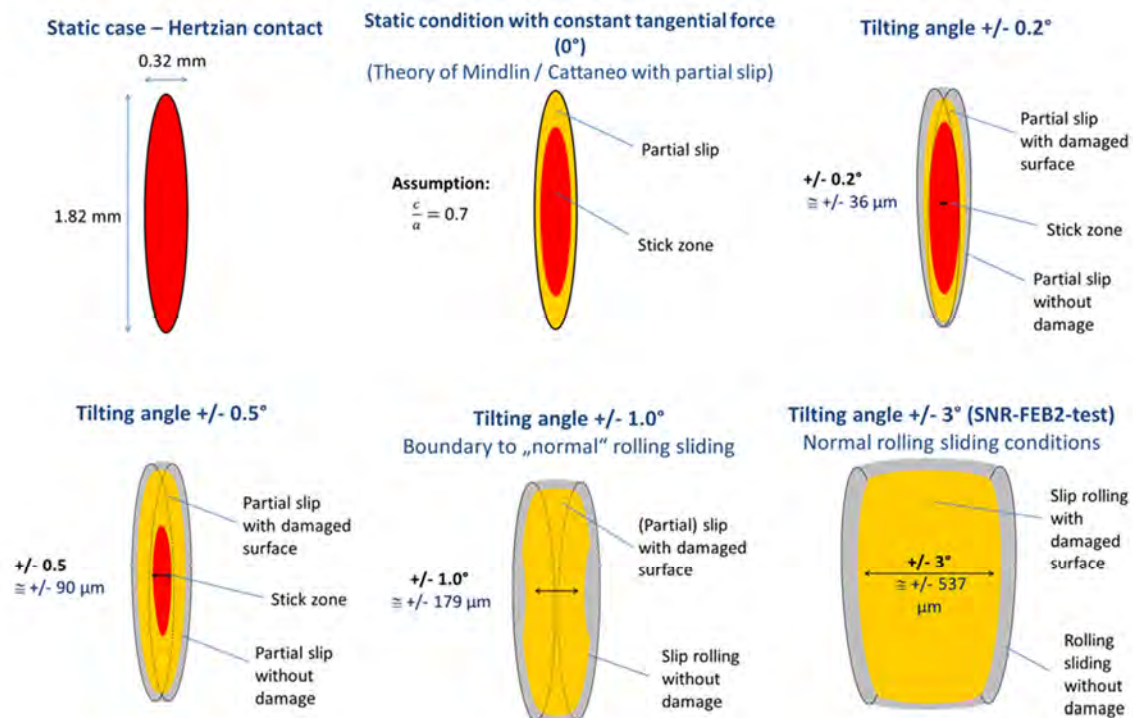
Figure 3: Sketch of the influence of the swivel angle on the contact zone; the specified numerical values apply to the standard conditions and the bearing type 51206; Parameters 750 N/ball; max. Hertzian contact pressure about 1.66 GPa

Grease is usually used in the referred applications. The greases are optimized for operating conditions that result in the dynamic stresses of highly loaded roller bearings. However what is needed for these optimal operating conditions is continuous rotating movements with an elasto-hydrodynamic lubricant film formation. They are often not suitable for preventing wear under pivotal

movement or micro movements caused by vibrations or very small pivoting angles. In practice there are several test methods for investigating false brinelling and standstill marks (e.g. ASTM D 4170 / Fafnir, SNR-FEB 2, HRE-IME vibration tester), but the results neither correlate with the individual test methods in general nor with the experience from practice. Often, these tests provide

different results when using the same lubricant. This is not surprising, however, if you take a closer look at the test conditions of the individual tests, for example, the bearing pivots +/- 6 degrees in the Fafnir test in the SNR test +/ 3 °. In the HRE-IME-riffle test, the bearing does not swing at all, but is exposed to a pulsating axial load. So it is not surprising that all test procedures test completely different lubricant properties, although they seem to have the same goal under the umbrella term "false brinelling test".

The Competence Centre for Tribology (CCT) at the University of Applied Sciences in Mannheim has one special false brinelling tester (Figure 4). The design is based on the SNR test rig but it has been improved at different points, for example to test original bearings under small angles. The test method and first results have already been presented at different tribology conferences, for example at the annual conference of the German association for Tribology [8]. With this test rig all the main influence parameters can be varied separately.
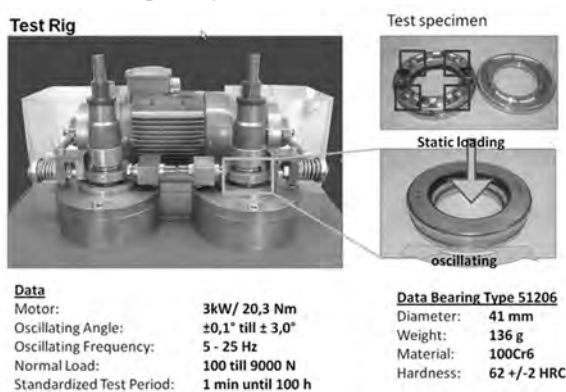

Data

Motor:	3kW/ 20,3 Nm
Oscillating Angle:	±0,1° till ± 3,0°
Oscillating Frequency:	5 - 25 Hz
Normal Load:	100 till 9000 N
Standardized Test Period:	1 min until 100 h

Data Bearing Type 51206

Diameter:	41 mm
Weight:	136 g
Material:	100Cr6
Hardness:	62 +/-2 HRC

Figure 4: Test rig at the CCT Mannheim

The standardized test parameters in Mannheim are an oscillating angle of +/- 0.5° and a load of 750 N/ball (C_0/P = 5.2) for the investigation of standstill conditions and the classical SNR-FEB2-parameters for larger tilting angles (+/- 3°, 25 Hz, 8000 N). These parameters are suitable to simulate real standstill effects and bearings under small tilting actions. These two tests are the basis of all comparative investigations.

In the contact between roller and raceway, base and counterbody approach each other due to the normal force. Additionally, tangential force is introduced through pivoting. When the pivoting is sufficiently large, it leads to macroscopic rolling, a type of movement caused by the overlapping of pure rolling and sliding, a difficult concept to comprehend. At small pivoting angle microscopic movement, a relatively complex process within the contact zone, takes place. Such movement can be partially compared to and explained by the effects of fretting. In this article, the three damage types:

- "true" brinelling,
- standstill marks and
- false brinelling

are described in detail. In addition, instructions are provided on how to reduce or avoid the respective damage.

2. Descriptions and definitions

2.1. *"True" Brinelling (plastic deformation, impacts)*

Brinelling is bearing damage due to mechanical overload or shock load during assembly or during operation. It is therefore not tribological damage. However, when the bearing is placed in service, the damaged area acts as a stress riser and the impacted areas will spall/flake prematurely.

The dents arise purely due to plastic deformation when the yield point of the material is exceeded. The typical marks have an ideal elliptical shape and show no oxidation. Often the dents show raised shoulders. In the marking you can usually still recognize the original surface structure (Figure 5). The grease is not changed or coloured around the contact areas Deformation marks arise due to errors in assembly and mechanical overload.
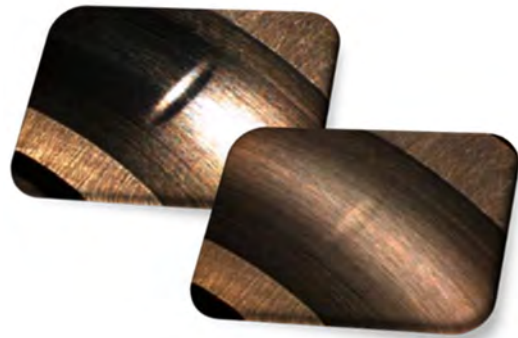

Figure 5: Plastic deformation (brinelling) in the raceway of an axial ball bearing (two different types of illumination)

If the load P is below the static load rating of the bearing (C_{stat}), such damage should not occur during normal operation. Thus, one of the most common ways that a bearing suffers true brinelling is from impacts during installation. The solution here is to ensure that all bearing fits are properly maintained. Mounting errors and higher shock loads should always be avoided.

2.2. *Standstill marks, fretting*

If a tangential force is added in addition to the static normal load due to elastic deformation or an initiated pivoting movement, micro-sliding movements occur in the contact zone between the rolling element and the raceway.

This effect was mathematically described independently by MINDLIN [9] and CATTANEO [10] in the middle of the last century. Considering two axially parallel cylinders under a constant normal force P with superimposed constant shear force Q (Q < μ*P), a static friction zone within the contact surface can be identified, whereas the edge slides partially. This is due to the fact that shear stress at the edge is indefinitely high and normal pressure tends to zero. Therefore the no-slip conditions close to the edges are not fulfilled which leads to partial sliding. With a gradual increase in shear force under constant normal force, the static friction zone decreases. Macroscopic sliding takes place once Q exceeds the product of μP (value of static friction). Reversing the applied load will result in less shear force but the derivation is not directly reversible. The same applies if the normal force increases or decreases. The influence of normal and tangential forces has been explicitly investigated in the paper of MINDLIN and DERESIEWICZ [11].

However, MINDLIN and CATTANEO investigated a purely linear tangential motion. In a rolling bearing, the movement is more complicated because the rolling elements go into a rolling motion at a sufficiently large pivoting angle.
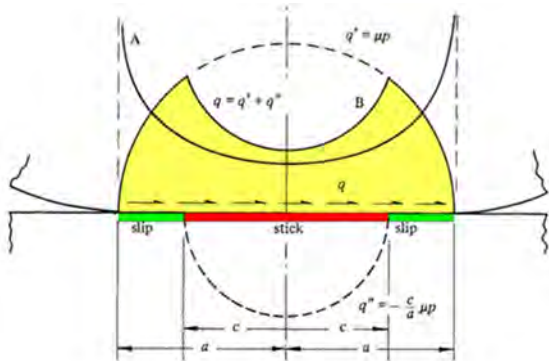

Figure 6: Stick and slip zones in contraformal point or line contact; sketch based on [9]

JOHNSON developed contact models for rolling contacts in a deep groove ball bearing on the basis of these considerations for purely translatory movements [12].

Elastic deformation in the contact zone can lead to micro-sliding too under the condition that both bodies have different elastic properties. Under this condition, free rolling forms stick and slip zones within the contact zone. In the case of standard rolling bearings, both the rolling elements and the raceway have elastic properties which are nearly the same, so this point does not have to be considered. However, this does not apply to hybrid bearings, which are ceramic rolling elements in steel raceways.

With both the base body and counter body having the same elastic properties, stick and slip zones will form when a ball under normal loading rolls freely (without acceleration or deceleration) along a running groove due to the conformability in one direction. Under these circumstances, the area of contact is elliptic. The points on the area of contact have different track radiuses and circumferential velocity, proving that partial micro-sliding exists. Only two lines in the contact area showed pure rolling with sticking (Figure 7).
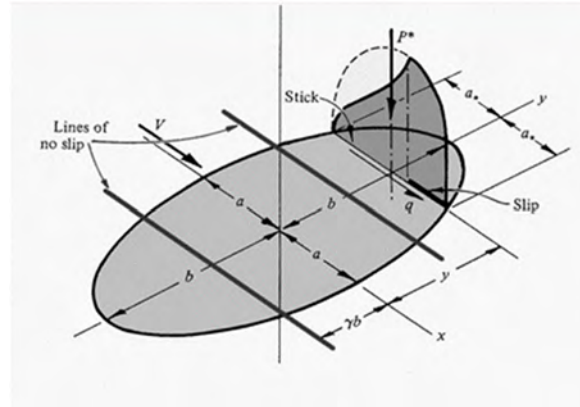

Figure 7: Stick/Slip zones in elliptical contact of a ball in a deep groove ball thrust bearing [12]

A lower coefficient of friction and/or a high conformability will lead to a larger sliding area.

These theoretical approaches can be found clearly in the contact zone of practical standstill experiments. The contact area can be divided into different zones, some of them optically discernible (Figure 8). Clearly visible are the undamaged adhesion zone in the centre of the marks (inner ellipse) and the damaged microglide or partial slip zone (between the inner and middle ellipse). This correlates with results under linear oscillated sliding (fretting test) of e.g. SUNG-HOON and SEOK-JU [13]. However, what also has to be considered is that the type of the movement is not the same because of the additional rolling part. At closer observation an outer zone, known as the influence zone can be discerned. The size of this outer ellipse correlates with the calculated Hertzian contact surface. In some cases this area shows a smoothing of the surface or colour changes that could indicate chemical reactions between the lubricant and the material. There is no relative movement in the centre of the elliptical mark (nonslip region or stick zone). Both, the base body and counter body adhere. On the edge, however, there are micro slip movements and local tension peaks which are caused by elastic deformation, bearing movements or shifting of the pressure centre, and these can cause extensive surface damage (Figure 9).
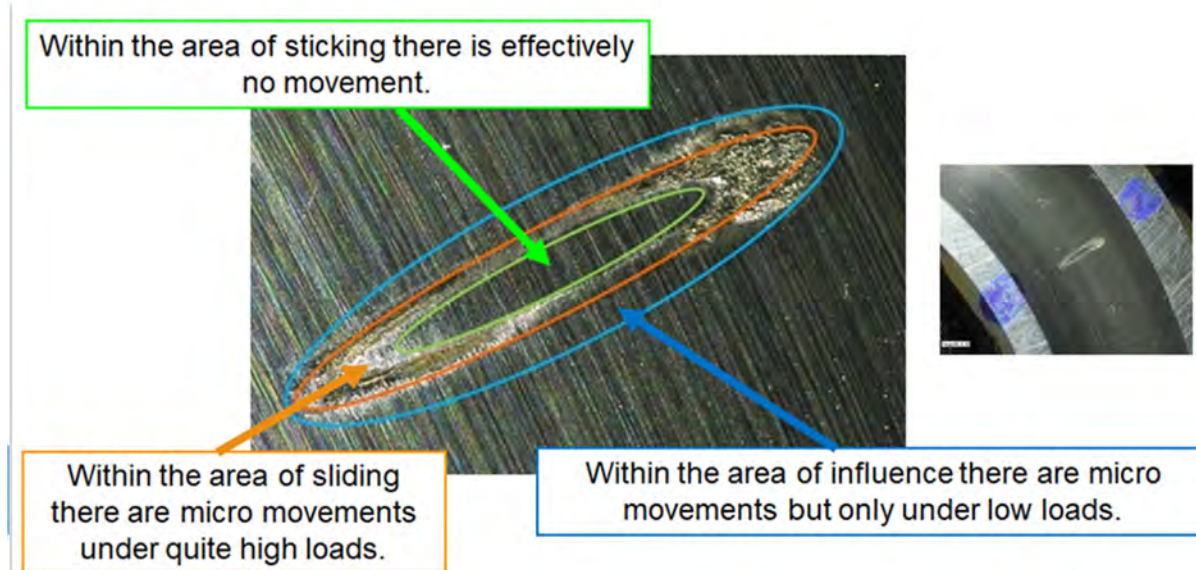
Figure 8: Different zones within the Hertzian contact area; Length 1.82 mm; width 0.32 mm; max contact pressure 1.66 GPa

The extreme damaging effect of small movements in false brinelling contact can be estimated by studying different contact models [12]. In the case of a constant surface load with superimposed constant tangential force at the beginning and end of the contact surface infinitely high stresses theoretically arise. These are released in practice by micro movements. At the boundary between sticking and sliding, cracking may occur due to the high local stresses, which is clearly shown by FIB images of standstill marking (Figure 10).
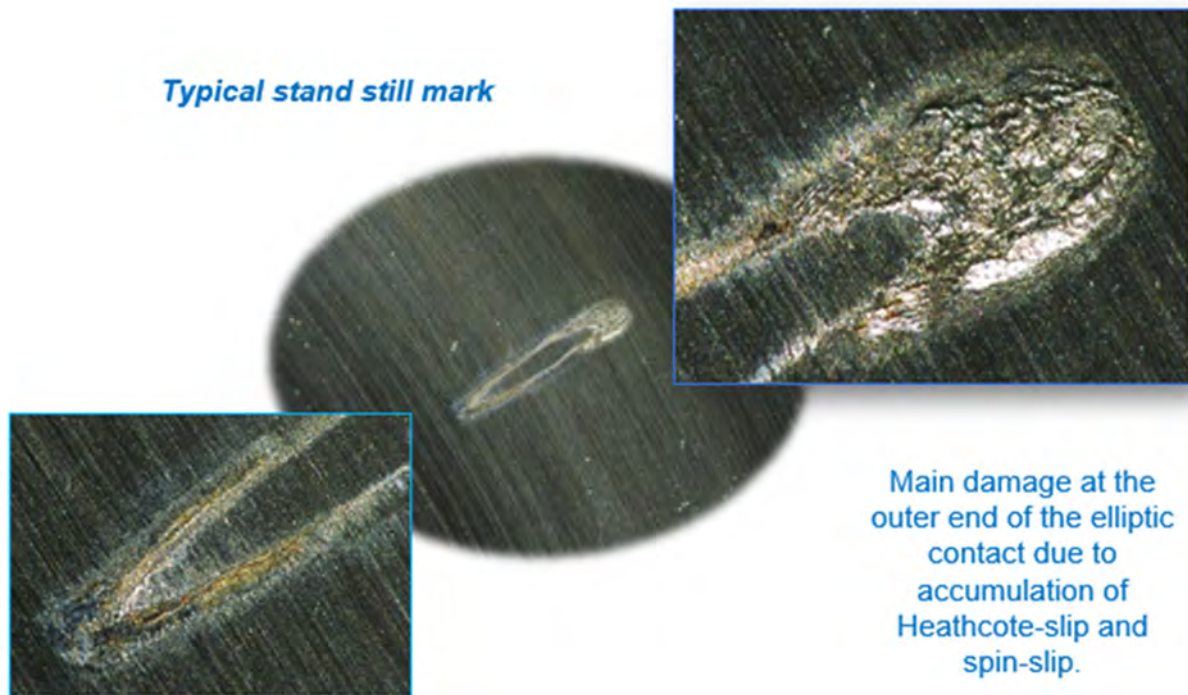
Figure 9: Typical standstill mark with low tribooxidation but severe disruption

Figure 10: FIB-Preparation of an outer glide zone. Left picture: FIB crater, right picture micro structure with a crack in detail [14]

2.3. *False brinelling*

Larger swivel angles which open the contact zone cyclically, lead to other damage and a different damage development. PHANER-GOUTORBE et al. investigated the surfaces of false brinelling marks with the help of a scanning tunnelling microscope (STM) and documented the changes [15]. Current research at the Competence Centre shows similar damage developments and mechanisms [16].
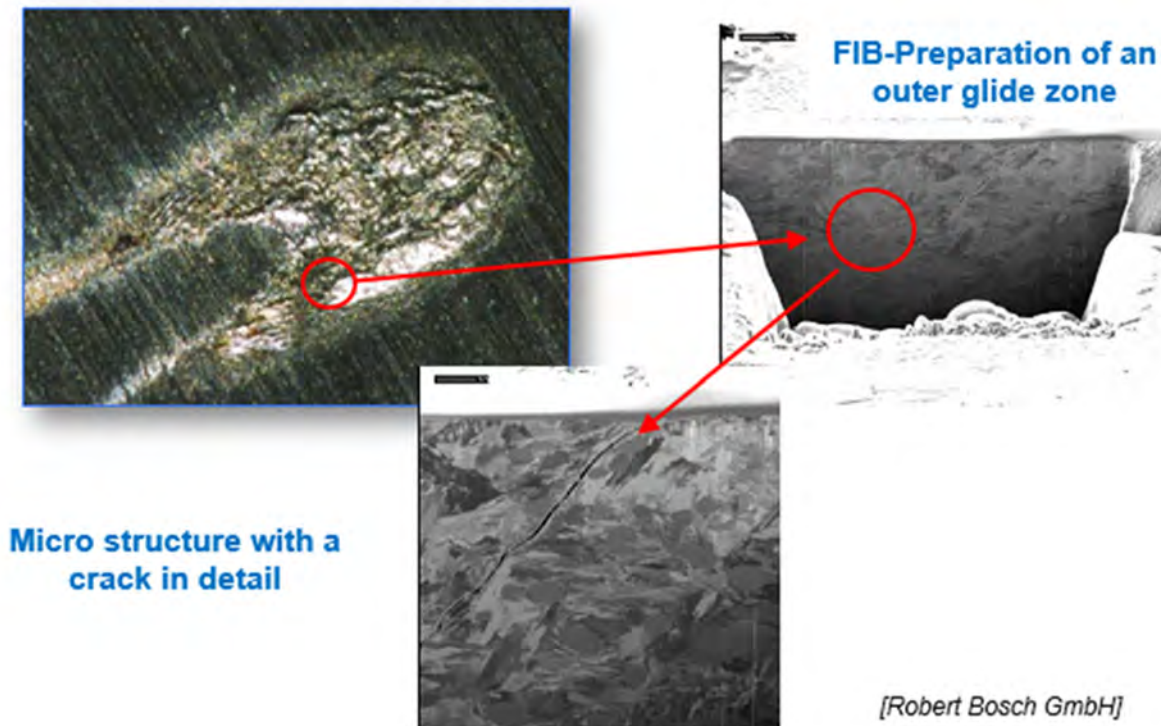
The images shown in figure 11 and figure 12 are each individual experiments. The experiments were not continued again. This would lead to strong distortions.

Looking more closely at the markers in the SEM, complex damage mechanisms can also be seen within the contact area (Figure 12).

The pictures show that at the beginning of the damage there is a plating-on of partially oxidized wear particles. This layer formation decreases with time and is only occasionally recognizable after 30 minutes. Instead, the typical wear recess is formed. In this trough massive multidirectional material shifts occur. On the edge of the mark you can see plastically deformed material due to local pressure increases caused by the wear particles resulting in tensions that are above the yield point of the material.
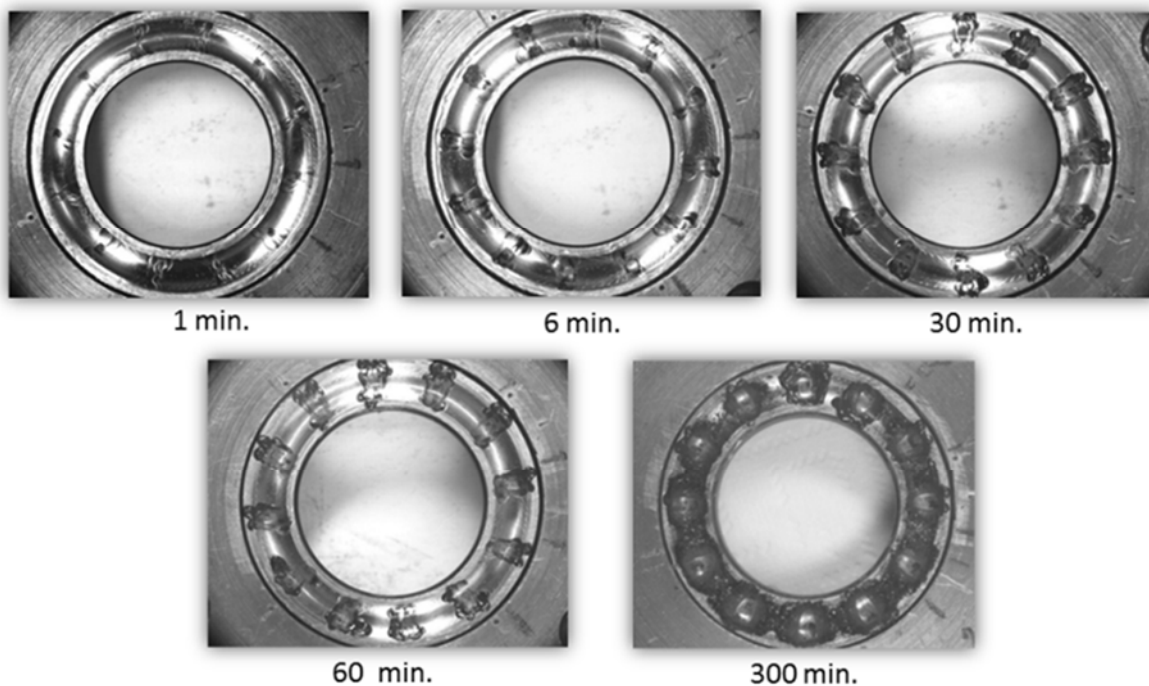

Figure 11: Development of typical false brinelling damage over cycle number (24 cycles per second). Clearly visible is the colouration of the grease by generated wear particles, the thickening and the failure after 300 min
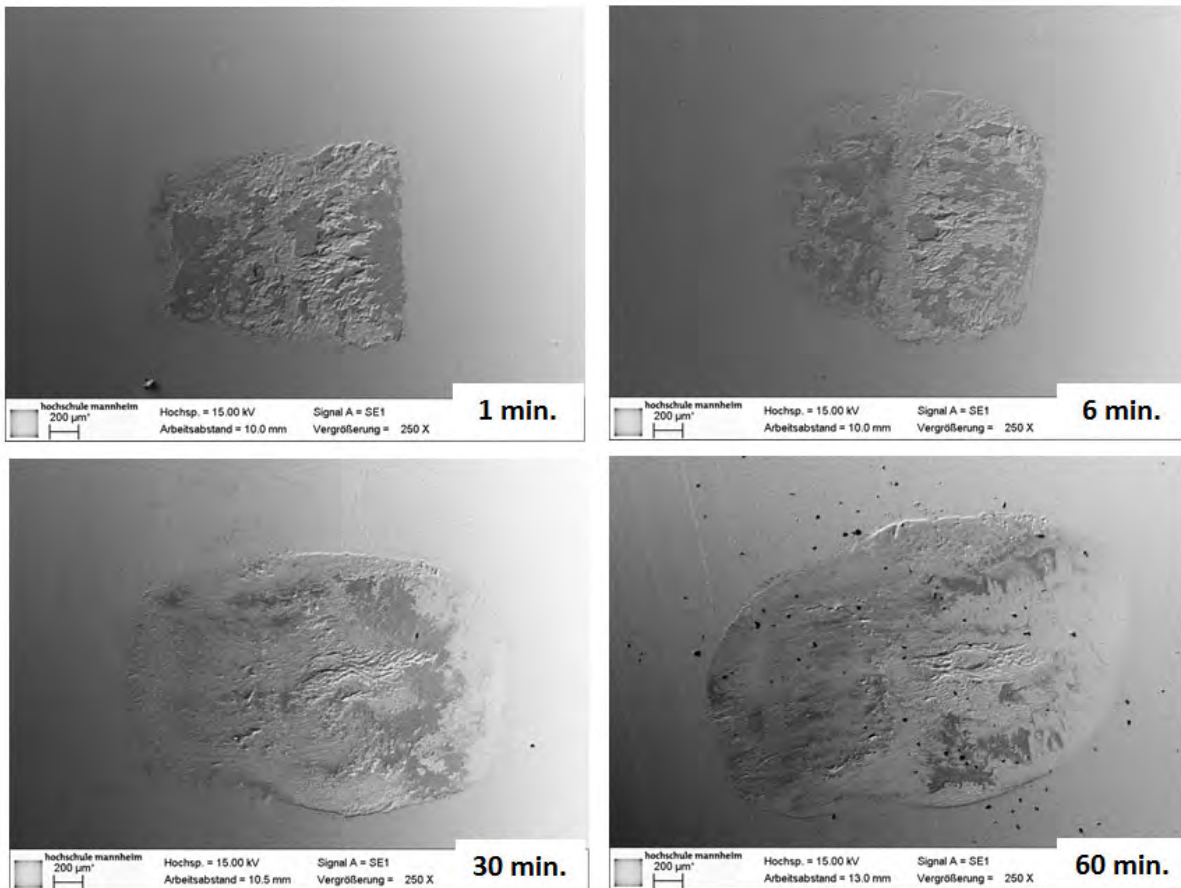
Figure 12: SEM pictures of the wear mark of a typical SNR-run with a poor grease (magnification 250x); travelling path of the ball under these conditions about +/- 0.5 mm

3. Influence factors

3.1. *Lubricants*

For the theoretical consideration of the possible damaging effect of certain operating states, various factors must be taken into account. One of these is the lubricant used, which has a significant impact on the individual wear mechanisms. For example, there are lubricants that are prone to severe tribo-oxidation or others that are more likely to show adhesive damage.

The following pictures show the influence of the base oil on the signs of wear within the standstill marks. All tests were conducted with standard test parameters for standstill conditions.

Materials 100Cr6, raceway grinded, balls polished, hardened 60 – 62 HRC, normal load 750 N per ball means a max. Hertzian contact pressure of 1.66 GPa, a contact area of 1.82 mm by 0.32 mm and a traveling path of the ball of approx. +/- 90 µm. For oils, it must be assumed that the contact points are always supplied with sufficient lubricant so the risk of starvation is significantly reduced. These tests took 6 hours and were a bit longer than typical grease tests (1.3 h).

Depending on the lubricating effect of the oil used, it leads to higher lubricity and thus less damage due to disruption. The ester shows clear advantages over the PFPE. Mineral oils showed quite good results with little advantages for paraffinic-based oils. The results of PAO were poorer than that of mineral oils [16].

Figure 13 Representative standstill mark after a 6-hour test with mineral oil (ISO VG 32)

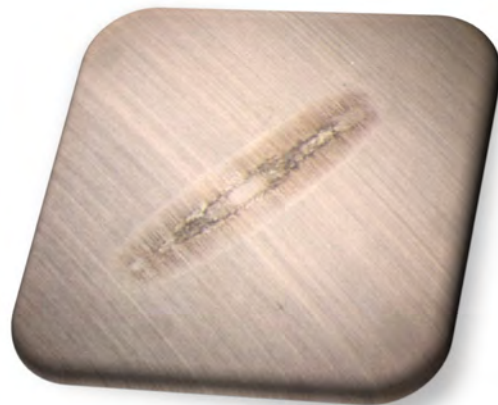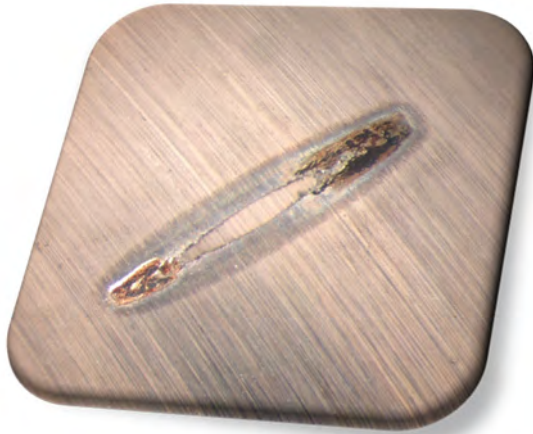*Figure 14 Representative standstill mark after a 6-hour test with PFPE oil*

Figure 15 Representative standstill mark after a 6-hour test with a TMP ester oil

These tests show once again that the viscosity does not have much influence at these small pivoting angles. In the SNR test with a swivel angle of +/- 3 ° and thus the cyclic opening of the contact point, oils never showed any damage after the standard test period of 50 hours.

Generally, there are very few scientific results published by the lubricant companies. An interesting work comes from the company Lubrizol, which in 2010 conducted a study on lubricant developments for false-brinelling conditions, The laboratory tests were carried out on the Fafnir test rig according to ASTM D 4170 (pivoting angle +/- 6 °; 2450 N, 30 Hz, 22 hr, room temp.). A history of the analysed 478 tests shows the distribution of the results:

• 36 grease samples had very good results (<1 mg);

• 62 samples ranged from 1 to 2 mg.

• Mass losses above 2 mg below 5 mg still reached by 113 greases.

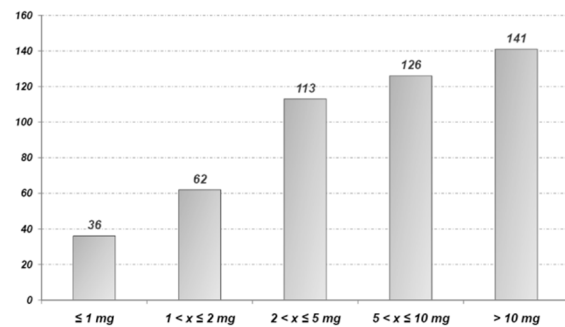• 141 samples showed extreme wear of over 10 mg.

Figure 16 Overview Fafnir-test results acc. ASTM D 4170 at the company LUBRIZOL [17]

This shows that lubricant developers are quite successful in developing greases for these conditions. The company KLÜBER reports in [18] on their efforts to develop lubricants that help against standstill damage and false-brinelling damage. These investigations also confirm the significant influence of the swivel angle on the resulting damage and the effective wear mechanisms. KUHN shows that under standard SNR-FEB2 conditions (+/- 3 °) the base oil viscosity has a significant influence on the damage. For oils below 180 mm² / s the oil flow behaviour and thus the additive transport are much better than with higher viscous base oils. The same applies roughly to the NLGI class.

In tests carried out by KLÜBER, a grease of NLGI grade 2 shows massive wear, which decreases markedly in the case of a class 1 grease and, with suitable additives, can be reduced to almost zero. This approach shows no effect at low angle and low frequency standstill conditions. This, too, correlates with the results obtained at the CCT Mannheim. KLÜBER can prove that a suitable additive (in combination with solid lubricants) and the use of special pretreatment fluids work well at larger tilt angles. In addition to the improved oil flow behaviour what probably also helps is the greater energy input to activate the additive chemistry.

3.2. *Ball material, coatings and raceway roughness*

For hybrid bearings you have to consider the modulus of elasticity of the ceramic rolling elements. At higher modulus of elasticity (e.g. silicon nitride $>Si_3N_4$ with an E-modulus of 320 MPa), the maximum pressure increases significantly and the contact area becomes smaller. Thus, the ratio of the rolling path to the contact width changes. The slip distribution in the contact zone also changes. There are also certain advantages due to the lower adhesion tendency of the steel / ceramic pairing. For the same modulus of elasticity (e.g., ZrO_2 with an E-modulus of 205 MPa), the positive effect on the somewhat lower adhesion tendency is reduced. Damage to the steel tread due to tribocorrosion is virtually eliminated.
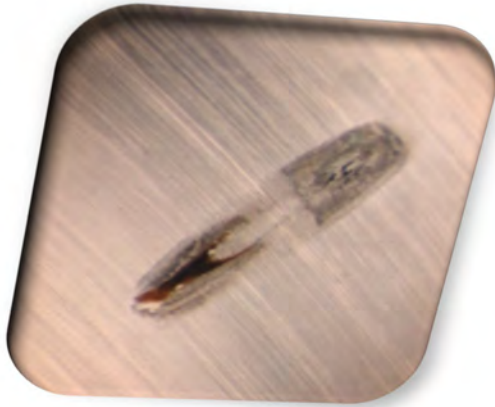
Figure 17 Representative standstill mark after a 1.3 hours test (24 Hz, 750 N/ball) with a wheel bearing grease and Si_3N_4-balls.

Random tests were conducted to examine the effect of different coatings. Carbon nitride coatings could not withstand the applied load under standstill conditions. A DLC coating however showed excellent results, and this feature certainly has a large potential for development. The drawbacks are the high cost and the fact that the coatings have to be sufficiently wear-resistant in normal operation. Black oxides raceways were tested in the SNR-FEB2 test with several greases and showed little improvement compared to standard bearings.

The effect of the raceway roughness could just be tested with hand-prepared bearings. In tests under standstill conditions, rougher raceways showed advantages which could be explained by the better lubrication conditions. The deeper roughness valleys can store the lubricants better and can provide more lubricant where necessary. The higher local compression at the roughness peaks may also have a positive effect on partial sliding. Under SNR-FEB2 conditions we found no influence of the raceway roughness.

3.3. *Temperature*

Temperature has a major influence on the flow behaviour of the lubricants used. Since the flow behaviour is more critical at larger pivoting angles due to the windscreen wiper effect, the influence of temperature at these kinematic conditions is also significantly higher. This is also shown in all the test series at the CCT Mannheim. In almost all tests the damage increases with decreasing temperature. We know of no grease that at -10 ° C in the SNR test does not fail after a maximum of 5 hours (instead of the 50 h).

3.4. *Kinematics and slip within the contact zone*

In a first project phase at the CCT, all the main values of the load collective were varied separately. This revealed that normal force is only of secondary importance. Damage increases with increased normal force, but not as much as may be expected. The effect of oscillation frequency is also less marked than expected. The damage increase observed when the frequency increases may also partly originate from higher mass changing forces. These frequencies are normally not high frequencies, such as those occurring with electromagnetic stimulation. This is a field that we have not been able to examine as the test bench only allows a maximum frequency of 25 Hz.

From a mechanical point of view, contact pressure plays a major role. However, the two decisive variables in our view are the pivoting angle and the slip distribution in the contact. The slip within the contact surface consists of three individual components: macroscopic slippage due to inertial forces during acceleration processes (roller slip / cage slip), which prevent ideal rolling; the spin slip as a result of the radial extent of the contact zone and a portion of differential slip (micro-slip or Heathcote-slip) due to the elastic deformation and the formation of the real contact surface.
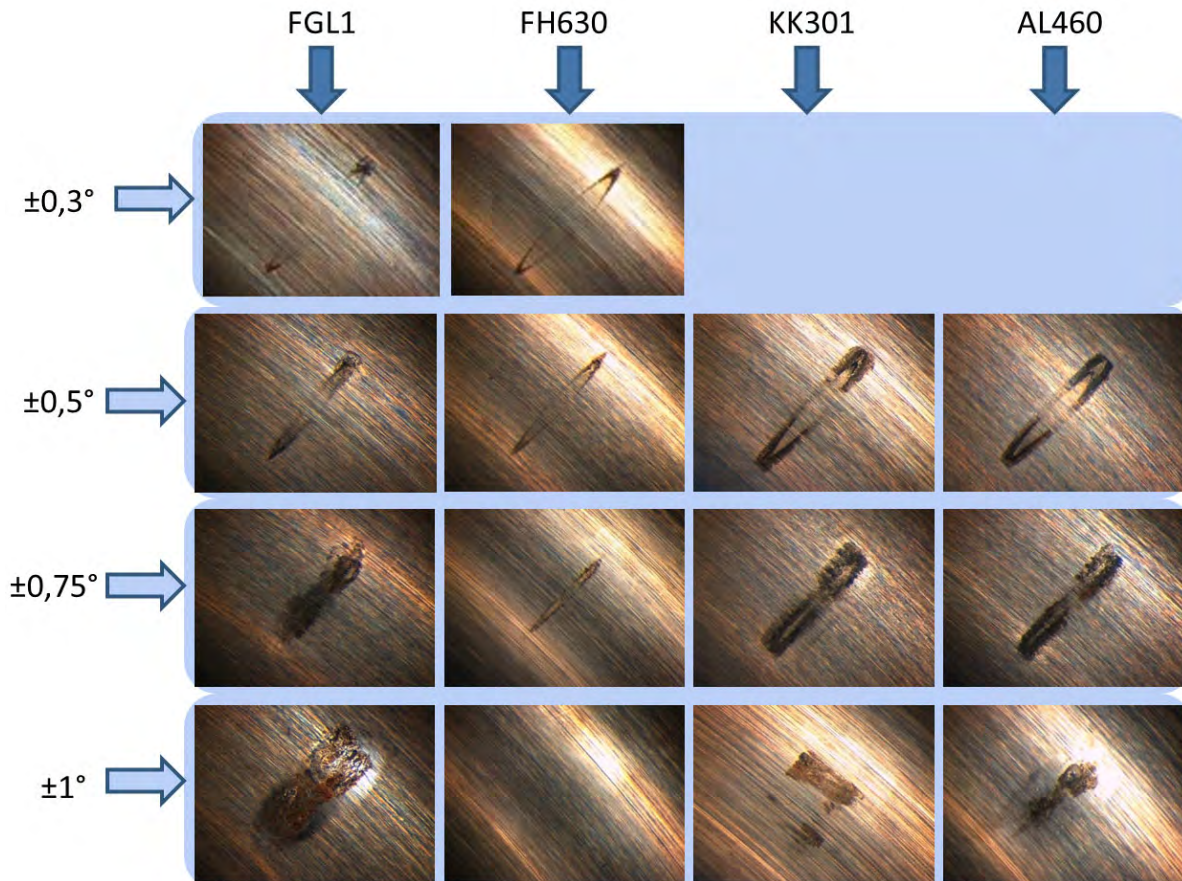
Figure 18: Comparison of the influence of the pivoting angle with different greases after 117 000 load cycles and a normal load of 750 per ball. For a description of the greases see table 1

Table 1: Data and description of the used reference greases

Label	Thickener	Base oil	Additives	Base oil viscosity @ 40° [mm²/s]	Base oil viscosity @ 100° [mm²/s]	NLGL class	Opertaing Temperature [°C]	Typical application
FH630	Li-12-Hydroxistearat	Mineral oil naphth.	EP, Corr.; AO	24	4	1	-40 / 80	High speed journal and roller bearings; locks
FGL1	Lithium complex grease	Mineral Oil naphth.	no inform.	64	9	1	-40/120	Roller bearings; linear guides
AL460	Lithium/Calcium-soap	Mineral oil	EP	460	28	2	no inform.	Highly loaded roller bearings (construction, mining, wind turbines)
KK301	Lithium soap	PAO	no inform.	300	23	1	-30 /120	Highly loaded roller beraings with low speeds; vibrational loaded bearings;

,

3.5. *Simulation of false brinelling*

Information about slip, pressure and frictional work in the contact zone can help to understand the occurrence of wear in reciprocating contacts. The Institute of Machine Design and Tribology developed a finite-element simulation model to predict the contact behaviour in oscillating ball bearings [19].

A schematic representation of the model can be seen in Figure 19 for an angular contact ball bearing. The model simulates a ball between the two segments of bearing rings in motion. The inner ring segment is fixed at all degrees of freedom while the motion and load act on the outer segment. The rolling element between the two segments is guided by contact forces, which in turn are governed by contact geometry and kinematics. The coefficient of friction needs to be estimated for the model. In literature, several estimations and measurements for the coefficient of friction under different operating parameters and with different lubricants can be found [20, 21, 22]. Similar models can be found, for example in Ref. [23].

When predicting slip in the contact, special attention is paid to the meshing in the contact zone. The relative displacements between the nodes are calculated. The contact pressure is calculated as well.

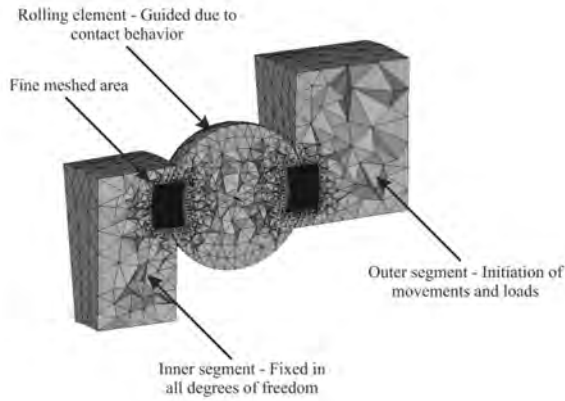The model is designed completely parametrically, thus allowing the analysis of several bearing geometries.

Figure 19: Schematic representation of the simulation model for a ball bearing

The calculated sliding displacements between the nodes can be used to determine the frictional work density w_d for each element through the multiplication of the sliding displacement u, the coefficient of friction μ and the contact pressure p:

$$w_d = u \cdot \mu \cdot p$$

The frictional work determines the work which is transferred into the near surface due to friction forces and slip and is therefore an indicator to estimate wear in oscillating applications by comparison with experimental results. Primarily the shape and distribution of the frictional work density are compared with the shape of the damaged area. Furthermore, the maximum values of the frictional work density can help to understand the wear rate in contact. A detailed review of the frictional work can be found in Ref. [19] [24].

Figure 20 shows the simulative results for the operating conditions for the experiments shown in Figure 18.

While the bearing geometry had equal properties for all simulations and experiments, the pivoting angles were varied. The simulative results in Figure 20 show the maximum value of frictional work density for each pivoting angle. All simulative results were achieved with and estimated coefficient of friction of 0.15 and 0.30.

As expected, an increasing amplitude as well as an increasing CoF leads to higher values of the maximum frictional work density. The typical shape of the damage can be found in the simulation as well. Due to the superposition of spin and Heathcote-slip, the damage is most pronounced in the upper half, since spin and Heathcote-slip have the same direction. This behaviour can be found in the simulations as well as in the experiments.

After the starting points of the pivoting only a minute amount of frictional work is dissipated. Subsequently, the frictional work steadily increases while additional elastic deformations build up.

To a certain amplitude, the displacement is mainly accommodated by tangential elastic deformations, leading to a linear increase of the specific frictional work density. Beyond this amplitude, sliding sets in and the tangential force and thereby the frictional work density stays constant. For the given operating parameters, this phenomena starts to occur between pivoting angles of $\pm 0.5°$ to $\pm 0.75°$, depending on the CoF. The conditions at this point are similar to conditions during continuous rotation.

The CoF is highly affected by the lubricant and the operating parameters. Furthermore, the number of cycles affect the CoF since lubricant may be squeezed out of the contact so that the lubricant cannot separate the surfaces from each other any further [25]. Therefore, best comparisons between simulative and experimental results are achieved for dry contact conditions and few cycles. For lubricated contacts, the results fit well when accurate information on the CoF is known. Nevertheless, the archived simulative results show good agreement with the experimental results shown in Figure 18. The shape as well as the position of the maximal frictional work density fit with the shape of the damage and the position of the maximal wear rate. The closer the experimental conditions lead to dry contact behaviour, the more the comparison agree with the simulative results.
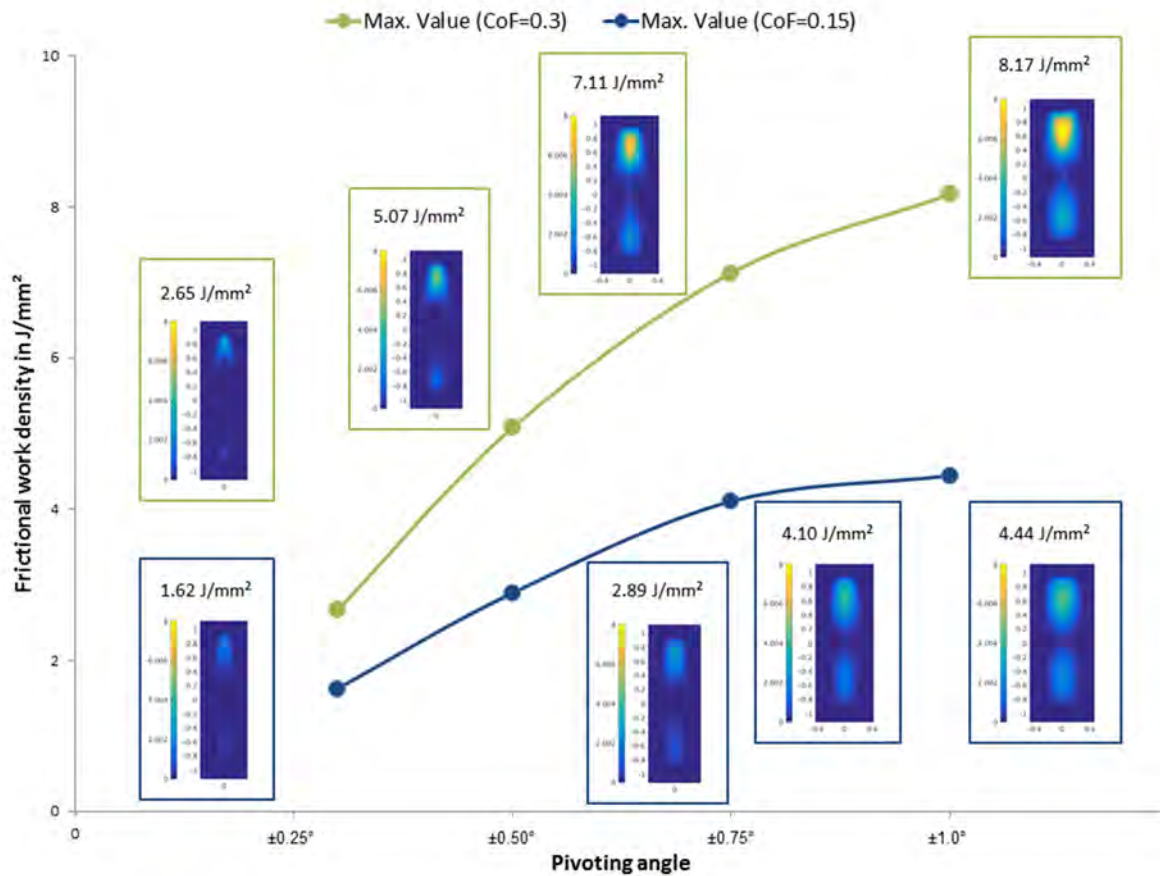
Figure 20: Frictional work density for different pivoting angles

Figure 21 shows a comparison between experiments at the Institute of Machine Design and Tribology and a simulative result. For the experiment an angular contact ball (7208) was used. The number of cycles in the experiment was set to 100, 1000 and 10000. For the experiment, grease lubrication was used and the simulative CoF was 0.3. The simulative results show good agreement for 1000 cycles, when wear begins to develop. For increasing numbers of cycles, the shape as well as the maximum of frictional work concur with the shape and the wear rate of the damaged area. Progressing wear rate makes the comparison harder.
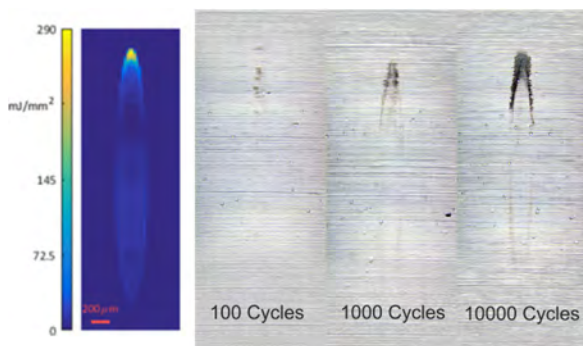
Figure 21: Comparison of experimental and simulative results for an angular contact ball bearings for 0.1° and 600 N rolling element load.

The slip is one main cause for the formation of wear. A detailed study of the relative slip in contact was conducted for a pivoting angle of $\pm 0.5°$ and $\pm 1.0°$ with a CoF of 0.3. The bearing geometry of the experiments in Figure 18 was used.

The results of this analysis are shown in Figure 23. Each contact in the figure represents a characteristic point during the oscillation. The first contact represents the slip right after the oscillation. The oscillation progresses until right before the reversal point. The arrows in the figure show the direction of slip.
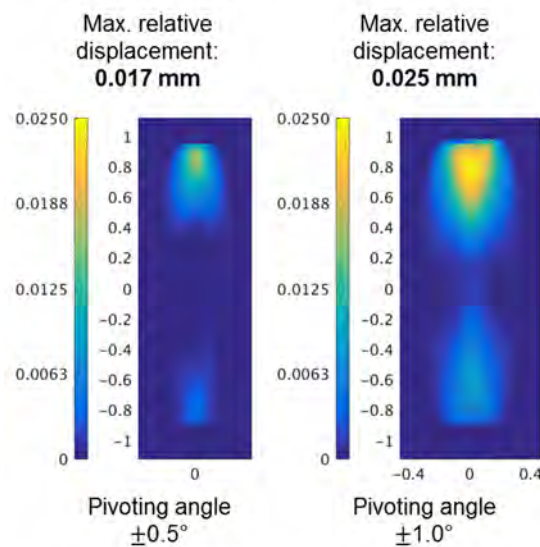
Figure 22: Maximum relative displacement while pivoting

The images show clearly the already described superposition of spin and Heathcote-slip.

The dominance of the spin-slip becomes visible from the variation of slip directions. The areas without relative movement can be recognized as well, since no arrows are shown in these areas. For a pivoting angle of $\pm 1.0°$, the effect of elastic deformations is visible

when comparing the last two images. It can be seen that the area without relative slip is nearly identically.

Figure 23: Value of slip for ±0.5 (top) and ±1.0 pivoting angle (bottom)

Furthermore the direction of maximum slip in the annulus area of the contact zone is perpendicular to the longitudinal axis of the contact area. The value of slip shortly before the reversal point is shown for both pivoting angles in Figure 22.

4. General information

In the following, we would like to mention two other points that would be important to compare the results of global research better. It is no longer necessary to mention, hopefully, that in the presentation of te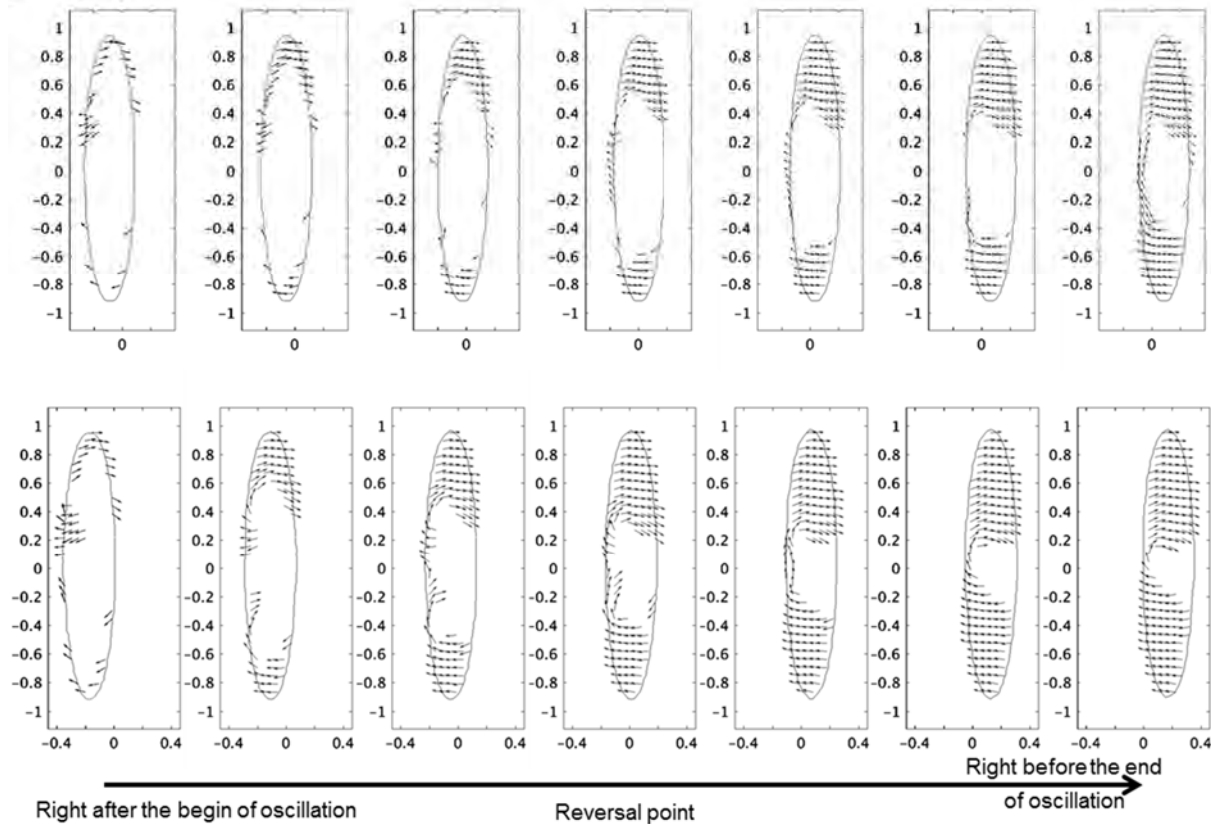st results, all sizes of the load collective and the description of the elements of the tribosystem must always be given. Without these full details, the results are not scientifically assessable.

4.1. *Referenced pivoting angle*

Due to the fact that bearing diameters in different application vary strongly, the swivel angle should always be converted to a rolling path for reasons of comparability. This path must then be related to the contact surface width. HARRIS et. al designate this critical angle as a "critical dither angle". Similar to HARRIS, we suggest calculating the ratio of the Hertzian contact width to the rolling path.

The relationship between the path travelled by the rolling elements (l) and the width of the contact zone (2·b) is the appropriate criterion.

For values above 1, the contact zone is revealed.

In our standard test with the bearing 51206 and a swivel angle of +/- 0.5° calculation results in a value of 0.56.

Experiments have shown that this is a particularly critical area.

4.2. *Objective value for the damage classification*

So far, the objective description of the damage in standstill markings is still a big problem. Since the markings look very different depending on the boundary conditions and the lubricant, an objective evaluation is difficult. A good approach could be to consider the change of the S_a value. If one compares the value determined within the mark with the original value for the undamaged trace, one obtains a characteristic value which, thanks to the averaging, does not react too sensitively to individual points, but is nevertheless sufficiently sensitive.

5. Possible Solutions

In the following, solution approaches for the three damage mechanisms brinelling, false brinelling and standstill marks are summarized (true brinelling only in the graphical overview in figure 24).

5.1. *False Brinelling:*

The damage progress is mainly influenced by the flow characteristics of the oil or grease. This explains the advantage of oils compared to greases and the bigger problems at low temperatures

- Greases with a low NLGI-class, low base oil viscosity and high oil separation have best results.
- Classical EP- and AW- additives and solid lubricants show a positive effect.

(See results of the company Klüber Lubrication presented at the VDI-congress "Roller bearings" 2015 in Schweinfurt [17] or

results of several industrial projects at the Competence Centre for Tribology).

5.2. *Standstill Marks:*

- The flow characteristic of the grease plays nearly no role.
- EP or AW-additives show no effect. Corrosion additives seem to have a certain effect.
- Different base oils show completely different results. Fluids with a good lubricity and low friction such as ester oils reduce the stresses [16].
- Until now, there is no grease that is able to protect surfaces completely from damage. However, it can have a big influence on the development of the damage.
  Best results were achieved with greases based on mineral oil and thickened by Lithium soap [16].
- Hard coatings seem to be a suitable but expensive solution.

.

Figure 24: Overview and suitable solutions

6. Conclusions

False brinelling and standstill marks are created by the interaction of different mechanisms in the contact zone:

- The lubricant is literally pushed out of the friction area by micromovement and high local pressure. This leads to a lack of lubricant and the typical wear mechanisms of abrasion and adhesion.

- The micromovement activates the surface energy (in particular the microcontacts on the surface asperities). This leads to tribo-chemical reactions down to a depth of several nanometres. Protecting layers on the surface are removed.

- Microcracks not detectable on superficial inspection are caused by load changing on the surface. When exposed to further load, these cracks result in more extensive and deeper particle break-off.

The three damage mechanisms described above cause the production of wear particles and reaction products which are not pushed out of the contact area due to a lack of "real" relative movement and thus have a strong abrasive effect. This phenomenon correlates with the formation of fretting corrosion (tribo-chemical corrosion) and normally leads to damage progression and deep indentations which cover the traces of the original damage mechanism. In further damage progression and bearing rotation there are additional wear mechanisms (in particular abrasion and surface disruption), which overlap and add to the covering of the real cause of damage. Depending on the predominance of one or several of the mechanisms described above, there are different types of standstill marks.

The predominance of one mechanism depends on the load conditions – and within these mainly on the oscillation angle. Another damage factor with strong influence is the lubricant used.

Due to their better flow properties, oils are in general more effective than greases in preventing damage due to lack of lubrication. Oils may also be more suitable when it comes to preventing tribo-chemical corrosion, as oils achieve more reliable surface wetting and thus prevent the formation of dry friction oxides (Fe_2O_3), which, due to their abrasiveness, lead to quickly progressing damages. However, most typical roller bearing applications need greases as lubricants.

It is absolutely necessary to differentiate different damage phenomena in dependence of the boundary conditions in order to make the right decisions for the solution of the problem.

References

[1] J. O. Almen (1937) Lubricants and False Brinelling of Ball and Roller Bearings; *Mechanical Engineering*, 59(**6**), 415-422.

[2] F. Schwack, G. Poll (2016) Service Life of Blade Bearings. Problems Faced in Service Life Estimation of Blade Bearings. *Windtech International 2016*, November/December, 19–22.

[3] M. Stammler, G. Poll (2014) Schadensmechanismen in Rotorblattlagern, GfT-Reibung, Schmierung und Verschleiss, Göttingen, 2014.

[4] M. Grebe (2014) New investigations and approaches to explain standstill marks on roller bearings (False Brinelling); Slovak Technical University (STU); Synopsis Dissertation-Exam.

[5] Th. Münzing, H.G. Binz (2014) Challenges of the sizing of ballscrews for their use in the primary flight control system of a helicopter, 58th Ilmenau Scientific Colloquium; Technische Universität Ilmenau, 08 – 12 September 2014.

[6] T. Harris; J.H. Rumbarger; C.P. Butterfield; Wind Turbine Design Guideline DG03 (2009) Yaw and Pitch Rolling Bearing Life; *Technical report NREL/TP 500-42362*, National Renewable Energy Laboratory, Golden (Colorado, U. S.).

[7] F. Schwack, M. Stammler, G. Poll, A. Reuter (2016) Comparison of life calculations for oscillating bearings considering individual pitch control in wind turbines, *Journal of Physics: Conference Series,* 753 (**11**),112013.

[8] M. Grebe; P. Feinle: Brinelling, False-Brinelling, "false" False-Brinelling; Tribologie-Fachtagung 2006: "Reibung, Schmierung und Verschleiß" in Göttingen; Tagungsband II, ISBN Nr. 3-00-003404-8, GfT, Moers, 2006, Band II S. 49-1-49-1.

[9] R. D. Mindlin (1949) Compliance of Elastic Bodies in Contact, *Journal of Applied Mechanics*, September 1949; No. **16**, S. 259 - 268; ASME New York; ISSN 0021-8936.

[10] C. Cattaneo (1938) Sul contatto di due corpi elastici, *Rendiconti dell´Accademica nazionale die Lincei*, 27; 474-478.

[11] R. D. Mindlin; H. Deresiewicz (1953) Elastic Spheres in Contact Under Varying Oblique Forces
Journal of Applied Mechanics, 20(1953), 327 -344.

[12] K. L. Johnson (2003) Contact Mechanics Cambridge University Press, 9th Edition; 2003; ISBN 0 521 34796 3.

[13] Y. Sung-Hoon; Y. Seok-Ju (2007) Friction and Wear Characteristics Due to Stick-Slip under Fretting Conditions, *Tribology Transactions*, 50(**4**), 564 – 572.

[14] CCT Internal report (2006) FIB/XB investigations at raceways after false brinelling test; Bosch department CR/ARA; Hr. Steeb, Nr. 2006-0476; 15.5.2006.

[15] M. Phaner-Goutorbe; C. Barthou; L. Porte; B. Vannes (1997) Scanning tunneling microscopy study of wear induced by false brinelling on rolling bearings, *Applied Surface Science*, 108(**1**)45 – 51.

[16] M. Grebe; False-Brinelling und Stillstandsmarkierungen bei Wälzlagern – Schäden bei Vibrationsbelastung oder kleinen Schwenkwinkel; Expert-Verlag Renningen, ISBN 978-3-8169-3351-9; 2017..

[17] G. Fish; F. Herrero: Fretting Wear; ELGI AGM; Kiev Ukraine; 2010.

[18] M. Kuhn: Spezialschmierstoffe für False Brinell beanspruchte Wälzlager; 11. VDI-Fachtagung "Gleit- und Wälzlagerungen 2015"; VDI-Berichte 2257, ISBN 978-3-18-092257-7; 2015.

[19] F. Schwack, F. Prigge, G. Poll (2018) Finite element simulation and experimental analysis of false brinelling and fretting corrosion, Tribology International, 126, 352-362.

[20] A. Lenart, P. Pawlus, A. Dzierwa, J. 2016 The effect of surface topography on dry fretting, 17th Nordic Symposium on Tribology - 14-17 June 2016 - Hämeenlinna, Finland.

[21] D. Godfrey, J. M. Bailey (1954) Coefficient of friction and damage to contact area during the early stage of fretting: Part 2, *N.A.C.A. Techn. Note 1954* (3144) (1954) 1055.

[22] J. M. Bailey, D. Godfrey (1954) Coeiffcient of friction and damage to contact area during the early stage of fretting: Part 1, N.A.C.A. Techn. Note 1954 (3144) (1954) 1055.

[23] C. Schadow, L. Hundt, A. Kießling, D. Bartel, L. Deters (2016) False brinelling in angular contact ball bearings - a comparison of experimental data with fem-simulations. *Proceedings of bearing world 2016*, Hannover. 2016. p. 82–85.

[24] H. Krause, G. Poll (1986) Wear of whell-rail surfaces, *Wear* **113**(1), 103-122

[25] F. Schwack, A. Byckov, N. Bader, G. Poll (2017) Time-depending analyses of wear in oscillating bearing applications, STLE, 21-25 May 2017 Atlanta (**72**).

WEC failure on the inner ring of roller bearings under dynamic conditions

Hubert Schwarze[1], Bramila Tarigan[1], Jörg Loos[2], Toni Blass[2], Wolfram Kruhöffer[2]

[1] *Institute of Tribology, Clausthal University of Technology, www.itr.tu-clausthal.de*

[2] *Schaeffler Technologies AG & Co. KG, www.schaeffler.de*

Abstract– The influence of dynamic load conditions (multistage radial load and oscillating rotational speed) on the formation of White Etching Cracks (WECs) was studied by using the new test bench "PWD4".

In preceding investigations NU222 bearings were tested at Schaeffler under periodically variable radial loads but without any electrical current flow. In these tests WECs were reproducibly generated on the outer rings due to hydraulic churning losses and moderate cage slip values.

On the PWD4 test bench WECs could be produced on the outer rings of NU215 bearings also under low cage slip of less than 1%. The damage pattern was similar to the bearings NU222. The low cage slip and the circumferential position of the WEC indicate that roller slip was the main cause for the WEC formation on the outer rings.

When applying similar test conditions to cylindrical roller bearings with brass cage and increased clearance, cage slip went up. This setup led to severe WEC formation on the inner ring. These results indicate that cage slip is an essential influence parameter for the WEC formation on inner rings of roller bearings.

Keywords – White Etching Crack, White Etching Area, slip, rotational oscillation, roller bearing

---

1. Introduction

Rolling bearings made of common bearing steel fail in some applications e. g. wind turbine gearboxes with White Etching Cracks (WEC) before reaching their calculated rating life (Evans [4], Stadler, et al. [3]). The premature failures of roller bearings in planetary gears can be found at different positions, such as the planets bearings, intermediate shaft and high-speed shaft bearings (Stadler, et al. [3]). In these cases the WECs mostly occurred on bearing inner rings. Until now the mechanism responsible for WEC formation on inner ring is still in discussion. A hydrogen uptake of the steel during operation due to additional loads like electrical current flow (Loos, et al. [14]) or high friction energy in the rolling contact (Tarigan, et al. [1], Loos, et al. [2], Kruhöffer, et al. [9], Ruellan [7], Greco, et al. [5], Gould, et al. [6]), are currently considered as the most likely WEC root cause. It has also been observed (Rumpf [19]), that primary spheroidised carbide disintegration may play a key role in the formation and development of white etching microstructure in both WECs and white etching bands.

To investigate the influence of slip on the life of roller bearings, bearing tests with type NU222 were carried out by Schaeffler on the R4G test rig (Loos, et al. [2]). The cylindrical roller bearings NU222 were run with a constant rotational speed under alternating high and low radial load. To increase the friction energy, the roller bearings were supplied with a large oil supply rate. Overlubrication ($Q > Q_{limit}$) closely linked with high splashing losses causes high roller element slip and high cage slip during the low radial load phase.

The bearing tests were conducted under good lubrication condition (viscosity ratio $\kappa = 4.2 = \nu/\nu_1$) with a typical wind turbine transmission oil (Loos, et al. [2]).
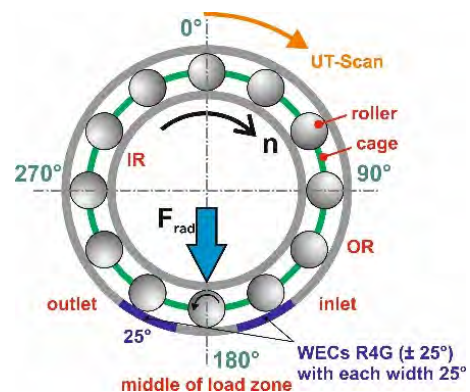
Figure 1-1: WEC formation on outer ring of the NU222 bearing with brass cage on R4G test rig

In these bearing tests WEC formations could be generated reproducibly on the outer ring of the NU222 without additional electrical current. WECs appeared uniformly in two zones (inlet and outlet) with each circumferential width 25° and located 25° before and after the maximum load zone (Loos, et al. [2]), see Figure 1-1. Rolling elements and inner rings showed no WEC formation.

2. Experimental procedures

2.1. *PWD4 Test rig*

Based on load conditions of bearings in wind turbine gearboxes, a new PWD4 test rig was designed, that enables testing of roller bearings under a combined highly dynamic load (radial load and angular acceleration). On the PWD4 test rig four roller bearings type NU215 can be run simultaneously with following combined loads (Tarigan, et al. [1]):

- Radial load: The test bearings can be loaded statically and dynamically up to a maximum load of $F_R = 100\ kN$.
- Angular acceleration to increase the slip respectively the friction energy: The roller bearings can be driven with dynamic rotational speed and oil supply overlubrication ($Q > Q_{limit}$).

Figure 2-1: Side view of the PWD4 test rig

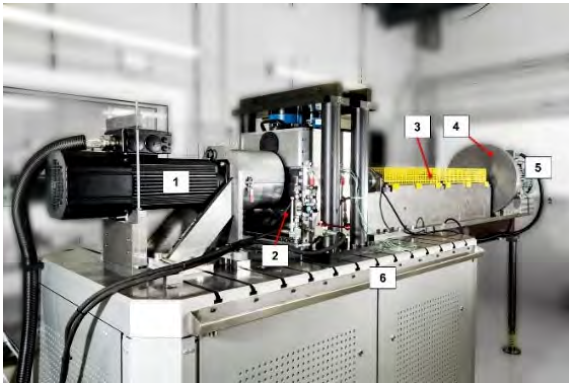The PWD4 test rig consists of a double oscillator (a drive motor and a servomotor), see Figure 2-2. Both motors are connected by a long torsion shaft. The drive motor can run the drive shaft with constant rotational speed up to a maximum of $n_D = 2600\ rpm$ and the servomotor induces a superimposed dynamic rotational speed with a maximum amplitude of $n_S = 500\ rpm$ (dynamic) at a constant frequency of $f = 55\ Hz$. This sinusoidal function enables a maximum twisting angle of approximately $\theta_{max} = +/-6°$.

The twisting angle was determined in preliminary tests and measured by means of strain gages. Q_{max} corresponds to a dynamic speed of $n_S = +/- 500\ rpm$. Since the tests presented here were

carried out at +/- 400 rpm, the maximum torsional angle was not completely reached. The PWD4 test rig was designed for a total rotational speed of $n_T = 3000\ rpm$ resulting from the sum of static and dynamic rotational speeds (see Figure 2-2).
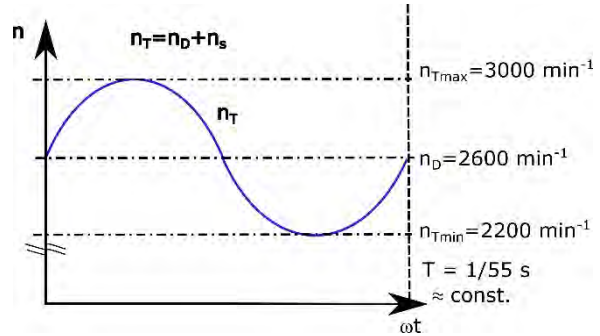
Figure 2-2: Dynamic rotational speed on the PWD4 test rig

2.2. *Influence of cage material and clearance on cage slip under static and dynamic rotational speed*

Two cage types (polyamide and brass) and two bearing clearances (Δs_1 und Δs_2) were used for the bearing tests on the PWD4 test rig. The influences of different cage materials and bearing clearances under static and dynamic speed rotation on cage slip for low radial load levels are illustrated in Figures 2-3 and 2-4.

The roller bearing NU215 with polyamide cage and small clearance (green lines) showed low cage slip ($\sim < 1\%$) under constant rotational speed of $n_D = 2600\ rpm$ as well as under dynamic rotational speed of ($n_D = 2600\ rpm$, $n_S = 400\ rpm$ and $f = 55\ Hz$). These conditions induced a twisting angle of θ less than $6°$ on the inner ring. In contrast, the bearings with increased clearance (blue lines) and brass cage (red lines) show a rapidly decrease in rotational speed below a minimum load.

Figure 2-3: Influence of cage material and bearing clearance on cage slip under static rotational speed $n_D = 2600\ rpm$

The polyamide cage of the NU215 roller bearing has a lower mass compared to the brass cage. These results give a hint that higher cage slip can be obtained by increasing cage inertia and/or operating clearance.

Figure 2-4: Influence of cage material and bearing clearance on cage slip under dynamic rotational speed (n_D = 2600 rpm, n_S = 400 rpm, f = 55 Hz
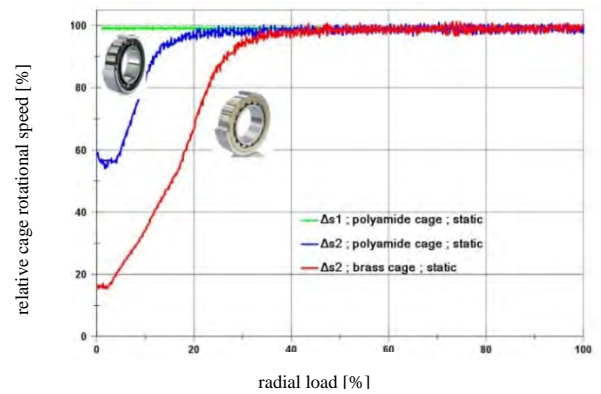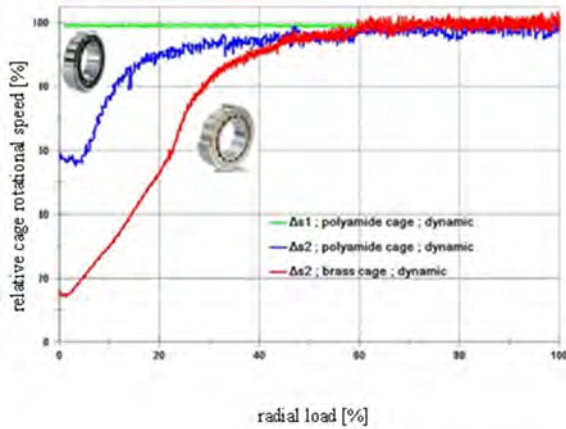
In addition to the radial load F_R, operating clearance Δs, oil supply rate Q and material of cage (mass), other parameters like oil viscosity η and rotational speed n play a major role in cage slip behaviour (van Lier [10], O'Brien, et al. [11]).

3. Results and discussion

In the scope of this work bearing tests were carried out on the PWD4 test rig with different configurations:

- Bearing type NU215 with polyamide cage and small clearance Δs_1 [a]
- Bearing type NU215 with brass cage and high clearance Δs_2 [a]

3.1. *Load condition*

These two variants were tested analogous to the load conditions (low and high load) which were set on the R4G test rig of Schaeffler with roller bearing type NU222, [1], [2].

3.2. *Analysing WEC formation*

To detect the location of WEC formation in roller bearings without destroying the rings, an ultrasound scan (frequency: 25 MHz) was made. To visualize subsurface WECs, the entire circumference (0° - 360°) of the inner and outer rings was scanned by ultrasound, see Figure 3-2. The cross sections of the damaged rings were grinded, polished and etched with 2% alcoholic nitric acid (nital), then examined under reflected light or by raster electron microscopy.

3.2.1. *WEC formation on OR with low cage slip*

The roller bearings type NU215 with reduced operating clearance Δs_1 and polyamide cage have always run under low cage slip (~ < 1%) and failed with a similar damage pattern as type NU222 (R4G) with two WECs zones on the outer ring (OR), see Figure 3-1.

[a] Standard values, no special manufacturing
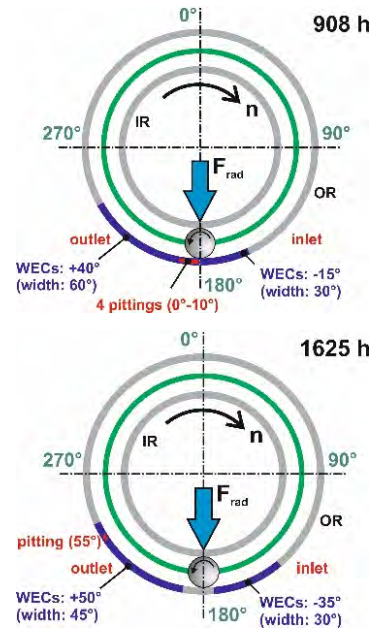
Figure 3-1: WECs formation on outer ring) of NU215 with reduced operating clearance and polyamide cage

The WEC zones of roller bearing type NU215 were measured unsymmetrically to the central load zone, 15° - 30° in the inlet zone and 45° - 60° in the outlet zone. The inner rings and rolling elements showed no WEC formation. The results of the bearing tests with reduced operating clearance Δs_1 and polyamide cage indicated that roller slip was the main cause of WEC formation on the outer ring (Tarigan, et al. [1]).

3.2.2. *WEC formation on inner ring (IR)*

The bearing tests on the PWD4 test rig with increased operating clearance Δs_2 and brass cage resulted in massive WECs formation on the inner rings. Ultrasound scan identified subsurface WECs in the entire circumference (0° - 360°) and axial width of inner ring raceway, see Figure 3-2. WECs were found innumerous beneath pittings as well as in areas where no macroscopic damage was observed, see Figure 3-3. More than ten pittings distributed completely on the inner ring were found, as shown in Figure 3-3 (top).
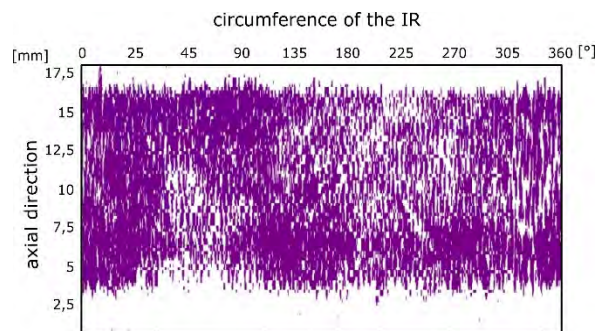
Figure 3-2: Ultrasound scan (frequency: 25 MHz) of first IR failure with ten pittings on inner ring (IR). WECs formation is illustrated by violet color (approx. 300μm depth)

Figure 3-3: Macroscopic damages on IR (top). Subsurface WECs (depth of 100 – 360 µm) without pitting on raceway (bottom)

Investigation by means of raster electron microscope analysis showed that the cracks began from subsurface without any identified initial damage positions. The outer ring (OR) and the rolling elements of this bearing failure contained no White Etching Crack (WEC).

The second inner ring failure showed WECs formation with a circumferential width of 35° and a pitting with axial cracks on inner ring (IR), as in Figure 3-5.

Although the outer ring had no macroscopic damage, WEC formation appeared in the outlet zone with a circumferential width of 20° and beneath the raceway at a depth of 150-340 µm, see Figure 3-4 (bottom).
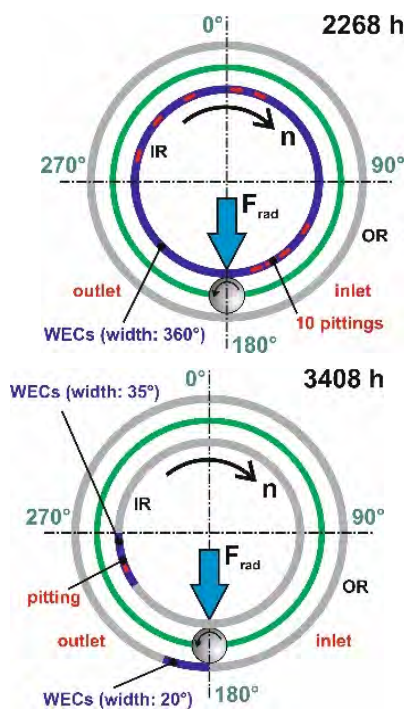
Figure 3-4: WECs formation of first IR failure (top) with massive pittings. WECs formation of second IR failure (bottom) with a macroscopic damage on IR

Detailed view by raster electron microscopy did not indicate non-metallic inclusions in fractured surface. The rolling elements did not have WEC formation. The results of bearing test type NU215 with increased operating clearance Δs_2 and brass cage showed that the inner ring becomes more WEC critical than the outer ring if a certain elevated cage slip occurs.
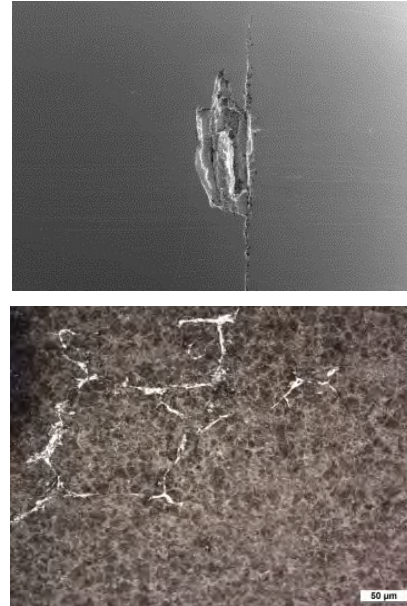
Figure 3-5: Macroscopic damage on IR with axial cracks (top). WECs formation beneath inner ring raceway (depth of 125 – 570 µm) (bottom)

3.3. *Weibull distribution*

Figure 3-6 shows the Weibull distributions of all tested roller bearings type NU215 (polyamide cage, small clearance Δs_1 vs. brass cage, large clearance Δs_2) with WEC formation.
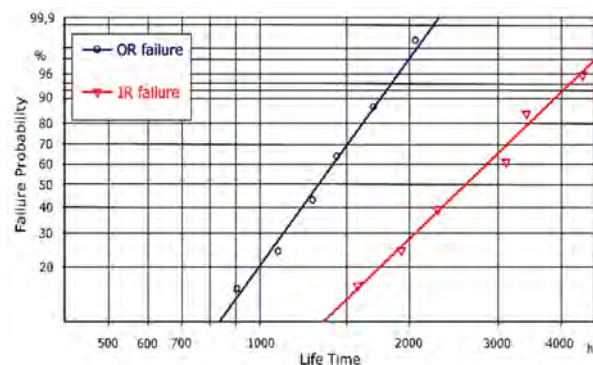
Figure 3-6 Life time of roller bearing type NU215 based on Weibull distribution with WEC formation

Since the outer ring is stationary and the maximum load is acting always at the same location (180 deg.), the OR damage occurs in the load zone and earlier than the cage slip induced inner ring damage.

The inner ring, on the other hand, rotates and frequently leaves the highly loaded area, which results in a distribution of the damage locations over the entire circumference of the inner ring. Therefore,

although cage slip has a detrimental effect on the roller bearing performance, WEC damage to the inner ring occurs later.

The elevated cage slip of the NU215 with brass cage and larger clearance Δs_2 led to an increased sliding velocity v as well as kinematic friction energy accumulation $e_{a,kin}$ on the inner ring which provides an explanation for the higher WEC risk at the inner ring (Kruhöffer, et al. [9], Loos, et al. [17]).

The occurrence of WEC damage was determined using acceleration sensors placed on each rolling bearing. If a critical acceleration amplitude or acceleration rise rate is exceeded, the test is stopped and the abnormal rolling bearing was dismounted and replaced by a new one.

4. Conclusions and outlook

Cylindrical roller bearings type NU215 were tested on the new test rig "PWD4". To realize a high slip and a large friction energy accumulation, the test bearings were run under rotational oscillation and overlubrication causing elevated splashing losses.

The radial load conditions (two alternating load levels) of the R4G rig (Schaeffler) with roller bearing type NU222 were adapted to bearing type NU215 on the PWD4 test rig. Two configurations of roller bearing type NU215 were run on the PWD4 test rig under the same test conditions. The bearings with a reduced clearance and polyamide cage have a little slip tendency and even no notable cage slip ($\sim < 1\%$) at low radial loads. These test bearings failed due to WEC formation on the outer rings. This and the position of the WECs indicate that roller slip is the main cause of WECs formation on outer ring.

Further tests were conducted with increased clearance and a brass cage. This configuration produced more cage slip in the low load phase with and without dynamic rotational acceleration. Under the same test conditions on the PWD4 test rig, the samples showed massive WEC and pitting formation on the inner rings. These results give a hint that cage slip is an essential influence parameter for WEC cause on the inner ring of roller bearings.

Notation

$e_{a,kin}$	Friction Energy Akkumulation
f	Frequency
n_D	Rotational Speed of Drive Engine
n_S	Rotational Speed of Servo Engine
n_T	Total Speed
v	Sliding Velocity
F_R	Radial bearing Load
Q	Oil Flow
$Ds_{1,2}$	Bearing Clearance
k	Viscosity Ratio
v	Kinematic Viscosity
v_1	Reference Viscosity
Q_{max}	Twisting torsional angle
IR	Inner Ring
OR	Outer Ring
R4G	Schaeffler Test Rig
PWD4	ITR Test Rig

References

[1] B. Tarigan, H. Schwarze, J. Loos, T. Blass, W. Kruhöffer: Prüfstand zur Erprobung der WEC-Bildung an Wälzlagern unter Drehdynamik. GfT-Tagungsband, September 2017, Göttingen

[2] J. Loos, H. Wehner, M. Smolenski, et al.: Factors increasing the risk of WEC – formation in large-size bearings with full fluid film lubrication. Bearing World conference Hannover (2016), http://bearingworld.org/

[3] K. Stadler, A. Stubenrauch: Premature Bearing Failures in Wind Gearboxes and White Etching Cracks, Power Transmission Engineering, October 2014

[4] M. H. Evans: White structure flaking (WSF) in wind turbine gearbox bearings: effects of "butterflies" and white etching cracks (WECs). Material Science and Technology (2012)

[5] A. Greco, B. Gould: The Influence of Sliding and Contact Severity on the Generation of White Etching Cracks. Tribology Letters 60 (2015), 1-13

[6] B. Gould, A. Greco: Investigating the Process of White Etching Crack Initiation in Bearing Steel. Tribology Letters (May 2016)

[7] A. Ruellan Du Crehu: Tribological analysis of White Etching Crack (WEC) failures in rolling element bearings. Mechanics of materials, INSA de Lyon, NTT: 2014ISAL0116, 2014

[8] J. Loos, W. Kruhöffer: Einfluss der Reibbeanspruchung auf die WEC-Bildung in Wälzlagern. Tribologie und Schmierungstechnik 62. Jahrgang 4/2015

[9] W. Kruhöffer, J. Loos: WEC Formation in Roller bearings under Mixed Friction: Influences and "Friction Energy Accumulation" as Indicator. Tribology Transactions 2016, Vol. 0, No. 0, 1-14

[10] H. van Lier: Schädlicher Wälzlagerschlupf. FVA Abschlussbericht 663 I 2015

[11] K. T. O'Brien, C. M. Taylor: Cage Slip in Roller Bearings. Journal of Mechanical Engineering Science 15(5), 370-378, 1973

[12] A. Ruellan, F. Ville, X. Kleber, et al.: Understanding White Etching Cracks (WEC) in rolling element bearings under the effect of hydrogen charging. 40th Leeds-Lyon Symposium on Tribology & Tribochemistry Forum (2013), September 4-6, 2013, Lyon, France

[13] W. Holweger, M. Wolf, D. Merk, T. Blass, M. Goss, J. Loos, S. Barteldes, A. Jakovics: White etching crack root cause investigations. Society of Tribologists and Lubrication Engineers (2014)

[14] J. Loos, M. Goß; I. Bergmann: Influence of Currents from Electrostatic Charges on WEC Formation in Roller bearings. Tribology Transactions (June 2016)

[15] J. Loos, T. Blass, J. Franke, W. Kruhöffer, I. Bergmann: Einflüsse auf die WEC-Bildung in Wälzlagern. VDI-Berichte Nr. 2257 (2015)

[16] W. Holweger, J. Loos: Beeinflussung der Wälzlagerlebensdauer durch neue Werkstoffphänomene in speziellen Anwendungen. Antriebstechnisches Kolloquium ATK 2011, ISBN 978-3-940565-83-9, (2011)

[17] J. Loos, W. Kruhöffer, D. Merk, J. Kerstiens, M. Smolenski: Berechnungsansätze für die WEC-Neigung unter reibenergetischer Wälzbeanspruchung. VDI-Berichte Nr. 2308 (2017)

[18] F. Guzman, M. Özel, P. Pinard: Gefügeveränderungen in Wälzlagerringen mit Rissen als Folgeschaden. FVA Abschlussbericht 707 II (2016)

[19] V. Rumpf: A Study on Microstructural Alterations in White Etching Cracks, Dark Etching Region and White Etching Bands in Rolling Contacts, University of Southampton, Faculty of Engineering and the Environment, PhD Thesis (2018)

Characterization of electrical lubricant properties for modelling of electrical drive systems with rolling bearings

Dani Bechev[1], Timo Kiekbusch[1], Bernd Sauer[1]

[1] *University of Kaiserslautern, Institute of Machine Elements, Gears and Transmission, bechev@mv.uni-kl.de,*
timo.kiekbusch@mv.uni-kl.de, sauer@mv.uni-kl.de

Abstract– Unintended current flow in rolling bearings can damage bearing components and lubricant. Various parasitic bearing currents can cause ripples on the raceways or burned lubricants with significantly changed properties. This can lead to premature machine failures in areas where variable-speed inverter-controlled electric motors and generators are used. To avoid such failures, the correct description of the rolling bearings is an essential aspect for modeling the (electrical) behavior of electrical systems. Their behavior, in turn, strongly depends on the properties of the lubricant (breakdown field strength, permittivity, conductivity, etc.).

In order to investigate these properties under realistic conditions in rolling contacts, two test benches were developed and set up at the University of Kaiserslautern at the Institute of Machine Elements, Gears and Transmissions. With the first test setup, it was possible to research the electrical-physical conditions in rolling contacts of rolling bearings as well as the role of the lubricant and the lubricant film thickness for the current flow and resulting damages.

In order to determine the relevant lubricant properties and related damages precisely under real operating conditions, a further test setup was developed and set up. A four-ball tester has been modified in such a way that current flow and electrical lubricant properties of an axial groove ball bearing can be investigated for various operating conditions. The current flow at the individual contact was investigated and the electrical lubricant properties were determined by impedance measurements. Also, lubricant and raceway damage mechanisms were analyzed.

Keywords – electrical properties, bearing voltage

1. Introduction

Unintended current flow in rolling bearings can damage bearing components and lubricant [1], [2].

Various parasitic bearing currents (recharging, EDM (electric-discharge-machining), circulating-bearing and rotor-earth currents) can cause e.g. ripples on the raceways or burned lubricants with significantly changed properties [3]. The damages are presented in Figure 1. This damages are typical for applications in the field of railway technology, vehicle technology and electro-mobility, as well as in many other sectors. The bearing failures can lead to premature machine failures in areas where variable-speed inverter-controlled electric motors and generators are used [4]. Frequency converters are used to control the rotational speed of the electrical machines. They generate a common mode voltage (U_{CM}) by superimposing three pulse-width modulated square-wave voltage courses due to high switching frequencies of their semiconductor elements of more than 10 kHz. Due to the fast switching operations of the insulated gate bipolar transistors used in the converters (IGBT), steep voltage jumps occur on the clock edges. The very fast voltage change results in high gradients in the output voltage of the inverter [5], [6], [7]. The voltage arriving at the bearing corresponds to the bearing voltage U_b that occurs in the electric machine. The BVR (Bearing Voltage Ratio) describes the voltage drop across the bearing. The BVR characterizes the capacitive voltage divider of the electric motor and is equal to the bearing voltage U_b divided by the common-mode voltage U_{CM} [7]. The BVR not exceed 10%. This means that with an electric machine running at 600V, 60V can cause damage to the rolling bearing.

EDM-currents can be observed, when the lubricant film between the rolling element and the raceway cannot resist to the parasitic voltage applied to the bearing and breakdown occurs. Generally, a voltage builds up, which is characterized by its typical form (three steps up, three steps down) with no high current. When there is a breakdown, a voltage discharge process can be recognized and high discharge current flows through the contact. [8]

To avoid such failures, the correct modelling of the rolling bearings is an essential aspect for modelling the (electrical) behavior of electrical systems. Their behavior, in turn, strongly depends on the properties of the lubricant (breakdown field strength, permittivity, conductivity, etc.).

In order to investigate these properties under realistic conditions in rolling contacts, two test benches were developed and set up at the University of Kaiserslautern, at the Institute for Machine Elements, Gears and Transmissions. With the first test setup (two axially preloaded angular ball bearings), it is possible to investigate the electrical-physical conditions in rolling contacts of rolling bearings as well as the role of the lubricant and the lubricant film thickness for the current flow and resulting damages. An axially loaded bearing is tested under well-defined mechanical and electrical conditions.
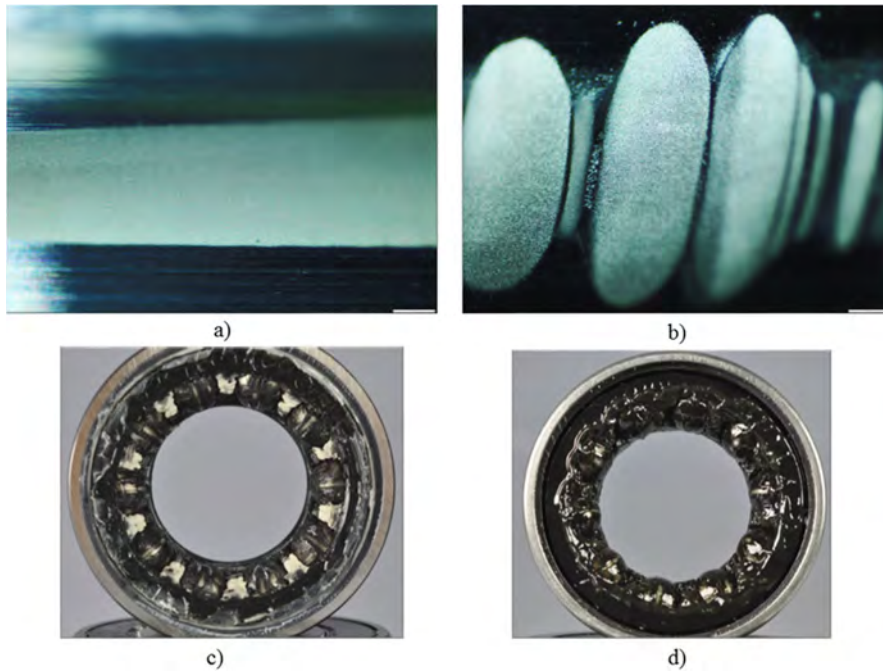
Figure 1: Bearing and lubrication damages, a) craters, b) riffles, c) and d) burned lubricant

As analysis parameters, the high-frequency time courses of bearing current and voltage are evaluated with regard to the occurring bearing current types and thus changes in the electrical and tribological behavior. It was found that lubricant and lubricating film thickness have a significant effect on the electrical behavior. Rolling bearing and lubricant damage could be reproducibly generated and assigned to the respective current types. [8]

In order to determine the relevant lubricant properties and related damages even more precisely under real operating conditions, a further test setup was developed and set up as part of the research project FVA 650 II "Methodology for the practical characterization of electrical lubricant properties to improve the computational prediction of bearing currents" at the Research Association Drive Technology (FVA). A four-ball tester has been modified in such a way that current flow and electrical lubricant properties of an axial ball bearing can be investigated for various operating conditions. The electrical conditions at the individual rolling contacts are investigated using a modified axial ball bearing with one rolling element made of 100Cr6 and fourteen ceramic rolling elements (Si3N4). The current flow in the individual contacts are investigated and the electrical lubricant properties are determined by impedance measurements.

2. Basics

2.1. *Electrical properties of Materials*

For the determination of the electrical properties of lubricants there is currently no standardized measuring method. In order to improve the prediction of bearing currents and to better understand the mechanism of the different degrees of damage, it is necessary to know these properties of the lubricants. The electrical parameters of the lubricants are the relative permittivity, the breakdown field strength and the specific electrical resistance. Relative permittivity studies have been performed for various base oils in [4], [9], [10], [11] and in [12], [13] for various greases. Results from [14] show that there are large deviations between the relative permittivity for base oil and lubricating grease. Values for breakdown field strength are available in the literature for mineral oil. Studies in [14] also show that deviations of about 33% occur between the literature values and the measured value obtained in the research project. Published specific electrical resistance values can be found in the literature for graphitized grease in [1], [15].

2.1.1. *Relative permittivity ε_r*

The relative permittivity ε_r indicates the electrical polarization of a dielectric. A test standard (DIN EN 60247 [16]) exists for this purpose, but is only used for transformer oils at 90 °C and at atmospheric pressure. In rolling bearing applications, the temperature ranges are significantly wider (-40...120°C) and the pressures are considerably higher (up to 4600 MPa) due to the high surface pressure. Based on this method, several investigations have already been carried out to find a relationship between frequency, pressure, temperature and relative permittivity [17]. It was found that the measurements in the investigated area correlate well with the Clausius-Mossotti equation [18] and a frequency change has influence. The application of this equation requires knowledge of the relative permittivity at atmospheric pressure and reference temperature.

2.1.2. *Breakdown field strength E*

The breakdown field strength E indicates the highest field strength that can be applied to a material without it failing as an insulating medium. The DIN standard DIN EN 60156 [19] is available for their determination. Its focus is on low-viscosity (ISO VG 7 to ISO VG 10) transformer oils. No investigations were carried out or analytical approaches developed to determine the pressure and temperature dependence of the breakdown field strength. In particular, the distance used in the standard (2.5 mm) differs significantly from the much smaller distance (<2 µm) present in the EHL contact.

2.1.3. *Specific electrical resistance ρ*

The specific electrical resistance ρ or its inverse, the electrical conductivity κ, describes the electrical conductivity of a material. The measurement of the electrical conductivity of mineral oils is described in DIN EN 51412 [20]. The temperature dependence of this measured variable has been known for a long time, e.g. for copper or other conductor materials. For insulating materials, such as the base oil of the lubricant, such investigations, especially depending on the pressure, have not been in focus up to now and have therefore not been investigated in detail. However, there is a distinction between high- and low-resistance lubricants [21], which allows a rough characterization. Currently, lubricants with a lower specific resistance are being developed. Standard roller bearing greases have a specific electrical resistance of 10^{11} Ωcm. Newly developed lubricating greases with ionic liquids have a specific electrical resistance of 10^7 Ωcm, which can lead to better conduction of harmful bearing currents. [22]

2.2. *Electrical properties of an EHL contact*

In this chapter, the EHL contact area is observed from an electrical point of view. Rolling element surface and roller bearing surface are in contact. Voltage is applied to the two components. There is lubricant between the surfaces. This is shown in Figure 2. You can see asperities that are in contact and those that are not. Very low contact resistance is formed between the asperities that are in contact. A capacitance is not build-up. A capacitance can build up between the asperities, when those are not in contact. On the basis of this representation, a total bearing resistance R and a total bearing capacitance C can be formed.

This detailed examination of the contact area is very difficult to realize, as it requires an exact description of the contact surface and asperity interaction.

To simplify this problem, the Hertzian surface area is used as the contact surface area and not the real surface area. This simplification can lead to inaccuracies in the determination of the electrical lubricant properties, as the real contact surface area differs from the Hertzian surface area. The lubricating film is described by the central h_0 and the minimum h_{min} height of the lubricating film. The central lubricating film thickness is used to determine the electrical properties of the lubricant and the minimum lubricating film thickness is used to determine the breakdown field strength in the lubricated contact.

The electrical properties of an EHL contact can be characterised as a system of capacitance and resistance. Resistance R and capacitance C can be calculated from the measured impedance Z, phase angle φ, central film thickness h_0 and Hertzian contact aria A_{Hertz}. To determine the maximum field strength E, the breakdown voltage of the lubricant U and the minimal lubricant film thickness h_{min} need to be known. The breakdown voltage can be measured using a Breakdown-Analyzer (Figure 6) or directly derived from the electrical behavior of the bearing. The following equations can be used to calculate the relative permittivity, the specific electrical resistance and field strength. The requirement is that the capacitance and resistance of the individual contacts are known.

$$C = \varepsilon_0 * \varepsilon_r * (A_{Hertz}/h_0) \qquad \text{(Eq. 1-1)}$$
$$R = (\rho * h_0)/A_{Hertz} \qquad \text{(Eq. 1-2)}$$
$$E = U/h_{min} \qquad \text{(Eq. 1-3)}$$

When examining the rotating rolling bearing, it should be taken into account that from a tribological and electrical point of view the bearing can change its behavior based on different lubrication conditions.
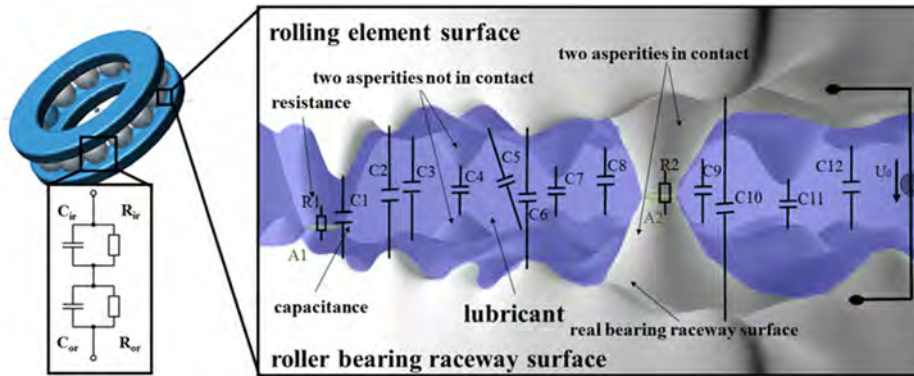

Figure 2: Detailed picture of an EHL contact with resistances R, capacitances C and real contact area A

These lubrication conditions are linked to the formation of the lubricating film and are dependent on e.g. speed, force and temperature.

2.3. *Electrical equivalence of the lubrication conditions*

As described in [5] and [6], [8], [14] the conditions in the rolling contact can be divided into five different lubrication states from an electrical point of view.

Lubrication condition I: The thickness of the lubricant film on the inner and outer rings is sufficient to ensure that the voltage over the

bearing can be fully maintained over both the outer and inner ring sides. The occurring bearing currents are recharging currents.

Lubrication condition II: The lubricant film thickness is sufficiently large only on one ring side so that the voltage can be completely held there. The lubricating film between the other ring and the rolling element can be broken-through. In addition to recharging currents, partial discharges also occur between the rolling element and inner ring.

Lubrication condition III: The charge can be held neither on the outer ring nor on the inner ring side by the lubricant film. The state

is characterized by recharging and discharge currents (EDM currents).

Lubrication condition IV: The voltage cannot be fully held on one ring. On the other ring, the lubricant film thickness is so thin that metallic contacts of the asperities occur (mixed lubrication). In this state, both EDM and recharging currents occur on one ring, the current flows resistively on the other ring.

Lubrication condition V: The thickness of the lubricant film on both rings is so small that metallic contacts of the asperities and thus current flow in the contact points occur (mixed friction). The prevailing currents are resistive currents.

To determine the electrical lubricant properties, the bearing should be in lubrication condition I, II or III. In these three lubrication states, a separating lubricating film occurs in the contact area. This lubricating film can then be characterized by suitable electrical measuring methods. In lubrication condition IV and V, there may be electrical contacts between the asperities of the contact partners, which leads to a short circuit. The electrical measuring methods are difficult to use.

2.4. *Electrical measuring methods*

In the context of this work, three electrical measurement methods are analyzed. These are the resistance measurement, the capacitive measurement method and the measurement of impedance and phase angle.

2.4.1. *Resistance measurements*

Resistance measurements are used to estimate the metallic contact and to identify if there is metal-to-metal contact [23]. With a separating lubricating film, the resistance is very high. The metallic contact between the surfaces leads to a lower resistance. Furey [23] and [24] defines a limit for an insulating lubricating film. This number is 10 kΩ. This method can be used to determine how large the asperity load share is under mixed friction conditions. This method is well suited for measurements in the mixed friction area and less applicable for examinations in full lubrication conditions [25]. This means that this method cannot be used to determine the electrical properties of lubricants.

2.4.2. *Capacitive measuring method*

A measurement method that is widely used is capacitive measurement method [26], [27], [28]. If the rolling bearing is operated in full lubrication, the bearing can charge capacitively and is therefore regarded as a capacitor. In [29] Barz further developed a system for capacitive measurement of lubricant film thickness. This system is used in [25] and [30]. This system is based on the constant current charge of the capacitor. In a rolling bearing contact, a separation is made between the capacitance of the inlet area, the Hertzian area and the outlet area. The capacitance of the Hertzian region is dominant. To take these capacitances into account in the contact, Barz defines a correction factor kc. Through measurements and calculations, Barz has determined that the correction factor $k_c = 3.5$ is for spindle bearings. When charging with constant current of a capacitor with constant capacitance, the voltage has a linear characteristic. When the capacitor is completely discharged and charged with a constant current I_0, the time t_{load} charge until the specified voltage U_{max} is reached is measured. The charging time is proportional to the measured total capacitance C_{total} (Eq. 1-4). The measurements with the capacitive

measuring method can be distorted when asperities come into contact, or during breakdown. This method is suitable for investigations in the full lubrication condition and for the detection of mixed friction [25]. The capacitive measuring method is also suitable for characterizing the electrical lubricant properties.

$$C_{total} = (I_0/U_{max}) * t_{load} \qquad (Eq.\ 1\text{-}4)$$

2.4.3. *Measurements of impedance*

Impedance is a quantity that can be used to characterize the electrical state of the system. The phase angle determines whether the system is inductive, capacitive or resistive. At a phase angle of +90° the system is inductive. At an angle of 0°- resistive and at a phase angle of -90° the system behaves capacitive. When measuring rotating bearings under low load, low temperature, and high speed, it is expected that the system will have a higher capacitive component and phase angle in the vicinity of -90°. At constant speed and force and temperature increase, the bearing may change from full film lubrication condition to mixed lubrication. The phase angle will then change from -90° to 0°. This is shown in Figure 3.
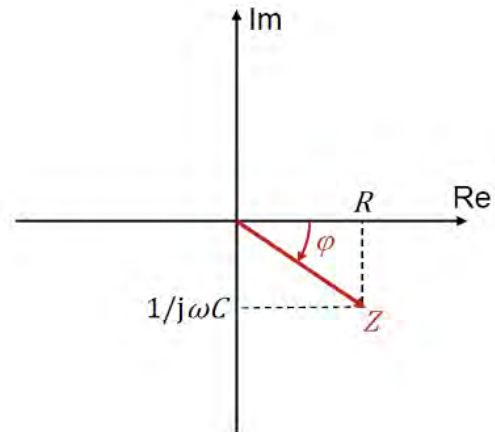

Figure 3: Principle of impedance measurement

The resistance R and capacitance C can be calculated using equations (Eq. 1-5) and (Eq. 1-6).

$$R = Z * \cos(\varphi) \qquad (Eq.\ 1\text{-}5)$$

$$C = 1/(Z * \sin(\varphi) * \omega) \qquad (Eq.\ 1\text{-}6)$$

By measuring the impedance and the phase angle it is possible to determine the capacitance and resistance of the rolling bearing contact and thus the electrical properties of the lubricant under the relevant conditions, high pressure, high temperature and shearing.

3. Test benches and measuring technology

3.1. *Test setup 1- Two bearing test rig*

This test rig is divided in two parts, mechanical part and electrical part. As shown in Figure 4, at each test rig, two bearings 7305-B-2RS-TVP are mounted.

The first one is mounted on the motor side, which is the test bearing. This bearing is electrically charged. After performing the tests, bearing and grease damages are observed. The second bearing which is mounted on the other side, has a support function. This bearing is electrically isolated. On this part, no damages are observed as expected. [8]

The mechanical and electrical features of the test rig are shown in the next list. There is a possibility to variate the axial force, speed and the temperature. The electrical part of the test rig consists of a power supply, a frequency converter, star connection of resistors and a capacitive voltage divider. With the help of a capacitive voltage divider, different types of electrical machines and electrical motors can be modelled. The information about the electrical part of the test rig is shown in the next list, too.

- Axial force variation: 0 N to 10 kN
- Speed: up to 3000 rpm
- Temperature variation: cooling and heating from 15 °C up to 100 °C
- Switching frequency: up to 50 kHz
- Rotational frequency: up to 100 Hz
- Capacitors $C_{ws} / C_{wr} / C_{rs}$: variable
- Bearing voltage: up to 60 V
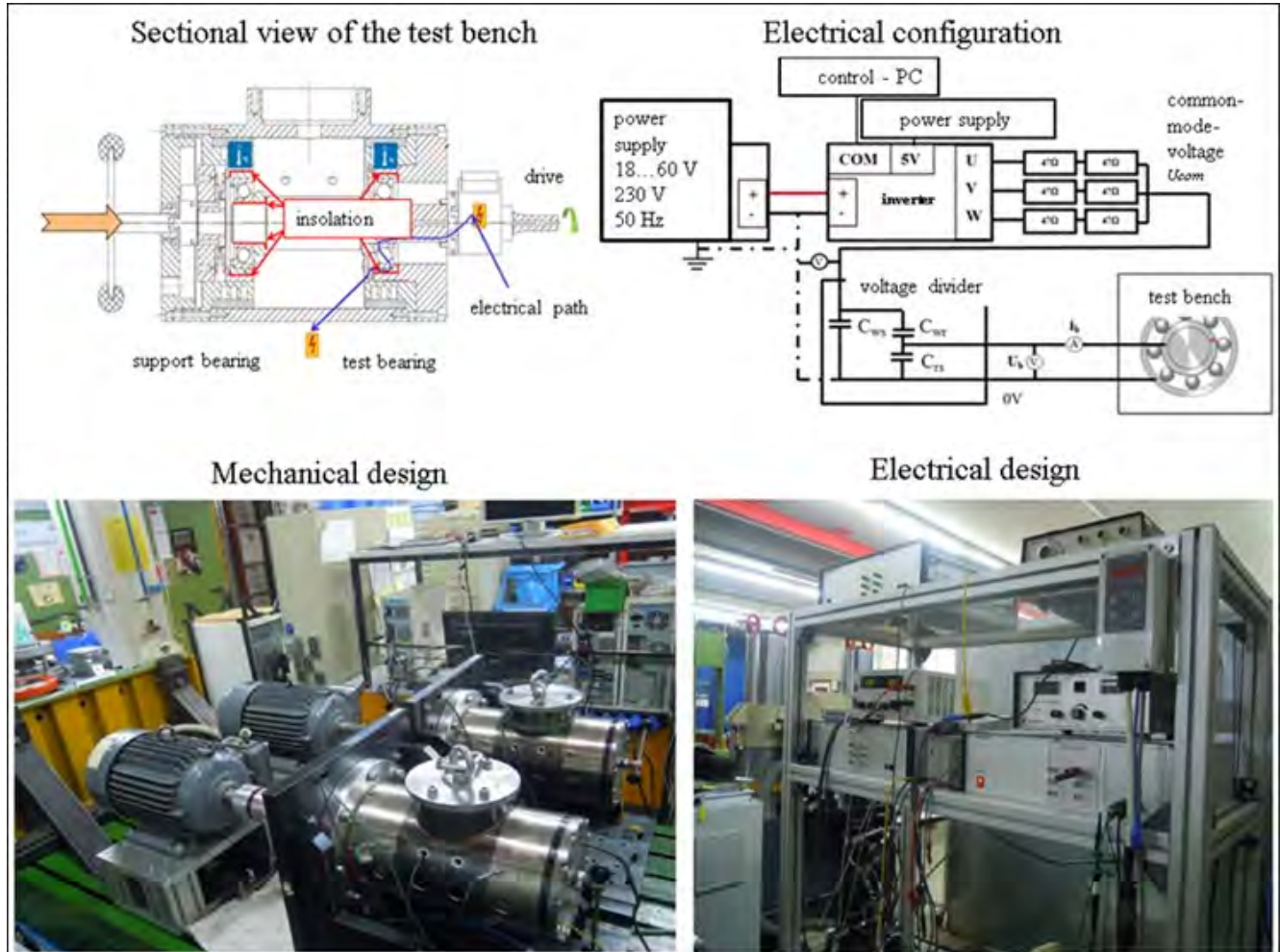- Bearing current: up to 10 A

Figure 4: Two bearing test rig

Various electric motors can be simulated and tested on this test bench with the aid of the variable capacitive voltage divider

3.2. *Test Setup 2- Modified four-ball tester*

The four-ball tester is a test setup for investigating lubricants under high load and rotational speed. The standard device was modified to investigate current and electrical lubricant properties in axial deep groove ball bearings. Current, temperature control and temperature measurement on the rotating part of the bearing are realized by in-house developed slip ring. In addition, water-cooling on the rotating shaft is used to reach lower operating temperatures. On the stationary ring, the temperature can be measured and regulated by heating cartridges and water-cooling. Figure 5 depicts the newly-developed bearing adapter for the four-ball tester. With

this test setup, it is possible to apply defined voltage and current or to measure the impedance or the capacitance of the lubricated bearing under controlled and reproducible conditions.

The advantage of this rolling bearing adapter is the small installation space and the need for only one test bearing, which reduces costs. This adapter can be installed in a standard four-ball device, which is an advantage for many owners of such a tribological measuring device. This adapter was developed for the practical characterization of the electrical lubricant properties and investigations of the current flow in the rolling bearings. Despite the high level of development of the technology today, there are not so many testing devices for determining the electrical lubricant properties under realistic operating conditions.
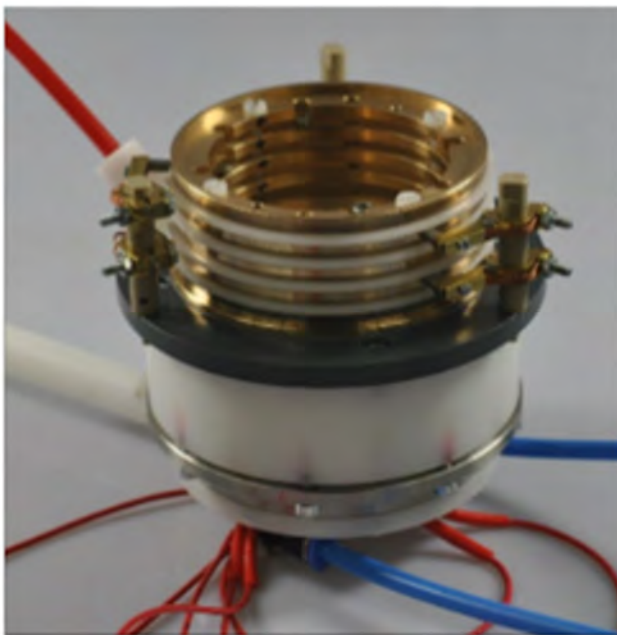
Features of the modified four-ball tester:

- Speed: 100-6000 rpm
- Load: 35-12000 N
- Temperature: 0-120 °C
- Cooling: shaft and housing
- Heating: shaft and housing
- Lubricant: oil and grease
- Bearing voltage: up to 60 V
- Bearing current: up to 10 A

3.3. *Standard laboratory equipment for analysis of electrical lubricant properties*

Several measuring instruments are required to investigate the electrical lubricant properties. To determine the breakdown field strength, a capacitor can be used in which the insulation layer between two electrodes can be passed through if the permissible voltage is exceeded. To determine the relative permittivity and the specific electrical resistance, a capacitor design can also be used. However, two different measuring principles are used. To determine the breakdown field strength, voltage should be applied to the medium between the plates of the capacitor until a breakdown occurs. To determine the permittivity and the specific electrical resistance of the medium, the impedance and phase angle or the resistance and capacitance of the medium should be measured.

Figure 5: Modified four-ball tester, a) newly developed bearing adapter, b) bearing adapter mounted in the standard four-ball tester, c) modified bearing, d) standard bearing 51208

The same measuring principles can be used to determine the electrical lubricant parameters in the rolling bearing. If the rolling bearing is operated in full lubrication, a lubricating film builds up. The bearing can be charged capacitively. The bearing can be charged by increasing the voltage in order to specifically produce EDM breakdowns. After evaluation of the breakdown voltage, the breakdown field strength in the bearing can be determined. The specific electrical resistance and the relative permittivity in the rolling bearing can then be determined by impedance measurements or measurements of resistance and capacitance.

3.3.1. *Breakdown-Analyzer*

The Breakdown-Analyzer (Figure 6) is a standard measuring instrument for testing the breakdown field strength of various transformer oils. The device works by increasing the voltage between two electrodes at a fixed distance until the breakdown voltage limit is reached.

The lubricant is penetrated and the voltage is detected. The dielectric strength of the material is determined by the ratio of the breakdown voltage to the distance between the electrodes. Unfortunately, there is no standard describing how the oils and greases for rolling bearing lubrication are to be investigated. The existing standards for testing transformer oils specify test conditions that are very different from the operating conditions in the bearing. For this reason, this work includes tests under the conditions described in [19] and also under modified test conditions.

Figure 6: Breakdown-Analyzer

3.3.2. *Capacitor for liquid examinations*

The capacitor for liquid examination is a standard measuring instrument for determining the capacitance and thus the relative permittivity of liquids and lubricating oils. Between two disc electrodes with a fixed distance 1,3 mm a space is formed in which the relative permittivity of the oils can be determined. First, a reference measurement is carried out with air.

After the reference measurement has been carried out, the lubricants can be examined. The measuring instrument is connected to an impedance measuring device. The capacitance of the air and the fluid is measured and evaluated. The relative permittivity is determined.

4. Evaluation of the electrical behavior of the bearing

The evaluation of the measurements is carried out by means of a software programmed on the Institute of Machine Elements, Gears and Transmissions in Matlab®. For evaluation of the measurements, bearing voltage and bearing current values are recorded. The evaluation method is shown graphically in Figure 7. The following parameters are determined for each operating point:

•Average number of EDMs $\overline{\mathrm{N}}$

•Average EDM bearing voltage amplitude $\overline{u_b}$

•Average EDM bearing current amplitude $\overline{i_b}$

For each of these parameters, the arithmetic mean is formed in each case. In addition, the full lubrication time fraction is calculated for each measurement block. This indicates the average duration (in %) of the total measuring time per operating point, in which the bearing is in the full lubrication condition. The capacitive and discharge currents are counted as currents in fully lubricated bearings. From the ratio of the clock edges of the common-mode voltage to the number of fully lubricated current events, the full-time lubrication proportion can be determined. [8]
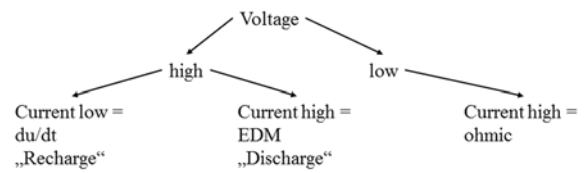

Figure 7: Method for evaluation of the electrical behavior of the bearing [8]

5. Methodology for determining the relevant electrical lubricant properties

A methodology for determining the electrical lubricant properties is developed on the basis of the theoretical principles presented and the existing equipment. The methodology is based on measurements with the Breakdown-Analyzer, capacitor for liquid examinations, modified four-ball tester and two-bearing test rig. The aim is to develop a practical testing methodology with which the electrical lubricant properties can be characterized.

In the first step, only lubricating oils are tested because the standard measuring equipment is available to examine the oil properties. In the second step, the existing equipment have to be modified so that the electrical lubricant properties of lubricating greases can also be determined. The methodical procedure consists of five steps. This is shown in Figure 8.

The information from the calculation of the lubricant film thickness and the contact surface, the results from the tests carried out with the Breakdown-Analyzer and with the capacitor for liquid examinations are compared with the results from measurements on the rotating rolling bearing on the modified four ball tester and on the two bearing test rig. The electrical parameters are determined on the basis of the tests carried out. The most important steps are presented in the following list.

- Determination of the lubricating film thickness and the contact area
- Breakdown measurements on the Breakdown-Analyzer
- Breakdown measurements with applied voltage at the four ball tester (at the bearing)
- Impedance measurements at the four ball tester
- Calculation of the characteristic values

6. Measurements with the Breakdown-Analyzer

Exemplary, the breakdown voltages of a pure mineral oils ISO VG 100 (FVA 3 reference oil) and ISO VG 460 (FVA 4 reference oil) was measured for different temperatures. The FVA oils are lubricants with well-known properties.

For the lower and higher temperature range, larger field strengths could be measured. In the range between room temperature and approximately 70°C, the breakdown field strengths were constant at a very low value below 5 kV/mm for the FVA 4 oil. The results are shown in Figure 9. The breakdown field strength for the FVA 3 oil is at lower temperatures low, about 5kV/mm and rises from 60 °C up to over 20 kV/mm.

Figure 10 shows the results of the investigations on the Breakdown-Analyzer with variation of the distance between the electrodes. It can be seen that with reduction of the distance the breakdown field strength increases.

Figure 10: Measured field strength in respect to the space between the electrodes for mineral oil FVA 3 ISO VG 100 and FVA 4 ISO VG 460, 25 °C

7. Measurements with the capacitor for liquid examinations

After the preparation of the capacitor for liquid examinations, a reference measurement was first carried out with air. The aim of this measurement is to determine a reference value of the structure with intermediate medium air. An impedance measuring device (Bode 100) was used to measure the capacitance of the setup over the entire frequency spectrum. The results of this first measurement are shown in Figure 11 in grey. The FVA 4 oil was then filled into the Liquid Test Fixture. With the help of the impedance measuring device the capacitance of the body, filled with oil, was measured. Figure 11 presents the two results. It can be seen that the capacitance of the air is lower than the capacitance of the FVA 4 oil. The capacitance can be measured in the range from 100 Hz to 10 kHz without large fluctuations in the measurement signal. In the range from 10 kHz to 10^6 Hz the resonance column of the construction can be seen.
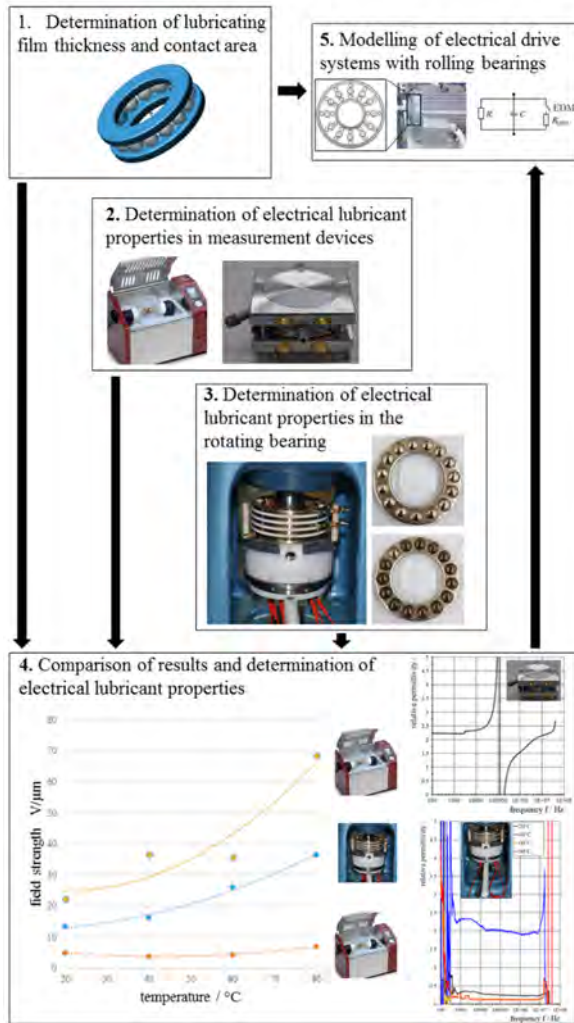

Figure 8: Methodology for determining of the electrical lubricant properties

It is interesting, that high and low temperature give the same results, the field strength is high.
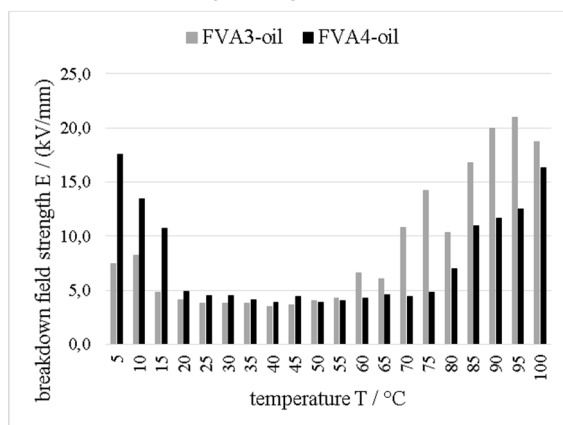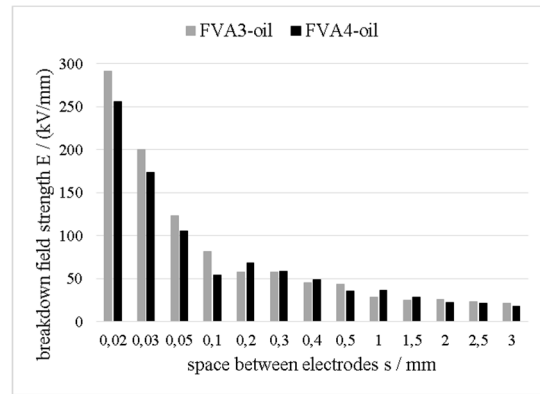

Figure 9: Measured field strength in respect to lubricant temperature (mineral oil FVA 3 ISO VG 100 and FVA 4 ISO VG 460)
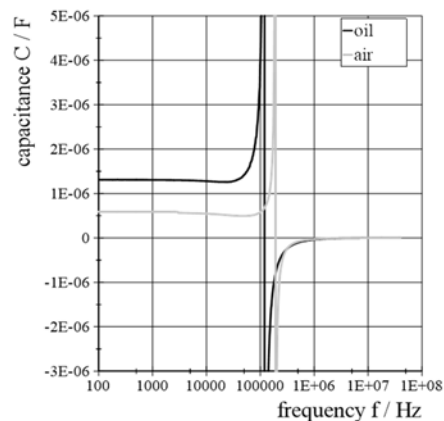
Figure 11: Capacitance of air and FVA 4 reference oil (ISO VG 460), measured with capacitor for liquid examination

No values may be used from this range. The relative permittivity of the oil can be determined from these two measurements. For the calculation of ε_r, *Eq. 1-7* was used. C_o is the capacity of the test cell filled with oil and C_a is the capacity of the test cell filled with air.

$$\varepsilon_r = (C_o/C_a) \qquad \qquad (Eq.\ 1\text{-}7)$$

The results for relative permittivity are shown in Figure 12. The relative permittivity of oils FVA 3 and FVA 4 is between 2 and 2,5. The grease Arcanol Multi 3 and the base oil of this grease were also examined. It can be seen that the oils FVA 3 and FVA 4 have similar relative permittivity and the relative permittivity of the base oil of grease Arcanol Multi 3 is very different from the permittivity of the grease. This may be due to the grease structure, the lithium thickener of the grease or the unknown additives.
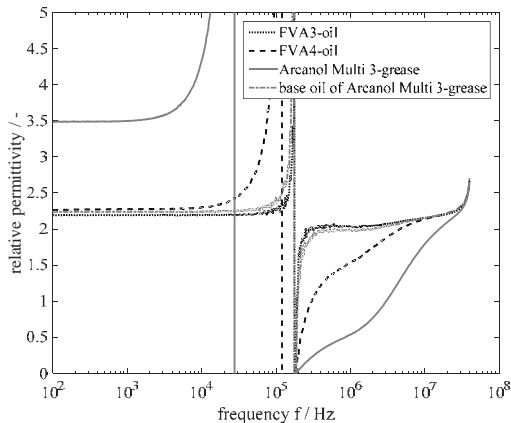

Figure 12: Relative permittivity of FVA 3 and FVA 4 reference oils and of grease Arcanol Multi 3 and its base oil.

8. Measurements on the modified four-ball tester

Two types of measurements were accomplished on the modified four-ball tester. During the first type, an electrical voltage is applied over the bearing. It is possible to measure and analyze the EDM currents and to determine the breakdown voltage in the fluid film. The second type is an impedance measurement of the bearing. From this measurement, the electrical properties of the lubricants can be derived.

Lubricant and lubricating film thickness have a significant effect on the electrical behavior of the system [6], [8]. In [31], it is shown that the average value of the EDM breakdowns in a 7305 bearing is different for different greases and additionally depends on the temperature and on the lubricating film thickness. Similar experiments were carried out for the publication at hand with the FVA 4 reference oil and with standard (15 steel balls) and modified axial groove ball bearings (1 steel ball, 14 ceramic balls) of the type 51208.

The results in Figure 20 show the evaluated average number of EDM-events per second. Depending on the bearing variant, there are two areas with higher breakdown occurrences. This is due to the different ball material combinations. The variant with only one steel ball reaches the EDM range of film thickness – which should be the same for both variants – at higher temperatures and therefore lower viscosity.

8.1. *Preliminary investigation at standstill without lubricant*

In order to get to know the system behavior, impedance measurements were first carried out without lubricant at a constant load of 200 N and a temperature variation of 5 °C to 90 °C when the system was at a standstill. When measuring impedance at standstill without lubricant, it can be expected that the rolling elements will electrically connect the rolling bearing rings and that a low impedance will be measured and a phase angle close to 0°.

Figure 13 shows the impedance measurements and Figure 14 shows the phase angle measurements for three thrust bearings. These are three bearings 51208 with different numbers of rolling elements. The full black line shows the results for a bearing with two rolling elements of Si3N4 and a rolling element of 100Cr6, the dashed line shows the results for a bearing with three rolling elements of 100Cr6 and the dotted line for 15 rolling elements of 100Cr6. It can be seen that the rolling bearing rings are electrically connected via the rolling elements and that the total bearing resistance decreases with an increase in the number of rolling elements from 100Cr6. This information can be used when modelling the entire system.

In order to investigate the thermal expansion of rolling elements made of Si3N4 compared to 100Cr6, two further tests were carried out under the same test conditions. A rolling bearing with three rolling elements made of Si3N4 and a rolling bearing with 14 rolling elements made of ceramic and a rolling element of 100Cr6 were examined. The results of the experiments are shown in Figure 15 and Figure 16. The full black line shows the results for a measurement with three rolling elements made of Si3N4 and the dashed black line shows the results for 14 rolling elements made of ceramic and one rolling element made of 100Cr6.

Figure 13: Impedance measurements at standstill without lubricant by varying the temperature
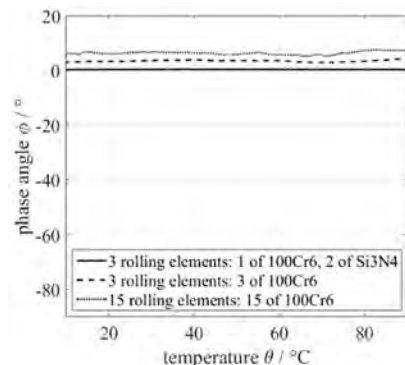
Figure 14: Phase angle measurements at standstill without lubricant by varying the temperature

Significant differences can be seen between the impedance curves for these two rolling bearings. As expected, the rolling bearing with three rolling elements made of Si3N4 is insulating throughout the entire test. The ceramic rolling elements perform their function and electrically separate the two rolling bearing rings. The modified rolling bearing with 14 rolling elements made of Si3N4 and one rolling element made of 100Cr6 has an insulating behavior up to approx. 25-30°C. In this temperature range the impedance is high, which shows an electrical insulation of the rolling bearing rings.

From approx. 10°C a strong drop of the impedance values can be seen (Figure 15). From 30 °C the rolling bearing impedance is in the range of 100 to 1000 Ω. As the temperature increases, the rolling element of 100Cr6 expands faster than the rolling elements of Si3N4. Due to the expansion of the rolling element made of 100Cr6, probably more asperities touch each other and therefore the total bearing impedance decreases.

Before the test, the diameters of all rolling elements were measured. It was found that the rolling element of 100Cr6 is 0.002 mm smaller than the rolling element of Si3N4. At the beginning of the test, the rolling element of 100Cr6 is smaller and during the test due to thermal expansion becomes larger and electrically connects the rolling bearing rings. The same expected behavior is also observed with the phase angle. At the beginning of the test the phase angle is high, which shows that the system behaves capacitively and the rolling bearing rings are electrically decoupled. As the temperature increases, the phase angle shows that the system changes from a capacitive to a resistive state. By measuring the impedance and phase angle, the lubrication conditions of the rolling bearing can be characterized. It is interesting how the system will then behave in contact with lubricant.
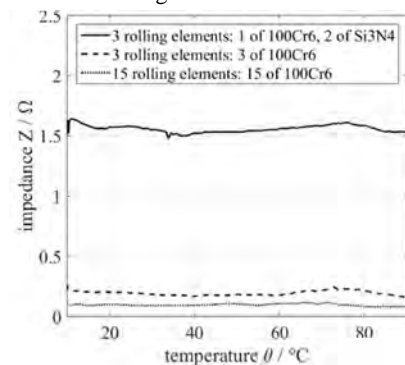

Figure 15: Impedance measurements at standstill without lubricant by varying the temperature

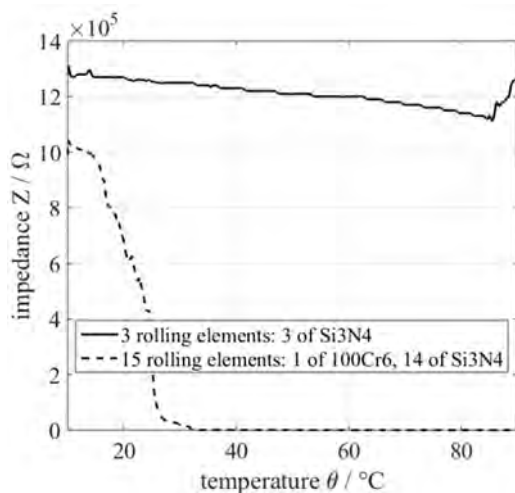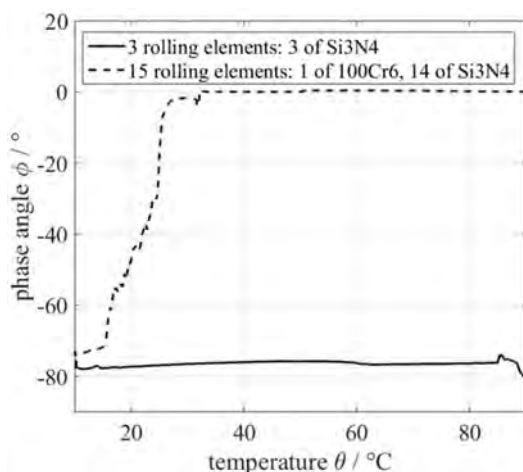*Figure 16: Phase angle measurements at standstill without lubricant by varying the temperature*

8.2. Determination of electrical lubricant properties by impedance measurements on rotating rolling bearings

Two types of tests can be carried out with the rotating rolling bearing. The first type of test are impedance measurements to determine the relative permittivity and the specific electrical resistance. The second type of test is the application of voltage to the bearing and the evaluation of EDM breakdowns. The breakdown field strength is determined by the lubricant. These two types of tests determine the most important electrical parameters on the real system.

Impedance measurements are carried out within the scope of this work to determine the electrical properties of lubricants. Rolling bearings are examined at a speed of 1000 rpm, load of 200 N and temperature of 5 °C to 120 °C. The bearing is lubricated with FVA 4 oil. The results of a test are shown in Figure 17.
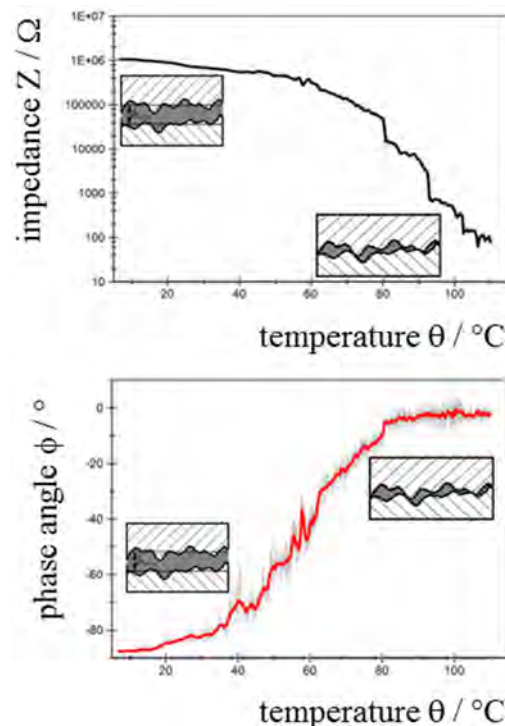
Figure 17: Measurement of impedance and phase angle on rotating rolling bearing with FVA 4 reference oil with variation of temperature and constant load 200 N and speed 1000 rpm

It can be seen that in the lower temperature range the impedance is high and the phase angle is about -90°. This means that a separating lubricating film is detected in the rolling bearing contact. The bearing can be charged capacitively, therefore the system has a capacitive behavior. Increasing the temperature at the same load and speed reduces the lubricant film thickness. At approx. 90 °C the limit of 10 kΩ defined by Furey is reached. From approx. 90 °C the phase angle is almost 0°. This means that the system is operated in mixed friction. In mixed friction, several roughness asperities are in contact. The metallic components are electrically connected to each other. This condition is a great challenge for measurement equipment. The short circuits between rolling

elements and rolling bearing rings cause fluctuations in the measuring signal. In this tribological lubrication condition it is difficult and even impossible for physical reasons to determine the electrical lubricant properties. By measuring the impedance and the phase angle it was determined that a distinction between mixed friction and full lubrication is possible. After the impedance and phase angle measurements the relative permittivity and the specific electrical resistance can be determined.

After the conversion of the impedance and the phase angle into relative permittivity and specific electrical resistance, it was determined that the values are not plausible. The relative permittivity is much higher than expected and the specific electrical resistance much lower than expected.

For this reason, comparative measurements were carried out with a second impedance meter.

Bode 100 is a vector network analyzer and impedance meter. The frequency range of this device is from 1 Hz to 50 MHz. The frequency spectrum can be varied automatically during a measurement. In this way the system behavior can be investigated in a wide frequency spectrum. With this measuring device, the capacitance of the rolling bearing was determined. At a speed of 1000 rpm, force of 200 N and temperature variation of 20 °C to 120 °C, the rolling bearing capacitance was determined. The results are presented in Figure 18.

As the temperature increases, the viscosity of the FVA 4 oil decreases. For this reason the height of the film becomes smaller. The distance between the metallic components becomes smaller and the capacitance increases.

The figure also shows another effect. The measuring signal quality is better in the temperature range from 20 °C to 80 °C. Fluctuations up to approx. 1000 Hz can be seen and from approx. 10^7 Hz. In the range from 1000 Hz to 10^7 Hz the quality of the signal is good. There are few fluctuations. For measurements at 100 °C and 120 °C the system is in mixed friction. Little lubricant is in the rolling bearing contact. Many asperities are touching. The capacitance is very high and the quality of the signal has many fluctuations. Because of the investigation of the wide frequency spectrum it can be determined that there is a frequency range from approx. 100000 Hz to approx. 10^7 Hz in which the measuring signal fluctuates little. This means that a plausible measurement is still possible in this frequency range.

The relative permittivity of FVA 4 oil at 20, 40, 60 and 80 °C for the frequency spectrum from 100 Hz to 10^7 Hz was determined on the basis of the values of the rolling bearing capacitance. The results are shown in Figure 19.

The relative permittivity determined on the basis of the measurement is in the range of approx. 1.25 to 3.5. With the capacitor for liquid examinations a value of 2.3 was determined at room temperature and room pressure. The deviation between 1.25, 2.3 and 3.5 can be explained by the fact that much higher pressures and temperatures act in the rolling bearing contact. The temperature during the test with the rotating bearing was measured on the housing near the rolling bearing ring. For this reason, a deviation between the bearing ring temperature, lubricant temperature and housing temperature is to be expected. However, the relative permittivity determined with the capacitor for liquid examinations

and the relative permittivity determined in the rotating bearing are well matched.
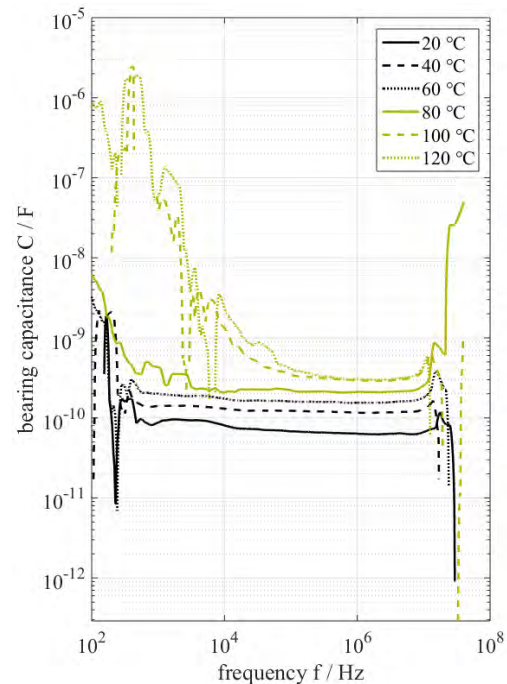
Figure 18: Measurement of the rolling bearing capacitance at the rotating rolling bearing by varying the temperature and constant load 200 N and speed 1000 rpm

8.3. Determination of the breakdown field strength at the rotating rolling bearing

Within the scope of this work, tests were also carried out with the electric voltage applied to the rolling bearing to determine the breakdown field strength of the FVA 4 oil. A low bearing voltage level of 20 V was selected. This voltage level was determined using the measurements taken on the Breakdown-Analyzer.

Figure 19: Relative permittivity of FVA 4 reference oil

The measurements on the Breakdown-Analyzer (Figure 9 and Figure 10) show that at a temperature variation in the range of 20°C to 80°C and a distance of 2 mm between the electrodes, the breakdown field strength of the lubricant is approx. 5 V/mm. With a distance variation of the electrodes and room temperature, the values of the breakdown field strength are between 20 and 70 kV/mm. For this reas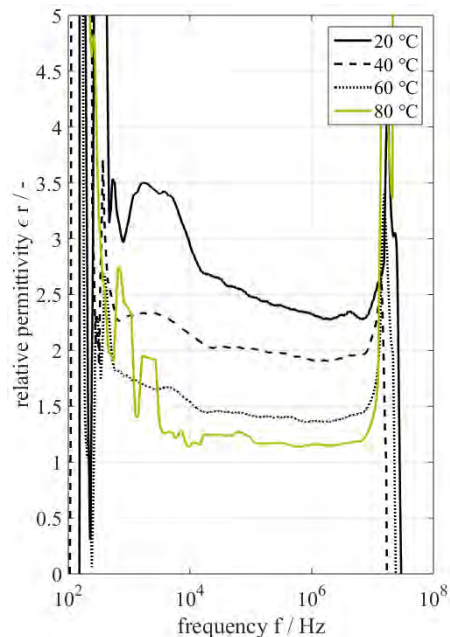on, a medium voltage level has been selected so that EDM breakdowns can be detected on the rolling bearing. If the bearing voltage is too low, the insulating lubricating film can prevent EDM breakdowns. If the voltage is too high, the bearing voltage may be much higher than the voltage that the lubricating film can hold and ohmic currents may flow through the rolling bearing.

Two types of bearings were examined in the tests with voltage applied to the bearing. The first bearing type is the standard bearing 51208 with 15 rolling elements of 100Cr6, the second bearing type is the modified rolling bearing 51208 with 14 rolling elements of Si3N4 and one rolling element of 100Cr6. The speed of the tests is 1000 rpm, the force is 200 N. The temperature varies from approx. 15 °C to 90°C. The rolling bearings were lubricated with FVA 4 oil. For each test, a voltage of 20 V was applied to the rolling bearing. The frequency is 10 kHz, the speed is 1000 rpm and the load is 200 N. Because of the temperature increase at the same load and speed, the lubricant film height is reduced. At lower temperatures of approx.15 °C the roller bearing runs under full film lubrication conditions. There are no breakdowns. At a certain moment, when the quality of the lubricant film is insufficient, EDM breakdowns are detected. EDMs are detected when voltage collapse occurs and a high current flows simultaneously. The detected breakdowns are evaluated. The average EDMs per second, the average breakdown voltage and breakdown current as well as the minimum and maximum values of breakdown voltage and breakdown current are evaluated. The results for the average EDM number per second for six experiments are shown in Figure 20.

The results for the tests with the standard rolling bearing with 15 rolling elements of 100Cr6 are shown using the black lines. The results of the tests with the modified rolling bearing are shown with the yellow lines. The results of the tests with the standard bearing show a pronounced maximum number of EDMs per second. This is the expected behavior of an applied voltage system in which the lubricant film height varies from full lubrication to mixed friction. Similar results for measurements with greases were presented in [31].

EDM breakdowns on standard bearings start at approx. 18°C. The maximum is at approx. 20°C. From 40°C no more breakdowns can be detected. With the modified rolling bearing, the EDM breakdowns start at approx. 45°C. In the temperature range up to approx. 90°C no clear maximum of EDM breakdowns was observed. In the temperature range from approx. 45°C to 90°C there are continuous EDM breakdowns. One reason for this is the smaller rolling element diameter of the rolling element made of 100Cr6. Calculations of the rolling element expansions of the rolling elements made of ceramic and steel have shown that from a temperature of 47°C the rolling elements have the same size. It's a very good match to the beginning of the breakdown range. During the tests it was found that the heating of the standard rolling bearing is much faster than the heating of the modified rolling bearing due to friction. It was also determined that the temperature of the rotating and the stationary ring of the rolling bearing should be the same, if possible, so that the measurements can be reproduced. The uniform cooling of the bearing ring and the start of the test at the same temperature of the bearing rings is important for reproducible testing.
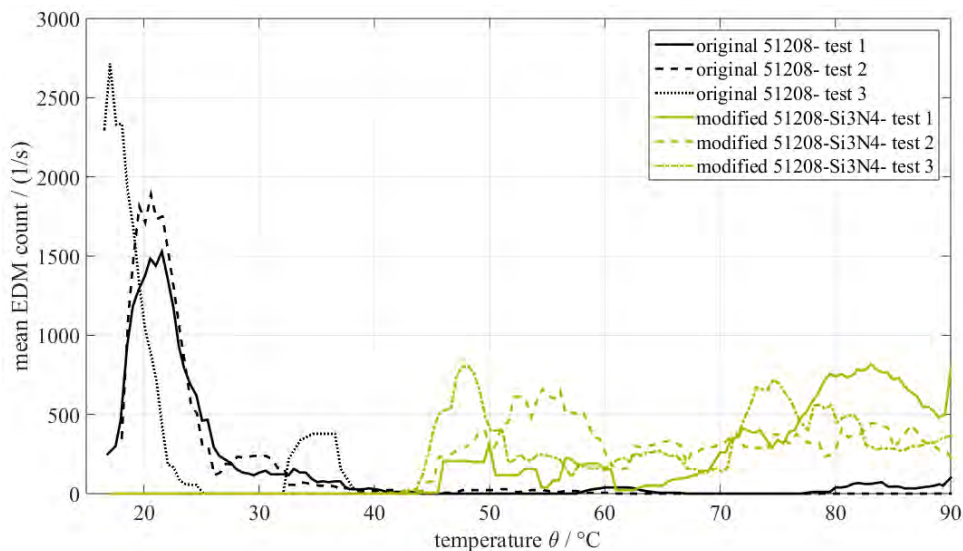
Figure 20: Investigation of the average number of the EDM breakdowns in respect to the temperature for standard bearings 51208 with steel balls and modified 51208-Si3N4 (1 steel ball, 14 Si3N4 balls); three measurements per bearing variant

At the same time as evaluating the average EDM number per second, the average breakdown voltage was also evaluated. The results are shown in Figure 21. It can be seen that in the range of 20 to 40 °C the average breakdown voltage is higher and decreases as the temperature increases. As the height of the lubricating film decreases as the temperature increases, it cannot hold the applied voltage and there are breakdowns. Impedance measurements showed that the system has an impedance of

approx. 10000 Ω at 80 °C, which means that the transition to mixed friction takes place. For this reason, not many breakdowns in the higher temperature range can be detected because the system has resistive behavior.

To determine the breakdown field strength in the rotating bearing, the minimum lubricating film thickness for the investigated conditions was calculated. The results for the calculated lubricant film thickness and for the measurements on the roller bearing are shown in Table 1-1.

Temperature / °C	h_{min} / µm	U_{mean} / V	E_b / V/µm	
20	1,01	13,5	13,4	
40	0,43	7,1	16,3	
60	0,23	6	26,1	
80	0,14	5,1	36,4	

Table 1-1: Calculated values for the minimum lubricant film thickness and for the breakdown field strength and measured values for the average breakdown voltage in the rolling bearing.

The results for the measurements with the Breakdown Analyzer and with variation of the oil temperature and with variation of the distance between the electrodes are shown in Table 1-2.

Temperature / °C	E_{BA75T} / V/µm	
20	4,9	
40	3,9	
60	4,3	
80	7	
Distance between electrodes / mm	E_{BA75A} / V/µm; (mm)	
2	22,4	
1	36,7	
0,5	36	
0,2	68,6	

Table 1-2: Results of measurements on the Breakdown Analyzer by varying the temperature and varying the distance between the electrodes with the FVA 4 reference oil.

The measured values on the Breakdown Analyzer differ from the measured values on the rotating rolling bearing. However, the values are in the same ratio to each other. As the distance between the electrodes or between the bearing surfaces is reduced, the breakdown field strength increases. With the variation of the temperature the values remained in the range of

5 V/µm. There can be several reasons for differentiating between the values. Geometrically, these are two different capacitors with different geometries. This means that the formation of the electric field is different in the rolling bearing and in the Breakdown-Analyzer. This can cause the breakdowns to occur at a different voltage level.
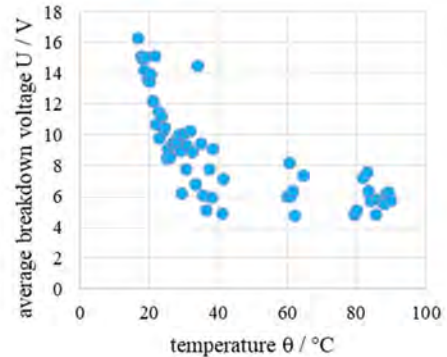

Figure 21: Average breakdown voltage for a test with bearing 51208 at 20 V, 200 N, 1000 rpm and FVA 4 reference oil with variation of temperature

Another possibility would be the pressure during the breakdown. The pressure greatly influences the breakdown field strength of the lubricant. As the pressure increases, the breakdown field strength increases, which can justify the increase in this value during measurements in the rolling bearing, as higher pressures act in the bearing [32].

The breakdown behavior of lubricants is a very interesting and important topic for the modelling of the overall system. For this reason, further investigations are to be carried out until this subject area and the processes in the rolling bearing have been investigated.

9. Conclusions

Within the scope of this paper, different methods for determining the electrical lubricant properties are presented. On the one hand, the properties can be determined with the aid of laboratory measuring instruments at standstill. In a Breakdown-Analyser the breakdown voltage and breakdown field strength can be determined. With the help of the capacitor for liquid examinations the relative permittivity and the specific electrical resistance can be determined. However, the test conditions do not correspond to the higher pressures and temperatures in the rolling bearing contact. For this reason, a rolling bearing adapter was developed which allows the determination of the electrical lubricant properties directly on the rolling bearing. With the help of impedance and phase angle measurements, capacitance and resistance of the system can be characterized and the relative permittivity and the specific electrical resistance can be determined. EDM breakdowns can be generated by applying electrical voltage to the rolling bearing. The breakdown field strength of the lubricant can be determined by evaluating these breakdowns in the bearing. The methodology developed in the context of this paper will be used to investigate the electrical lubricant properties of oils and greases.

Acknowledgment

References

[1] G. Preisinger: Cause and effect of bearing currents in frequency converter drive electrical motors – investigation of electrical properties of rolling bearings, PhD thesis, TU Wien, (2002).

[2] A. Romanenko: Study of inverter-induced bearing damage monitoring in variable-speed-driven motor systems, PhD thesis, Lappeenranta University of Technology, (2017).

[3] A. Muetze: Bearing Currents in Inverter-Fed AC Motors, PhD thesis, TU Darmstadt, (2004).

[4] H. Tischmacher, S. Gattermann: Einflussgrößen auf Lagerströme bei umrichtergespeisten Elektromotoren, VDI-Berichte 2202, (2013), p. 45-59.

[5] B. Radnai, T. Kiekbusch, B. Sauer: Schmierfilmdickenabhängige Entladevorgänge in strombelasteten Wälzlagern. in: ant Journal, Nr. 3 (2014), p. 22-27.

[6] B. Radnai, T. Kiekbusch, B. Sauer: Einfluss der Schmierfilmdicke auf den Stromdurchgang an Wälzlagern, (VDI Berichte, 2257), in: VDI-Fachtagung Gleit-und Wälzlagerungen 2015. Gestaltung, Berechnung, Einsatz, (2015), p. 91-103.

[7] Y. Gemeinder, M. Schuster, B. Radnai, B. Sauer, A. Binder: Calculation and validation of a bearing impedance model for ball bearings and the influence on EDM-currents, XXI International Conference on Electrical Machines (ICEM´2014), Berlin, (2014), p. 1798-1804.

[8] B. Radnai: Wirkmechanismen bei spannungsbeaufschlagten Wälzlagern, PhD thesis, TU Kaiserslautern, 2016.

[9] T. Zika: Electric discharge damaging in lubricated rolling contact, PhD thesis, TU Wien, (2010).

[10] E. Taslak, O. Arikan, C. F. Kumru, O. Kalenderli: Analyses of the insulating characteristics of mineral oil at operating conditions, Electr Eng; 100:321-331, Yildiz Technical University, Istanbul, Turkey, (2018).

[11] A. Joshi, J. Blennow: Electrical characterization of bearing lubricants, Annual Report Conference on Electrical Insulation and dielectric phenomena, Chalmers University of Technology Gothenburg, Sweden, (2014).

[12] A. Jagenbrein: Investigations of Bearing Failures due to Electric Current Passage, PhD thesis, TU Wien, (2005).

[13] R. A. El-Adly, G. M. Turky: Comparative study between prepared electrical grease and the imported one, Egyptian Journal of Petroleum 27, p. 209-213, Egypt, (2018).

[14] B. Radnai, Y. Gemeinder, B. Sauer, A. Binder: Schädlicher Stromdurchgang (FVA 650 I, Heft 1127), Forschungsvereinigung Antriebstechnik e.V., Frankfurt, (2015).

[15] H. Stache, S. Petri: Vor Entladungsschäden schützen – Elektrisch leitfähiges Wälzlagerfett vermeidet Spannungsüberschlag, Der Konstrukteur – Sonderheft "Antreiben – Steuern – Bewegen", (2008), p. 106–107.

[16] DIN EN 60247: Isolierflüssigkeiten – Messung der Permittivitätszahl, des dielektrischen Verlustfaktors (tan δ) und des spezifischen Gleichstrom-Widerstandes, Berlin: Beuth Verlag, (2005).

[17] O. Kreil: Einfluss der Oberflächenstruktur auf Druckverteilung und Schmierfilmdicke im EHD-Kontakt, PhD thesis, TU München, (2008).

[18] R. Schrader: Zur Schmierfilmbildung von Schmierölen und Schmierfetten im elastohydrodynamischen Wälzkontakt, PhD thesis, Gottfried Wilhelm Leibnitz Universität Hannover, (1988).

[19] DIN EN 60156: Isolierflüssigkeiten, Bestimmung der Durchschlagspannung bei Netzfrequenz, Berlin: Beuth Verlag, (1996).

[20] DIN 51412: Prüfung von Mineralölerzeugnissen – Bestimmung der elektrischen Leitfähigkeiten, Berlin: Beuth Verlag, (2013).

[21] H. Phrashad: Tribology in Electrical Enviroments, Elsevier, Amsterdam, 2006.

[22] K. D. Schuster: Kampf der Elektroerosion, in: Der Konstrukteur, Produkte und Anwendungen, Konstruktionselemente, (2017).

[23] M. J. Furey: Metallic Contact and Friction between Sliding Surfaces, ASLE TRANSACTIONS, 4:1, 1-11, DOI: 10.1080/05698196108972414, (1961).

[24] M. J. Furey: Surface Roughness Effects on Metallic Contact and Friction, ASLE TRANSACTIONS, 6:1, 49-59, DOI: 10.1080/05698196308971998, (1963).

[25] C. Wittek: Charakterisierung des Schmierungszustandes im Rillenkugellager mit dem kapazitiven Messverfahren, PhD thesis, Gottfried Wilhelm Leibnitz Universität Hannover, (2017).

[26] K. Jablonka, R. Glovnea, J. Bongaerts: Evaluation of EHD films by electrical capacitance, Journal of Physics D: Applied Physics 45, University of Sussex, Brighton, UK, (2012).

[27] T. Maruyama, K. Nakano: In Situ Quantification of Oil Film Formation and Breakdown in EHD Contacts, Tribology Transactions, DOI: 10.1080/10402004.2018.1468519, (2018).

[28] R. S. Heemskerk , K. N. Vermeiren, H. Dolfsma: Measurement of Lubrication Condition in Rolling Element Bearings, ASLE TRANSACTIONS, 25:4, 519-527, DOI: 10.1080/0569819820898312, (1982).

[29] M. Barz: Die Schmierfilmbildung in fettgeschmierten schnelllaufenden Spindellagern, PhD thesis, Gottfried Wilhelm Leibnitz Universität Hannover, (1996).

[30] N. Bader, A. Furtmann, H. Tischmacher, G. Poll: Capacitances and lubricant film thicknesses of grease and oil lubricated bearings, STLE, Atlanta, (2017).

[31] D. Bechev, T. Kiekbusch, B. Radnai, B. Sauer: Untersuchung der Auswirkungen von leitenden und nichtleitenden Schmierfetten auf die Oberflächeneigenschaften bei spannungsbeaufschlagten Wälzlagern, GfT-Tagung, Göttingen, (2017).

[32] M. Koch, M. Fischer, S. Tenbohlen: The breakdown voltage of insulation oil under the influences of humidity, acidity, particles and pressure (International Conference APTADM). Wroclaw, Poland, Sept, (2007), p. 26-28.

Investigation of Rolling Bearing Condition Monitoring Techniques Based on Long Term Run-to-Failure Vibration Data

Reza Golafshan[1], Georg Jacobs[2], Joerg Berroth[3]

[1] *RWTH Aachen University, Institute for Machine Elements and Systems Engineering (MSE)*
reza.golafshan@imse.rwth-aachen.de

[2] *RWTH Aachen University, Institute for Machine Elements and Systems Engineering (MSE)*
georg.jacobs@imse.rwth-aachen.de

[3] *RWTH Aachen University, Institute for Machine Elements and Systems Engineering (MSE)*
joerg.berroth@imse.rwth-aachen.de

Abstract – Vibration-based Condition Monitoring (CM) techniques assume that failure probabilities can be determined based on the current operating status of individual machines. These techniques, therefore offer an opportunity for replacing defected parts or performing desired adjustments in time to preclude failure. Rolling bearings play a major role in rotating machines dynamics, so that their faults can adversely affect the machine performance, and eventually lead to complete failure. The present paper aims to study, discuss, and compare common techniques in the field of rolling bearing fault detection and diagnosis based on vibration signal processing. For this, some basic and advanced methods including statistical parameters and diagnostic methods, respectively, for detection and localization purposes are investigated using bearing run-to-failure vibration datasets. In addition to show and discuss advantages and limitations of the most common statistical parameters, the well-known Principal Component Analysis (PCA) is used for extracting the optimal features and reducing the dimension of extracted features. In line with the purposes of the present study, a recently proposed method based on autocorrelation function is also tested experimentally, illustrating the progression of bearing fault. The results obtained here imply that the effectiveness of bearing fault indicators (features) can be improved using post processing and data fusion techniques. This can increase the capability of early fault detection of vibration analysis for rolling bearings.

Keywords – Condition Monitoring; Vibration Analysis; Bearing fault pattern analysis; Rolling bearing fault diagnosis; Principal Component Analysis (PCA)

1. Introduction

There is nowadays no doubt that a modern and well-integrated maintenance strategy can lead to optimum productivity and efficiency of industrial machines [1, 2]. Modern maintenance strategies (e.g. predictive or proactive) increase the probability that a machine or component can run in the required manner over its design life-cycle with a minimum amount of maintenance and downtime. These maintenance strategies are optimally integrated to take advantage of their respective strengths, and maximize facility and equipment reliability while minimizing life-cycle costs. The goal is to reduce the Life-Cycle Cost (LCC) of a facility to a minimum to obtain the desired reliability and availability [3]. In this regard, the predictive or proactive maintenance strategies use primarily non-destructive Condition Monitoring (CM) testing tools to assess machinery health status and performance [4]. With the increasing use of Condition Monitoring Systems (CMS) on industrial machines, a large number of researches have been under taken for diagnostic purposes in sub-components in, for example, a drivetrain [5, 6]. Among a wide range of CM tools, mechanical vibration signals monitoring is known as one of the most robust and common methods. It is widely accepted that vibration analysis is capable of finding machine element fault(s) and their location(s) [7]. In a vibration-based fault detection and fault diagnosis system, mechanical damage is referred to changes on geometric properties of the analyzed machine. These sudden changes may generate additional dynamic forces acting in the system. Then, based on the system responses, damage/faults can be detected and localized [8]. Since all machines vibrate even in their good operational condition due to interactions between machine components, the captured vibrations signals are required to be analyzed using signal post-processing techniques [9, 10].

Due to the critical role of rolling bearings in global vibration levels of rotating machines, vibration-based fault detection for bearings is considered as one of the most common and reliable approaches in ma-chine condition monitoring. Statistics show that 30% of rotating machinery faults are caused by rolling bearings [11], and 90% of the total amount of different rolling bearing faults are related to either an inner or outer race flaw (pitting) [12]. Rolling bearings faults can lead to serious problems such as noise and high vibration level up to the total loss of a drivetrain and degrade the performance in many mechanical engineering applications such as centrifugal pumps [13], drivetrain of wind turbines [14], gearboxes [15], and railway vehicles [16]. Therefore, many diagnosis methods aim to identify the bearing fault symptoms in the vibration signal measured from a system with suspected faulty bearing(s). The mechanical faults on bearing surfaces give raise to the vibration signals at the certain intervals, depending on fault location. By analyzing the changes and novelties in the vibration trend, bearing faults can then be detected and diagnosed. In general, signal processing techniques applied for bearing applications comprise three phases, namely, detection, diagnostic, and prognostic [7].

With reference to the findings in [3], Figure 1 shows the failure distribution of thirty identical 6309 type deep groove ball bearings installed on bearing life test machines and run to failure, using standard test procedures. Here, the x-axis represents the individual bearing being tested while the y-axis is the number of revolutions achieved prior to fatigue failure of the individual bearing. The wide variation in bearing life prevents the use of any effective time-based or classical maintenance strategy, and this suggests more and more studies on the bearing condition monitoring.
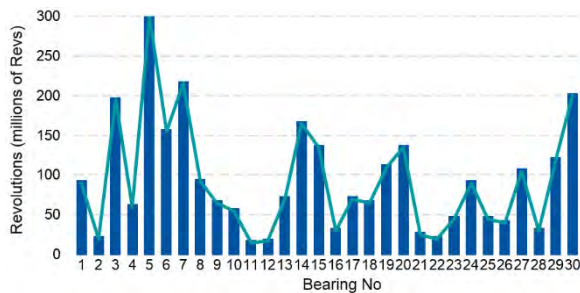

Figure 1: Rolling bearing life Scatter; adapted from [3].

The rolling bearing fault detection methods can be broken-down into three well-known signal domains (i.e. time, frequency, and time-frequency), where some parameters in various domains (features) are extracted and analyzed accordingly. Fault feature extraction of rolling bearing vibration signals is carried out using statistics. As mentioned, when rolling bearing faults occur, time and frequency statistical features of vibration signal change. By trending these features of the monitored bearing over time, the status of the corresponding bearing can be detected. A large number of fault indicators are investigated and proposed in the literature [17, 18, 19], most of them suitable for a specific operating condition with potential limitations in application due to environmental conditions including noise effects.

Attempts at analyzing large numbers of original features are motivated by how to effectively extract the potential features responsible for fault characterization. In a typical monitoring processes, hundreds of variables each of which for a specified time window are measured over time. While these measurements (features) can bring in useful signatures about the operating status, at the same time they can introduce more complexities because of the high dimensionality. To overcome this, some data reduction/fusion techniques can be used.

Principal Component Analysis (PCA) [20], also known as the Karhunen–Loeve transform, is a basic method in the system of multivariate analysis. By transforming a complex dataset to a simple one with lower dimension, PCA reduces the less significant information in dataset for further computing. Because of its excellent capability in extracting relevant information from confusing datasets, PCA has been successfully applied in numerous areas including data compression, feature extraction, image processing, pattern recognition and process monitoring in recent years [21, 22]. PCA is one of the most popular multivariate statistical methods used for process monitoring and data compression/fusion. When PCA-based feature extraction is used for example for, machine bearing fault classification, it is believed that reduced dimensional data which is arranged along the principal eigenvectors could represent features effectively. In gearbox applications, it is shown that the low-dimensional principal component can represent the statistical features of the measured signals to characterize and monitor gearbox conditions.

In terms of fault diagnostics and fault localizations, although many signal processing methods for bearing diagnosis have been studied and published [10], a robust fault diagnosis algorithm suitable for non-stationary operating conditions for complex machines remains a challenge.

Among a wide range of diagnosis methods for rolling bearings, AutoCorrelation analysis [23] appears to be one of the powerful tools due to both de-noising and diagnostic features of the autocorrelation function, which makes it a very valuable tool for fault detection purposes [7]. In general, for a periodic component in the signal, autocorrelation function yields high levels of correlation for the corresponding component. This is the key factor of the autocorrelation function in revealing the repetition frequencies (e.g. bearing fundamental frequency) in a captured vibration signal even in a low signal-to-noise ratio (SNR) environment. Recently, in [24] it is proposed that a combination of the recursive autocorrelation analysis and AR-based signal modelling can improve the reliability of envelope analysis for rolling bearing fault diagnosis.

The rest of this present paper is organized as follows: the section 2 -"Theoretical framework" details the fundamentals of rolling bearing vibration-based fault detection and diagnostic. Also, a brief summary of previously proposed fault diagnosis method, Recursive Autocorrelation Analysis (RAC), as well as PCA is presented here for the sake of completeness and clarity. In the section 3 - "Description of the test-rig and tests procedures" the case studies used are presented. Section 4 - "Results and discussion" addresses the applications of the discussed methods with the vibration signals obtained from field tests. Finally, conclusions are drawn in section 5 - "Conclusions."

2. Theoretical framework

In this section, starting from spectral analysis, the fundamentals of vibration-based fault detection and diagnosis for rolling bearings are stated. In addition, the recently proposed, Recursive Autocorrelation (RAC) Analysis and the well-known PCA are summarized.

2.1. *Bearing fault pattern analysis*

In general, the bearing fault patterns in terms of some progressive stages of damages can be shown and analyzed using spectral analyses. These fault patterns are investigated in the literature and technical reports [25, 26], and are shown in Figure 2 adapted from [27]. Close inspection of these four spectra representing four distinct fault stages can provide useful information about the failure modes. Figure 2 shows the spectrum frequency content during four stages of bearing failure. A normal bearing or newly installed bearing will show no frequencies except those associated with shaft phenomenon such as balance or misalignment.
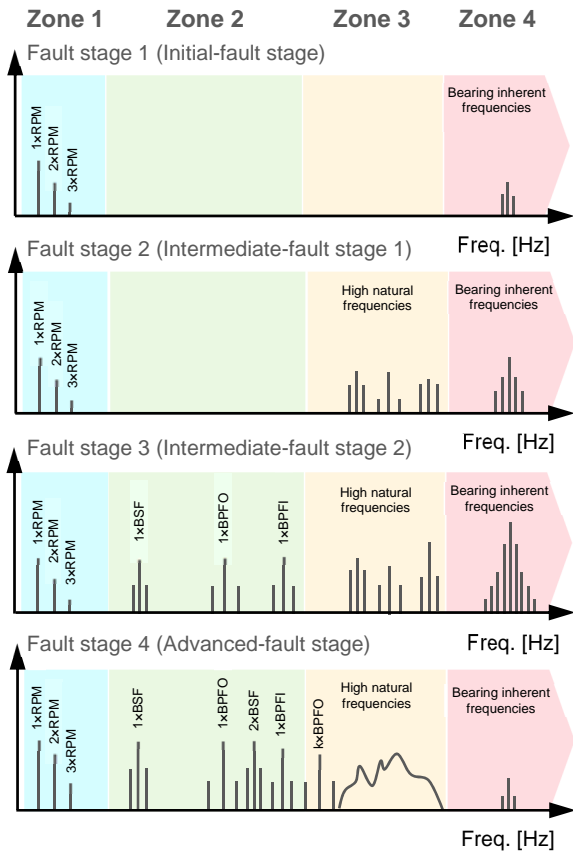
Figure 2: Fault patterns of rolling bearing damage stages; adapted from [27].

Fault stage 1 begins to generate signals associated with natural resonances of the bearing parts as defect begins to excite the sub-components. At this stage, micro-defects and tiny crack initiation causes very high frequency impulsive signals in zone 4. However, Acoustic Emission (AE)-based techniques as the ultra-frequency methods are typically used for the faults at this stage, rather than vibration analysis. Physical inspection of the bearing at this stage may not show any identifiable defects. Fault stage 2 condition, called intermediate-fault 1, produce impulsive high-energy vibration signals correspond to rotor-bearing total system high frequencies in zone 3. Signs of defects may be found upon inspection. At fault stage 3, called intermediate-fault 2, as the faulty area becomes large, impulsive signals due to the localized fault produce the corresponding bearing fundamental frequency(s). Harmonics of these frequencies may also appear depending upon the quantity of defects and their dispersal around the bearing races. The well-known envelope analysis is the most common method for detecting the bearing faults at this stage. Fault stage 4 is the last condition before catastrophic failure of the bearing and break-down. This stage is associated with numerous modulated fundamental frequencies and harmonics indicating that the defects are distributed around the bearing races.

Using the above mentioned spectral information, rolling bearings can be diagnosed and location of the faults can be detected. As a matter of fact, time do-main signals need to be transformed to the frequency domain.

2.2. *Bearing feature extraction and fault detection*

Online and continuous condition monitoring techniques are generally based on extracting some statistical parameters in the time or the frequency domains. Here, the goal is to approve and verify the existence of a fault on rolling bearing. For this, a large number of potential statistical features for bearing fault detection have been proposed in the literature, and are readily available. These statistical parameters (features) are designed to represent a specific vibration signal. Basic and common statistical features in the time domain include Root Mean Square (RMS), Kurtosis [28], Variance, Crest Factor, Skewness, shape factor (i.e. RMS - mean value) [29], and bearing defect factor (i.e. peak value - RMS) [30]; and advanced features including Singular Values (SV) and entropy [31, 32]. Teager Energy RMS and Teager Energy Kurtosis are also features obtained using energy time domain signal [33, 34]. In addition to time domain features, frequency domain features such as ball, cage, inner race, and outer race energy, which compute the energy level around the corresponding fault frequency are also used for detection purposes [35].

High dimensionality of the extracted features can bring extra and unnecessary complexities. As there is no globally-accepted method and monitoring feature for rolling bearings, some time and frequency domains features need to be derived from captured vibration signals. However, using data reduction/fusion techniques may overcome this issue.

2.2.1. *Principle Component Analysis (PCA)*

Principal component analysis (PCA) is a linear technique for dimensionality reduction by maintaining as much variance as possible [13]. PCA constructs a low dimensional representation of the data that describes as much of the variance in the data as possible. This is done by finding a linear basis of reduced dimensionality for the data, in which the amount of variance in the data is maximal. Although it is a linear method, the performance of PCA is efficient for dimensionality reduction in bearing applications, which can reduce the complexity of signal processing.

Though the more features selected from original data, the more information about operating condition might be maintained, but the computational cost increase. Moreover, some of the features exacted may be closely relevant to others that reduce the significance of large amount of computing. Fortunately, PCA provides a means to the identification of the most representative features and the decrease of the dimension of the feature space.

The N dimension matrix $Y(y_1, y_2, ..., y_N)$ is the feature vector matrix consisting of the N features (parameters) acquired in the feature extracting process and its column vectors are the dimension feature vectors. According to [11], the covariance matrix of Y is calculated as

$$C_y = \sum_{i=1}^{N}(y_i - \bar{y})(y_i - \bar{y})^T \qquad (Eq.\ 2\text{-}1)$$

where N stands for the number of samples and $\bar{y}$ is the mean vector of each feature vector that is given by

$$\bar{y} = \frac{1}{N}\sum_{i=1}^{N}y_i \qquad (Eq.\ 2\text{-}2)$$

The eigenvalue of C_y can be calculated by

$$\lambda v = C_y v \qquad (Eq.\ 2\text{-}3)$$

where λ ist he eigenvalue of C_y and ν is the eigenvector of C_y. At most d eigenvalues $\lambda_i (i = 1,2, \dots, d)$ are calculated and $\lambda_1 > \lambda_2 > \dots > \lambda_d$, corresponding to eigenvector $\nu_i (i = 1,2, \dots, d)$. Then the principle component of ν_i can be obtained by projecting sample y_j to eigenvector ν_i as

$$PC_{ij} = \nu_i^T (y_j - \bar{y}) \qquad (Eq.\ 2\text{-}4)$$

The first principal component accounts for as much of the variability in the data as possible, and each succeeding component accounts for as much of the remaining variability as possible. After the PCA process, most information of the original signal remains in the first several principal components. Therefore the properties of the original data can be approximately represented by the first m (m < d) principal components.

2.3. Bearing fault diagnosis

Envelope analysis, as the most common method for bearing fault diagnosis, is based on demodulation of high frequency resonance associated with bearing element impacts. For rolling element bearings, when the rolling elements strike a local fault on the inner or outer race, or a fault on a rolling element strikes the inner or outer race, an impact is produced. These impacts (impact train) modulate a signal at an associated bearing pass frequency, such as Cage Pass Frequency (CPF), Ball Pass Frequency Outer Race (BPFO), Ball Pass Frequency Inner Race (BPFI), and Ball Fault Frequency (BFF). In many cases, ball passing frequency is modulated with BPFO or BPFI. Consequently, a complex frequency spectrum may result-in from this process. In addition, captured raw rolling bearing vibration signals certainly contain some background noise due to environmental conditions and it frequently makes interpretations of the spectrum quite complex. As a result, some de-noising and signal enhancement processes are strongly recommended in the literature in order to get a smoother spectrum which can be used to extract diagnostic information.

4.1.1. Recursive Autocorrelation (RAC) analysis

Autocorrelation is defined as a delayed correlation of the time domain signals, which is a useful tool in cyclostationary signal processing for extracting the periodic components (i.e. repeating patterns) that may be covered by background noise. The autocorrelation function, R_{xx}, is defined as a repetition detector or self-similarity detector for a time domain signal, $x(t)$. Mathematically and in its continuous form, it is expressed as [7]

$$R_{xx}(\tau) = \lim_{T \to \infty} \int_0^T x(t)\, x(t + \tau)\, dt \qquad (Eq.\ 2\text{-}5)$$

and in its discrete version as

$$R_{xx}(k) = \sum_{n=-\infty}^{\infty} x(n)\, x^*(n - k) \qquad (Eq.\ 2\text{-}6)$$

where T, τ, and k are the measurement period, the time delay, and any integer, respectively. Also * stands for complex conjugative. Noted that for a real function $x = x^*$. Based on the Wiener-Khinchin theorem, if the Fourier transform of a series, $x(t)$, is $X(f)$, and if the autocorrelation function of the series is R_{xx}, then the Fourier transform of R_{xx} yields $S_{xx}(f) = |X(f)|^2$, i.e. power spectrum of $x(t)$. It is noteworthy that in general, autocorrelation requires a normalization (e.g. biased or unbiased) to produce an accurate estimate. From the definition, it is expected that for a weakly defined noise signal (e.g. white noise), the autocorrelation is zero everywhere except at $\tau = 0$.

As originally proposed in [24], and further improved in [24a], the present paper proceeds from the latter feature of the autocorrelation function in dealing with noise and random components, and proposes a recursive-based implementation of it by eliminating a few first time lags in each recursive order to minimize the noise effects. On the other hand, the autocorrelation function itself has repetition characteristics in the sense that autocorrelation function detects not only the repetition periods but also the integer multiples of the repetition periods of the time domain signal. This feature of the auto-correlation function allows one to determine the repetitions in the time domain signal more precisely by computing the correlation of the autocorrelation function with itself in a recursive manner. If the autocorrelation function is carried out r times, the rth order recursive autocorrelation function for a real and one-sided signal (time series) can be defined as [24]

$$R_{xx}(k_r) = \sum_{k_{r-1}=1+m}^{N} R_{xx}(k_{r-1})\, R_{xx}(k_{r-1} - k_r) \qquad (Eq.\ 2\text{-}7)$$

where k_r is the rth shifting factor (i.e. time delay), $R_{xx}(k_0)$ is regarded as the original signal, $x(n)$, and N is the number of captured data-points available in signal. Also, m is the first few time lags, which represents the random components.

The complex autocorrelation can similarly be obtained using the complex signals. Noted that, the resulting spectrum is real-valued and not any more symmetric around the Nyquist frequency. The imaginary part of $x(t)$, $x_H(t)$ may be estimated using Hilbert Transform (HT). Then, the complex signal can be formed as

$$E(t) = x(t) + jx_H(t) \qquad (Eq.\ 2\text{-}8)$$

The so-called envelope signal is the magnitude of this complex analytic signal.

Figure 3 shows the flowchart summarizing the pro-posed algorithm for rolling bearing applications. First, the captured vibration signal passes through the pre-whitening process by an AutoRegressive (AR)-based signal modelling prior to further recursive enveloping and autocorrelation processes. The so-called RAC spectrum is obtained by applying the FFT on the envelope signal. The recursive loops, including enveloping and autocorrelation function, may repeated until the detectability of amplitude of the RAC spectrum at the bearing fault frequency starts to reduce. In all recursive orders, the "biased" autocorrelation functions are estimated and autocorrelation functions are normalized such that the value of the function at zero time delay is set to 1.0.
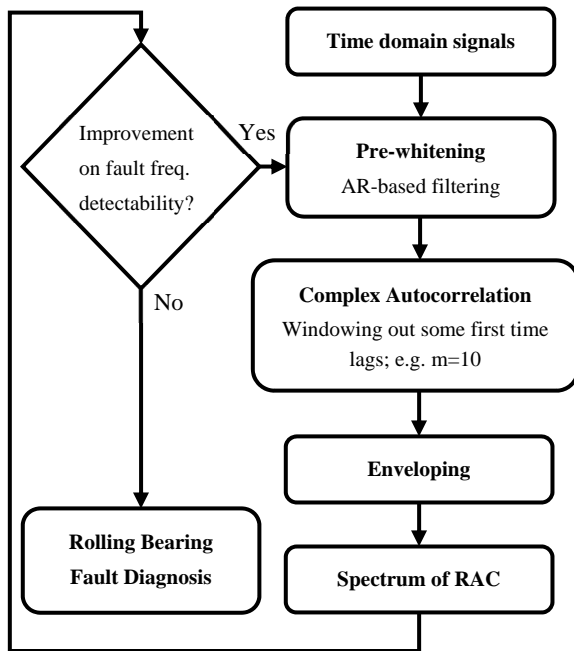
Figure 3: Flowchart of the previously proposed RAC method for rolling bearing fault diagnosis purposes.

It is expected that the recursive autocorrelation approach will enhance the features of autocorrelation function in revealing the repetition components and eliminating the random components. The recursive autocorrelation function then tends to amplify the diagnostic signal in rolling bearing fault detection. From the definition, in the autocorrelation function, all sinusoidal components are converted to cosines, meaning that all harmonics of a particular periodicity line up in phase once per period and make the most impulsive signal possible for those components, and this can possibly be interpreted as enhancing the periodicity. However, autocorrelation does enhance the fundamental frequency, but to the detriment of its higher harmonics. This is a drawback of using autocorrelation for condition monitoring purposes, which can be partially counterbalanced by its excellent diagnostic feature in revealing the periodic component and noise eliminat-ing by windowing out the first few time lags in a recursive manner. The recommended window size for the noise elimination process is first 10 time lags. Similar to the original envelope analysis, RAC can also be used to derive the fault frequencies and corre-sponding magnitudes for online and continuous mon-itoring purposes.

3. Description of the test-rig and tests procedures

In this section a brief description of the test setup as well as tests procedures is given in some detail. The run-to-failure test measurements are conducted at the Center for Intelligent Maintenance Systems (IMS) of the University of Cincinnati with support from Rexnord Corp. in Milwaukee, WI. [36, 37], which are freely available to study and publish under NASA depository license. A schematic and a picture of the test-rig are shown in Figure 4 and Figure 5, respectively.
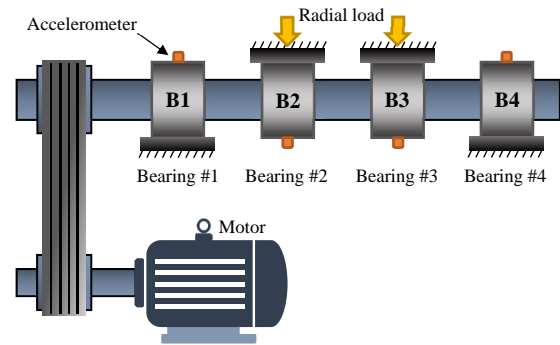

Figure 4: Schematic bearing test-rig at the Center for Intelligent Maintenance Systems (IMS), adopted from [36].

The bearing test-rig consisted of four test bearings on one shaft. The shaft was driven by an AC motor and coupled by rub belts. The rotation speed was kept constant at 2000 rpm. A radial load of 6000 lbs. (26.67 kN) was added to the shaft and bearing by a spring mechanism. All the bearings were force lubricated. An oil circulation system regulated the flow and the temperature of the lubricant. A magnetic plug installed in the oil feedback pipe was continuously collecting debris from the oil as evidence of bearing degradation. All tests were stopped when the accumulated debris adhered to the magnetic plug exceeded a certain level and cause an electrical switch to close.
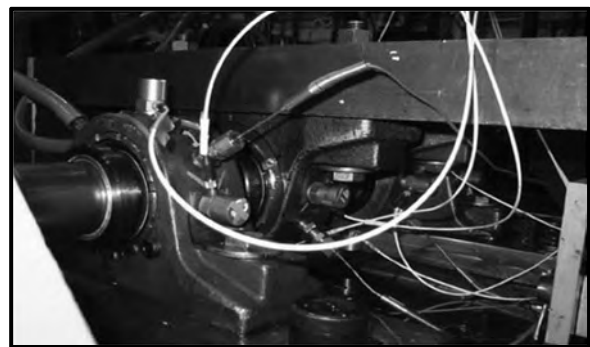

Figure 5: A picture of the test-rig, from [36].

All the four test bearings are Rexnord ZA-2115 double row bearing with 16 rollers in each row. This bearing type has a pitch diameter of 71.5 mm, a roller diameter of 8.4 mm and a tapered contact angle of 15.17°. Based on these geometry information, the corresponding bearing fault frequencies are calculated. The vibration signals are acquired with a sampling frequency of 20 kHz per channel by a National Instruments DAQ Card 6062E data acquisition card. The data recorder is equipped with low-pass filters at the input stage for anti-aliasing. Each sample with 20,480 data points is collected every 10 min. The acceleration sensor is the PCB-353B33 High Sensitivity ICP accelerometer and installed on the bearing housing. Three sets of tests are carried out. All tests are stopped until a significant amount of metal debris was found on the magnetic plug of the test bearing. Test 1 ended up with an inner race defect in bearing 3 and a roller element defect in bearing 4. At the ends of test 2 and test 3, outer race defects occurred in bearing 1 and bearing 3, respectively. Noted that all failures occurred after exceeding designed life time of the bearing which is more than 100 million revolutions.

Three inspection photos from test one and two as well as the corresponding trend of RMS for the entire life cycle are shown in Figure 6. Pre-results in Figure 6 reveal that the RMS trend can generally be divided into two stages. For example, for B3 of test 1, in the first stage, during the first 30 days of operation, no underlying trend can be observed. After the test had been carried out for 30 days (approximately 86.4 million cycles), the RMS started to slightly increase and the rate of change also increased. The time domain feature, RMS, also shows that most of the bearing fatigue time is consumed during the period of material accumulative damage, while the period of crack propagation and development is relatively short. This means that if the traditional threshold-based condition monitoring approaches are used, the time available for the maintenance crew to respond prior to catastrophic failure after a defect is confirmed is very short. An early warning approach that can detect the defect at the early stage is demanded so that enough buffer time is available for maintenance and logistical scheduling. Another important information from Figure 6 is the inconsistent degradation patterns for all test bearings. Even all the test bearings are the same type and are tested under the same operational condition, their RMS trends still show strong inconsistence.

4. Results and discussion

4.1. *Fault detection*

For all case studies, a total number of 41 bearing health indicators (fault features) in which 9 in time-domain and 32 in frequency domain are extracted for experimental investigations. Frequency domain features include the bearing fundamental fault frequencies

and their higher harmonics. However, for the sake of brevity, the results of two case studies, as example, are shown in this section. Here, each captured dataset consists of 1 s of measurement at a specific interval of 10 minutes. Figure 7 presents some basic and advanced time domain-based features related to B3 of test 1. Results presented here can reflect the effectiveness and performance of these features in early bearing fault detections for the test bearing. In fact, close inspection of the results in Figure 7, in particular comparing all the features together, reveal that while some parameters react to the fault initiation at a late stage, singular values (average of first five singular values of the corresponding constructed Henkel matrix using vibration data), RMS, and the amount of entropy (from thermodynamics) of run-to-failure vibration signals are more sensitive to the bearing fault. As seen, some features (e.g. entropy) capture a sudden jump, indicating a fault initiation.

Similar to the previous case study, using vibration data, but this time for B1 of test 2, the corresponding time domain features are plotted in Figure 8. As in the previous case study, all the statistical parameters show individual behavior over time. Again, the singular values shows the superior fault detection capability over some basic and common statistical parameters. However, based on the results presented here and those results obtained from previous case study, once again it is seen that there is no-globally accepted parameters for condition monitoring purposes. In order to guarantee the robustness of the CM tool, a wide range of parameters should be extracted. This suggests to use a self-adaptive data size reduction technique.
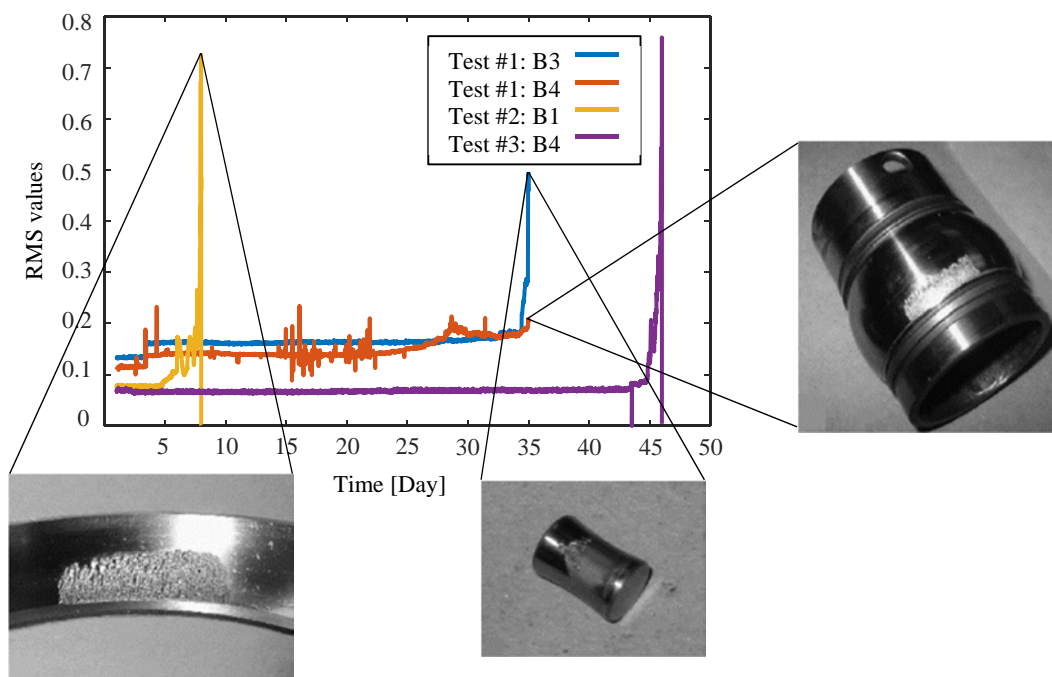

Figure 6: Run-to-failure tests conducted at the IMS test-rig in terms of RMS values for bearings life cycle, showing fault degradation patterns; pictures from [36].
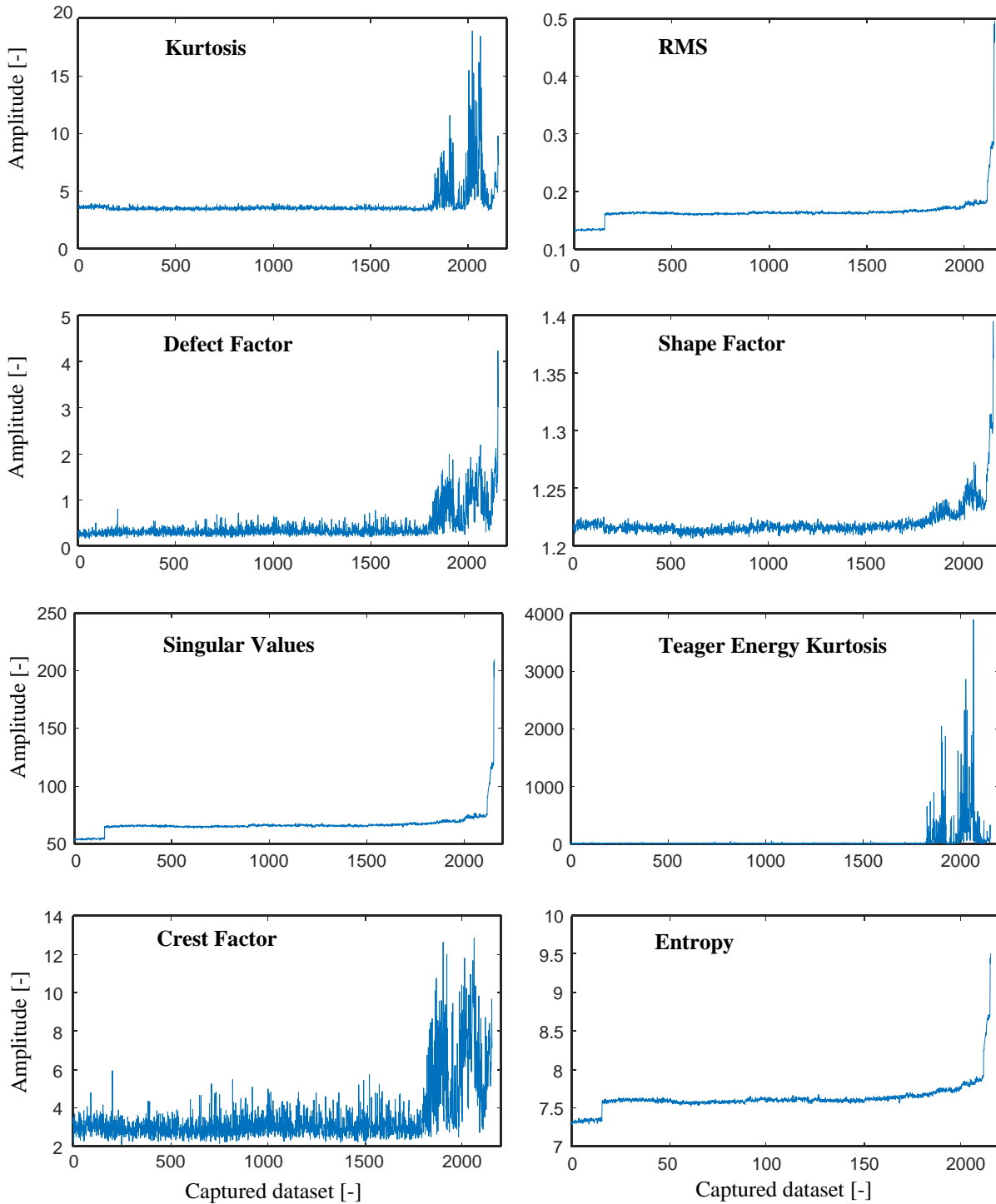
Figure 7: Calculated some well-known time domain features (indicators) related to B3 of test 1.

As explained in the section 2.2.1, PCA can project a number of features into the Principle Components (PCs). These calculated PCs can then represent the input features. Figure 9 shows the first three PCs, describing a total of 41 health indicators (features) of B3 of test 1. 96% of whole the data fed into principle component analysis is explained by PC1, 3.5% by PC2, 0.4% by PC3, and 0.1% by the rest PCs. This also can be seen by trend analysis of PCs shown in Figure 9, where PC1 may introduce an excellent monitoring opportunity instead of dealing with much individual parameters. In addition, Figure 10 presents the projection of 3 PCs, as the most important PCs, using a 3D plot. While PC 1 varies in a

range of 200, PC 2 varies in a range of 30, and 14 for PC 3. Results in Figure 10 confirm all the findings in Figure 9. Similar to test 1, Figure 11 shows principle component analysis results for test 2, but this time using first two PCs, as these two PCs carry the most information. In this case, PC1 and PC2 show the maximum variations. Therefore, unlike the previous case, only two PCs are considered for further investigations. After processing by the PCA algorithm, PC 1 obtained in a self-adaptive manner behaves as the optimum fault feature for this case study. The results for both case studies shown here suggest that the accumulated contribution of the first two PCs reaches more than 99.5% accuracy.
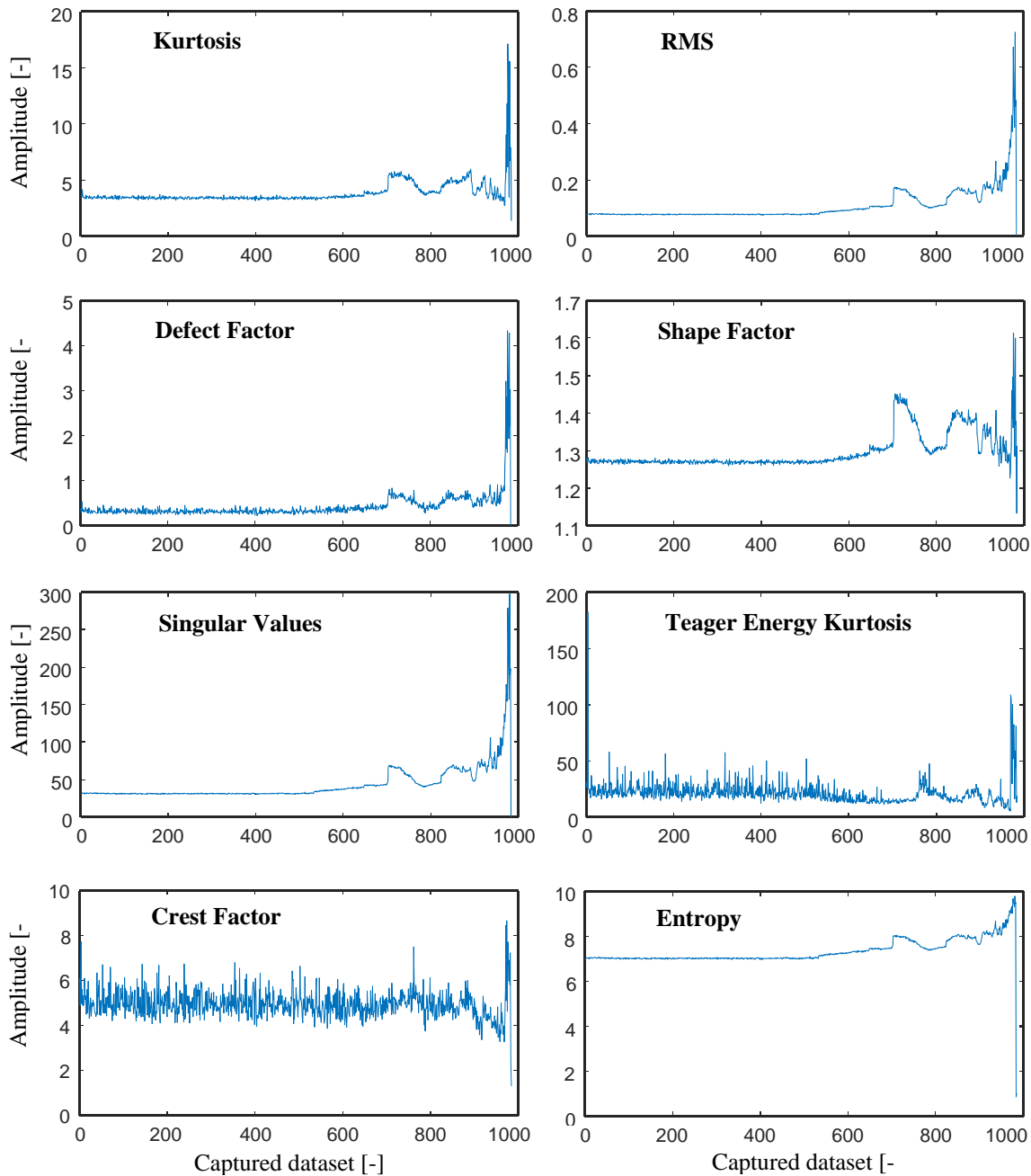
Figure 8: Calculated some well-known time domain features (indicators) related to B1 of test 2.

In both the case studies, it is shown that PC 1 can be a reliable single-parameter, which takes advantages of most relevant parameter(s) and ignores non-irrelevant ones. As it is neither desirable nor practical to deal with a wide range of parameters or indicators, projection of all significant parameters in one single parameter can significantly increase the reliability of a CMS.

It is also worth stating that from the definition accuracy of PCA results depends on quality of the inputs (i.e. health indicators) as it is only a reflection of whole input data.

4.2. *Fault diagnosis*

In the previous section, it is shown that the existence of bearing faults can be detected using statistical parameters together with PCA, as a data fusion method. As a final experimental study, the performances of the envelope and RAC analyses for fault diagnostic purposes are assessed using run-to-failure data for B1 of test 1. Figure 12 and Figure 13 show trends of magnitude of BPFO and its higher harmonics obtained using the envelope analysis and RAC analysis, respectively. As can be seen, frequency spectrum obtained for the RAC method is more sensitive to fault frequencies compared to state-of-the-art envelope analysis. Based on the results in Figure 12 and Figure 13, RAC can immediately react to localized faults on rolling bearings by enhancing the fault features in frequency domain.

RAC method is more sensitive to fault frequencies compared to state-of-the-art envelope analysis. Based on the results in Figure 12 and Figure 13, RAC can immediately react to localized faults on rolling bearings by enhancing the fault features in frequency domain.
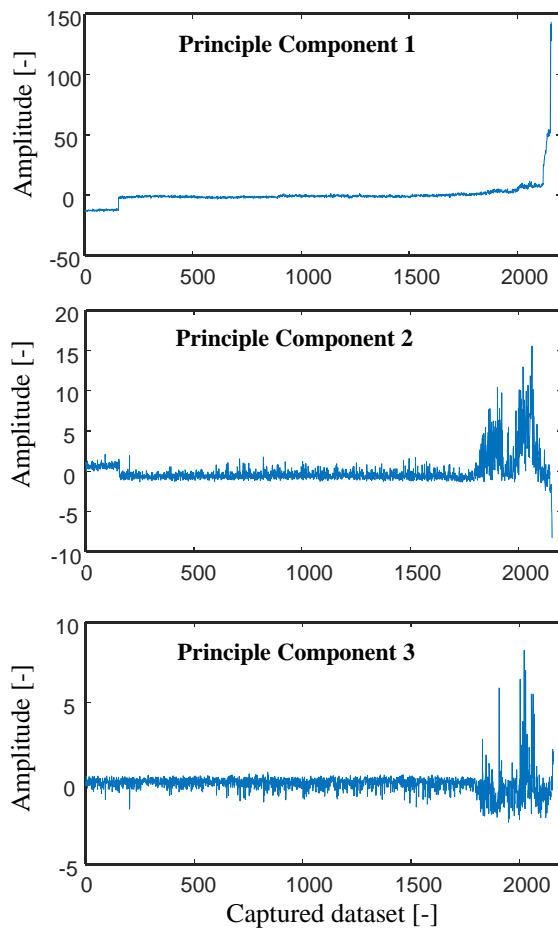

Figure 9: First three principal components (PCs) obtained for health indicators for B3 of test 1.
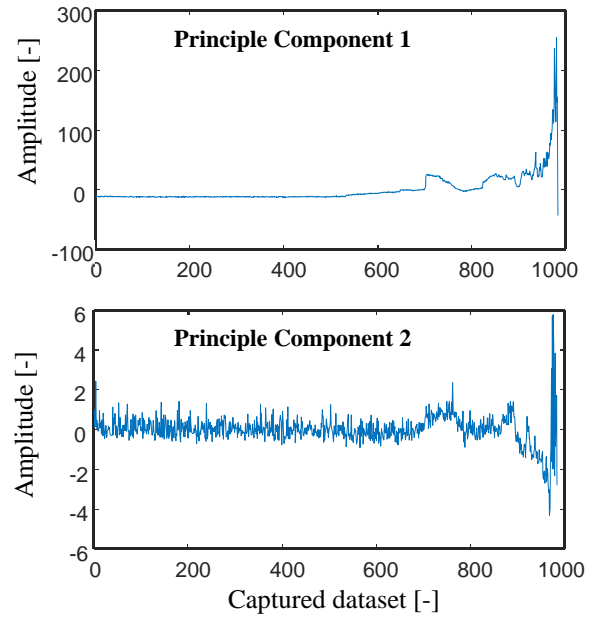

Figure 11: First two principal components (PCs) obtained for health indicators for B1 of test 2.
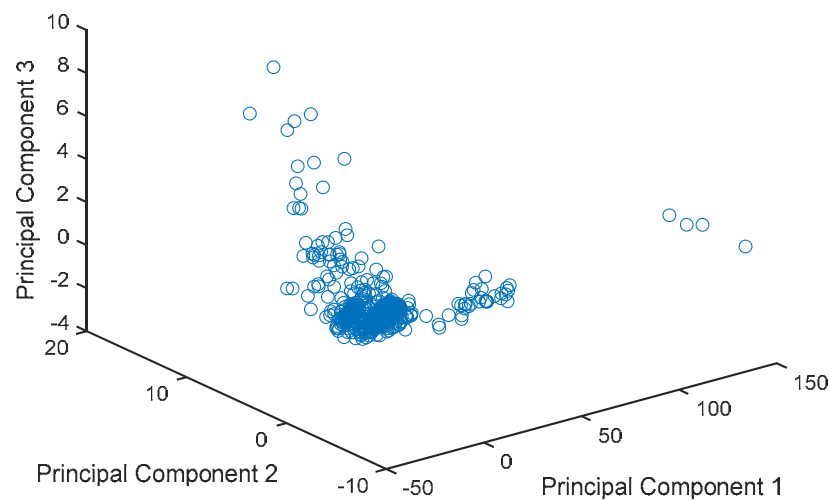

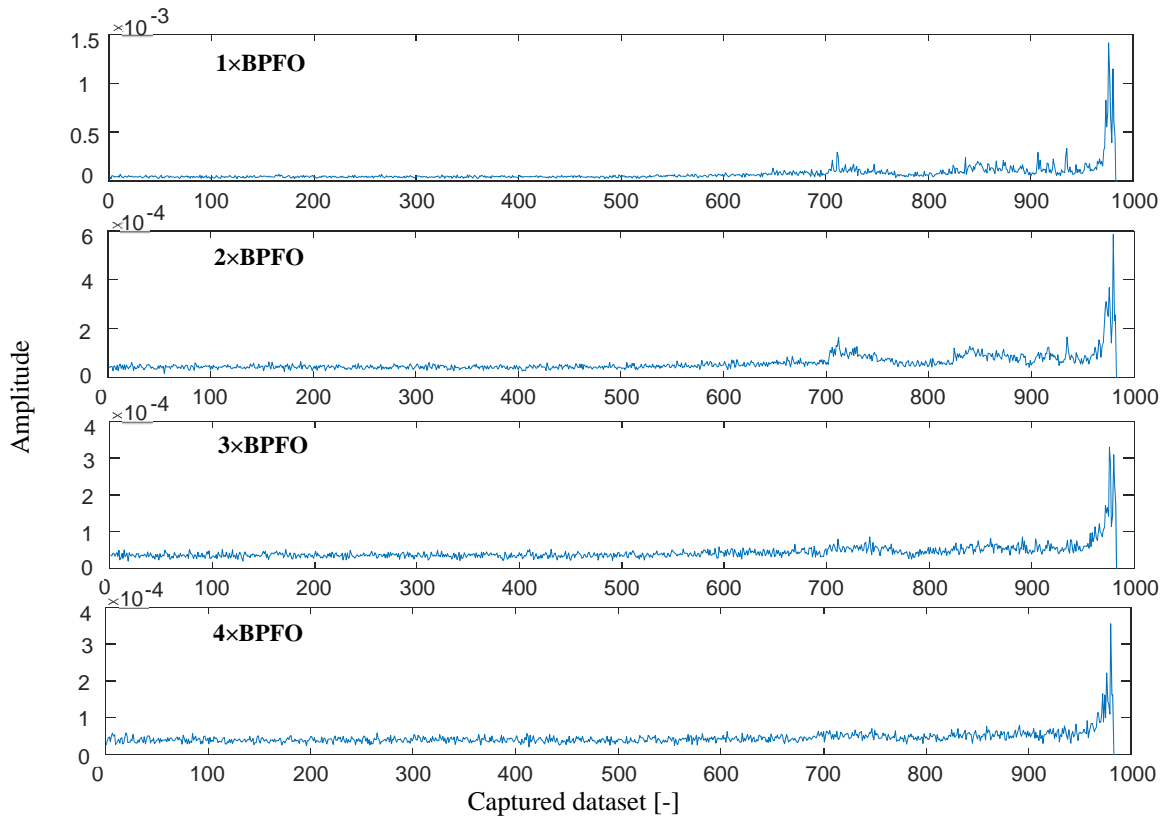Figure 10: The 3D projection of PCs of B3 for test 1.

.

Figure 12: Fault diagnosis results indicating a propagation of an outer race fault on B1 of test 2 using envelope analysis.
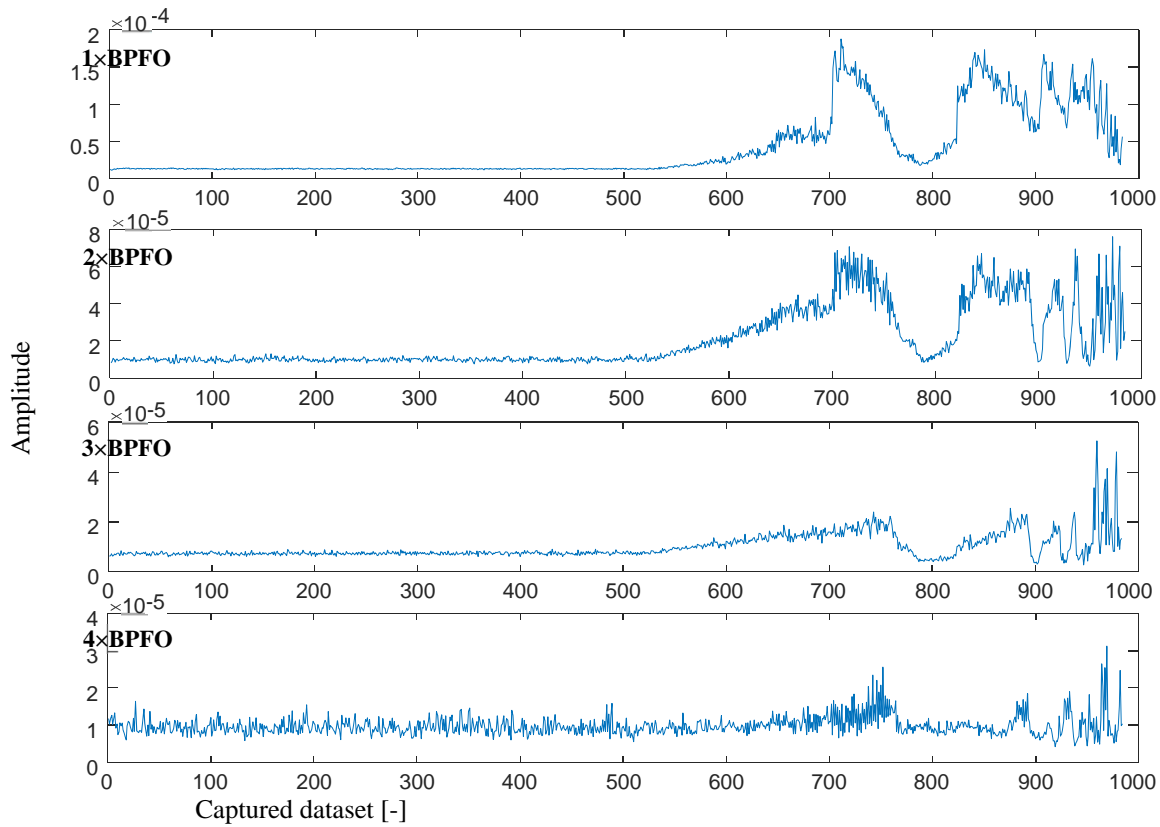

Figure 13: Fault diagnosis results indicating a propagation of an outer race fault on B1 of test 2 using RAC analysis.

5. Conclusions

In order to avoid the costly and time-consuming maintenance and repairing process, a modern and robust maintenance strategy for rotating machines is required to include vibration-based rolling bearing fault detection and diagnosis scheme.

In this present study, various statistical- and energy-based health monitoring parameters, as bearing fault features, have been studied and investigated in some detail. Using long-term vibration data captured from some run-to-failure tests, it is shown that relying on Kurtosis and/or RMS parameters, as the most common features, may not be sufficient for a reliable bearing condition monitoring system. To overcome this issue, a number of parameters need to be calculated from captured vibration signals. However, this can lead to redundancy of the generated and processed data. As a result, the application of Principle Component Analysis (PCA) in data fusion and data size reduction is shown. It is also observed that the fault detectability of a bearing monitoring system, which calculate some health indicators, can be enhanced by PCA.

In terms of bearing fault diagnostics, a previously proposed method, namely, Recursive Autocorrelation (RAC) analysis, is tested using run-to-failure datasets. The diagnostic results presented here show that the frequency domain-based fault features using the RAC method can lead to an earlier fault detection compared to the traditional envelope analysis, and therefore can be considered as a potential alternative for envelope analysis in real-world industrial applications. However, further investigations should be performed on the RAC method, in particular for signals obtained from a complex system, e.g., gearbox in a drivetrain, to assess its performance in the presence of other vibration sources.

Acknowledgement

References

[1] C. K. Mechefske, (2001) Using Fuzzy Linguistics to Select Optimum Maintenance and Condition Monitoring Strategies, Mechanical Systems and Signal Processing, 15 (6) 1129-1140.

[2] A. E. Baldin, (1986) Technical Diagnostic- and Condition-based Maintenance for Better Plant Availability, Measurement, 4 (1) 7-22.

[3] NASA Reliability-Centered Maintenance Guide (RCM) for Facilities and Collateral Equipment, (2008) US National Aeronautics and Space Administration, September.

[4] X. Zhou, L. Xi and J. Lee, (2007) Reliability Engineering & System Safety, Reliability-centered Predictive Maintenance Scheduling for a Continuously Monitored System Subject to Degradation, 92 (4) 230-534.

[5] K. Jemielniak, (1999) Commercial Tool Condition Monitoring Systems, The International Journal of Advanced Manufacturing Technology, 15 (10) 711-721.

[6] Z. Hameed, Y. S. Hong, Y. M. Cho, S. H. Ahn and C. K. Song, (2009) Condition Monitoring and Fault Detection of Wind Turbines and Related Algorithms: A Review, Renewable and Sustainable Energy Reviews, 13 (1) 1-39.

[7] R. B. Randall, (2011) Vibration-based Condition Monitoring: Industrial, Aerospace and Automotive Applications, Chichester: John Wiley & Sons, Ltd.

[8] R. Golafshan, G. Jacobs, M. Wegerhoff, P. Drichel and J. Berroth, (2018) Investigation on the Effects of Structural Dynamics on Rolling Bearing Fault Diagnosis by Means of Multibody Simulation, International Journal of Rotating Machinery, Article ID 5159189, 18 Pages.

[9] N. Tandon and A. Choudhury, (1999) A Review of Vibration and Acoustic Measurement Methods for the Detection of Defects in Rolling Element Bearings, Tribology International, 32 (8) 469-480.

[10] M. Cerrada, R. Sanchez, C. Li, F. Pacheco, D. Cabrera, J. V. Oliveira and R. E. Vasquez, (2018) A Review on Data-driven Fault Severity Assessment in Rolling Bearings, Mechanical Systems and Signal Processing, 99 (2018) 169-196.

[11] F. Wang, J. Sun, D. Yan, S. Zhang, L. Cui and Y. Xu, (2015) A Feature Extraction Method for Fault Classification of Rolling Bearing based on PCA, Journal of Physics: Conference Series, 628 (2015) 012079.

[12] L. Shuang and L. Meng, (2007) Bearing Fault Diagnosis Based on PCA and SVM, In Proceedings of the 2007 IEEE International Conference on Mechatronics and Automation, Harbin, China, August 5 - 8.

[13] N. R. Sakhthivel, B. B. Nair, M. Elangovan, V. Sugumaran and S. Saravanmurugan, (2014) Comparison of Dimensionality Reduction Techniques for the Fault Diagnosis of Mono Block Centrifugal Pump Using Vibration Signals, Engineering Science and Technology, an International Journal, 17 (1) 30-38.

[14] R. Golafshan, M. Wegerhoff, G. Jacobs and A. I. Ozay, (2017) Vibration-based Condition Monitoring for Wind Turbines: Applications of Singular Value Decomposition, In Proceedings of 17th Drive Train Technology Conference (ATK2017), Aachen, Germany, 7-8 March.

[15] J. Antoni and R. B. Randall, (2002) Differential Diagnosis of Gear and Bearing Faults, ASME Journal of Vibration and Acoustics, 124 (2) 165-171.

[16] R. W. Ngigi, C. Pislaru, A. Ball and F. Gu, (2012) Modern Techniques for Condition Monitoring of Railway Vehicle Dynamics, Journal of Physics: Conference Series, 364 (2012) 012016.

[17] C. Sobie, C. Freitas and M. Nicolai, (2018) Simulation-driven Machine Learning: Bearing Fault Classification, Mechanical Systems and Signal Processing, 99 (2018) 403-419.

[18] J. Singh, A. K. Darpe and S. P. Singh, (2018) Rolling Element Bearing Fault Diagnosis Based on Over-Complete Rational Dilation Wavelet Transform and Auto-Correlation of Analytic Energy Operator, Mechanical Systems and Signal Processing, 100 (2018) 662-693.

[19] Y. Ren, W. Li, Z. Zhu, Z. Tong and G. Zhou, (2017) A New Fault Feature for Rolling Bearing Fault Diagnosis Under Varying Speed Conditions, Advances in Mechanical Engineering, 1-11(6) 9.

[20] Q. B. He, Z. H. Feng and F. R. Kong, (2006) Principal Component Representations for Machine Noise Monitoring, Guangxue Jingmi Gongcheng/Optics and Precision Engineering, 14 (2006) 1093-1099.

[21] M. Gonzalez-Audicana, J. L. Saleta, R. G. Catalan and R. Garcia, (2004) Fusion of Multispectral and Panchromatic Images Using Improved IHS and PCA Mergers Based on Wavelet Decomposition, IEEE Transactions on Geoscience and Remote Sensing, 42 (2004) 1291-1299.

[22] I. Y. Tumer and E. M. Huff, (2003) Analysis of Triaxial Vibration Data for Health Monitoring of Helicopter Gearboxes, Journal of Vibration and Acoustics, 125 (2003) 120-128.

[23] B. M. Gur and C. Niezrecki, (2007) Autocorrelation Based Denoising of Manatee Vocalizations Using The Undecimated Discrete Wavelet Transform, Journal of The Acoustical Society of America, 122 (2007) 188-199.

[24] Reza Golafshan and K. Y. Sanliturk, (2016) Rolling Bearing Fault Diagnosis Using Recursive Autocorrelation and Autoregressive Analyses, In Proceedings of the 23rd International Congress on Sound and Vibration, Athens, Greece, 10-14 July.

[24a] R. Golafshan, M. Wegerhoff, G. Jacobs and K. Y. Sanliturk, (2017) A New Approach for Vibration-based Rolling Bearings Fault Detection in Non-Stationary Operating Conditions, In Proceedings of Schwingungen: Berechnung, Überwachung, Anwendung, Nürtingen, Germany, 10-11 October

[25] STI Field Application Note: Rolling Element Bearings, (2012) REB, Sales Technology, Inc., League City TX.

[26] H. Qin, H. Luo and N. Eklund, (2009) On-Board Bearing Prognostics in Aircraft Engine: Enveloping Analysis or FFT, Air Force Research Laboratory, USA, No. 200925.

[27] L. C. K. Reuben and D. Mba, (2014) Bearing Time-to-Failure Estimation using Spectral Analysis Features, Structural Health Monitoring, 13 (2) 219-230.

[28] J. Antoni and R.B. Randall, (2006) The Spectral Kurtosis: Application to The Vibratory Surveillance and Diagnostics of Rotating Machines, Mechanical systems and signal processing, 20 (2) 308-331.

[29] H. Wang and P. Chen, (2009) A Feature Extraction Method Based on Information Theory for Fault Diagnosis of Reciprocating Machinery, Sensors, 9 (4) 2415-2415.

[30] E. Bechhoefer, D. He and P. Dempsey, (2011) Gear Health Threshold Setting Based On a Probability of False Alarm, In Proceedings of Annual Conference of the Prognostics and Health Management Society, Montreal QC, Canada, 25-29 September.

[31] M. Lei, G. Meng and G. Dong, (2017) Fault Detection for Vibration Signals on Rolling Bearings Based on the Symplectic Entropy Method, Entropy, 19 (11) 607.

[32] T. Han, D. Jiang, X. Zhang and Y. Sun, (2017) Intelligent Diagnosis Method for Rotating Machinery Using Dictionary Learning and Singular Value Decomposition, Sensors, 17 (4) 689.

[33] L. Deng and R. Zhao, (2014) Fault Feature Extraction of a Rotor System Based on Local Mean Decomposition and Teager Energy Kurtosis, Journal of Mechanical Science and Technology, 28 (4) 1161-1169.

[34] J. Lv and J. Yu, (2018) Average Combination Difference Morphological Filters for Fault Feature Extraction of Bearing," Mechanical Systems and Signals Processing, 100 (2018) 827-845.

[35] J. Zhu, T. Nostrand, C. Spiegel and B. Morton, (2014) Survey of Condition Indicators for Condition Monitoring Systems, In Proceedings of Annual Conference of the Prognostics and Health Management Society, Fort Worth, Texas, USA, 29 September - 02 October.

[36] H. Qiu, J. Lee, J. Lin and G. Yu, (2006) Wavelet Filter-based Weak Signature Detection Method and Its Application on Rolling Element Bearing Prognostics, Journal of Sound and Vibration, 289 (4-5) 1066-1090.

[37] J. Lee, H. Qiu, G. Yu, J. Lin, and Rexnord Technical Services, IMS - University of Cincinnati, (2007) Bearing Data Set, NASA Ames Prognostics Data Repository (http://ti.arc.nasa.gov/project/prognostic-data-repository).